

博士論文
Doctoral Dissertation

Fast localization of coalescing binaries
with gravitational wave detectors and low
frequency vibration isolation for KAGRA
(重力波検出器による連星合体の早期方向特定
及びKAGRAのための低周波防振)

令和元年 12 月博士（理学）申請

A Dissertation Submitted for the Degree of Doctor of
Philosophy

December 2019

東京大学大学院理学系研究科
天文学専攻

Department of Astronomy, Graduate School of Science,
The University of Tokyo

藤井 善範
Yoshinori Fujii

Abstract

The first detection of a gravitational wave (GW) signal from the coalescence of two neutron stars by the LIGO-Virgo network in coincidence with an electromagnetic transient opened the era of multi-messenger astronomy [1]. In order to expand GW astronomy with better sky localization, better sky coverage, and more precise parameter estimation [2, 3], the global network of advanced GW detectors will be extended with KAGRA [4, 5] and LIGO-India [6]. In the upcoming years, it is expected that the detectors in the network will have heterogeneous sensitivities, with detectors still at an early configuration and commissioning stage being less sensitive than the more advanced detectors.

We investigate the expected performance regarding fast sky localization of coalescing binaries with a network of three or four GW detectors having heterogeneous sensitivities, such as the LIGO-Virgo, LIGO-KAGRA and LIGO-Virgo-KAGRA network. A hierarchical approach can be used in order to make an effective use of information from the least sensitive detector. In this approach, the presence of an event seen in coincidence in the two more sensitive detectors triggers a focused search in the data of the third (and fourth), less sensitive, detector(s) with a lower SNR threshold.

We show the expected fast localization performance when a hierarchical search is implemented into a GW-EM follow-up pipeline composed of MBTA and Bayestar. We confirm that the hierarchical search will improve both the localization accuracy and precision compared to those achieved by a double coincidence search with the two LIGO detectors alone. The hierarchical network effectively improves the localization accuracy and precision when threshold SNR for the lower sensitivity detector is set to around 3.5 provided that the BNS range of that the detector is greater than 20% of the more sensitive detectors in the case where the detector network is composed of the two LIGO detectors and the Virgo detector. In the case where the detector network is composed of the two LIGO detectors and KAGRA detector, we found a clear sky localization improvement when the relative sensitivity of KAGRA becomes greater than 20% of the more sensitive detectors. In addition, the hierarchical network by four detectors will improve the localization accuracy and precision when threshold SNR for the lowest sensitivity detector is set to around 3.5 provided that the BNS range of that the detector is greater than 30% of most sensitive detectors. This result assumes that the sensitivity of the middle sensitive Virgo detector is half of the LIGO one.

Consequently, we conclude that once the sensitivity of the third or fourth

detector reaches the required one, the search with this hierarchical approach will be most useful when adding new, less sensitive detectors to the network, as they are undergoing commissioning.

As another aspect, operating a fourth robust interferometer is of paramount importance to achieve high network duty cycle and also to reduce the chances to miss detectable events.

Generally the mirrors of the ground-based GW detectors are suspended in order to realize a situation where the test masses are in free-fall condition, and also in order to attenuate the vibration transmission from the ground to the mirror. Since we use multi-pendulum system for suspension system, we have to damp the mechanical resonances and freeze the mirrors in order to start GW observation. Consequently, a system which enables to damp the mechanical resonances rapidly and to suppress the mirror residual motion, is required for more robust interferometer operation. Such system is realized by active controls with sensors and actuators implemented on the suspension system.

KAGRA detector is 3-km interferometric ground-based GW detector in Japan, whose construction started in 2012. KAGRA is now being commissioned and is planned to join to the network in second half of O3 as the fourth detector.

We construct active control system for the low-frequency vibration isolation system for KAGRA, especially for the suspension system which holds the arm cavity mirrors. The target is to achieve required performance for acquiring the interferometer lock.

The suspensions which hold the arm cavity mirrors are called Type-A system, which has 13.5 m height, and which consists of 9 stage-pendulum. The lower 4 stages of the Type-A system are to be operated at cryogenic temperature for the detector noise reduction. For the purpose of cooling, the stages of the lower 4 stages are connected each other with high purity aluminum cables, called heat links. The absorbed heat on the mirror flows to upper stages and is then extracted to the cryostat structure through the heat links including its vibration isolation system. I.e, Type-A suspension is mechanically large and a highly complex system.

We then conduct the following tests for the evaluation of the KAGRA Type-A suspension and its control system:

1. suspension mechanical response,
2. damping control performance for the mechanical resonance damping mode,
3. RMS suppression control performance for the lock-acquisition phase.

Based on the first test, we conclude that the assembled Type-A suspension has the characteristics of the pendulum, although some of the unexpected resonances which would be related to the heat link system are observed. From this issue, we find that we have to include the heat link system in the model of the suspension

mechanics for the further precise estimation. From the second test, we confirm that the installed damping control system satisfies its requirement for the lock-recovery mode. The third test demonstrates the feedback control system using displacement sensors by a feed-forward system with seismometer on the ground effectively suppressed the mirror residual motion and it satisfies the requirement in the time scale of 1 min.

Consequently, we conclude that this work contributes to accomplishment of KAGRA suspension local control system toward the more robust operation.

Acknowledgements

I sincerely thank all of you who shared the time with me in there five years and half.

Table of Contents

Abstract	1
Acknowledgements	4
1 Introduction	9
1.1 General relativity and Gravitational waves	9
1.1.1 Gravity in general relativity	9
1.1.2 Theoretical expression of gravitational waves	10
1.1.3 Properties of gravitational wave	11
1.1.4 Emission of gravitational wave	14
1.2 Expected astrophysical sources	20
1.2.1 Compact binary coalescence	20
1.2.2 Supernovae	20
1.2.3 Stochastic background	20
1.3 Detection with interferometer	21
1.3.1 Basic principle	21
1.3.2 Fabry-Perot cavity	23
1.3.3 Fundamental noise sources	24
1.3.4 Power recycling technique and Resonant side-band extraction	26
1.4 Data analysis for compact binary coalescence	28
1.4.1 Antenna Patterns	28
1.4.2 Matched filtering	28
1.5 Detector network and multi-messenger observation	29
1.5.1 Source localization	29
1.5.2 Multi-messenger observation	30
1.6 Targets and Outline	30
2 Benefit of adding detectors to the observation network	33
2.1 Fast localization with heterogeneous network	34
2.2 Calculation set up	35
2.2.1 Simulated data set and injections	36
2.2.2 Generating artificial triggers for Virgo	40
2.2.3 Attributing parameters to Virgo triggers in HLV-network .	40
2.2.4 Generating artificial triggers for KAGRA	43
2.2.5 Attributing parameters to KAGRA triggers in HLK-network	43
2.2.6 Generating artificial triggers for Virgo and KAGRA	45
2.2.7 Figures of merit	45
2.3 Expected performance of heterogeneous HLV-network	46
2.3.1 Sky localization performance	46

2.3.2	Dependence on the sensitivity of Virgo detector	46
2.4	Expected performance of heterogeneous HLK-network	49
2.4.1	Dependence on the sensitivity of KAGRA detector	49
2.4.2	Comparison to HLV-network performance	51
2.5	Expected performance of heterogeneous HLVK-network	54
2.5.1	Dependence on the sensitivity of the fourth detector KAGRA	54
2.6	Summary	58
3	Low Frequency Vibration Isolation	59
3.1	Seismic motion	59
3.2	Passive vibration isolation	62
3.2.1	Basic principle	62
3.2.2	Mechanical filters for gravitational wave detectors	70
3.2.3	Inverted pendulum	70
3.2.4	Geometric Anti-Spring	72
3.3	Active vibration isolation	76
3.3.1	Feedback control	76
3.3.2	Feedback control with feed-forwarding	80
4	KAGRA Type-A Seismic Attenuation System	83
4.1	Optical layout of KAGRA detector	83
4.2	Displacement noise requirement	84
4.3	Overview of KAGRA suspensions	87
4.4	Mechanical Systems of Type-A suspension	90
4.4.1	Pre-isolation stage	92
4.4.2	GAS filter chain	95
4.4.3	Suspension rod	97
4.4.4	Magnetic damper	97
4.4.5	Bottom-Filter damping system	98
4.4.6	Cryogenic payload	100
4.5	Cooling system	101
4.6	Expected isolation performance	103
4.7	Sensors and Actuators	104
4.7.1	Linear Variable Differential Transducer	104
4.7.2	Inertial sensor	105
4.7.3	Optical levers	107
4.7.4	Reflective photo sensor	107
4.7.5	Coil-magnet actuator	109
4.7.6	Seismometer	110
4.7.7	Digital signal processing	111
5	Suspension control design	113
5.1	Requirements	113
5.1.1	Control phases	113
5.1.2	Requirement on damping time	114

5.1.3	Requirement on RMS velocity	114
5.1.4	Requirement on RMS angular fluctuation	117
5.1.5	Requirement on longitudinal displacement	117
5.1.6	Requirement on Type-A suspension control	117
5.2	System modeling	119
5.2.1	3D rigid-body dynamics	119
5.2.2	State-space representation	120
5.3	Basic control topology	121
5.4	Controls for calm-down phase	123
5.4.1	Servo system	123
5.5	Controls for lock-acquisition phase	125
5.5.1	Suppression with sensor correction technique	125
5.6	Controls for observation phase	128
6	Performance test of local control for KAGRA Type-A suspen- sion	129
6.1	Suspension configuration	129
6.1.1	Mechanical and environmental configuration	129
6.1.2	Sensor and actuator arrangement	130
6.2	Mechanical response	131
6.2.1	Diagonal transfer functions	131
6.2.2	Effect of heat-links and its vibration isolation system . . .	142
6.2.3	Summary of mechanical system characterization	142
6.3	Performance of mechanical vibration isolation	143
6.3.1	Measurement set up	143
6.3.2	Measurement	144
6.3.3	Summary	145
6.4	Performance of damping control	147
6.4.1	Servo system	147
6.4.2	Decay time measurement	151
6.4.3	Further steps for the damping system	156
6.5	Performance of seismic noise suppression control	158
6.5.1	Control system	158
6.5.2	Impact on a local suspension	161
6.5.3	Residual motion	167
6.6	Summary of the performance test	169
7	Conclusion and future works	171
7.1	Conclusion	171
7.1.1	Fast localization with heterogeneous detector network . . .	171
7.1.2	Type-A local suspension control	172
7.2	Future works	174
7.2.1	Type-A local suspension control	174

A	Supplemental note for study of fast localization	175
A.1	Typical parameters for data analysis	175
A.2	Triggered event population	177
A.2.1	LIGO-Virgo network case	177
A.2.2	LIGO-KAGRA network case	177
A.2.3	LIGO-Virgo-KAGRA network case	177
A.2.4	Dependence on the sensitivity of the fourth detector KA- GRA with different SNR thresholds in Virgo	186
B	Detailed characteristics of Type-A suspension	189
B.1	Simulated eigen mode list of Type-A suspension	189
B.2	Type-A suspension configuration during the measurement	195
B.3	Axis difference among the X-arm cavity and X-arm suspensions	196
B.4	Position dependence of LVDT noise floor	197
B.5	Measured decay time constant table	199
C	Supplementary note for sensor correction system	201
C.1	Impact on X-arm cavity displacement signal	201
C.1.1	Setting for ITMX suspension	201
C.1.2	Impact on X-arm cavity displacement	201

Chapter 1

Introduction

The existence of gravitational waves (GWs) was predicted by A. Einstein in 1916 according to his theory of general relativity [7]. 100 years after the prediction, a GW signal from the coalescence of two black holes was detected for the first time in 2015 by the Laser Interferometric Gravitational-wave Observatory (LIGO) in the U.S. [8]. In 2017, the first detection of a GW signal from the coalescence of two neutron stars by LIGO-Virgo network in coincidence with an electro-magnetic transient was achieved and this opened the era of multi-messenger astronomy [1].

This chapter describes the background of detection of GWs, the target and the outline of this thesis. Section 1.1 summarizes the theoretical aspect of GWs. Section 1.2 introduces GW sources expected to be detected. Section 1.3 describes the interferometric detection method, which is used for the current GW detectors. Section 1.4 briefly summarizes how an analysis is processed for the search for the compact binary coalescence (CBC) sources. Section 1.6 summarizes the target and outline of this thesis.

1.1 General relativity and Gravitational waves

1.1.1 Gravity in general relativity

In general relativity (GR), the Einstein field equation describes the relationship between the metric of spacetime and the mass distribution as:

$$G_{\mu\nu} \equiv R_{\mu\nu} - \frac{1}{2}g_{\mu\nu}R = \frac{8\pi G}{c^4}T_{\mu\nu}. \quad (1.1)$$

The variables in eq (1.1) are summarized as follows:

- $g_{\mu\nu}$: Metric tensor, which characterizes the geometry of spacetime. $g_{\mu\nu}$ is a dimensionless quantity and is defined as the inner product of basis vectors:
 $g_{\mu\nu} \equiv \mathbf{e}_\mu \cdot \mathbf{e}_\nu$.
- $T_{\mu\nu}$: Energy-momentum tensor, which characterizes mass distribution. The elements of $T_{\mu\nu}$ include the following quantities:

T_{00} : Energy density, T_{i0} : i th element of momentum density,
 T_{0j} : j th element of energy flux,
 T_{ij} : Stress tensor in non-relativistic fluid dynamics ($i, j = 1, 2, 3$).

- $G_{\mu\nu}$: Einstein tensor
- $R_{\mu\nu} \equiv R^\alpha_{\mu\alpha\nu}$: Ricci tensor, which is defined by

$$R^\mu_{\alpha\beta\gamma} \equiv \frac{\partial\Gamma^\mu_{\alpha\beta}}{\partial x^\gamma} - \frac{\partial\Gamma^\mu_{\alpha\gamma}}{\partial x^\beta} + \Gamma^\mu_{\lambda\gamma}\Gamma^\lambda_{\alpha\beta} - \Gamma^\mu_{\lambda\beta}\Gamma^\lambda_{\alpha\gamma},$$
 where $\Gamma^\mu_{\alpha\beta} \equiv g^{\mu\nu} \left(\frac{\partial g_{\beta\nu}}{\partial x^\alpha} + \frac{\partial g_{\alpha\nu}}{\partial x^\beta} - \frac{\partial g_{\alpha\beta}}{\partial x^\nu} \right)$.
- $R \equiv g^{\mu\nu}R_{\mu\nu}$: Scalar curvature (or Ricci scalar).
- G : Gravitational constant.
- c : Speed of light.

In the eq (1.1), the line element ds between two points x^μ and $x^\mu + dx^\mu$, which are infinitesimally separated from each other, is $ds^2 = (dx^\mu \mathbf{e}_\mu) \cdot (dx^\nu \mathbf{e}_\nu) = g_{\mu\nu} dx^\mu dx^\nu$, where $\mathbf{e}_\mu, \mathbf{e}_\nu$ denote the basis vectors of the coordinates. In spacetime which is described by the metric $g_{\mu\nu}$ as defined above, the motion of a free particle is explained by its geodesic equation:

$$\frac{d^2 x^\alpha}{d\tau^2} = \Gamma^\alpha_{\mu\nu} \left(\frac{dx^\mu}{d\tau} \right) \left(\frac{dx^\nu}{d\tau} \right), \quad (1.2)$$

where τ is an arbitrary parameter. By using these equations, GR concludes that what we observe as gravity is a curvature of spacetime. The characteristics of gravity are described by the metric in GR. The more details in this chapter are described in [9].

1.1.2 Theoretical expression of gravitational waves

The equation which describes the GWs are derived from the Einstein equation; first, we derive eq (1.1) in a weak gravitational field. Since spacetime is flat if there is no gravity, we assume that the spacetime is mostly flat in the weak gravitational field. In the weak field, the metric $g_{\mu\nu}$ is explained by the superposition of a metric of flat spacetime, that is, Minkowski metric $\eta_{\mu\nu}$ and that of a small perturbation $h_{\mu\nu}$:

$$g_{\mu\nu} = \eta_{\mu\nu} + h_{\mu\nu} + \mathcal{O}(h^2), \quad (|h_{\mu\nu}| \ll 1). \quad (1.3)$$

In above equation, $h_{\mu\nu}$ describes actual spacetime as a perturbation from Minkowski spacetime. The quantities in eq (1.3) are defined for following calculation:

$$h^\mu_{\ \nu} \equiv \eta^{\mu\lambda} h_{\lambda\nu}, \quad h^{\mu\nu} \equiv \eta^{\mu\alpha} \eta^{\nu\beta} h_{\alpha\beta}, \quad h \equiv \eta^{\mu\nu} h_{\mu\nu}. \quad (1.4)$$

By rearranging eq (1.1) using a formula $g^{\mu\nu} = \eta^{\mu\nu} - h^{\mu\nu} + \mathcal{O}(h^2)$, we obtain eq (1.5). I note that $g_{\mu\nu}$ denotes the inverse matrix of $g^{\mu\nu}$, and that terms in h^2 and higher are neglected in this calculation.

$$\begin{aligned}
G_{\mu\nu} &= \frac{8\pi G}{c^4} T_{\mu\nu} \\
&\simeq R_{\mu\nu} - \frac{1}{2}\eta_{\mu\nu}R \\
&= \frac{1}{2}(-\square h_{\mu\nu} + \partial_\nu\partial^\alpha h_{\mu\alpha} + \partial_\mu\partial^\alpha h_{\nu\alpha} - \partial_\mu\partial_\nu h - \eta_{\mu\nu}\partial^\alpha\partial^\beta h_{\alpha\beta} + \eta_{\mu\nu}\square h), \quad (1.5)
\end{aligned}$$

where $\partial_\mu \equiv \frac{\partial}{\partial x^\mu}$, $\partial^\alpha = \eta^{\alpha\nu}\partial_\nu$ and $\square \equiv \partial^\alpha\partial_\alpha = \eta^{\alpha\beta}\partial_\alpha\partial_\beta = -\frac{1}{c^2}\partial_t^2 + \nabla^2 = -\frac{1}{c^2}\frac{\partial^2}{\partial t^2} + \frac{\partial^2}{\partial x^2} + \frac{\partial^2}{\partial y^2} + \frac{\partial^2}{\partial z^2}$. Here, by applying a gauge transformation which satisfies the following condition:

$$\partial^\alpha h_{\mu\alpha} - \frac{1}{2}\partial_\mu h = 0, \quad (1.6)$$

we obtain the below equation:

$$\square \left(h_{\mu\nu} - \frac{1}{2}\eta_{\mu\nu}h \right) = -\frac{16\pi G}{c^4} T_{\mu\nu}. \quad (1.7)$$

This equation is called the linearized Einstein equation. In most cases, eq (1.7) is expressed as follows by using another tensor $\bar{h}_{\mu\nu} \equiv h_{\mu\nu} - \frac{1}{2}\eta_{\mu\nu}h$:

$$\square \bar{h}_{\mu\nu} = -\frac{16\pi G}{c^4} T_{\mu\nu}. \quad (1.8)$$

This $\bar{h}_{\mu\nu}$ is called trace-reversed tensor, and has the relationship below:

$$\bar{h} \equiv \bar{h}^\mu{}_\mu = -h^\mu{}_\mu = -h. \quad (1.9)$$

Note that $\bar{h}_{\mu\nu}$ satisfies $\partial_\mu \bar{h}^\mu{}_\nu = 0$, under the condition of eq (1.6). Eq (1.8) explains the wave equation of the $\bar{h}_{\mu\nu}$ which describes the small perturbation $h_{\mu\nu}$ from the Minkowski metric. Eq (1.8) also implies that $\bar{h}_{\mu\nu}$ propagates away from the source of the energy-momentum tensor $T_{\mu\nu}$ with the speed of light c . Here, If a vacuum condition $T_{\mu\nu} = 0$ ($= R_{\mu\nu} = R$), i.e., a spacetime without masses is considered, eq (1.8) becomes

$$\square \bar{h}_{\mu\nu} = 0. \quad (1.10)$$

Consequently, the expression becomes similar to the wave equation for electromagnetic waves which propagate in vacuum. This ripple of the spacetime $\bar{h}_{\mu\nu}$, which propagates with speed of light c , describes a GW.

1.1.3 Properties of gravitational wave

Here we briefly explore the properties of GWs which propagate in vacuum, by considering a monochromatic plane wave:

$$\bar{h}_{\mu\nu} \equiv a_{\mu\nu} e^{ik_\alpha x^\alpha} = a_{\mu\nu} \exp[i(\mathbf{k} \cdot \mathbf{r} - \omega t)], \quad (1.11)$$

where k^α denotes the wave vector $k^\alpha = (\omega/c, k^1, k^2, k^3)$, $a_{\mu\nu}$ describes its amplitude via a 4×4 matrix of constant numbers. Here, we can choose the following gauge conditions so that $a_{\mu\nu}$ (or $\bar{h}_{\mu\nu}$) holds only information about the GWs []:

$$\bar{h}_{0\nu} = 0, \quad (1.12)$$

$$\bar{h}^i{}_i = 0, \quad (1.13)$$

$$\partial_j \bar{h}^{ij} = 0. \quad (1.14)$$

The set of conditions eq (1.12) to (1.14) is called the transverse traceless (TT) gauge. In most cases, GWs are discussed under this gauge. Under this gauge, we obtain the following properties of GWs:

- Eq (1.12) says that GWs have only space element.
- Eq (1.13) says that GWs are traceless and thus the difference between $\bar{h}_{\mu\nu}$ and $h_{\mu\nu}$ vanishes due to this equation ($\bar{h}_{\mu\nu}^{\text{TT}} = h_{\mu\nu}^{\text{TT}}$).
- Eq (1.14) says that GWs are transverse waves.

Here, by inserting eq (1.11) into eq (1.14), we obtain the following equation:

$$k^j a_{ij} = k^j \bar{h}_{ij} = 0. \quad (1.15)$$

This equation describes that the wave vector is orthogonal with \bar{h}_{ij} . In addition, if we consider a plane GW which propagates along the z axis, we get the below $a_{\mu\nu}$ by using the equations $k^\mu = (k^0, k^1, k^2, k^3) = (\omega/c, 0, 0, \omega/c)$, $a_{12} = a_{21}$ and $a_{11} + a_{22} = 0$:

$$a_{\mu\nu}^{\text{TT}} = \begin{pmatrix} 0 & 0 & 0 & 0 \\ 0 & a_+ & a_\times & 0 \\ 0 & a_\times & -a_+ & 0 \\ 0 & 0 & 0 & 0 \end{pmatrix}. \quad (1.16)$$

This expression implies that GW have two degrees of freedom.

Polarization

The remaining two degrees of freedom appear as polarizations. These two polarizations are called *plus* and *cross* mode according to the distortion shapes. If we suppose that some free point masses are put in a circle around a point (0,0,0) whose radius is given by L . First, the line element ds^2 between the origin and one of the masses is

$$\begin{aligned} ds^2 &= - (cdt)^2 + dl^2 \\ &= - (cdt)^2 + (1 + h_+)dx^2 + 2h_\times dx dy + (1 - h_+)dy^2 + dz^2. \end{aligned} \quad (1.17)$$

If a two dimensional plane is considered, dl^2 becomes:

$$dl^2 = (1 + h_+)dx^2 + 2h_\times dx dy + (1 - h_+)dy^2. \quad (1.18)$$

In this condition, if a GW is injected along the z axis, the infinitesimal distances between the origin and one of the masses, dx , dy vary as

$$dl^2 \simeq dx'^2 + dy'^2 \quad (1.19)$$

$$\begin{pmatrix} dx' \\ dy' \end{pmatrix} = \begin{pmatrix} 1 + \frac{1}{2}h_+ & \frac{1}{2}h_\times \\ \frac{1}{2}h_\times & 1 - \frac{1}{2}h_+ \end{pmatrix} \begin{pmatrix} dx \\ dy \end{pmatrix}. \quad (1.20)$$

Finally, if we use $(dx, dy) \equiv (L \cos \theta, L \sin \theta)$, the proper distance l is

- if $h_+ \neq 0, h_\times = 0$;
according to $dl^2 = (1 + h_+)dx^2 + (1 - h_+)dy^2 \simeq L^2(1 + h_+ \cos 2\theta)$,

$$l \simeq L \times \left(1 + \frac{1}{2}h_+ \cos 2\theta\right) \quad : \quad + \text{ mode}, \quad (1.21)$$

- if $h_+ = 0, h_\times \neq 0$;
according to $dl^2 = dx^2 + dy^2 + 2h_\times dx dy \simeq L^2(1 + h_\times \sin 2\theta)$,

$$l \simeq L \times \left(1 + \frac{1}{2}h_\times \sin 2\theta\right) \quad : \quad \times \text{ mode}. \quad (1.22)$$

By inserting $h_+ = a_+ \exp[i(kz - \omega t)]$, or $h_\times = a_\times \exp[i(kz - \omega t)]$ into these equations, the location of the masses become as shown in Figure 1.1.

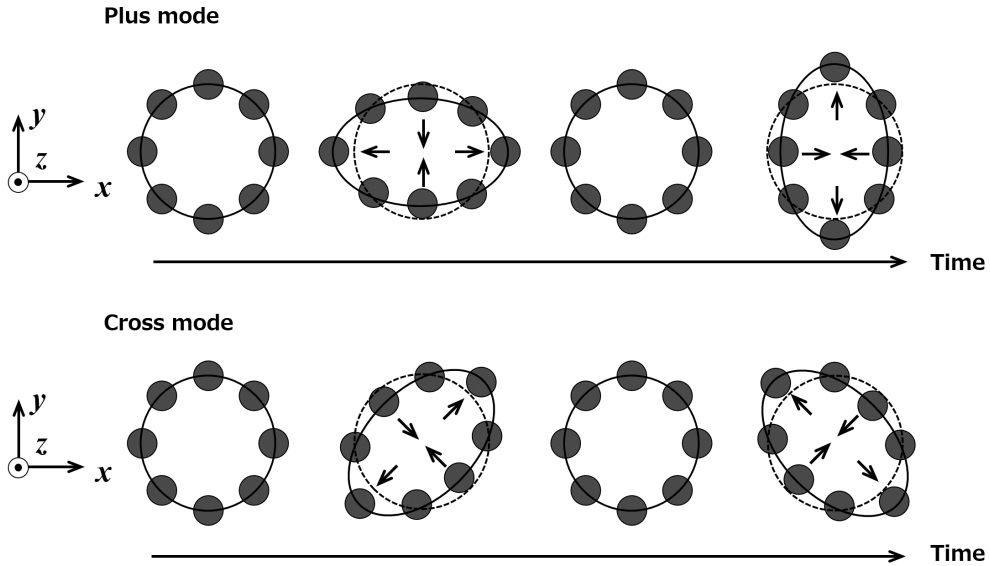


Figure 1.1: Polarizations of a GW. Black points denote free particles. If a GW incidents into $+z$ axis, the positions of free particles arrayed in circle are changed as shown in this figure.

Effect on free point mass

We consider how a GW affects free point masses here. If we suppose that a free point mass is at rest at a coordinate and is then exposed to a GW (in the TT gauge), the geodesic equation of the free point mass is expressed by

$$\frac{dU^\alpha}{d\tau} + \Gamma^\alpha_{\mu\nu} U^\mu U^\nu = 0, \quad (1.23)$$

where U^α denotes the coordinate velocity of the mass. Then due to $h_{\beta 0}^{TT} = 0$, the initial acceleration of the mass is always 0:

$$\left(\frac{dU^\alpha}{d\tau}\right)_{\text{initial}} = -\Gamma^\alpha_{00} = \frac{1}{2}\eta^{\alpha\beta}(\partial_0 h_{\beta 0} + \partial_0 h_{0\beta} + \partial_\beta h_{00}) = 0. \quad (1.24)$$

This implies that if we choose the TT gauge, the basis changes so that the each mass stays at the original coordinate position.

Here we examine the behavior of the proper distance between two free point masses. If we set the masses at origin $(0,0,0)$ and $(L,0,0)$, the proper distance l is

$$\begin{aligned} l &= \int |ds^2|^{1/2} = \int |g_{\alpha\beta} dx^\alpha dx^\beta|^{1/2} \\ &= \int_0^L |g_{xx}|^{1/2} dx \simeq |g_{xx}(x=0)|^{1/2} \times L \\ &\simeq \left\{1 + \frac{1}{2}h_{xx}^{TT}(x=0)\right\} \times L, \end{aligned} \quad (1.25)$$

where $h_{xx}^{TT}(x=0)$ is a non-zero term. Thus the eq(1.24) and eq(1.25) implies that neither of the two masses move but the proper distance l is changed if a GW is injected. Consequently, we can sense the GWs by observing the proper distance(s) between two (or more) masses. In addition, according to eq(1.25), the length shift due to the GW injection ΔL is described by

$$\frac{\Delta L}{L} = \frac{1}{2}h, \quad (1.26)$$

where h is the spatial distortion in the measurement direction.

1.1.4 Emission of gravitational wave

Here we take a look at the GW emissions according to the linearized Einstein equation. First, we transform eq (1.8) using a Green's function for the d'Alembert operator $G(x^\sigma - y^\sigma)$:

$$G(x^\sigma - y^\sigma) = -\frac{1}{4\pi|\mathbf{x} - \mathbf{y}|} \delta(|\mathbf{x} - \mathbf{y}| - (x^0 - y^0)) \theta(x^0 - y^0), \quad (1.27)$$

$$\square G(x^\sigma - y^\sigma) = \delta^{(4)}(x^\sigma - y^\sigma) \quad (1.28)$$

where $\sigma = 0, 1, 2, 3$, $\delta(x)$ and $\theta(x)$ denote Dirac's δ function and a step function respectively. We also assume that \mathbf{x} and \mathbf{y} are the observing location and the source position respectively. Hence the distance between \mathbf{x} and \mathbf{y} is $|\mathbf{x} - \mathbf{y}| = \{\delta_{ij}(x^i - y^i)(x^j - y^j)\}^{1/2}$. Note that $\theta(x^0 - y^0)$ is equal to 1 where $x^0 > y^0$ is satisfied, otherwise it equals to 0. With this setting, $\bar{h}_{\mu\nu}$ is expressed as below by using eq (1.8), eq (1.27) and eq (1.28), if we assume that the observation point is far enough away compared to the size of the source, that is, $r \equiv |\mathbf{x}| \gg |\mathbf{y}|$:

$$\begin{aligned}\bar{h}_{\mu\nu}(t, \mathbf{x}) &= -\frac{16\pi G}{c^4} \int G(x^\sigma - y^\sigma) T_{\mu\nu}(y^\sigma) d^4 y \\ &= \frac{4G}{c^4} \int \frac{T_{\mu\nu}(ct - |\mathbf{x} - \mathbf{y}|, \mathbf{y})}{|\mathbf{x} - \mathbf{y}|} d^3 y, \\ &\simeq \frac{4G}{rc^4} \int T_{\mu\nu}(ct - r, \mathbf{y}) d^3 y.\end{aligned}\quad (1.29)$$

For the next step, here we consider the local energy-momentum conservation, i.e., $\partial_\nu T^{\mu\nu} = 0$. Under this condition, we obtain the relationship $\partial_\alpha \partial_\beta (T^{\alpha\beta} x^\mu x^\nu) = 2T^{\mu\nu}$ and the integration below:

$$\int T^{ij} d^3 y = \frac{1}{2c^2} \frac{d^2}{dt^2} \int T^{00} y^i y^j d^3 y = \frac{1}{2} \frac{d^2}{dt^2} \int \rho y^i y^j d^3 y. \quad (1.30)$$

Then if we define a quadrupole mass distribution I_{ij} as:

$$I_{ij} \equiv \int \rho y^i y^j d^3 y, \quad (1.31)$$

\bar{h}_{ij} is given by eq (1.32), From eq (1.29):

$$\bar{h}_{ij}(t, \mathbf{x}) = \frac{2G}{rc^4} \ddot{I}_{ij}(ct - r). \quad (1.32)$$

In this expression, we find that the amplitude of a GW is proportional to the second derivative of the quadrupole with respect to time. Here, if we consider the TT gauge, eq (1.32) becomes

$$\bar{h}_{ij}^{\text{TT}}(t, \mathbf{x}) = \frac{2G}{rc^4} \ddot{\mathcal{I}}_{ij}(ct - r), \quad (1.33)$$

$$\text{where } \bar{h}_{ij}^{\text{TT}} = \left(P_i^k P_j^l - \frac{1}{2} P_{ij} P^{kl} \right) \bar{h}_{kl}, \quad P_j^i \equiv \delta_j^i - n^i n_j, \quad n^i \equiv x^i / r,$$

$$\mathcal{I}_{ij} \equiv \int \rho \left(x^i x^j - \frac{1}{3} \delta_{ij} r^2 \right) d^3 x.$$

In summary, GWs are generated when the quadrupole moment changes with time.

A typical luminosity of a GW is approximately summarized here using a formula is given by:

$$\frac{dE_{\text{GW}}}{dt} = \frac{G}{5c^5} \langle \ddot{\mathcal{I}}^{ij} \ddot{\mathcal{I}}_{ij} \rangle. \quad (1.34)$$

If the source is characterized by mass M , size R , emitting time duration T and the velocity $v = R/T$, eq (1.34) becomes

$$\begin{aligned} \frac{dE_{\text{GW}}}{dt} &\sim \frac{G}{c^5} \left(\frac{MR^2}{T^3} \right)^2 \sim \frac{c^5}{G} \left(\frac{GM}{Rc^2} \right)^2 \left(\frac{v}{c} \right)^6 \\ &\sim 3.6 \times 10^{59} [\text{erg/s}] \left(\frac{GM}{Rc^2} \right)^2 \left(\frac{v}{c} \right)^6 \\ &\sim 1.0 \times 10^{26} \times L_{\odot} \left(\frac{r_s}{2R} \right)^2 \left(\frac{v}{c} \right)^6, \end{aligned} \quad (1.35)$$

where r_s denotes the Schwarzschild radius $2GM/c^2$. Moreover, if the virial theorem ($Mv^2 \sim GM^2/R$) is available in this system, eq (1.35) becomes

$$\frac{dE_{\text{GW}}}{dt} \sim 1.0 \times 10^{58} [\text{erg/s}] \left(\frac{r_s}{R} \right)^5 \sim 2.6 \times 10^{25} \times L_{\odot} \left(\frac{r_s}{R} \right)^5. \quad (1.36)$$

More particularly, if we consider two equal-mass objects which follow Kepler's law, the luminosity is expressed as the following assuming that $2GM \sim (2\pi/T)^2 R^3$ is available,

$$\frac{dE_{\text{GW}}}{dt} \sim 1.2 \times 10^5 \times L_{\odot} \left(\frac{1\text{s}}{T} \right)^{10/3} \left(\frac{M}{M_{\odot}} \right)^{10/3}. \quad (1.37)$$

We then have the luminosity about $1.2 L_{\odot}$ when these parameters are to set $T = 1$ s, $M = M_{\odot}$. This implies that detectable GWs come not from events on the earth but from violent celestial events.

Approximate estimation: GW from coalescing binary

Based on the above, we briefly check the typical properties of GWs such as amplitude and frequency. We consider a system composed by two point-particles in a plane in uniform circular motion with the Newton's gravitational force as shown in Figure 1.2. The masses are m_1 and m_2 respectively, and Ω is the angular frequency of the uniform circular motion. In this estimation, we assume that we can neglect the tidal force compared to the gravitational force in the system. In this setting, we obtain the positions of the two particles in the center-of-mass system as:

$$\mathbf{r}_1 = \left(\frac{m_2}{M} a \cos(\Omega t + \Phi), \frac{m_2}{M} a \sin(\Omega t + \Phi) \right), \quad (1.38)$$

$$\mathbf{r}_2 = \left(-\frac{m_1}{M} a \cos(\Omega t + \Phi), -\frac{m_1}{M} a \sin(\Omega t + \Phi) \right). \quad (1.39)$$

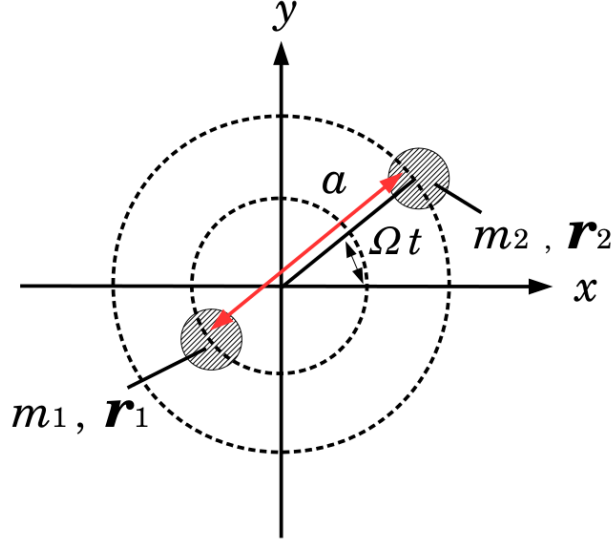


Figure 1.2: A binary system composed by two point-particles in a plane in uniform circular motion with the newton's gravitational force.

In the above, the quantities are defined as follows: gravitational constant G , the distance between the two particles a and total mass $M(= m_1 + m_2)$, respectively.

In this system, by following eq (1.32), the amplitudes of GW of the *plus*- and *cross*-mode h_+ , h_\times are described by:

$$h_+ = - \frac{2}{ra} \frac{Gm_1}{c^2} \frac{Gm_2}{c^2} \cos(2\Omega t_{ret} - 2\phi + 2\Phi) (\cos^2 \theta + 1), \quad (1.40)$$

$$h_\times = - \frac{2}{ra} \frac{Gm_1}{c^2} \frac{Gm_2}{c^2} \sin(2\Omega t_{ret} - 2\phi + 2\Phi) 2 \cos \theta, \quad (1.41)$$

where t_{ret} is defined by $t_{ret} = t - r/c$. For this calculation, we assume that the the observation point is at the origin of the coordinate, and the binary system is at (r, θ, ϕ) . Since we assume that the tidal force is negligible compare to the gravitational force, the frequency of the GWs f_{GW} from this system is given by:

$$f_{GW} = 2\Omega = \frac{1}{\pi} \sqrt{\frac{GM}{a^3}} = \frac{1}{\pi} \sqrt{\frac{G(m_1 + m_2)}{(R_1 + R_2)^3}}. \quad (1.42)$$

We then think the time evolution. Since the energy of the system is decreased by the emission of GW, their orbital distances decrease, and this causes the frequency of the GWs to increase until the moment of coalescence. By assuming that GW takes away the energy of the system, we obtain the following about the orbital radius a :

$$\dot{a} = - \frac{64}{5} \frac{G^3 m_1 m_2 M}{c^5} \frac{1}{a^3} \equiv - K \frac{1}{a^3}. \quad (1.43)$$

By choosing the initial condition as $a(t_{ret} = t_0) = 0$, the time evolution of a is written as $a = [4K(t_0 - t_{ret})]^{1/4}$. From eq (1.42) and eq (1.43), the derivative of the frequency of GW is also written as:

$$\dot{f}_{\text{GW}} = \frac{96}{5}\pi^{8/3} \left(\frac{GM_c}{c^3}\right)^{5/3} f_{\text{GW}}^{11/3}, \quad (1.44)$$

where $M_c = (m_1 m_2)^{3/5} / M^{1/5}$, which is so-called chirp mass. We then obtain the followings as the time evolution of the frequency f_{GW} and the strain amplitude h_+ , h_\times :

$$f_{\text{GW}}(\tau) \sim 135 \text{ Hz} \left(\frac{M_c}{1.2M_\odot}\right)^{5/8} \left(\frac{\tau}{1\text{s}}\right)^{-3/8} \quad (1.45)$$

$$h(\tau) \sim 2.1 \times 10^{-23} \left(\frac{M_{\text{chirp}}}{1.2M_\odot}\right)^{5/3} \left(\frac{r}{200\text{Mpc}}\right)^{-1} \left(\frac{\tau}{1\text{s}}\right)^{-1/4}, \quad (1.46)$$

where τ is $t_0 - t_{ret}$, the time to coalescence. Figure 1.3 and 1.4 summarizes the time evolution of h_+ , a and f_{GW} , assuming a binary system composed by two point masses at 100 Mpc away whose masses are $1.4M_\odot$. A condition $\theta = \pi/2$, $\phi = 0$ is also assumed. For this example case, in order to get a GW amplitude larger than 10^{-21} in strain, we have to wait until about 20 sec before the collision. At that time the separation of the two objects is about 250 km based on eq (1.44). As in later section, with current sensitivities of the GW detectors, we would oftenly see the final scene of the coalescence.

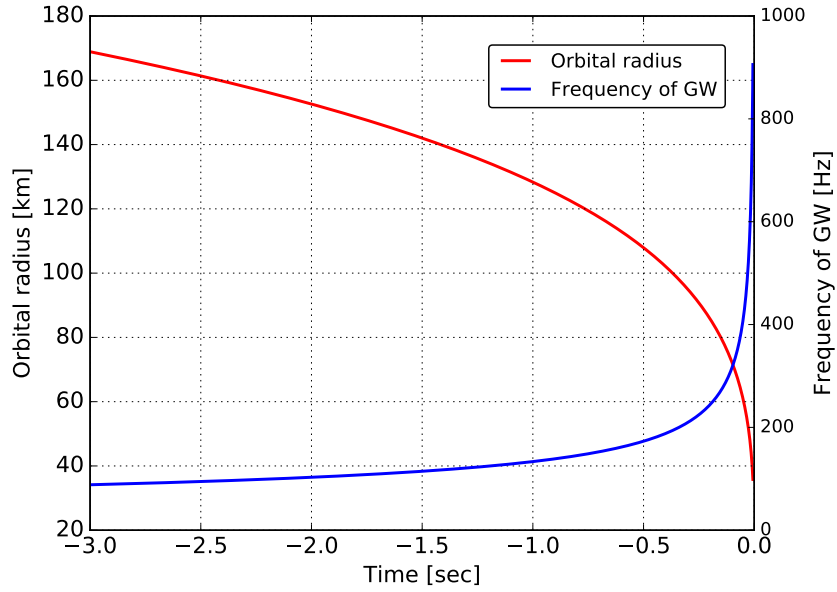


Figure 1.3: Final 3 sec time evolution of the orbital radius a and the frequency of GW f_{GW} , assuming a binary system composed by two neutron stars at 100 Mpc away whose masses are $1.4M_{\odot}$.

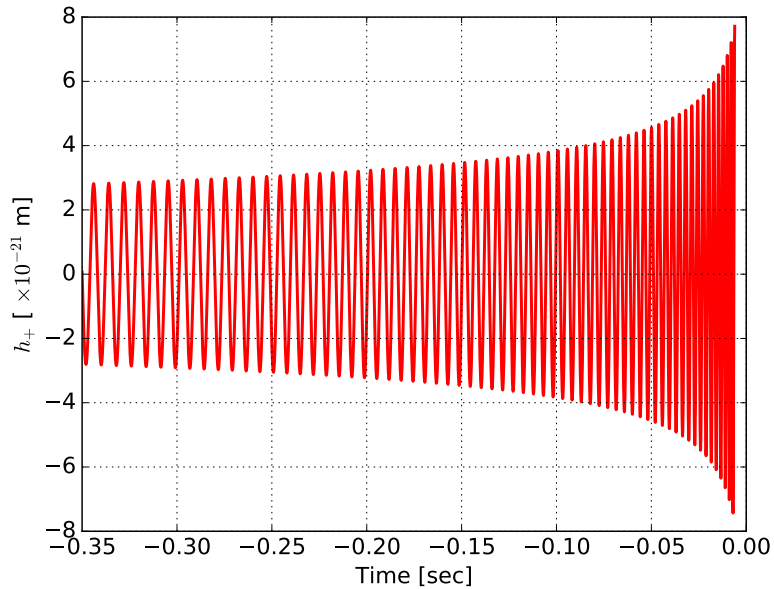


Figure 1.4: Final 0.35 sec time evolution of the strain amplitude of GW h_+ , assuming a binary system composed by two neutron stars at 100 Mpc away whose masses are $1.4M_{\odot}$. The final 0.35 sec is drawn.

1.2 Expected astrophysical sources

As examined in section 1.1.4, more promising GW sources are the astrophysical phenomena. This subsection introduces the typical properties of the GWs from expected astrophysical sources.

1.2.1 Compact binary coalescence

The compact binary merger such as neutron stars and black holes are important candidate sources of GWs. The compact binary coalescence is the most interesting GW source. The typical feature is introduced in section 1.1.4.

1.2.2 Supernovae

A core-collapse supernova is a candidate source which emits a large-amplitude gravitational wave. This is because it accelerates an huge amount of mass dramatically in a short period and asymmetrically. The prediction of the actual wave forms emitted from supernovae is challenging; however, progress in the field of numerical relativity allows the magnitude of the emitted gravitational waves to be estimated [10]. The amplitude from a supernova that happens in a nearby galaxy is of the order of $h \sim 10^{-22} - 10^{-21}$. According to the models for this calculation, the frequency of the gravitational waves emitted from the supernovae are spread widely around 1 kHz. Thus, supernovae in a nearby galaxy can be reasonable target sources for current gravitational wave detectors.

1.2.3 Stochastic background

A stochastic background of gravitational waves is expected from numerous unresolved astrophysical sources such as white dwarf binaries, cosmological origins such as inflation, phase transition in the early universe and cosmic strings [11]. The amplitude and the frequency of the gravitational waves with cosmological origins depends on the theory considered. Detection of stochastic backgrounds is generally conducted by investigating cross-correlation between observations by several detectors.

1.3 Detection with interferometer

This section describes how to detect the GWs with laser interferometric technique.

1.3.1 Basic principle

according to the polarization mentioned in section 1.1.3, We need to monitor the differential displacements of two masses in orthogonal directions. For detection of GWs, the simplest interferometric configuration would be a Michelson interferometer built with suspended mirrors as shown in Figure 1.5. As the result of interference, a fraction of the beam goes to the photodiode and the remainder goes back to the laser source. The output beam intensity at the photodiode P_{out} is then given by

$$P_{\text{out}} = \frac{1}{2}P_0(1 - \cos \delta\phi), \quad (1.47)$$

where P_0 , λ , and $\delta\phi = 2\pi(L_x - L_y)/\lambda$ represent the incident laser power, the wavelength of the laser beam, and the phase difference between the two optical paths, respectively. Consequently, We can obtain information about the phase shift by monitoring the beam intensity on the photodiode.

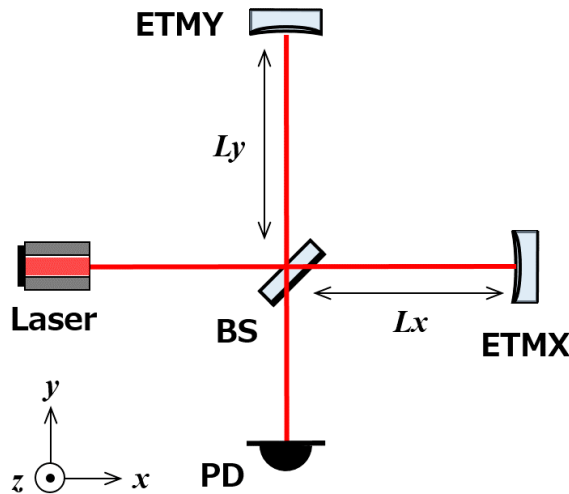


Figure 1.5: An optical configuration of a Michelson interferometer. ETMX(Y), BS, PD denote the end mirrors at X(Y) end, the beam splitter, and photo-detector, respectively.

We then calculate how the GW affects to the phase difference between the two optical paths $\delta\phi$. we suppose that a GW which has plus polarization and amplitude $h(t)$ is injected along the $+z$ direction. If we consider that one of the

photons comprised by the laser beam in the x direction, from eq (1.17) and this configuration, the line element ds^2 of the photon is given by

$$\frac{dx}{dt} = \frac{c}{\sqrt{1+h_+(t)}}, \quad (1.48)$$

by using $dy = dz = ds^2 = 0$. The round trip time Δt_1 of a photon between the beam splitter and one end mirror is given by:

$$\int_t^{t+\Delta t_1} \frac{dt'}{\sqrt{1+h_+(t')}} = \frac{2l_1}{c}. \quad (1.49)$$

If we use $(1+h)^{-1/2} \sim (1-h/2)$ by assuming $|h_+| \ll 1$, the above equation becomes

$$\Delta t_1 = \frac{2l_1}{c} + \frac{1}{2} \int_t^{t+\Delta t_1} h_+(t') dt'. \quad (1.50)$$

Since the first term is larger compared to the second term due to $|h_+| \ll 1$ on the right hand side, we can set the integral upper limit at $t + 2l_1/c$. Consequently, the phase shift ϕ_1 due to Δt_1 is written by

$$\phi_1 = \frac{2\pi c}{\lambda} \left(\frac{2L_x}{c} + \frac{1}{2} \int_t^{t+2L_x/c} h_+(t') dt' \right), \quad (1.51)$$

where λ is the wavelength of the laser. In the same way, the phase shift ϕ_2 for the other axis is given by:

$$\phi_2 = \frac{2\pi c}{\lambda} \left(\frac{2L_y}{c} - \frac{1}{2} \int_t^{t+2L_y/c} h_+(t') dt' \right). \quad (1.52)$$

By using ϕ_1 and ϕ_2 , the phase difference $\Delta\phi = \phi_1 - \phi_2$ of the two optical paths is

$$\begin{aligned} \Delta\phi &= \frac{4\pi}{\lambda} (L_x - L_y) \\ &+ \frac{2\pi c}{\lambda} \left(\frac{1}{2} \int_t^{t+2L_x/c} h_+(t') dt' + \frac{1}{2} \int_t^{t+2L_y/c} h_+(t') dt' \right). \end{aligned} \quad (1.53)$$

The first term is the phase shift due to the arm length shift, while the second term is the shift due to the GW transient. By assuming that $L_x \sim L_y = L$ for simplicity, the phase shift due to the GW (the second term) $\delta\phi_{\text{GW}}$ is written by

$$\delta\phi_{\text{GW}}(t) = \frac{2\pi c}{\lambda} \left(\int_t^{t+2L/c} h_+(t') dt' \right). \quad (1.54)$$

In a case where the change of $h_+(t)$ is slow enough, $\delta\phi_{\text{GW}}(t) = 4\pi h_+ L/\lambda$. The frequency response of the Michelson interferometer to GWs, $H_{\text{MI}}(\omega)$, is given by following equation by using the Fourier transform:

$$H_{\text{MI}}(\omega) = \frac{\tilde{\phi}_{\text{GW}}(\omega)}{\tilde{h}_{\text{GW}}(\omega)} = \frac{4\pi c}{\lambda} \exp(-i\omega L/c) \frac{\sin(\omega L/c)}{\omega l/c}. \quad (1.55)$$

where ω is an angular frequency of a GW. This equation implies that the response $|H_{\text{MI}}|$ is maximized at

$$L = \frac{\pi c}{2\omega} = \frac{c}{4f_{\text{GW}}}. \quad (1.56)$$

By following (1.55), ideally the optimal arm length for a GW of 250 Hz becomes 300 km, for example. Even though to construct a Michelson interferometer with large arm is one solution to increase a phase shift caused by GW transient, we cannot construct such a large-scale interferometer on the Earth. Thus some techniques to expand effective arm lengths are necessary for further sensitivity improvement.

1.3.2 Fabry-Perot cavity

One option to expand the effective optical path lengths is to Fabry-Perot cavities, in which the light is reflected multiple times while keeping the optical paths aligned. The light incident into the cavity is reflected many times between the mirrors. The optical configurations is illustrated in Figure 1.6. The frequency response of a Fabry-Perot Michelson interferometer (FPMI) to gravitational waves is given by

$$H_{\text{FPMI}}(\omega) = \frac{4\pi L\alpha}{\lambda} \frac{\exp(-i\omega L/c)}{1 - r_F r_E \exp(-2i\omega L/c)} \frac{\sin(\omega L/c)}{\omega L/c}, \quad (1.57)$$

when the two Fabry-Perot cavities are in resonance condition [12]. α is given by

$$\alpha = \frac{t_F^2 r_E}{1 - r_F r_E}, \quad (1.58)$$

where r_F and r_E denote the amplitude reflectivity of the front and end mirrors, and t_F represents the transmissivity of the front mirror. The bounce number in a Fabry-Perot cavity N is given by

$$N = \frac{2\sqrt{r_F r_E}}{1 - r_F r_E} = \frac{2\mathcal{F}}{\pi}. \quad (1.59)$$

Here \mathcal{F} denotes the sharpness of the resonance of the Fabry-Perot cavity and is called the finesse.

The amplitudes of the frequency responses H_{MI} and H_{FPMI} are shown in Figure 1.7 assuming that the arm lengths are set to 3 km in all cases, and that The finesse \mathcal{F} is set at 80 for FPMI.

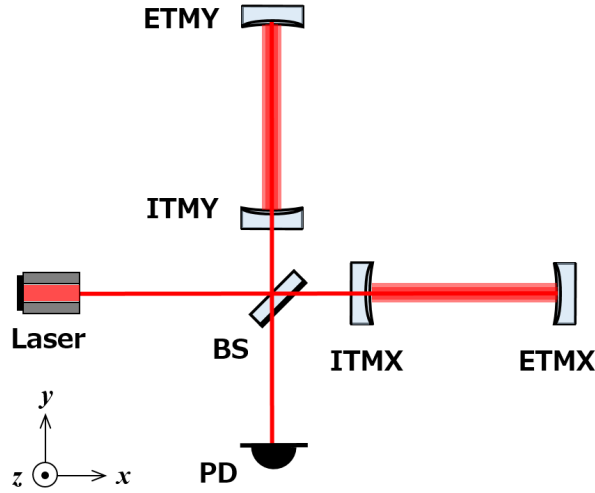


Figure 1.6: An optical configuration of a Fabry-Perot Michelson interferometer (FPMI). The input mirrors labeled ITMX(Y) are added to the configuration in Figure 1.5.

1.3.3 Fundamental noise sources

In a laser interferometric ground-based GW detectors, we have the following noise sources which fundamentally or possibly limit its sensitivity. The sensitivity of the detector is fundamentally limited by the seismic noise, thermal noise and shot noise. The other noise sources are the candidates possibly limit the sensitivity.

Seismic noise

At the low frequency, the sensitivity of a ground-based detector critically depends on vibrations of the optics induced by the seismic vibration. This is called seismic noise. In order to detect GWs with the ground-based detectors, the seismic motion have to be suppressed typically by 10^{-8} to 10^{-10} at 10 Hz. The seismic noise at higher than about 0.1 Hz is attenuated by using vibration isolation systems based on pendulum systems and springs. The seismic noise at lower frequency than about 0.1 Hz, which is related to the tidal morion of the ground for example, is compensated by using the strain signal sensed by the interferometer or geophysical interferometer developed in [13].

Thermal noise

Since the mirror and the suspension system are in thermal baths and receive energy from their surroundings, a random energy flow to and from the thermal baths can happen, and this causes a fluctuation of the optical paths of the interferometer. This noise is called thermal noise. In the field of GW detection,

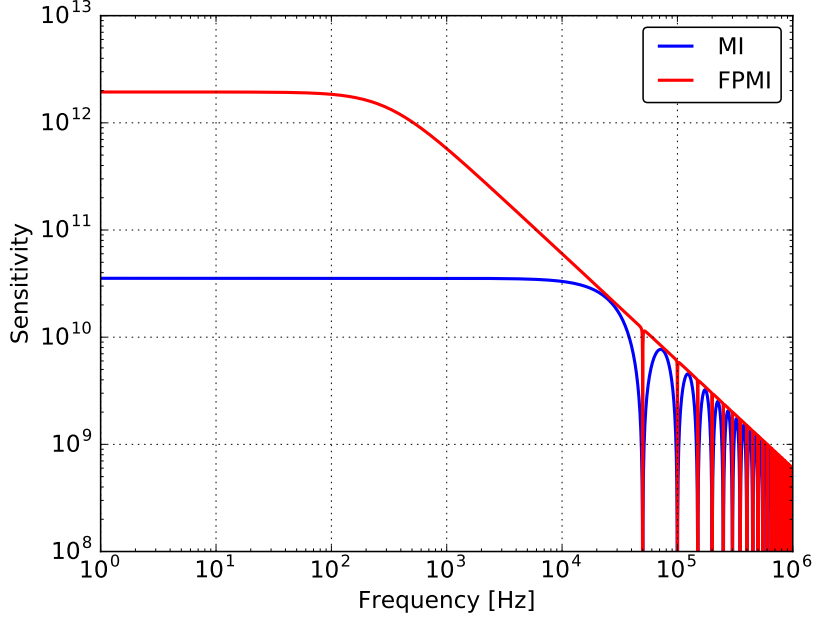


Figure 1.7: Amplitudes of the frequency responses H_{MI} and H_{FPMI} with 3 km arm length. MI and FPMI denotes Michelson interferometer and Fabry-Perot Michelson interferometer, respectively. The finesse \mathcal{F} is set at 80 for FPMI. The wavelength of the laser is assumed the following: $\lambda = 1064$ nm.

thermal noise induced in mirror substrates is called mirror thermal noise, while the noise caused in the suspension systems is called suspension thermal noise. In order to suppress the impact from the thermal noise, fused silica is typically used for room-temperature mirror substrates [14], while sapphire is a good candidate for cryogenic temperature mirror substrates [15],[16].

Shot noise

A photodetector counts the number of photons and converts it into photocurrent. In the process, the number of photons counted, or the electrons composing the photocurrent, has a probability distribution, which results in fluctuations of the measured rate. The noise induced by this fluctuation is called shot noise. The shot noise is a fundamental noise in optical power sensing, associated with the quantum nature of light. This noise in length sensing caused by the probability distribution is proportional to $\sqrt{P_{\text{in}}}$, where P_{in} is the incident power on the mirrors. While the signal amplitude of the gravitational wave is proportional to P_{in} , the signal to noise ratio is proportional to $1/\sqrt{P_{\text{in}}}$. Consequently the shot noise can be reduced by increasing the power of the laser.

Newtonian noise

It is expected that we would find the direct coupling between the moving ground and the optics due to Newtonian gravitational attraction. This is called Newtonian noise. Since the vibration isolation system attenuates mainly its mechanical motion, this noise cannot be reduced by the suspension system. One option to reduce this noise is to place the interferometer underground where the optics are less affected by the gravity gradient field of surrounding rocks. Another option is to subtract the noise by calculating the gravity gradient from measurements of the ground motion surrounding the optics [17].

Laser noise

since an interferometric GW detector monitors the length between the mirrors using the wavelength of the laser as a reference, noise of a laser such as frequency and intensity fluctuation, can degrade the detector sensitivity. In order to minimize the impact of the intensity fluctuation, the interferometer is operated at a dark fringe, where the photo-detector receives no light in the absence of GW signals.

Residual gas noise

Random motions of molecules can cause fluctuation of the refraction index in the optical paths of an interferometer and this causes fluctuations of the effective arm lengths. This noise is called the residual gas noise. In order to suppress the impact of this noise, the GW detectors are operated in an ultrahigh vacuum condition.

1.3.4 Power recycling technique and Resonant side-band extraction

For further improvement of the detector sensitivity, additional mirrors are added.

Power recycling

In order to reduce the shot noise, we want to increase the laser power. This is realised by putting a mirror at the incident-laser side. By reflecting the light which comes back from the Michelson interferometer to it again, the laser power at BS becomes increased. This technique is called power recycling, the added mirror is called power recycling mirror (PRM). The cavity composed of PRM and the Michelson interferometer with ITMX(Y) and BS is called power recycling (PR) cavity.

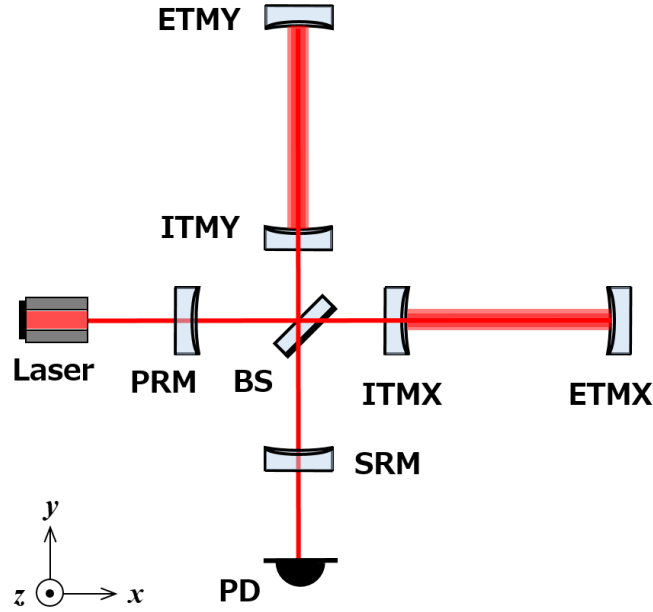


Figure 1.8: On optical configuration of Fabry-Perot Michelson interferometer with the power and signal recycling mirrors. The cavity composed of PRM and the Michelson interferometer with ITMX(Y) and BS is called power recycling (PR) cavity. On the other hand, the cavity composed of SRM and the Michelson interferometer with ITMX(Y) and BS is called signal recycling (SR) cavity.

Resonant side-band extraction

If the interferometer controls is done so that the Anti-Symmetric (AS) port¹, the common signal of the arm length signal would be found in the incident-laser side, while the differential signal is appeared in AS port. If a mirror is put at the AS port, and if a cavity composed of the newly added mirror, ITMX(Y) and BS, is kept in resonance, the finesse of the arm-cavities for the differential signal is decreased. By doing this, although the shot noise level at the lower frequency region is increased, at the higher frequency region, the shot noise level would be decreased. The added mirror is called signal recycling mirror (SRM) and the cavity composed of SRM and the Michelson interferometer with ITMX(Y) and BS is called signal recycling (SR) cavity.

These above techniques are used in the current ground-based GW detectors, and called dual recycling Fabry-Perot Michelson interferometer (DRFPMI). The schematic view of the optical configuration is shown in Figure 1.8.

¹The port which is not incident-laser side of a Michelson interferometer.

1.4 Data analysis for compact binary coalescence

This section briefly describes the essence of the analysis of the GWs from compact binary coalescence (CBC), which is called Matched filtering, and also the source localization with triangulation.

1.4.1 Antenna Patterns

As a starting point, we have to consider the angular dependence of the interferometer response to GWs. If we assume that the source is located at (θ, ϕ) , and the source is rotated by ψ . In this configuration, a GW signal $h(t)$ which the interferometer would detect becomes:

$$h(t) = F_+(\theta, \phi, \psi)h_+(t) + F_\times(\theta, \phi, \psi)h_\times(t), \quad (1.60)$$

where $h_+(t)$ and $h_\times(t)$ denote GW signals of the two polarizations. In this eq (1.60), F_+ and F_\times are called antenna pattern functions, and describe how the two GW polarizations are combined at the detector sensing. In this coordinate system, antenna functions are given by

$$F_+(\theta, \phi, \psi) = \frac{1}{2}(1 + \cos^2 \theta) \cos 2\phi \cos 2\psi - \cos \theta \sin 2\phi \sin 2\psi, \quad (1.61)$$

$$F_\times(\theta, \phi, \psi) = \frac{1}{2}(1 + \cos^2 \theta) \cos 2\phi \sin 2\psi + \cos \theta \sin 2\phi \cos 2\psi. \quad (1.62)$$

1.4.2 Matched filtering

Matched filtering is the analysis method oftenly used in searching GW signals from CBCs. The matched filter compares the measured signal to the theoretical signal by taking into account of the detector noise and it outputs signal-to-noise ratio (SNR), $\rho(t)$. For this purpose, the matched filtering needs theoretical wave forms corresponding to all the possible masses and the spins. These wave forms are called templates.

We assume that the detector outputs as the function of time t are given as:

$$x(t) = s(t) + n(t), \quad (1.63)$$

where $s(t)$ is a GW signal and $n(t)$ is the detector noise. The SNR $\rho(t)$ is given by²:

$$\rho^2(t) = 4Re \left[\int_0^\infty \frac{\tilde{x}(f) \tilde{u}^*(f)}{S_n(f)} df \right], \quad (1.64)$$

where $S_n(f)$ is the one-sided noise power spectral sensitivity, $\tilde{x}(f)$ and $\tilde{u}(f)$ are the spectra of $x(t)$ and $u(t)$ respectively, and $u(t)$ is the wave form called template. As

²technically we have other steps to reach $\rho(t)$. For more details, see [18]

supplemental note, in this calculation, we assume that $S_n(f)$ meets the followings:

$$\langle \tilde{n}(f)\tilde{n}^*(f') \rangle = \frac{1}{2}\delta(f-f')S(f), \quad (1.65)$$

where angle $\langle \dots \rangle$ denotes an ensemble average. $S(f)$ has dimension of Hz^{-1} , and satisfies $S(-f) = S(f)$. The factor of $1/2$ is inserted in the definition so that the total noise power is calculated by integrating over the range $0 \leq f < \infty$:

$$\langle n^2(t) \rangle = \int_0^\infty df S(f). \quad (1.66)$$

Consequently, the sets which give higher SNR $\rho(t)$ than a SNR threshold, are to be searched. The maximum SNR above the threshold is called a trigger, and the corresponding event is considered as a candidate event. The generated triggers are also used to make the detection network by several detectors.

1.5 Detector network and multi-messenger observation

1.5.1 Source localization

The position of the source in the sky is localized by triangulation techniques based on the arrival times at the various detectors. This is not only of cosmological interest but also essential for so-called electromagnetic follow-up observation.

By following [19], two-detector network can give the following distribution. Supposing that the source is located at position \mathbf{R} on the unit sphere, and consider two detectors separated by a distance (expressed in light seconds) of \mathbf{D} , in this situation, the difference in the time of arrival of the signal between the two sites is given by $(T_1 - T_2) = \mathbf{D} \cdot \mathbf{R}$. Then assuming that the two detectors have timing accuracies σ_1 and σ_2 , and the observed times t_1 and t_2 , the distribution of the reconstructed location \mathbf{r} would be given by

$$p(\mathbf{r}|\mathbf{R}) \propto p(\mathbf{r}) \exp \left[-\frac{(\mathbf{D} \cdot (\mathbf{r} - \mathbf{R}))^2}{2(\sigma_1^2 + \sigma_2^2)} \right]. \quad (1.67)$$

In the above, it is assumed that the measured time delay $(t_1 - t_2)$ is given by $\mathbf{D} \cdot \mathbf{r}$, and the timing accuracy of one detector is expressed as $\sigma \sim (2\pi\rho\sigma_f)^{-1}$, where ρ is observed SNR, and σ_f is the effective bandwidth of the signal in the detector which is calculated by $\sigma_f^2 = \overline{f^2} - \bar{f}^2$ with

$$\overline{f^n} = 4 \int_0^\infty df \frac{|\tilde{h}(f)|^2}{S(f)} f^n. \quad (1.68)$$

The distribution by three-detector network can be given in a similar way by:

$$p(\mathbf{r}|\mathbf{R}) \propto p(\mathbf{r}) \exp \left[-\frac{1}{2}(\mathbf{r} - \mathbf{R})^T \mathbf{M}(\mathbf{r} - \mathbf{R}) \right], \quad (1.69)$$

where the matrix \mathbf{M} which describes the localization accuracy, is given by

$$\mathbf{M} = \frac{\mathbf{D}_{12}\mathbf{D}_{12}^T}{\sigma_{12}^2} + \frac{\mathbf{D}_{23}\mathbf{D}_{23}^T}{\sigma_{23}^2} + \frac{\mathbf{D}_{31}\mathbf{D}_{31}^T}{\sigma_{31}^2}. \quad (1.70)$$

In the above, the pairwise timing accuracy is given by $\sigma_{ij}^2 = \sigma_i^2 + \sigma_j^2 + \sigma_i^2\sigma_j^2/\sigma_k^2$, where $k \neq i, j$.

Two-detector network will give a ring-shape reconstructed region since it is only possible to restrict the location of the source in the direction parallel to the separation \mathbf{D} between the detectors basically. In order to have a smaller reconstructed region, we need to have more detectors than three of them.

1.5.2 Multi-messenger observation

If we could find the source position by the GW detectors, we can start to probe the sky for signals of electromagnetic counterparts to astrophysical phenomena, such as supernova and binary neutron mergers with available optical telescopes, more effectively. Sky localization by gravitational wave detection will be poor by optical telescope standards, such as roughly up to 100 deg^2 for a coming a few years with the advanced detectors. Hence to be able to quickly scan the relatively large area of the sky, dedicated telescopes GW follow up is necessary, however, the correlated gravitational, electromagnetic and neutrino detections will play an important role in the discovery and subsequent study of astrophysical phenomena.

1.6 Targets and Outline

The first goal of this research is to estimate the impact on the performance of the fast localization of coalescing binaries when a newly constructed detector such as KAGRA enters the observation network by the GW detectors. More concretely, the target is to calculate the improvement on the size of the reconstructed sky maps with the following situation where:

1. the two LIGO detectors find an CBC event,
2. we then analyze the other lower sensitive detectors with a sub-threshold and with the one template reported by the LIGO detectors,

when the sensitivities of the lower sensitive detectors vary. From the estimated sky localization improvement, we obtain requirements for the sub-threshold and sensitivity for a lower sensitive detectors in this hierarchical approach.

The second goal is to build a local control system for the low-frequency vibration isolation system for KAGRA, especially for the system which suspends the arm cavity mirrors. The target is to achieves required performance for acquiring the interferometer lock.

As in section 1.3.3, the sensitivity of the ground-based GW detector is limited by the seismic noise at lower frequency than a few Hz. We then need a vibration isolation system in order to get the designed detector sensitivity. Improving the sensitivity at such lower frequency would allow us to have also to open an opportunity to find a new events such as intermediate-mass black hole merger. On the other hand, however, in order to start the observation by GW detectors, we should acquire the lock of all the complicated cavities and interferometer. To achieve this, we firstly need to construct a system to control the suspensions which the mirrors are suspended in, which enables:

1. to damp all the mechanical resonances rapidly,
2. to reduce the residual motion of the mirror and to keep the mirror orientation.

After the lock acquisition, we have to reduce the technical noise injection such as control noise, keeping the mirror residual small and keeping its orientation. In this research, I construct a system to deal with the resonance damping and the residual motion suppression, and test the performance with the requirements.

Chapter 2 addresses the work about the sky localization improvement. Chapter 3 introduces the basic idea of the lower frequency vibration isolation. Chapter 4 describes the KAGRA suspension system called KAGRA-SAS. Chapter 5 sets the requirements and designs the desired control system for KAGRA-SAS. Chapter 6 summarises the test of the designed and installed controls system. Consequently chapter 7 concludes this work.

Chapter 2

Benefit of adding detectors to the observation network

This chapter describes the benefit of adding new detectors to the network in terms of the fast sky localization performance of the coalescing binaries. We estimate the impact on the fast source localization with GW detectors when the detectors have heterogeneous sensitivities.

Adding GW detectors to the network benefits both the detection confidence and the sky localization of the source. Finding a GW signal in coincidence at a number of distantly separated locations, increases the confidence that the signals are coming from astrophysical sources, rather than from technical glitches in the detector outputs, which are expected to be uncorrelated. In addition, as mentioned in section 1.5, as the number of GW detectors increases, the sky localization becomes more precise, since triangulation techniques are used based on the arrival times at the various detectors for the localization of the source in the sky. The precise prediction of the source position provided by GW detectors plays a crucial role for the EM follow-up observation.

This work focuses on the sky localization performances, especially in the low-latency mode considering situations where the detector sensitivities are heterogeneous in the network detectors. This setting is motivated since we are already facing this configuration, and, likely, this will continue to be the case with more detectors coming on line in the future. In the US, the Advanced LIGO detectors started operation in 2015 following a decade of commissioning and operation of initial LIGO whose construction started in the 1990's. Advanced Virgo started operation two years later in 2017, after a period of commissioning and upgrade of initial Virgo whose construction had also started in the middle of 1990's. Then KAGRA detector whose construction started much later in 2012, is now being commissioned and is planned to join to the network in second half of O3. As a result, currently there are two higher sensitivity, one middle sensitive and one less sensitive detectors.

This chapter addresses the benefit of adding new detectors to the network made of the two higher sensitive detectors in terms of fast localization performance. The total number of detectors in the network in this work is set to three or four, and the calculation is done assuming 100% duty cycle for each detector. The following sections describe the details of this study. The discussion for the case of the LIGO-Virgo network with the hierarchical approach is reproduced from [20].

2.1 Fast localization with heterogeneous network

In the upcoming years, it is expected that the detectors in the network will have heterogeneous sensitivities, with detectors still at an early configuration and commissioning stage being less sensitive than the more advanced detectors. As written in the above, in this section, we investigate how to make an effective use of such a network in order to localize coalescing binaries at best.

Compact coalescing binaries are sources of particular interest for ground-based GW detectors. When detecting the signals from these events, we perform sky localization in a low-latency mode in order to trigger follow-up observations, especially in the electromagnetic spectrum. In a nutshell, low-latency search pipelines that specifically target CBC sources operate in the following way:

1. they process the data with matched filtering, based on a discrete set of templates covering a broad source parameters space, and they record triggers when the SNR of the filtered data exceeds some threshold [18].
2. Triggers coincident in several detectors are identified and used to reconstruct the sky location of the source.
3. Events with sufficient significance are then communicated to the astronomy community for follow-up observations.

The LIGO-Virgo Collaboration has been performing low-latency CBC searches with several pipelines: multi-band template analysis (MBTA) [21], GstLAL [22] and pyCBC Live [23]. Candidate events are uploaded to the GraceDb [24] and processed through the Bayesian rapid localization algorithm (Bayestar) [25] for fast position reconstruction, which generates probability sky maps.

With three or four detectors of heterogeneous sensitivities in terms of typical detection range for CBC sources, a hierarchical approach can be adopted in order to make an effective use of data from the less sensitive detectors. In this approach, the presence of an event seen in coincidence in the two more sensitive detectors triggers a focused search in the data of the third (and fourth), less sensitive, detector(s) with a lower SNR threshold. In this process we look for a signal in a small time window around the time of the identified coincidence and having the

same source parameters.

The following subsections explore the benefit that can be expected from such a hierarchical approach. Particularly this study was conducted in the framework of the MBTA pipeline, coupled to Bayestar for source localization, but the approach and results are quite general and could apply beyond the case of a specific pipeline. Section 2.2 describes the settings of the simulation and the figures of merit of the localization performance. Section 2.3 to 2.5 shows the simulated results.

2.2 Calculation set up

This study is based on simulated data previously generated in the context of [26] and analyzed in order to derive the sky localization performance obtained when post-processing MBTA triggers reported in [21] are used. The data set features 248 simulated signals from binary neutron star (BNS) sources, injected into simulated detector noise designed to match the expected initial performance of the Advanced LIGO detectors [26]. Although the corresponding detector sensitivity, which translated into a BNS detection range of 54 Mpc, does not match the more recent performance of the LIGO detectors, this is not an issue for this study, which depends primarily on the relative sensitivities of the detectors in the network and hardly on the absolute value of the BNS range. Therefore our results are relevant for the current and future LIGO-Virgo-KAGRA network.

In order to build a sky map for the location of a source, Bayestar processes information about the signal as it was measured in each detector (SNR, time and phase of arrival) and also takes as input the sensitivity curve of each detector, represented by the noise power spectral density (PSD). This study investigates the localization performance for the set of injections introduced above with the following network composed by LIGO, Virgo and KAGRA detectors:

- three-detector network made by LIGO-Virgo network,
- three-detector network made by LIGO-KAGRA network,
- four-detector network made by LIGO-Virgo-KAGRA network.

While for the LIGO detectors, the trigger information (SNR, time, and phase) is extracted from running the MBTA pipeline on the data, as was done in [21], for Virgo and KAGRA we use a different procedure. Since we want to explore several relative sensitivities of Virgo and KAGRA compared to LIGO, and several possibilities for the SNR threshold used in the Virgo analysis, but we want to avoid running the analysis multiple times, the Virgo and KAGRA triggers are artificially generated in a way that emulates the result of running the MBTA pipeline and is described below. The overview of main calculation flow is summarized in Figure 2.1.

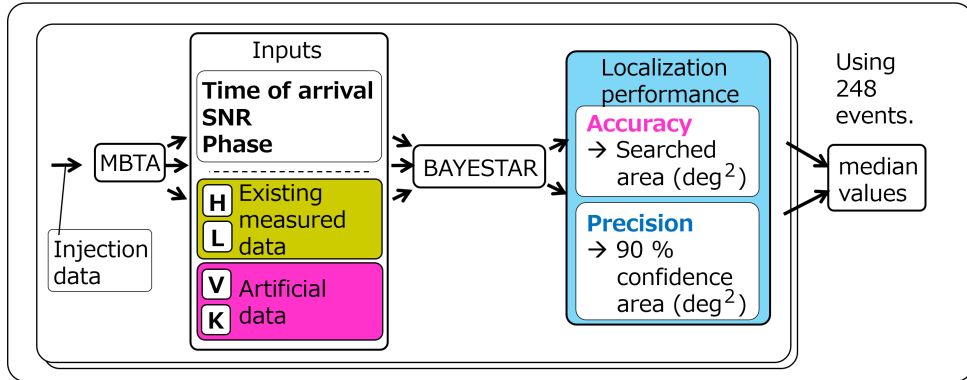


Figure 2.1: Overview of calculation flow. Using sky maps generated for 248 events processed by MBTA and Bayestar, we investigate the accuracy and precision of the localization, quantified by the median values of the searched area and 90% confidence area respectively. We repeat this calculation with different sensitivities and SNR threshold values for the least sensitive Virgo detector (or, less sensitive Virgo and KAGRA detectors).

2.2.1 Simulated data set and injections

The simulated data set used in this study was generated assuming noise curves based on early expectations of the 2015 performance of the detectors [26]. Since we want to explore various cases for the sensitivity of Virgo and KAGRA, the Virgo and KAGRA PSDs were rescaled to correspond to various relative values of the BNS range with respect to LIGO. The noise curves of the network detectors are drawn in Figure 2.2. The 248 BNS injections had component masses uniformly distributed between $1.2M_{\odot}$ and $1.6M_{\odot}$, and dimensionless component spins of up to 0.05. Although the original population of injections composed of 10,000 events was isotropically distributed in space, we consider 248 injections which are detected in the two LIGO detectors, which biases the source directions toward directions favorable for the LIGO detectors. The distribution of the 248 injections is summarized in Figure 2.3 and 2.4.

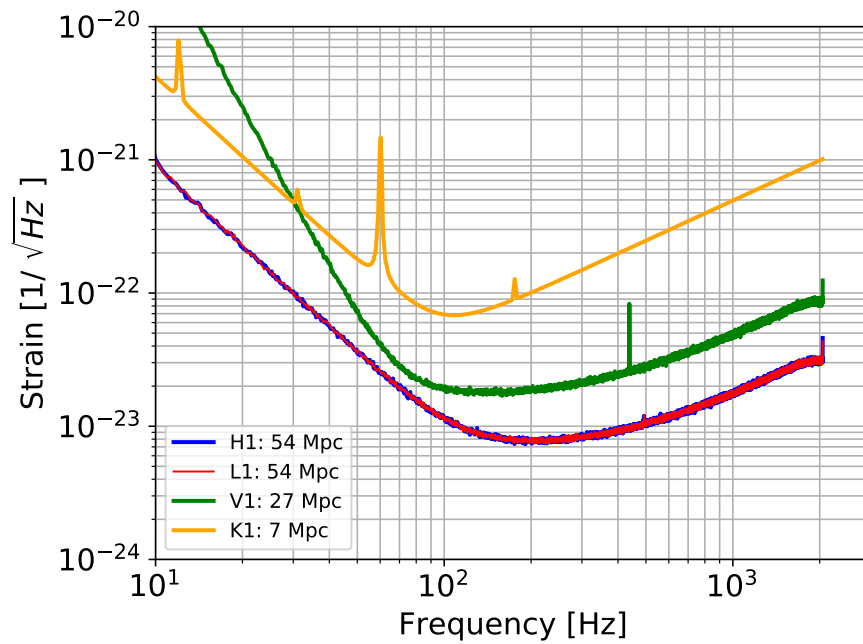


Figure 2.2: The assumed noise curves of the network detectors in amplitude spectral density (ASD). H1, L1, V1, K1 denote the name of the network detectors, i.e., LIGO-Hanford detector, LIGO-Livingston detector, Virgo detector and KAGRA detector, respectively. The distances show the BNS range of each detector. The Virgo and KAGRA PSDs were rescaled to correspond to various relative values of the BNS range with respect to LIGO.

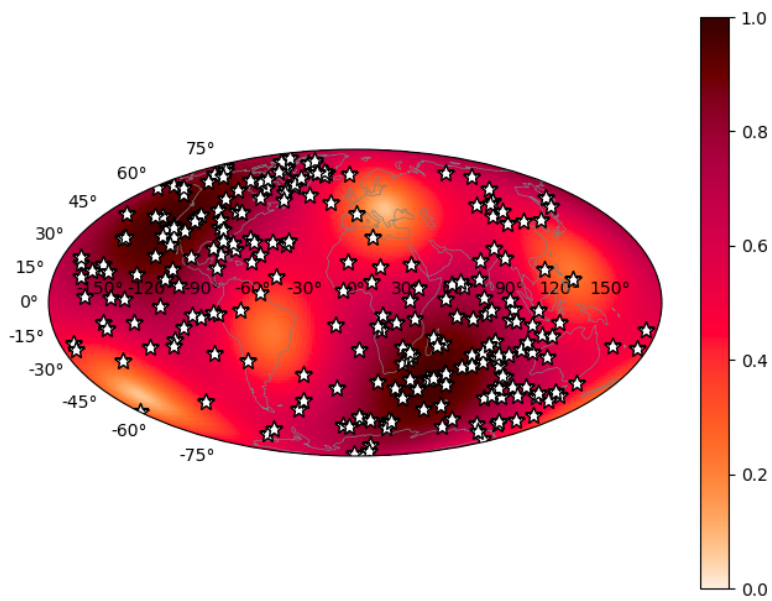
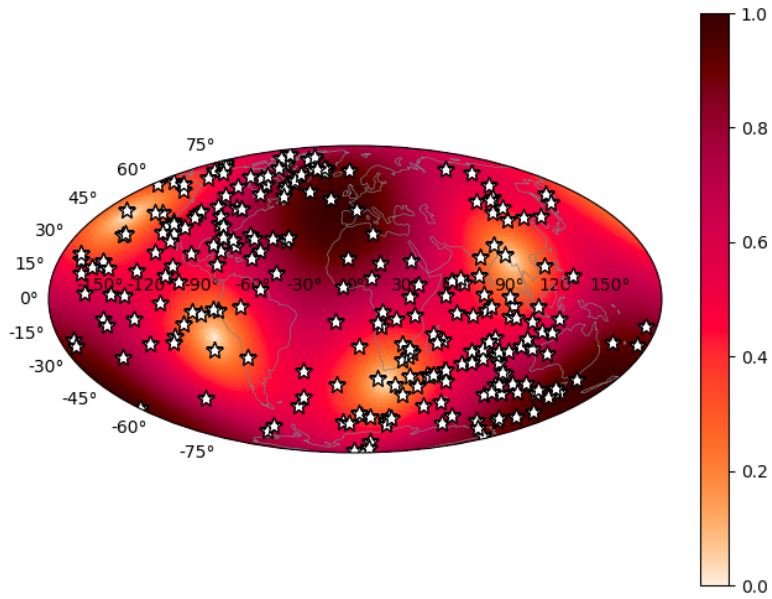
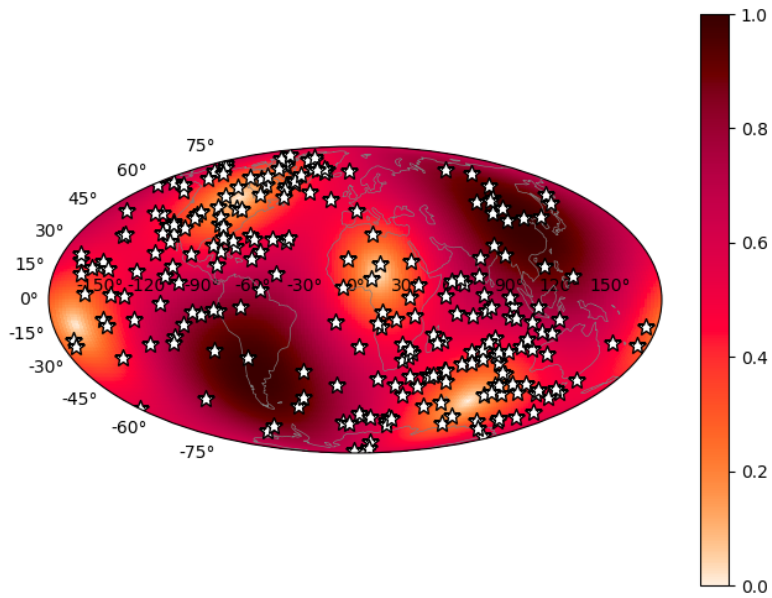


Figure 2.3: The sky locations of the 248 injections considered in this work are shown as stars on top of the color-coded combined antenna pattern of the two LIGO detectors. The sources are not uniformly distributed across the sky, but more favorably positioned with respect to the LIGO antenna pattern.



(a) With antenna pattern of Virgo detector



(b) With antenna pattern of KAGRA detector

Figure 2.4: The sky locations of the 248 injections considered in this work are shown as stars on top of the color-coded antenna pattern of Virgo detector (a) and KAGRA detector (b).

2.2.2 Generating artificial triggers for Virgo

We start from 248 injections detected as HL double coincidences. Depending on the outcome of the targeted search in the Virgo data obtained by looking for a trigger occurring close in time and with the same parameters as the HL coincidence, each of these can either remain a double coincidence if no trigger is found in Virgo (HL case), or else become a triple coincidence (HLV case). The latter case can appear in either one of two possibilities: the trigger found in Virgo is actually related to the injected signal (V_i case) or is related to detector noise (V_n case). The first step of the procedure is therefore to construct a set of injections with appropriate fractions of HL, V_i and V_n cases.

To assess the probability to get a V_n trigger, we need an estimate of the false alarm probability (FAP) in Virgo above a given SNR threshold, for a single template and a time window of 70 ms since we consider Virgo triggers within ± 35 ms of the LIGO triggers. This is derived from the SNR distribution obtained by running MBTA on representative subsets of O1 data, with about 2×10^5 templates, then assuming that the trigger rate is uniform across templates, and extrapolated below the SNR threshold of 6 applied in these analyses. The extrapolation used a Gaussian function, known to be a good approximation for the distribution of triggers at low SNR, which was confirmed by running small-scale analyses with lower SNR thresholds. We use two data sets, one corresponding to Virgo showing nominal behavior (quiet case) and one corresponding to a time of excess noise (noisy case). The SNR distributions are shown in Figure 2.5, along with the FAP as a function of SNR threshold that is derived from them.

For each injection, we estimate the SNR expected in Virgo SNR_V^{expected} from the known effective distance D_{eff}^V , allowing for some statistical uncertainty:

$$SNR_V^{\text{expected}} = 2.26 \times (\text{detection range}) \times 8/D_{\text{eff}}^V + \text{Gauss}(0, 1), \quad (2.1)$$

where $\text{Gauss}(\mu, \sigma)$ is a random number derived from a Gaussian distribution with mean μ and standard deviation σ . More details about the effective distance are given in section A.1. In this formula, the factor 8 is the SNR threshold used to define the horizon distance for an optimally located and oriented source, and the factor 2.26 connects horizon distance to detection range by averaging on source's location and orientation. The V_i case applies if SNR_V^{expected} is above the SNR threshold in Virgo SNR_V^{th} and there is no louder noise trigger, i.e. a random number p_V drawn from a uniform distribution between 0 and 1 is smaller than FAP. The probability of the V_n case depends on the probability of getting a noise trigger above SNR_V^{expected} or above SNR_V^{th} if SNR_V^{expected} is smaller than SNR_V^{th} , i.e. $\text{FAP}(\max(SNR_V^{\text{th}}, SNR_V^{\text{expected}}))$. The procedure is summarized in Table 2.1.

2.2.3 Attributing parameters to Virgo triggers in HLV-network

To produce sky maps for triple coincidences, we need to attribute parameters (SNR, time and phase of arrival) to the V_i or V_n triggers that supplement the

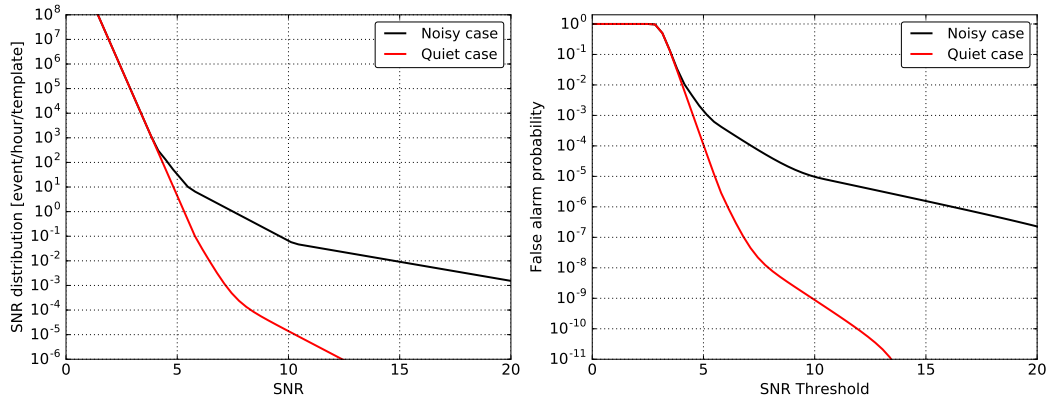


Figure 2.5: (*Left*) SNR distribution of noise triggers per hour and per template based on a measurement done during O1 and extrapolated for SNR below 6. The red curve was obtained on quiet data and the black curve on data with excess noise. (*Right*) False alarm probability (FAP) as a function of the SNR threshold, computed as $FAP = 1 - \exp(-R T)$, with R the rate of triggers above threshold per template, derived from the distribution on the left, and $T = 70$ ms. At low SNR threshold, FAP saturates at about 1 since the rate R becomes quite large.

HL double coincidence. This is done according to the procedure summarized in table 2.2. For V_i triggers we use parameters known from the injection metadata, and add ad-hoc statistical uncertainties. For the latter we started from educated guesses based on our experience of running the MBTA pipeline, which were then slightly adjusted to get consistent sky localization performances for HLV_i cases, i.e. making sure that the fraction of injections found within the area at a given confidence level matches that confidence level.

Table 2.1: Procedure for generating coincident events for LIGO-Virgo network. p_V is a random number from a uniform distribution between 0 and 1. FAP_V is the false alarm probability at a given SNR threshold in Virgo.

Conditions	Generated coincidences
if $p_V < FAP_V(\max(SNR_V^{th}, SNR_V^{expected}))$	H L V_n
else	
if $SNR_V^{expected} > SNR_V^{th}$	H L V_i
if $SNR_V^{expected} < SNR_V^{th}$	H L

Table 2.2: Procedure for attributing parameters to Virgo triggers. $t_{LIGO}^{measured}$ and $\phi_{LIGO}^{measured}$ represent, respectively, the measured time and phase of arrival at either the LIGO-Hanford or the LIGO-Livingston detector. For these parameters, we use the ones whose SNR is closer to the expected SNR of Virgo detector. $\Delta t^{injection}$ and $\Delta \phi^{injection}$ describe the simulated LIGO-Virgo differences of time and phase respectively. $\text{Random}[a : b]$ describes a random number uniformly drawn between a and b . We use 0.11 msec and 0.35 rad as typical measurement uncertainties at an SNR of 6 for the time and phase of arrival. These values have been adjusted so that the localization areas at a given confidence level are statistically self-consistent.

V_n : Virgo trigger from noise	
SNR	randomly drawn from the distribution shown in figure 2.5
Time	$t_{LIGO}^{measured} + \text{Random}[-35 \text{ msec} : 35 \text{ msec}]$
Phase	$\text{Random}[0 : 2\pi]$
V_i : Virgo trigger from injections	
SNR	$2.26 \times (\text{detection range}) \times 8/D_{\text{eff}}^V + \text{Gauss}(0, 1)$
Time	$t_{LIGO}^{measured} + \Delta t^{injection} + \text{Gauss}(0, 0.11 \text{ msec} \times 6/SNR_V^{expected})$
Phase	$\phi_{LIGO}^{measured} + \Delta \phi^{injection} + \text{Gauss}(0, 0.35 \text{ rad} \times 6/SNR_V^{expected})$

2.2.4 Generating artificial triggers for KAGRA

The basic idea is same as described in section 2.2.2. I.e, we generate K_i and K_n triggers in the same manner as Virgo trigger generation with the parameters for KAGRA. The difference is the time window used for the calculation of the FAP for KAGRA. We used 80 ms as the time window since we consider KAGRA triggers within ± 30 ms and ± 40 ms, based on the light flight time between LIGO-Hanford to KAGRA and LIGO-Livingston to KAGRA respectively. Consequently the FAP for KAGRA is slightly different from the FAP for Virgo, as shown in Figure 2.6. Other parameters are defined as:

$$SNR_K^{\text{expected}} = 2.26 \times (\text{detection range}) \times 8/D_{\text{eff}}^K + \text{Gauss}(0, 1), \quad (2.2)$$

$$SNR_K^{\text{th}} = (\text{SNR threshold in KAGRA}), \quad (2.3)$$

where D_{eff}^K is the effective distance for KAGRA. The procedure is summarized in Table 2.3.

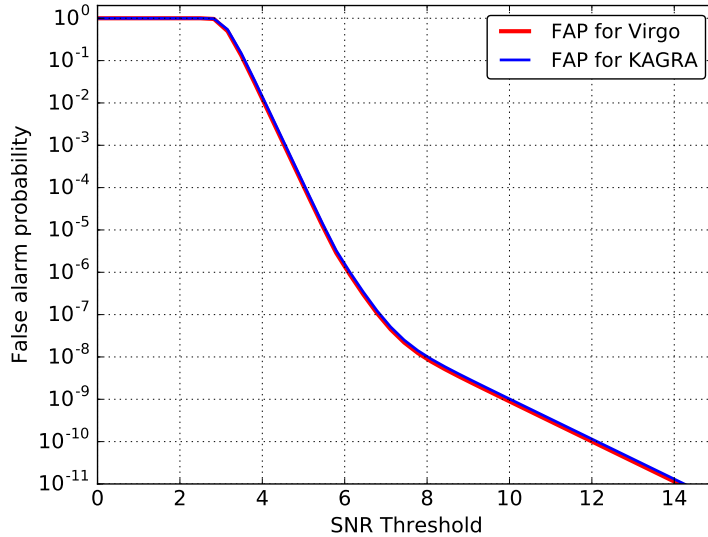


Figure 2.6: False alarm probability (FAP) for Virgo and KAGRA as a function of the SNR threshold, computed as $FAP = 1 - \exp(-R T)$, with R the rate of triggers above threshold per template, derived from the distribution on the left of Figure 2.5, and T for Virgo and KAGRA is set to 70 ms and 80 ms respectively.

2.2.5 Attributing parameters to KAGRA triggers in HLK-network

This process is also done in the same manner as summarized in section 2.2.3. The procedure is summarized in Table 2.4.

Table 2.3: Procedure for generating coincident events for LIGO-KAGRA network. p_K is a random number from a uniform distribution between 0 and 1. FAP_K is the false alarm probability at a given SNR threshold in KAGRA.

Conditions	Generated coincidences
if $p_K < FAP_K(\max(SNR_K^{th}, SNR_K^{expected}))$	H L K_n
else	
if $SNR_K^{expected} > SNR_K^{th}$	H L K_i
if $SNR_K^{expected} < SNR_K^{th}$	H L

Table 2.4: Procedure for attributing parameters to KAGRA triggers. $t_{LIGO}^{measured}$ and $\phi_{LIGO}^{measured}$ represent, respectively, the measured time and phase of arrival at either the LIGO-Hanford or the LIGO-Livingston detector. For these parameters, we use the ones whose SNR is closer to the expected SNR of KAGRA detector. $\Delta t^{injection}$ and $\Delta \phi^{injection}$ describe the simulated LIGO-KAGRA differences of time and phase respectively. $\text{Random}[a : b]$ describes a random number uniformly drawn between a and b . Again we use 0.11 msec and 0.35 rad as typical measurement uncertainties at an SNR of 6 for the time and phase of arrival. These values have been adjusted so that the localization areas at a given confidence level are statistically self-consistent.

K_n : KAGRA trigger from noise	
SNR	randomly drawn from the distribution shown in figure 2.5
Time	$t_{LIGO}^{measured} + \text{Random}[-30 \text{ msec} : 30 \text{ msec}]$, for HK-case $t_{LIGO}^{measured} + \text{Random}[-40 \text{ msec} : 40 \text{ msec}]$, for LK-case
Phase	$\text{Random}[0 : 2\pi]$
K_i : KAGRA trigger from injections	
SNR	$2.26 \times (\text{detection range}) \times 8/D_{\text{eff}}^K + \text{Gauss}(0, 1)$
Time	$t_{LIGO}^{measured} + \Delta t^{injection} + \text{Gauss}(0, 0.11 \text{ msec} \times 6/SNR_K^{expected})$
Phase	$\phi_{LIGO}^{measured} + \Delta \phi^{injection} + \text{Gauss}(0, 0.35 \text{ rad} \times 6/SNR_K^{expected})$

2.2.6 Generating artificial triggers for Virgo and KAGRA

This is a setting for the investigation of the four-detector case. The artificial trigger generation is processed in accordance with section 2.2.2 and 2.2.4. We also consider the triggers found in Virgo and KAGRA which are actually related to the injected signal (V_i and K_i case), and which are related to detector noise (V_r and K_r case). Parameters are attributed to these triggers as described in section 2.2.3 and section 2.2.5. The procedure is summarized in table 2.5.

Table 2.5: Procedure for generating coincident events for LIGO-Virgo-KAGRA network. p_V and p_K is a random number from a uniform distribution between 0 and 1. FAP_V and FAP_K is the false alarm probability at a given SNR threshold in Virgo and KAGRA respectively.

Conditions	Generated coincidences
if $p_V < FAP_V(\max(SNR_V^{th}, SNR_V^{expected}))$	
if $p_K < FAP_K(\max(SNR_K^{th}, SNR_K^{expected}))$	H L V_n K_n
else	
if $SNR_K^{expected} > SNR_K^{th}$	H L V_n K_i
else	H L V_n
else	
if $SNR_V^{expected} > SNR_V^{th}$	
if $p_K < FAP_K(\max(SNR_K^{th}, SNR_K^{expected}))$	H L V_i K_n
else	
if $SNR_K^{expected} > SNR_K^{th}$	H L V_i K_i
else	H L V_i
else	
if $p_K < FAP_K(\max(SNR_K^{th}, SNR_K^{expected}))$	H L K_n
else	
if $SNR_K^{expected} > SNR_K^{th}$	H L K_i
else	H L

2.2.7 Figures of merit

We use the 90% confidence area and the so-called searched area as figures of merit for the performance of the sky localization. The searched area is the area of the highest confidence region around the pixel of maximum probability, that includes the sky location of the injected GW signal. The 90% confidence area gives the precision, whereas the searched area quantifies the accuracy of the sky localization.

2.3 Expected performance of heterogeneous HLV-network

2.3.1 Sky localization performance

Using the settings in section 2.2.2 and 2.2.3, we generate sky maps of 248 events and investigate the localization performance by collecting the median values of searched area and 90% confidence area. This calculation is repeated with different SNR thresholds in Virgo. First, we assumed that the two LIGO detectors have the same range while the Virgo detector has 39% of the range of the LIGO detectors to roughly mimic the O2 sensitivity. The calculated performance is shown in Figure 2.7. The dots show the median of the localization areas over the set of injections and the uncertainties report the interquartile range. In order to check that the results were not overly sensitive to a particular realization of the random numbers used in the simulation, the procedure was repeated twice, and since the results were consistent, the figure reports the average (quadratic average) of the medians (uncertainties) obtained in the two trials. The relative detector sensitivities are written down as $1-1-x$, with x the ratio of the Virgo sensitivity compared to the two LIGO detectors.

The plots show that the optimal SNR threshold in Virgo is around 3. At this threshold, the localization is improved by about a factor of 4. In this configuration, about 51% of the 248 events are reconstructed as HLV_i triggers, 36% as HLV_n triggers, and 13% are HL triggers. The percentage of these three triggers changes depending on the Virgo threshold (these percentages depend on the Virgo sensitivity and threshold). In order to verify the artificial trigger generation in this work, we also actually run MBTA on Virgo data with a SNR threshold ranging from 5 to 10, and we obtained consistent median values for the searched area and 90% confidence area compared to the localization performance obtained with artificial Virgo triggers at those threshold as shown in Figure 2.8. Figure 2.7 also includes the localization performance when the lower sensitivity detector generates louder background triggers compared to a stable case. In this noisy case investigation, the SNR distribution and the FAP in Virgo are derived from the black curves instead of the red curves in Figure 2.5. This has no impact on the localization performance and in the following we work only in the quiet case.

2.3.2 Dependence on the sensitivity of Virgo detector

We calculate the localization performance for various BNS ranges of the Virgo detector. This is realized by scaling its expected SNR using (2.1) and its noise curve. The other settings are as described in section 2.2. The population of the HL, HLV_i and HLV_r events are summarized in section A.2. The expected performances in terms of searched area and 90% confidence area are shown in Figure 2.9. The hierarchical search with three detectors will improve the precision of the localization regardless of the value of the BNS range. On the other hand, if the BNS range for the lower sensitivity detector is too low, the accuracy of the localization will be slightly degraded since it will be more likely to get triple

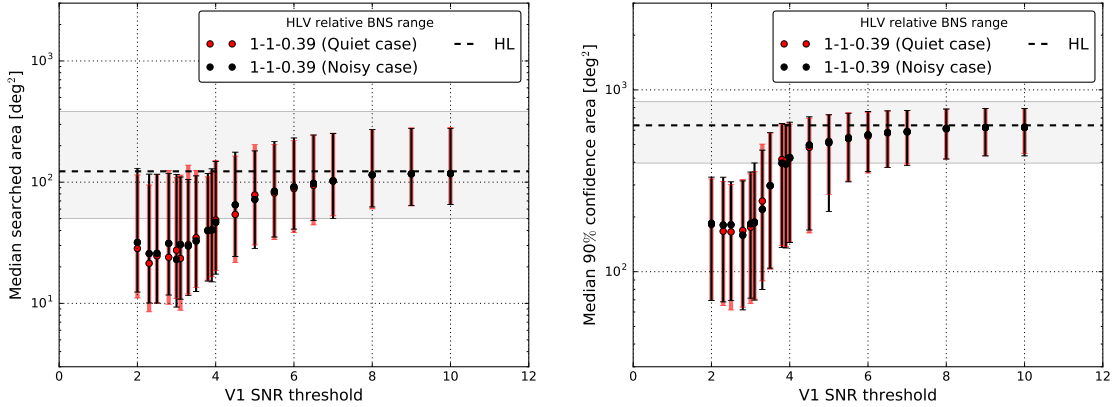


Figure 2.7: The sky localization performance of the heterogeneous network search by three detectors. These plots show the median with its interquartile range. The dashed black line shows the performance using the two LIGO detectors only. The red colored dots are for the case when the detector is quiet, while the black ones correspond to the noisy condition. The performances in the two cases are similar.

coincidences with Virgo noise triggers. However, this effect will not be so large; noisy Virgo triggers will mainly be found when the sensitivity is much lower than the sensitivities of the LIGO detectors. In this situation, the reconstructed sky maps will be similar to the ones obtained with the LIGO detectors only. Figure 2.8 shows the improvement in the performance for those events that become triple coincident events when Virgo is added to the network. Based on Figures 2.8 and 2.9, the lower sensitivity detector begins to improve the localization performance as soon as its sensitivity is 20% of the more sensitive detectors. Then the optimal SNR threshold lies in the range from 3 to 3.5. We find that as the sensitivity of Virgo approaches one third of the LIGO one, the accuracy and precision of the localization can be improved by about a factor of 3.

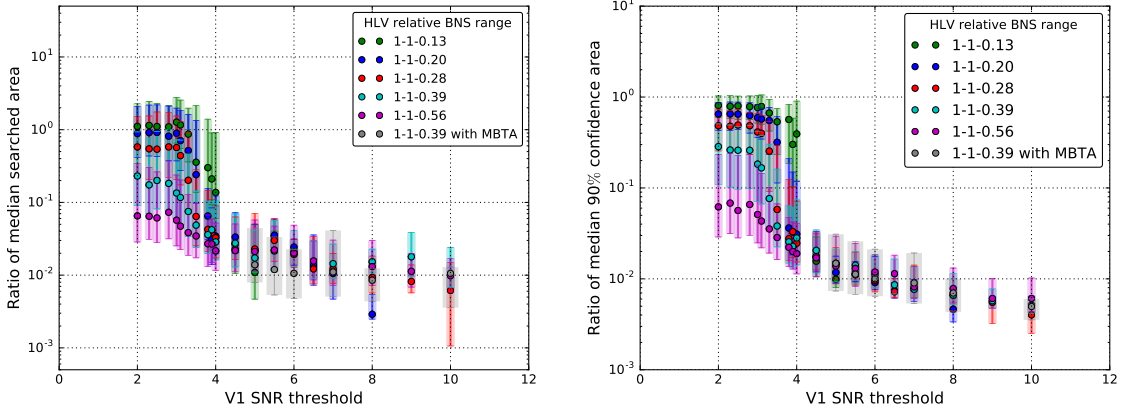


Figure 2.8: Ratio of the median searched area (*left*) and 90% confidence area (*right*) of HLV triggers to that of the same triggers treated as HL coincidences, with the interquartile ranges. As the sensitivity improves, HLV_n triggers become less likely whereas HLV_i triggers become more likely and benefit the localization performance.

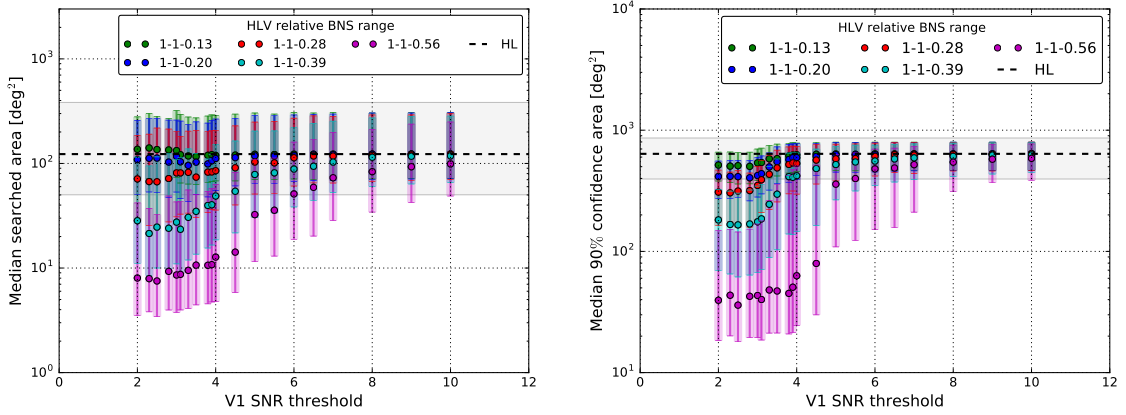


Figure 2.9: The median searched area (*left*) and 90% confidence area (*right*) with the interquartile ranges are shown as a function of the SNR threshold used in Virgo. Expected sky localization performance with the hierarchical search when the sensitivity of the Virgo detector is varied. The colors show the network configuration.

Concerning the sky maps, the reconstructed region by HLV coincident triggers will be a fraction of the area reconstructed by the two LIGO detectors only. If a coincident trigger is built from two LIGO signals and a noise Virgo trigger, the area pointed by the HLV network starts to shift from the source position, mostly due to the error on the detection time in Virgo. However, if the range of Virgo detector is much lower than the LIGO ones, the reconstructed area remains similar to the ring shape region reconstructed by the two LIGO detectors only

even when the Virgo trigger is due to noise. This hierarchical search will find ring-shaped sky maps when the sensitivity of the third detector is much lower than the higher sensitivity ones. As the sensitivity improves, the sky maps progressively turn into point-like regions inside the area by the two LIGO detectors.

2.4 Expected performance of heterogeneous HLK-network

With the same manner as HLV-network case, using the settings in section 2.2.4 and 2.2.5, we generate sky maps of 248 events and investigate the localization performance by collecting the median values of searched area and 90% confidence area. This calculation is repeated with different SNR thresholds in KAGRA, and also the procedure was repeated twice in order to check that the results were not overly sensitive to a particular realization of the random numbers used in the simulation. Based on the result shown in section 2.3.1, we consider a case where the less sensitive detector KAGRA generates background triggers stably in this calculation.

2.4.1 Dependence on the sensitivity of KAGRA detector

In the same way as in section 2.3.2, we calculate the localization performance for various BNS ranges of the KAGRA detector, by scaling its expected SNR using (2.2) and its noise curve. The population of the HL, HLK_i and HLK_n events are summarized in section A.2. The expected improvement ratio of the performance of HLK triggers to that of the same triggers treated as HL coincidences is shown in Figure 2.10. The expected performances in terms of searched area and 90% confidence area obtained from all the 248 events are shown in Figure 2.11. The relative detector sensitivities are written down as 1-1- x , with x the ratio of the KAGRA sensitivity compared to the two LIGO detectors.

The obtained results lead qualitatively to the same conclusions as in the HLV-network case. Based on Figures 2.10 and 2.11, the lower sensitivity detector begins to improve the localization performance as soon as its sensitivity is 28% of the more sensitive detectors. Then the optimal SNR threshold lies in the range from 3 to 3.5. We find that as the sensitivity of KAGRA approaches one third of the LIGO one, the accuracy and precision of the localization can be improved by about a factor of 1.5.

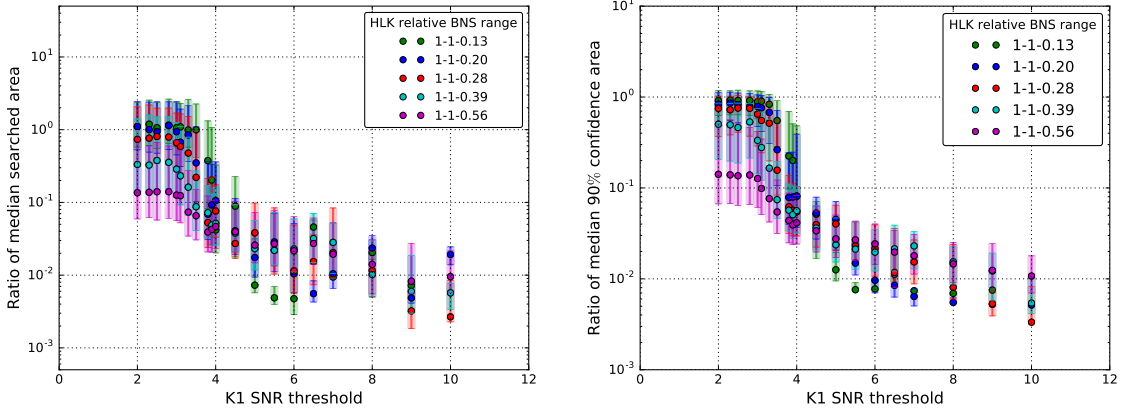


Figure 2.10: Ratio of the median searched area (*left*) and 90% confidence area (*right*) of HLK triggers to that of the same triggers treated as HL coincidences. As the sensitivity improves, HLK_n triggers become less likely whereas HLK_i triggers become more likely and benefit the localization performance.

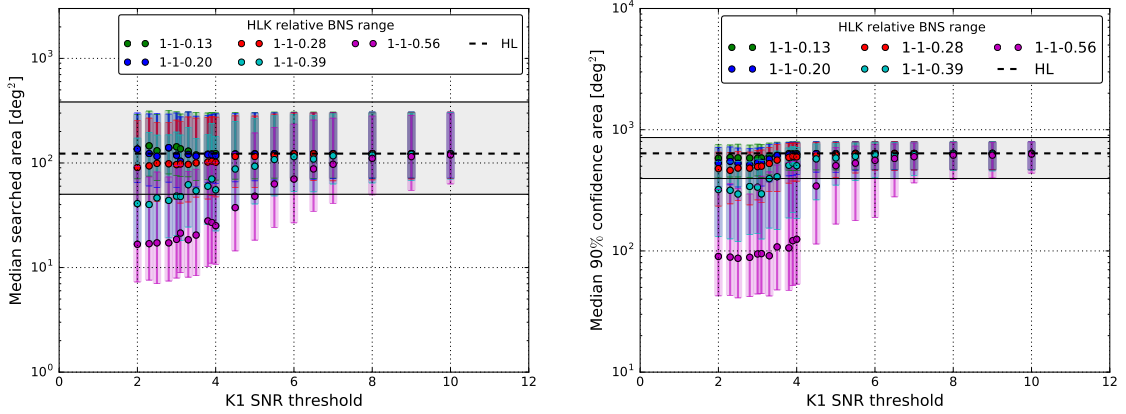


Figure 2.11: The median searched area (*left*) and 90% confidence area (*right*) are shown as a function of the SNR threshold used in KAGRA. Expected sky localization performance with the hierarchical search when the sensitivity of the KAGRA detector is varied. The colors show the network configuration.

2.4.2 Comparison to HLV-network performance

As seen in Figure 2.9 and 2.11, the size of the reconstructed sky maps by the HLK-network would become larger than that by the HLV-network, by roughly a factor of 2. This feature would come from the geometry of the network detector positions. The geometry of the HLK-network is slightly less favorable than the geometry of the HLV-network.

In order to test this statement, we confirm the followings.

1. The consistent sky localization performances for HLK_i are obtained, i.e. it is confirmed that the fraction of injections found within the area at a given confidence level matches that confidence level.
2. The population of HL, HLK_i , HLK_n triggers are mostly similar to the ones of HL, HLV_i , HLV_n .
3. The SNR distributions of HLK_i , HLK_n triggers are also similar to the ones of HLV_i , HLV_n .
4. This performance does not come from the difference of the used noise curves.

In addition, We investigate the performance by HLV-network and HLK-network with the events whose effective distances are close to each other as shown below.

Examination of localization performance with similar D_{eff} events

We select the HLV- and HLK-events whose difference of the effective distance is smaller than 10% (i.e, with a condition of $|1 - D_{\text{eff}}^V/D_{\text{eff}}^K| < 0.1$). We then calculate the localization performance with the pure injection parameters without adding the small random number derived from a Gaussian distribution. The result is shown in Figure 2.12. Although we find just 28 such events, this shows that the HLK-network would give larger-reconstructed sky maps compared to the ones by HLV-network in average. One example of the sky maps are drawn in Figure 2.14. The sky maps would imply that the reconstructed region by HK or LK information comparably more parallel to the ring-shape by HL information than the ring by HV or LV information. As a result, the intersection tends to be larger. This seems to connect to the geometry of the detector position. The detector triangles composed of the two LIGO detectors with Virgo and KAGRA detector is shown in Figure 2.13. This figure shows that the triangle made by HLK-detectors are flatter than the one made by HLV-detectors. In addition, the difference of the determinants of a matrix \mathbf{M} in section 1.5.1 as eq (1.70), is roughly by a factor of 2, which is consistent of the difference observed in the localization performance difference.

Based on the above, we would conclude that the performance by HLV-network would become better than that by HLK-network, due to the geometrical configuration of the detectors. The obtained results shown in Figure 2.11 are the counterpart for the performance by HLV-network in Figure 2.9.

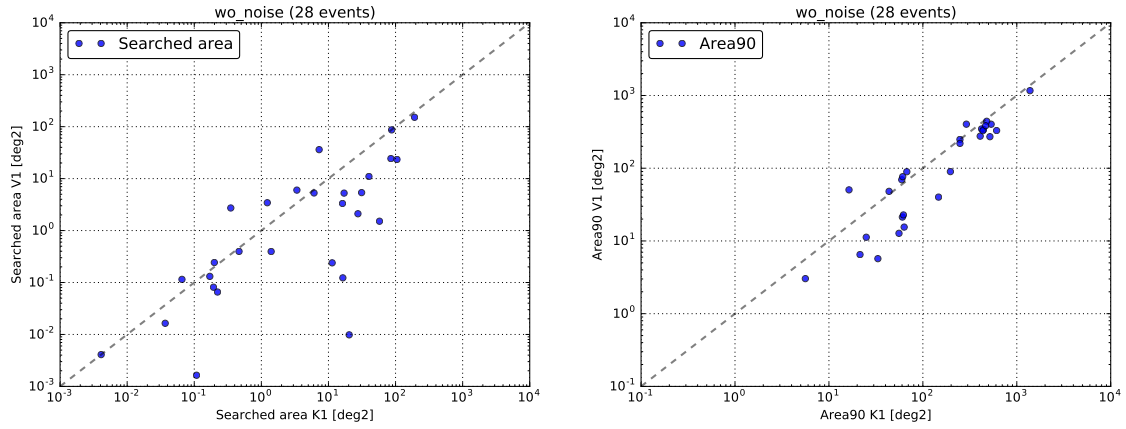


Figure 2.12: The sky localization performance by HLV- and HLK-network with similar D_{eff} events. These plots show the median values.

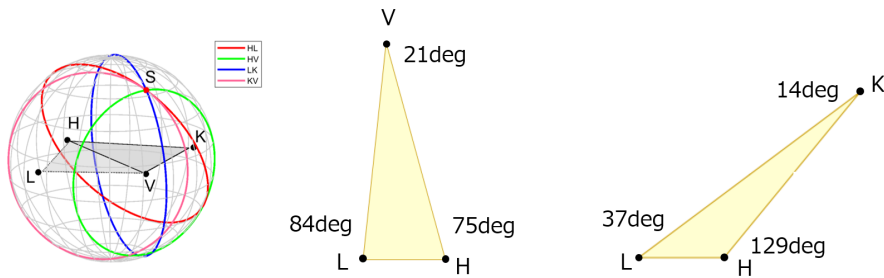
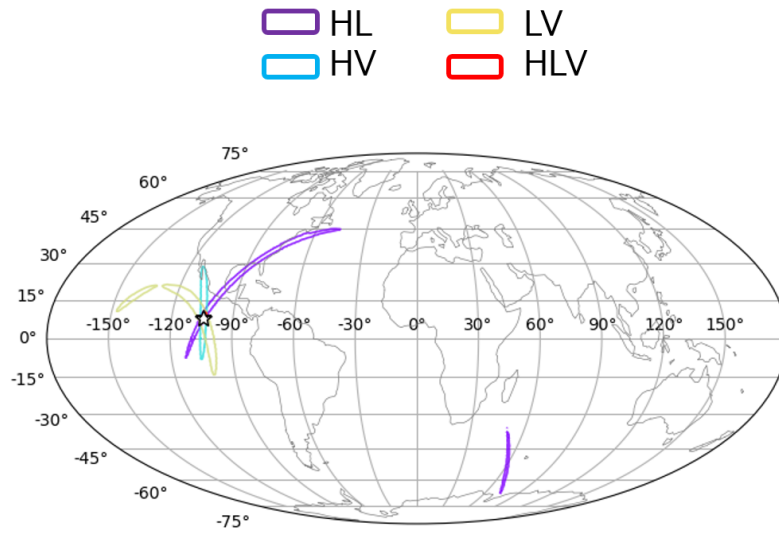
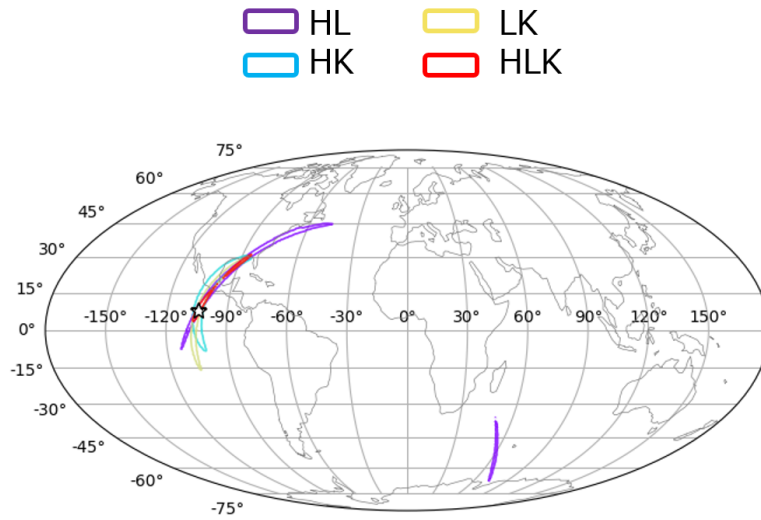


Figure 2.13: The triangles composed of the three detectors. H, L, V and K denote the LIGO Hanford detector, LIGO Livingston detector, Virgo detector and KAGRA detector. The triangle composed of the HLK detectors is more flatter than the triangle composed of the HLV detectors.



(a) Sky map example obtained by LIGO-Virgo network. The area reconstructed by HLV-network (red) is mostly hidden by the star.



(b) Sky map example obtained by LIGO-KAGRA network

Figure 2.14: Sky map example obtained by LIGO-Virgo network (a) and by LIGO-KAGRA network (b).

2.5 Expected performance of heterogeneous HLVK-network

In accordance with HLV- and HLK-network case procedure, using the settings in section 2.2.3, 2.2.5 and 2.2.6, we generate sky maps of 248 events and investigate the localization performance by collecting the median values of searched area and 90% confidence area. In this calculation, we assume that the sensitivity of Virgo detector is half of the sensitivities of the two LIGO detectors. This calculation is repeated with different SNR thresholds in KAGRA (from 2 to 10), and also done in different SNR threshold in Virgo (3.0, 3.5, 4.0 and 5.0). The procedure was repeated twice in order to check that the results were not overly sensitive to a particular realization of the random numbers used in the simulation. We also consider a case where the less sensitive detectors Virgo and KAGRA generate background triggers stably in this calculation.

2.5.1 Dependence on the sensitivity of the fourth detector KAGRA

The expected performances of the searched area and the 90% confidence area by this network are shown in Figure 2.15 to 2.18. Figure 2.15 shows the expected improvement ratio of the performance of HLVK triggers to that of the same triggers treated as HLV coincidences. Figure 2.16 shows the expected performances of the searched area and the 90% confidence area obtained from all the 248 events. These two figures draws the case where the SNR threshold for Virgo is to 5.0. Figure 2.17 and 2.18 reports the performance when the SNR threshold of Virgo detector is set to 3.5, with the same manner as Figure 2.15 and 2.16. The expected performances with other configuration are summarized in section A.2.4. We calculate this performance for various BNS ranges of the KAGRA detector, by scaling its expected SNR and its noise curve. The relative detector sensitivities are written down as 1-1-0.5- x , with x the ratio of the KAGRA sensitivity compared to the two LIGO detectors. The population of the HL, HLV_i , HLV_n , HLK_i , HLK_n , HLV_iK_i , HLV_nK_n , HLV_iK_n and HLV_nK_i events are summarized in section A.2.

Similarly to the HLK-network case, the lowest sensitive detector begins to improve the localization performance as soon as its sensitivity is 28% of the more sensitive detectors, based on Figures 2.16 and 2.18. Then the optimal SNR threshold lies in the range from 3 to 3.5. In the case where the SNR threshold of Virgo detector is set to 5.0, i.e where the information of Virgo detector is not much reflected to the sky maps, KAGRA detector information will contribute to improvement of the localization performance relatively significantly. On the other hand, in the case where the SNR threshold of Virgo detector is set to 3.5, i.e where the information of Virgo detector is already reflected to the sky maps, KAGRA detector information would contribute less to improving the localization performance

It must be noted that, Figure 2.15 and 2.17 report that as the detector sensitivity of KAGRA increases, the averaged performance by HLVK-network at higher SNR threshold in KAGRA detector becomes worse. This happens since

we start from the events detection by the LIGO detectors, which is unfavorable to KAGRA detector, and thus that happens since KAGRA detector finds more events which are less aligned to KAGRA detector as its sensitivity is increased.

Consequently, the lowest sensitivity detector begins to improve the localization performance clearly as soon as its sensitivity is one third of the most sensitive LIGO detectors, which is two third of the sensitivity of the middle sensitive detector Virgo, with the optimal SNR threshold lies in the range from 3 to 3.5. We find that as the sensitivity of KAGRA approaches half of the LIGO one (same as Virgo one), the accuracy and precision of the localization can be improved about to 7 deg^2 and 30 deg^2 respectively.

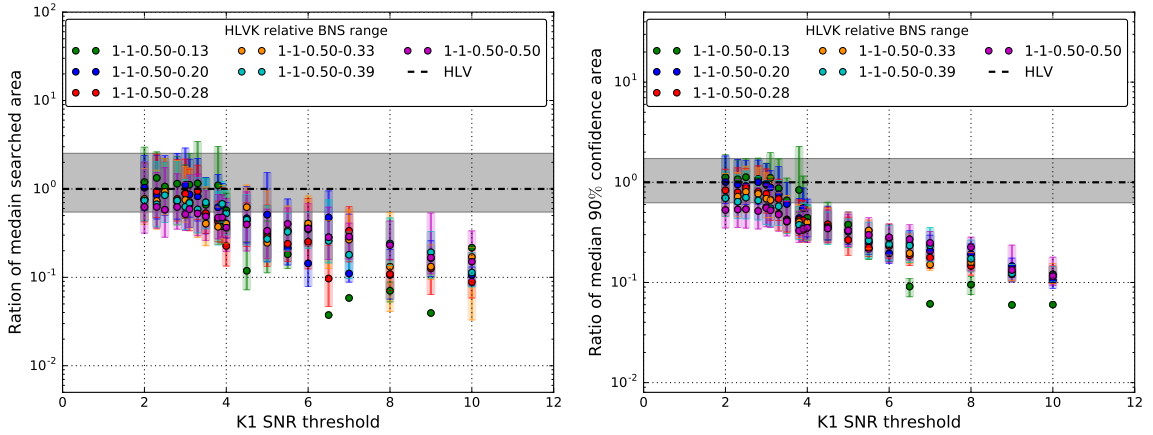


Figure 2.15: Ratio of the median searched area (*left*) and 90% confidence area (*right*) of HLVK triggers to that of the same triggers treated as HLV coincidences, when the sensitivity of the KAGRA detector is varied. The colors show the network configuration. This is the case where the SNR threshold for Virgo is set to 5.0.

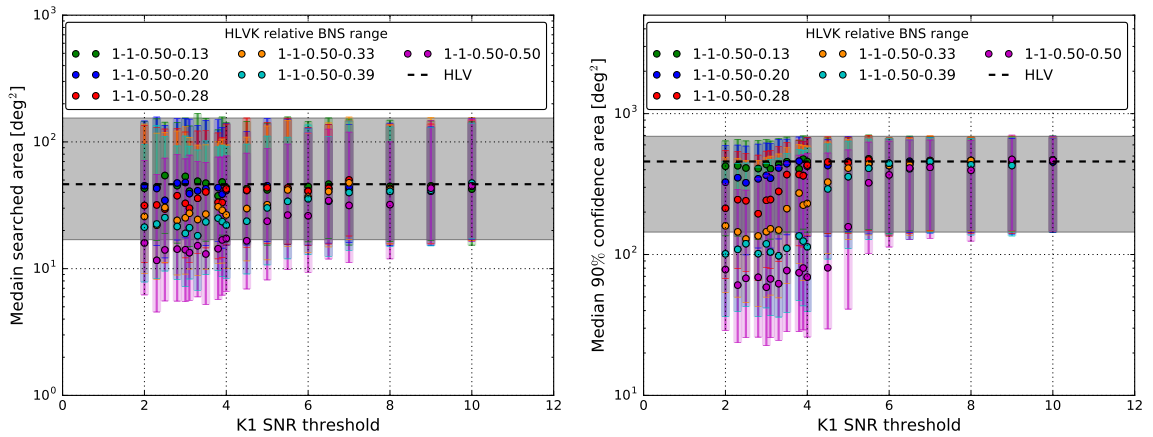


Figure 2.16: The median searched area (*left*) and 90% confidence area (*right*) are shown as a function of the SNR threshold used in KAGRA. Expected sky localization performance with the hierarchical search when the sensitivity of the KAGRA detector is varied. The colors show the network configuration. This is the case where the SNR threshold for Virgo is set to 5.0.

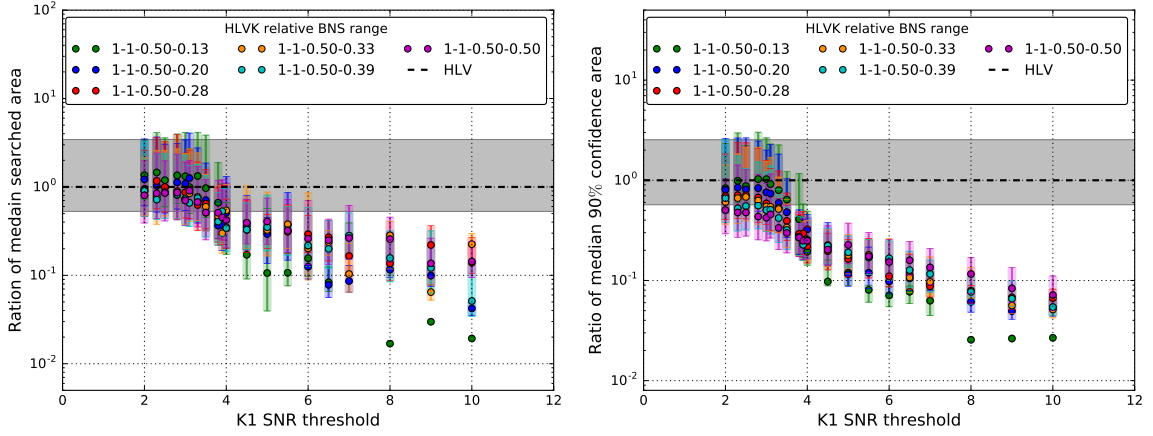


Figure 2.17: Ratio of the median searched area (*left*) and 90% confidence area (*right*) of HLVK triggers to that of the same triggers treated as HLV coincidences, when the sensitivity of the KAGRA detector is varied. The colors show the network configuration. This is the case where the SNR threshold for Virgo is set to 3.5.

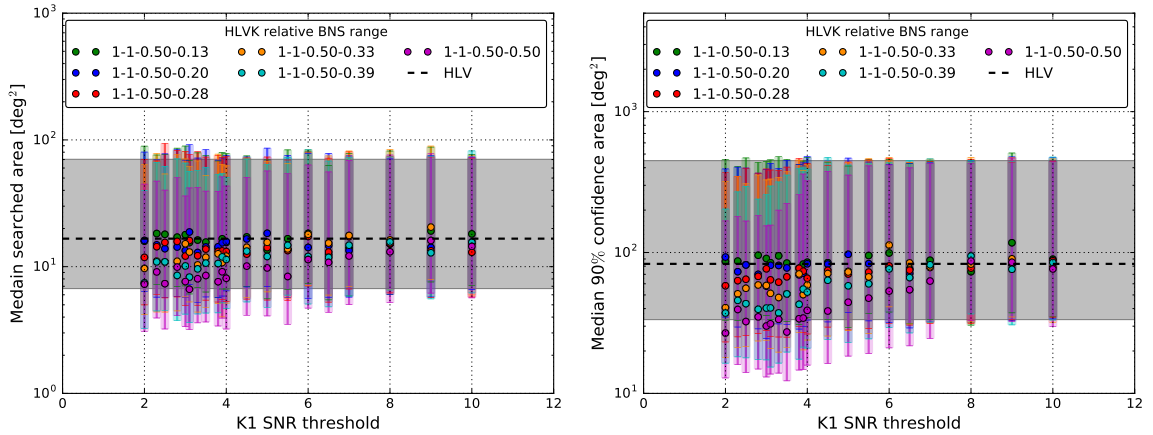


Figure 2.18: The median searched area (*left*) and 90% confidence area (*right*) are shown as a function of the SNR threshold used in KAGRA. Expected sky localization performance with the hierarchical search when the sensitivity of the KAGRA detector is varied. The colors show the network configuration. This is the case where the SNR threshold for Virgo is set to 3.5.

2.6 Summary

Using MBTA and Bayestar, we show the expected fast localization performance for GWs from compact binary coalescence when a hierarchical search is implemented into a GW-EM follow-up pipeline. We confirm that the hierarchical search will improve both the localization accuracy and precision compared to those achieved by a double coincidence search with the two LIGO detectors alone. The hierarchical network effectively improves the localization accuracy and precision when threshold SNR for the lower sensitivity detector is set to around 3.5 provided that the BNS range of that the detector is greater than 20% of the more sensitive detectors in the case where the detector network is composed of the two LIGO detectors and the Virgo detector. In the case where the detector network is composed of the two LIGO detectors and KAGRA detector, we found a clear sky localization improvement when the relative sensitivity of KAGRA becomes greater than 20% of the more sensitive detectors. In addition, the hierarchical network by four detectors will improve the localization accuracy and precision when threshold SNR for the lowest sensitivity detector is set to around 3.5 provided that the BNS range of that the detector is greater than 30% of most sensitive detectors. This result assumes that the sensitivity of the middle sensitive Virgo detector is half of the LIGO one.

Consequently, the search with this hierarchical approach will be most useful when adding new, less sensitive detectors to the network, as they are undergoing commissioning.

This study did not consider the aspect of the network duty cycle. Indeed the probability to have at least three detectors up and running increases considerably when a fourth detector is added to the network. This is another benefit of adding detectors to the network and reduces the chances to miss detectable events. This comes from a fact that sometimes a GW detector is not operational due to interferometer lock loss and/or maintenance operation. For example, assuming that all the detectors have an equal duty cycle of 80%, the duty cycle by three detectors in the three detector network would be about 51%. On the other hand, for a network made by four detectors, the duty cycle by three or four detectors becomes about 82%. This implies that in the three- and four-detector network, respectively about 49% and 18% of the detected events would have poor reconstructed sky position, even though all the network detectors have enough sensitivities. This is not suitable to the target of the EM follow up observation. This fact implies that operating a fourth robust interferometer is of paramount importance to achieve high network duty cycle.

Chapter 3

Low Frequency Vibration Isolation

As written in section 1.3.3, the seismic noise is the one of the fundamental noises for the ground-based GW detectors. In addition, in order to detect GWs, we have to realize a situation where the test masses are in free-fall condition. To meet these constraints, we suspend the core optics with pendulum system called Seismic Attenuation System (SAS), by taking care of the mechanical resonances in order not to drastically decrease the duty cycle. The following chapters focus on topic of the low frequency vibration isolation.

Seismic motion limits the detector sensitivity at low frequency by introducing vibration into the mirrors. In order to detect GWs and to achieve the target sensitivity for the ground-based GW detectors, the seismic motion have to be suppressed typically by 10^{-8} to 10^{-10} at 10 Hz. This chapter describes the characteristics of seismic noise and the basic techniques to reduce its contribution to the detector sensitivity limit.

3.1 Seismic motion

The ground vibrates continuously and randomly due to oceanic, atmospheric and human activities. The amplitude of the seismic vibration changes by a few orders of magnitude depending on the site and time, as well as on surrounding environment influences such as weather, industrial activities. The worldwide seismic background noise was investigated by J. Peterson [27]. He estimated typical seismic vibration based on data from a worldwide network of seismometers and constructed the high/low noise model, according to the upper and lower bounds of the measured power spectral densities. Figure 3.1 shows the spectra of ground motion of the high/low noise model, and that of KAGRA underground. The spectrum of seismic motion at the KAGRA site in the figure shows that from 1 year of measured seismic noise data. Seismic noise was measured by Trillium120QA at the 2nd floor in the X-end station in KAGRA underground. The general key features of the seismic-motion spectrum are:

1. At low frequencies below 1 mHz, the amplitude increases due to the tidal

deformation of the ground caused by the gravitational attraction from the sun and moon.

2. The peak measured at $0.1 \sim 0.5$ Hz is known as the microseismic peak and is mainly caused by oceanic wave activities. Thus the peak has a large magnitude along the coast while it is smaller in the middle of the continents [28].
3. The typical displacement amplitude spectra of the seismic motions at frequencies higher than ~ 1 Hz is given by

$$\tilde{x}_{\text{seismic}}(f) = A \times \left(\frac{f}{1 \text{ Hz}} \right)^{-2} \text{ m}\sqrt{\text{Hz}}, \quad (3.1)$$

The factor A is a constant which depends on sites and is typically about $10^{-9} \sim 10^{-6}$.

4. At around 10 Hz, the typical amplitude of the seismic vibration is larger than about $10^{-12} \text{ m}\sqrt{\text{Hz}}$. On the other hand, the required arm-length fluctuation of the GW detectors is on the order of $10^{-20} \text{ m}\sqrt{\text{Hz}}$. This implies that the displacement of the mirror caused by seismic vibration has to be attenuated by a factor of $10^{-10} \sim 10^{-8}$, for detection of GWs.

Based on the above, in GW detectors, the seismic vibration at frequencies of microseismic peak has an impact on stable interferometer operation by inducing optic vibration which is not coherent among the optics. To reduce this microseismic peak impact is one of the main purposes of the vibration isolation system GW detectors. In addition, at frequencies lower than about 1 mHz, such low-frequency seismic motion have to be compensated for the GW observation (in order to keep the locked situation) since the test masses of ground-based detectors move differentially following to the ground [13]. However, this compensation cannot be done with vibration isolation system since the typically lowest resonant frequency of the system is about a few ten Hz. For this treatment, we need to have the interferometer signal or the strain meter signal.

As other interests, it is known that, in the underground environment, the seismic vibration is reduced compared with that on the surface of the ground since the surrounding rocks tend to isolate the vibration from atmospheric and human activities on the surface [29]. This vibration mitigation due to the underground environment is effective above 1 Hz, where the atmospheric and human activities dominate. However the microseismic peak is not reduced much, since the origin of the microseismic peak is the motion which propagates through the continents.

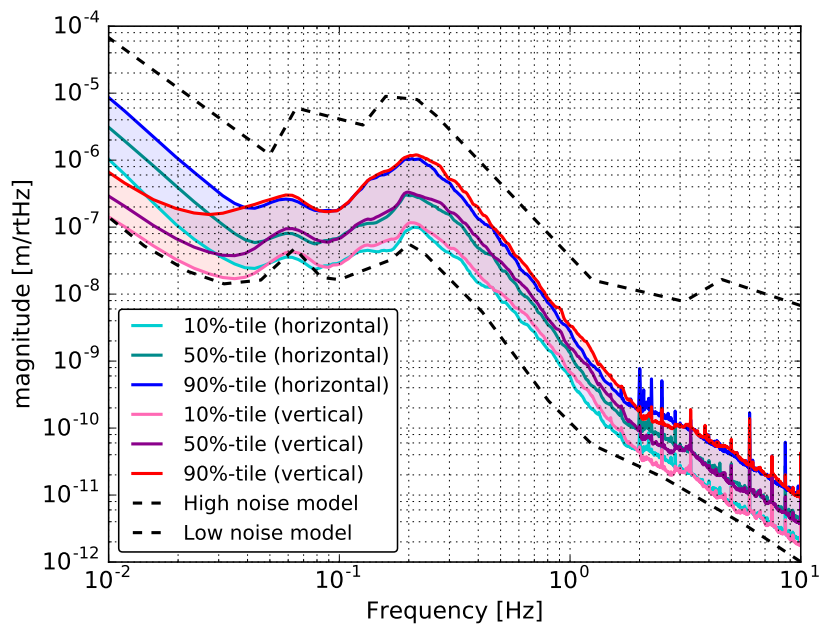


Figure 3.1: Spectrum of measured seismic motion at the KAGRA site in the stational state (solid curves) and the worldwide seismic noise from J. Peterson's study (dashed curves). The colored bands of the spectra of the KAGRA seismic motion denote the range between the 10 percentile to 90 percentile.

3.2 Passive vibration isolation

Seismic attenuation system is composed of multi-stage pendulum. The basic characteristics of pendulum system is addressed.

3.2.1 Basic principle

Harmonic oscillator

Isolating optics from seismic motion is realized by using mechanical filters composed of elastic components such as springs and suspension wires. For the simplest case, we here consider a single-pendulum system consisting of a mass m , and which is suspended by massless wire from a ceiling as in Figure 3.2. Its equation of motion is given by

$$m\ddot{x} = -\frac{mg}{l}(x - X), \quad (3.2)$$

where g denotes local gravitational acceleration, l is the length of the wire and x , X are the displacements of the payload and the suspension point respectively. Taking the Fourier transformation, the displacement transfer function from the ground to the mass becomes:

$$H(\omega) = \frac{\tilde{x}}{\tilde{X}} = \frac{\omega_0^2}{\omega_0^2 - \omega^2}, \quad (3.3)$$

where $\omega_0 = 2\pi f_0 = \sqrt{g/l}$ represents the resonant angular frequency of the suspension system. The transfer function of this system where the suspension wire length is set to 0.25 m and 1 m are shown in Figure 3.2 (*right*). This figure shows:

1. At low frequencies where $f \ll f_0$,
The suspended mass follows the motion of the suspension point.
2. Near the resonant frequency, where $f \simeq f_0$,
the amplitude of the transfer function increases substantially and goes to infinity at the resonant frequency.
3. At higher frequencies where $f \gg f_0$,
The amplitude of the transfer function decreases in proportional to f^{-2} .
4. The lower the resonant frequency is, the more improved the attenuation performance at high frequencies is.

In addition, the response of the mass when a external force is applied is obtained with eq (3.4) as eq (3.5).

$$m\ddot{x} = -\frac{mg}{l}(x - X) + F, \quad (3.4)$$

$$H_{\text{force}}(\omega) = \frac{\tilde{x}}{\tilde{F}} = \frac{1/m}{\omega_0^2 - \omega^2}. \quad (3.5)$$

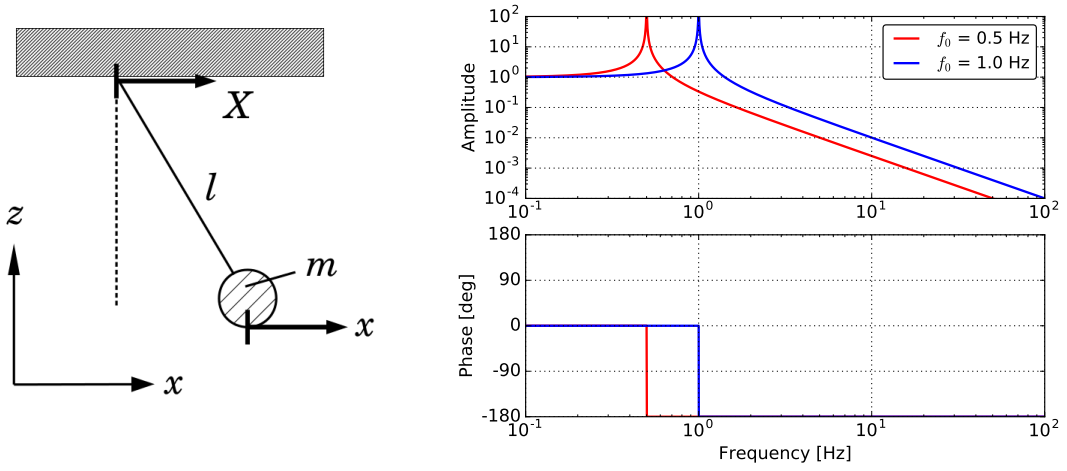


Figure 3.2: A single pendulum system (*left*) and its displacement transfer function (*right*) for the case where the length of the suspension wire is set to 1 m and 0.25 m (corresponding resonant frequencies are $f_0 = 0.5$ Hz, $f_0 = 1.0$ Hz respectively). The lower the resonant frequency is, the more improved the attenuation performance at high frequencies is.

This is called force transfer function in this work. The force transfer function is a useful tool to make a active control filter as in section 5.

Multi-stage suspension

In a multi-stage pendulum system, the vibration isolation ratio is proportional to f^{-2N} at a frequency higher than the resonant frequencies of the system, as in Figure 3.3. By implementing a sufficient number of isolation stages, we realize enough seismic attenuation performance in these high frequency region.

Additional note for the real life

• dissipation

In a realistic system, the transfer function in Figure 3.2 (*right*) has finite amplitude at the resonant frequency due to dissipation from such as residual gas damping, thermoelastic damping. The dissipation due to an elasticity in the elastic components is called structural damping. This is described by adding an imaginary part to the spring constant $k(1 + i\phi)$, where $k = m\omega_0^2$ and ϕ is the loss angle, which is defined as the phase angle by which displacement response would lag behind a sinusoidal driving force exerted on the payload. The typical value of ϕ is much less than 1. The loss angle is related to the quality factor of the oscillator by $Q = 1/\phi$.

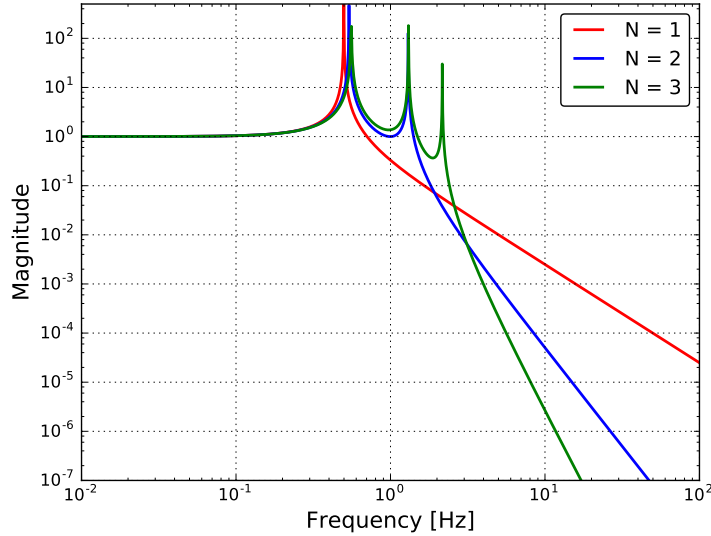


Figure 3.3: The amplitudes of the transfer functions from the suspension point displacement to an N -th stage mass displacement with $N = 1$ to 3. The total length of the suspension is set at 1 m in all cases.

• Couplings from vertical and rotational vibration

In an actual system, not only the horizontal ground vibration but also the vertical ground vibration contributes to the mirror displacement. This vertical-to-horizontal coupling can be caused by mechanical imperfections in each attenuation stage and also by the non-parallelism of the verticality at locations kilometers apart in the detector. Due to the curvature of the ground, the front and end mirrors of the Fabry-Perot cavities make an angle of $\alpha = L/2R_{\oplus}$ with the vertical direction for the interferometer, as shown in figure 3.4 (*left*), considering that L is the cavity length and R_{\oplus} is the radius of the earth. If the optic shifts vertically by δz , it couples to a variation $\alpha\delta z$ of the cavity length. Hence assuming a 3-km interferometer, the minimum coupling caused by earth curvature is $\alpha \sim 2 \times 10^{-4}$.

The rotational motions of the optic can also change the optical path length, as shown in figure 3.4 (*right*). If the laser beam locates at the center of the optic, the rotational motion of a mirror does not couple to the motion in the beam direction. However, the beam spot can be off-center to some extent in reality, and then an angular displacement causes a change of the optical path length. Assuming that the beam spot is off-centered by a distance d and the angle of the other test mass does not shift, the rotation angle of the optic $\delta\theta$ couples to the length variation along the beam axis by $d\delta\theta$.

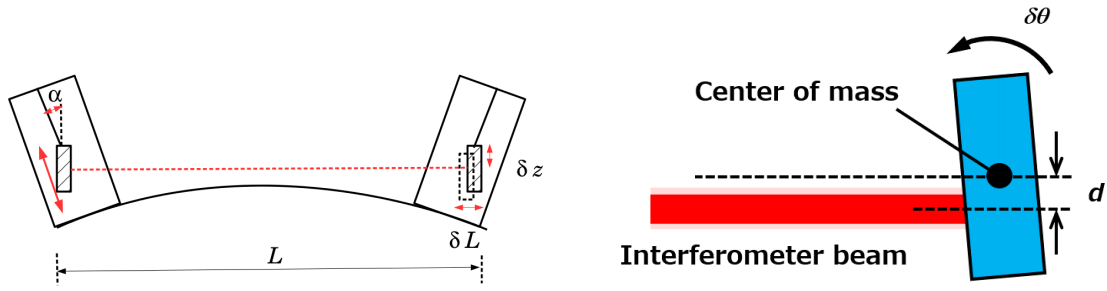


Figure 3.4: Couplings from vertical vibration due to the Earth curvature (*left*) and that from rotational motion due to beam shift (*right*).

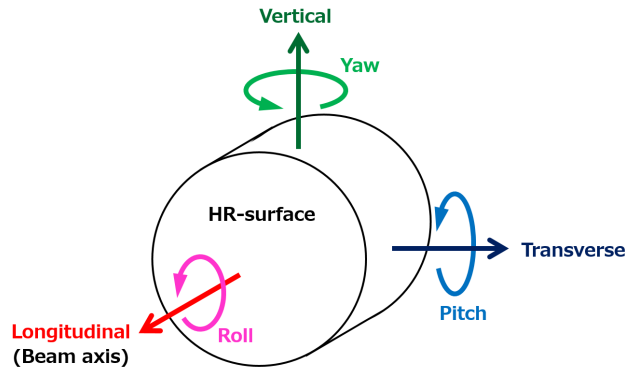


Figure 3.5: Definition of degree of the freedoms of the suspension motion. HR-surface shows the surface of the mirror with high-reflectivity coating.

Degree of freedom of the suspension

The above discussion is done for one-dimensional motions. However, in reality, we have to consider the motions in totally 6 degrees of freedom (dofs) for each body by assuming a 3-dimensional rigid body at least, regardless of internal motions such as elastic vibration. Conventionally we determine these 6 dofs, as longitudinal, transverse, vertical, roll, pitch, and yaw, as shown in Figure 3.5. Three translational axes (longitudinal, transverse and vertical) are the right-handed basis for center-of-mass motions, while three rotational axes (roll, pitch, and yaw) are defined so that rotations in right-handed screw around the translational axes are positive directions. In this thesis, these six dof are sometimes abbreviated to their initial letter such as (L, T, V, R, P, Y) hereafter.

Damping system

We see the multi-stage pendulum attenuates the input vibration at higher frequency than its resonant frequency. On the other hand, it is true that we large-

amplitude motion due to the mechanical resonances of the suspension system would be excited, and we have to damp them since this disturbs the interferometric operation.

An effective amplitude of the mirror fluctuation can be evaluated as the root-meansquare (RMS) amplitude. The RMS amplitude of a time-varying value $x(t)$ is given by:

$$x_{\text{RMS}} = \sqrt{\int_a^b d\omega S_x(\omega)}, \quad (3.6)$$

where $S_x(\omega)$ is the power spectral density of $x(t)$. The interval of the integral is set to a frequency region of interest.

A passive damping system is one option to suppress the large fluctuation of the mirror as described in the below. One benefit to introduce passive damping mechanism is to enhance robustness to unwanted disturbances such as earthquakes and actuation noise. The passive damping system can be modeled by adding a viscous damper which makes a braking force proportional to the relative velocity between the damper and the object to be damped. The equation of motion of such system is:

$$m\ddot{x} = -k(x - X) - \gamma(\dot{x} - \dot{X}), \quad (3.7)$$

where k denotes the spring constant, γ is the damping coefficient of the damper, and X represents the ground motion. The schematic view is shown in Figure 3.6. Taking the Fourier transform, the transfer function from the ground motion to the suspended mass is given by

$$H(\omega) = \frac{\tilde{x}}{\tilde{X}} = \frac{\omega_0^2 + 2i\eta\omega\omega_0}{\omega_0^2 + 2i\eta\omega\omega_0 - \omega^2} = \frac{\omega_0^2 + i\omega\omega_0/Q}{\omega_0^2 + i\omega\omega_0/Q - \omega^2}, \quad (3.8)$$

where the damping ratio $\eta = \gamma/2m\omega_0$ and $Q (= 1/2\eta)$ is the quality factor of the resonance.

The displacement transfer function with various quality factors are plotted in figure 3.7 (*left*). Figure 3.7 (*right*) shows the impulse response of a viscously damped mechanical oscillator with some quality factors.

The figure illustrates that the amplitude of the peak at the resonant frequency gets smaller when the damping gets stronger. It also indicates that the amplitude of the transfer function is proportional to f^{-1} instead of f^{-2} , where f is well above the frequency Qf_0 , if a damper is mechanically grounded. Thus, the performance of the mechanical filter is degraded at high frequencies in a viscously damped system. In addition, concerning an impulse response to a driving force on the suspended mass to test the robustness for the unwanted acceleration disturbance, when the system has small dissipation, the suspended mass moves a sinusoidal oscillation with decaying amplitude. The oscillation amplitude decays faster if the damping factor is increased. The decay time τ , in which the oscillation amplitude

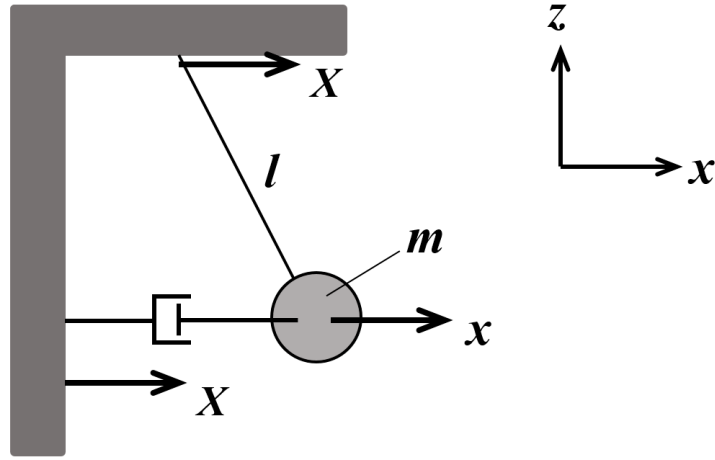


Figure 3.6: An example of a passively damped suspension system.

decreases by a factor of $1/e$, described by $\tau = 1/\eta f_0 = Q/\pi f_0$. In the critical damping condition where the damping factor $\eta = 1$ ($Q = 0.5$), the displacement of the suspended decays with decay time $\tau = 1/\omega_0$, without oscillation. In the over-damped condition where $\eta > 1$, the excited displacement amplitude is decreased but the decay time gets longer than that of the critically damped oscillator.

The degradation of vibration isolation performance due to a damper can be mitigated by isolating the damper from the ground with some mechanical filters. This technique is called flexible damping. By using the flexible damping the displacement transfer function from the ground to the mass will have additional resonant peak due to the spring for the damper, however, the roll off in high frequency region remains f^{-2} proportionality same as a system with no damping mechanism. Passive damping system in a GW detector is then basically suspended.

• Implementation of viscous dampers system

An eddy-current damper [30] is a viscous damping system often used in an actual vibration isolation system of a GW detector. An eddy-current damping system is composed of permanent magnets on one component acting on conductive objects placed on the oscillator to be damped. When a conductive material faces on a time-varying magnetic field, eddy currents are generated in the conductor. These currents induce a magnetic field with opposite polarity of the applied field and a delay due to the induced field decay, causes a resistive force. Figure 3.8 shows the working mechanism of an eddy current damper with a toy model. The damping coefficient of an eddy current damper is given by

$$\gamma_x = A\sigma B \frac{\partial B}{\partial x}, \quad (3.9)$$

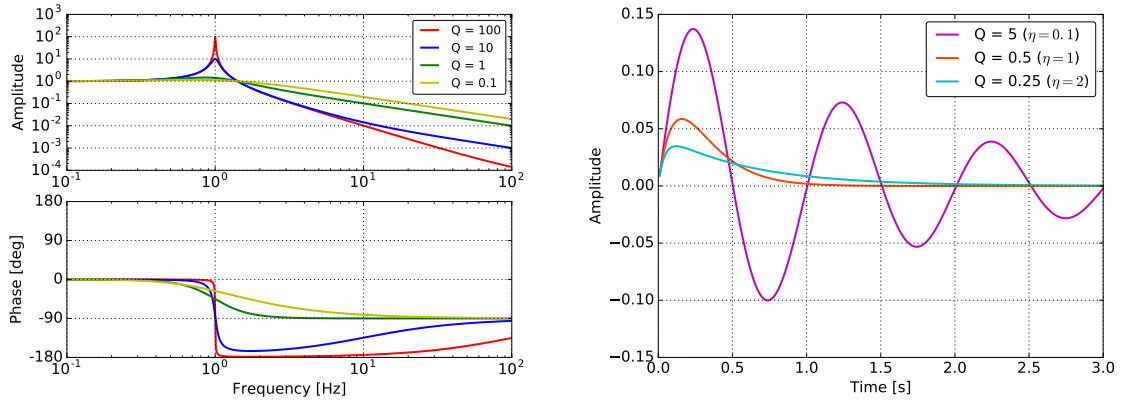


Figure 3.7: The transfer function eq (3.8) (*left*) and the response of a mechanical oscillator with a damper to an impulsive force injected to the suspended mass (*right*), with various Q factors (viscous damping factors).

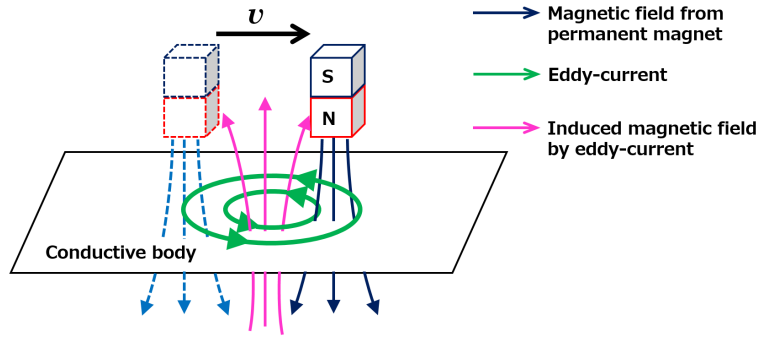


Figure 3.8: Working mechanism of an eddy-current damping system with a toy model.

where B is the magnetic field from the permanent magnet, σ denotes the electrical conductivity of the conductor and A represents a factor determined from the geometry of the conductor. Generally, a large damping strength is obtained by using a permanent magnet with strong magnetic field and a conductive object with large electric conductivity.

• Suspension thermal noise

One demerit of using such damping system is that the damping system can degrade the detector sensitivity by inducing thermal fluctuation of the suspended optics in the detection band. The fluctuation dissipation theorem provides a general relation between the frequency response of systems in equilibrium to external perturbation forces ($H_{\text{force}}(\omega)$) and the power spectral density of their

spontaneous fluctuations $S_{\text{thermal}}(\omega)$:

$$S_{\text{thermal}}(\omega) = -\frac{4k_B T}{\omega} \text{Im}[H_{\text{force}}(\omega)], \quad (3.10)$$

where k_b denotes the Boltzmann constant and T is the temperature. In particular, the power spectrum density of a harmonic oscillator's thermal fluctuations in a viscously damped system is described by

$$S_{\text{thermal}}(\omega) = \frac{4k_B T}{m} \frac{2\eta\omega_0}{(\omega_0^2 - \omega^2)^2 + 4\eta^2\omega_0^2\omega^2}. \quad (3.11)$$

In an actual multi-stage suspension, we locate the passive dampers well apart from the optics so that thermal fluctuations due to their dissipation can be filtered out by mechanical filters, and do not affect the detector sensitivity.

3.2.2 Mechanical filters for gravitational wave detectors

As in the above, we improve the attenuation performance at higher frequency by reducing the resonant frequency of a mechanical filter. In order to realize such system, the actual filters used in the GW detectors utilize anti-spring techniques. This subsection introduces the mechanical aspect of actually used mechanical filters.

The main key components of the mechanical filters are called the inverted pendulum (IP) and the geometric anti-spring (GAS) filter, which provide horizontal and vertical vibration isolation respectively. The resonant frequency of the IP can be lowered to about 30 mHz and it can passively attenuate the ground vibration at the microseismic peak (at about 0.1-0.5 Hz), which contributes significantly to the RMS amplitude of the suspended optic displacement and velocity. On the other hand, the resonant frequency of the GAS filter can be lowered to about 300 mHz. By using the GAS filter, we can obtain vertical vibration isolation performance comparable to the horizontal. This subsection introduces the basic characteristics of the IP and GAS filter.

3.2.3 Inverted pendulum

Working principle

An analytic model of the IP is shown in *left* of figure 3.9. The IP is composed of a flexure fixed to the ground, a rigid cylindrical leg connected onto it and a mass on the top of the leg. If one consider that the mass displaces horizontally from the vertical point, a restoring force acts on it, with an effective spring constant of

$$k_{\text{eff}} = \frac{k_{\theta}}{L^2} - \frac{Mg}{L}, \quad (3.12)$$

where k_{θ} denotes the bending spring constant of the flexure, M is the mass of the payload, and L represents the length of the IP leg, assuming that the mass of the leg m is negligibly small ($m \ll M$). The term k_{θ}/L^2 corresponds to the elastic restoring force of the flexure. The second term denotes a repulsive force due to gravitational anti-spring effect. According to eq (3.12), k_{eff} decreases as the mass of the payload increases and it goes to 0 when the mass reaches $M = M_c = k_{\theta}/gL$, which is called the critical mass M_c . The resonant frequency of the IP which is loaded with a mass lighter than M_c is given by

$$f_{\text{IP}} = \frac{1}{2\pi} \sqrt{\frac{g}{L} \left(\frac{M_c - M}{M} \right)}. \quad (3.13)$$

Displacement transfer function

Assuming that the IP leg has a uniform mass distribution between the flexure and the payload with its mass of m and moment of inertia of I , the displacement

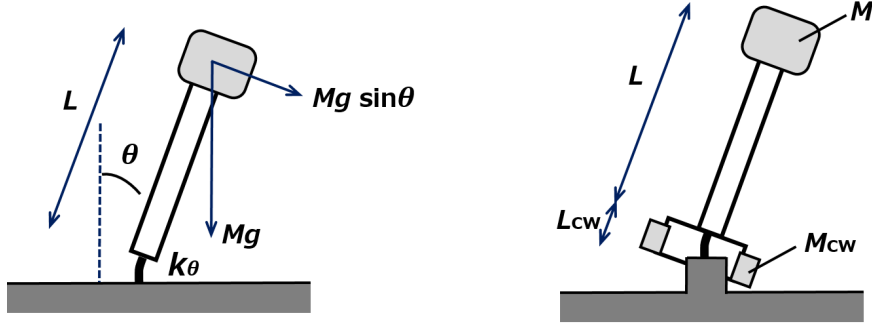


Figure 3.9: Analytic model of an inverted pendulum (*left*) and a schematic view of the inverted pendulum with the counter weight for the compensation of the center of percussion effect (*right*).

transfer function H_{IP} , from the ground displacement to the payload displacement on the IP, is given by [31]

$$H_{IP} = \frac{A + B\omega^2}{A - \omega^2},$$

$$\text{where } A = \frac{k_{\text{eff}}}{M + \frac{m}{4} + \frac{I}{L^2}}, \quad B = \frac{\frac{m}{4} - \frac{I}{L^2}}{M + \frac{m}{4} + \frac{I}{L^2}}. \quad (3.14)$$

According to eq (3.14), the amplitude of H_{IP} saturates at high frequencies due to the coefficient B . This saturation is known as the Center of Percussion (CoP) effect [31]. In order to minimize the CoP effect and to improve the isolation performance at high frequencies, the IP legs should be made as light as possible. For further compensation of the CoP effect, we can optimize the mass distribution of the leg by introducing a counter weight at the bottom of the leg, as shown in *right* of figure 3.9. In the actual SAS for GW detectors, three IPs are implemented into its most upper stage.

More details are summarized in [32, 33].

3.2.4 Geometric Anti-Spring

Working principle

The GAS filter has a set of radially arranged cantilever blades clamped on the base frame and to the central small disk called the keystone. The blades are bent when they are installed. The typical behavior of the GAS filter can be described by a simple analytical model shown in the *left* of Figure 3.10 [34]. In that model, a cantilever spring is represented as a combination of vertical and horizontal linear springs. The effective stiffness is obtained as the following procedure.

If we consider a situation where the suspended payload, whose mass is m , shifts vertically by z , as shown in figure 3.10 (*right*). The equation of motion of the suspended mass is described by

$$m\ddot{z} = -k_z(z - z_{eq} - l_{0z}) - 2k_x(l - l_{0x})\sin\theta - mg, \quad (3.15)$$

where k_x , l_{0x} are the stiffness and the natural length of the horizontal spring respectively, θ represents the angle between the horizontal axis and the horizontal spring at the clamp point, and l is the length of the horizontal spring when the payload shifts vertically by z . In addition, it is assumed a situation where the working point, which is the height where the forces of the horizontal springs cancel each other is called the working point z_{eq} , is given by $z_{eq} = m_0g/k_z + l_{0z}$, where g denotes the gravity acceleration, m_0 is the mass of the payload, k_z and l_{0z} are the stiffness and the natural length of the vertical spring respectively. It is also assumed that the force of the vertical spring balances the gravitational force on the suspended mass.

Then assuming x_0 is the horizontal distance between keystone and the clamping point of the spring, eq (3.15) becomes eq (3.17), by using $l = \sqrt{x_0^2 + z^2}$, z_{eq} and $k_x' = 2k_x$.

$$m\ddot{z} = -k_z\left(z - \frac{m_0g}{k_z}\right) - k_x' \left(1 - \frac{l_{0x}}{\sqrt{x_0^2 + z^2}}\right) z - mg \quad (3.16)$$

$$= -(k_z + k_x')z + k_x'l_{0x}\frac{z}{\sqrt{x_0^2 + z^2}} - (m - m_0)g. \quad (3.17)$$

Consequently, the effective stiffness k_{eff} of the modeled GAS filter is obtained as

$$k_{\text{eff}} = -\frac{\partial f}{\partial z} = (k_z + k_x') - \frac{k_x'l_{0x}x_0^2}{(x_0^2 + z^2)^{\frac{3}{2}}}, \quad (3.18)$$

$$\sim \left[k_z - \left(\frac{l_{0x}}{x_0} - 1 \right) k_x' \right], \quad (\text{if } x_0 \gg z). \quad (3.19)$$

Eq (3.19) implies that when the horizontal spring is compressed ($x_0 < l_{0x}$), it makes a repulsive force in the vertical direction and thnes k_{eff} is reduced from that of the vertical spring ($k_{\text{eff}} < k_z$), as the anti-spring effect. It also implies that the effective stiffness and the resonant frequency is tuned by tweaking the compression of the blades.

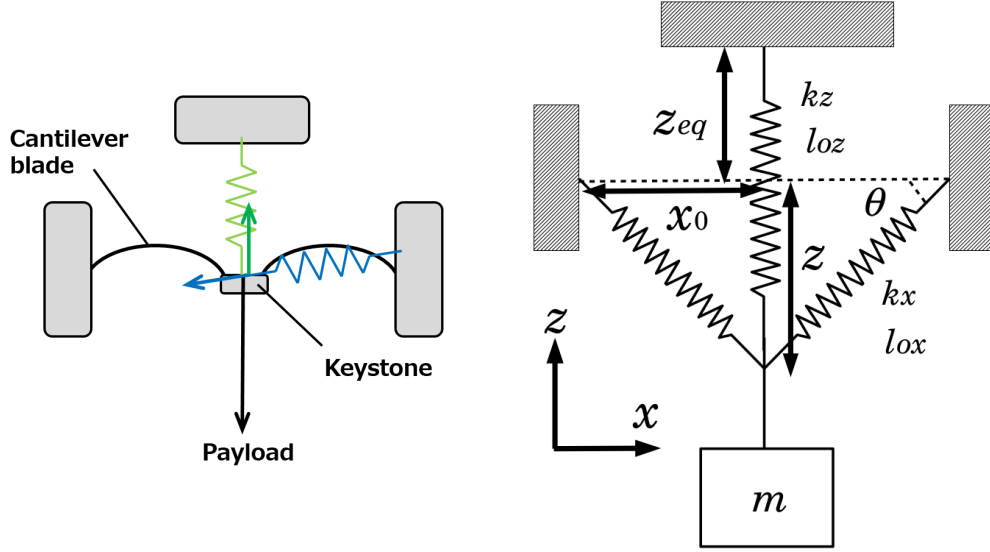


Figure 3.10: A schematic view of an analytical model of the GAS filter (*left*) and the definition of the parameters used in the calculation of the effective stiffness of the GAS filter (*right*).

Displacement transfer function

The displacement transfer function of the GAS filter, which is from the vertical displacement of the frame to that of the keystone, is given in the same form as that of the IP, as in eq (3.14). The attenuation performance saturates at high frequencies is typically limited to $\sim 10^{-3}$ for this time as well, due to the CoP effect. This saturation can be compensated by implementing a wand with a counter-weight in parallel with the blades, which is called magic wand [35].

Additional note for the real life

- **Effect of blade compression**

In an actual system, the compression of the GAS blades is tune so that the keystone balances the suspended payload at the working point. According to eq (3.19), k_{eff} can have a negative value depending on the compression, in which case the system becomes unstable and the GAS filter does not work properly. This is explained with eq (3.19) and the following equation:

$$m - m_0 = -\frac{(k_z + k_x')z}{g} + \frac{k_x' l_{0x}}{g} \frac{z}{\sqrt{x_0^2 + z^2}}, \quad (3.20)$$

which is obtained assuming the keystone is at its equilibrium position in eq (3.17). Using these equations Figure 3.11 shows the working point and the resonant frequency as the function of the suspended mass load, with some compression $C = (l_{0x} - x_0)/l_{0x}$ in the model. Typically, the compression is tuned so that the

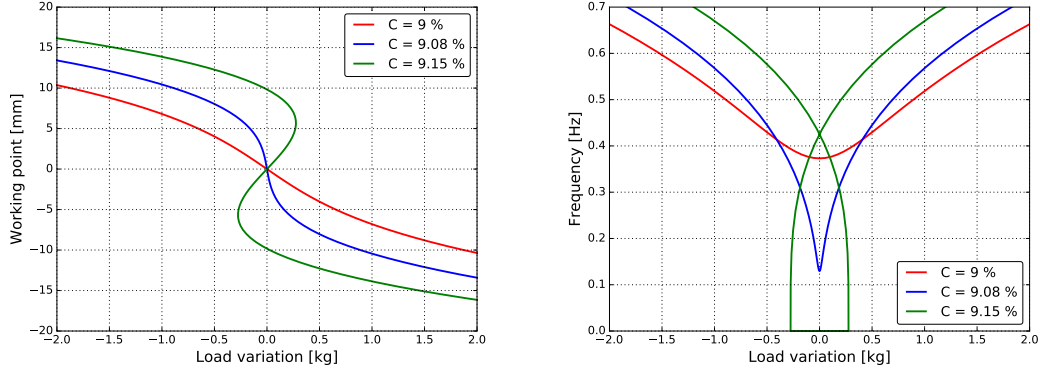


Figure 3.11: Working point height of the keystone (*left*) and its resonant frequency (*right*) as the function of suspended mass load, with various compression of the GAS blade, predicted with the model, when the following setting is used: $k_z = 1.0 \times 10^5$ N/m, $k_x' = 1.0 \times 10^6$ N/m and $l_{0x} = x_0 = 0.3$ m. It is assumed $m_0 = 200$ kg in the *right* panel.

GAS behaves like the case of 9% compression in figure 3.11. Consequently, we have to tune the suspended load so carefully in the real life.

• Thermal drift

Due to the softness, the vertical position of the keystone is drifted by a slight variation of the physical properties of the blade springs. The thermal drift of the keystone due to the temperature dependence of the Young's modulus of the blade spring material is a big problem in operating the GAS filter.

Assuming the GAS filter balances at the working point with a suspended mass of m , the optimal load to keep the keystone at the working point is changed with the temperature shift ΔT by:

$$\frac{\Delta m}{m} \sim \frac{1}{E} \frac{\partial E}{\partial T} \Delta T, \quad (3.21)$$

where E is the Young's modulus of the blade spring material. Supposing a small perturbation and the this shift is equivalent to an an additional force applied to the keystone ($\Delta F = \Delta mg$), the displacement due to thermal shift can be described by

$$\Delta z = \frac{\Delta F}{k_{\text{eff}}} = \frac{g}{\omega_0^2 E} \frac{\partial E}{\partial T} \Delta T, \quad (3.22)$$

where $k_{\text{eff}} = m\omega_0^2$ is the effective stiffness of the GAS filter and $\Delta F = k_{\text{eff}}\Delta z$. The temperature dependence with typical parameter $\frac{1}{E} \frac{dE}{dT} \sim 300 \times 10^{-6}$ [1/K] [36] is

$$\frac{\Delta z}{\Delta T} = 0.69 \text{ [mm/K]} \left(\frac{0.33 \text{ Hz}}{\omega_0/2\pi} \right)^2 \left(\frac{\frac{1}{E} \frac{\partial E}{\partial T}}{3.0 \times 10^{-4} \text{ [1/K]}} \right). \quad (3.23)$$

This implies that the position shift of the keystone gets more sensitive to the temperature if the resonant frequency is reduced by the anti-spring effect. In a previous measurement, it was confirmed that this estimation of the temperature dependence was consistent with a measurement when a GAS filter was tuned at 0.33 Hz [33].

3.3 Active vibration isolation

By using the mechanical filters in section 3.2.2, we can attenuate the seismic noise at higher frequency, however, we have to damp the mechanical resonances. Passive damping is one option to deal with this issue. Another option which is active vibration isolation system, is introduced here. Even though the used sensors and actuators can introduce their self-noises and can disturb the attenuation performance by the mechanical filters, the control system can take care not only damping but also steering and keeping the position and the orientation of the controlled stage. Feedback control is the most basic system for those purposes. This subsection introduces the basic idea of feedback control and some control systems used in the low frequency vibration isolation.

3.3.1 Feedback control

A simple example is shown in Figure 3.12. We consider a case where we want to control a suspended stage with an actuator which applies a force from the ground.

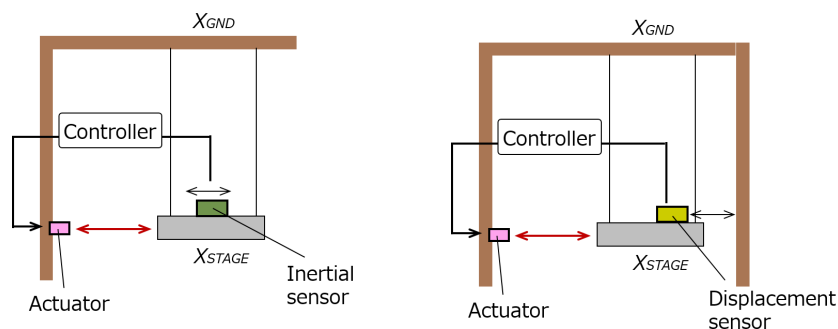


Figure 3.12: A simple model of feedback control with an inertial sensor (*left*) and with displacement sensor (*right*).

Feedback control with inertial sensor

In a case where we have an inertial sensor which senses the suspended mass motion as shown in Figure 3.12 (*left*), the corresponding block diagram becomes as shown in Figure 3.13. By following the diagram, we assume that the displacement transfer function and the actuator response of the suspended mass is given by P_s and P_a respectively. The actuator noise coupling X_{stage}/N_{act} , the sensor noise coupling X_{stage}/N_{inert} and the seismic noise coupling X_{stage}/X_{GND} are calculated

respectively as

$$\frac{X_{\text{stage}}}{N_{\text{act}}} = \frac{P_a}{1+G}, \quad (3.24)$$

$$\frac{X_{\text{stage}}}{N_{\text{inert}}} = \frac{-G}{1+G}, \quad (3.25)$$

$$\frac{X_{\text{stage}}}{X_{\text{GND}}} = \frac{P_s}{1+G}, \quad (3.26)$$

where G denote the open loop gain which is given by $P_a F_{\text{fb}} S_{\text{inert}}$. The sensor response is described by S_{inert} in this system. Then an external disturbance and the seismic noise coupling are to be suppressed by $1/(1+G)$. On the other hand, the sensor noise can induce the vibration depended on the feedback filter shape F_{fb} where $|G| \ll 1$, since eq (3.25) becomes close to $G = P_a F_{\text{fb}} S_{\text{inert}}$ there. In a pendulum P_a and P_s becomes smaller and smaller with f^{-2N} where N is the number of the stages, and thus the filter shape can have an impact to the residual motion of the mass at higher frequency region.

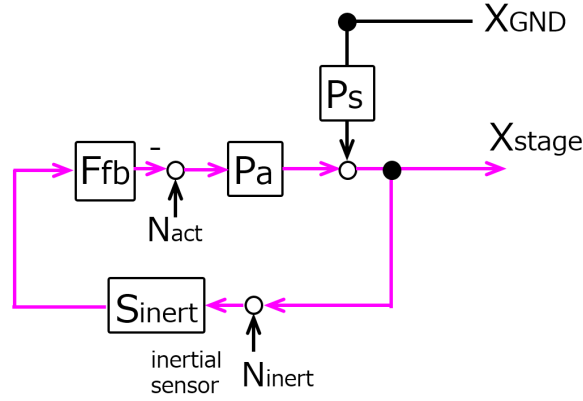


Figure 3.13: Block diagram of the system shown in Figure 3.12 (*left*).

Feedback control with displacement sensor

On the other case where we have an inertial sensor which sense the suspended mass motion, the corresponding block diagram becomes as shown in Figure 3.14. With the same manner in the above, the actuator noise coupling $X_{\text{stage}}/N_{\text{act}}$, the sensor noise coupling $X_{\text{stage}}/N_{\text{inert}}$ and the seismic noise coupling $X_{\text{stage}}/X_{\text{GND}}$ are obtained respectively as

$$\frac{X_{\text{stage}}}{N_{\text{act}}} = \frac{P_a}{1+G}, \quad (3.27)$$

$$\frac{X_{\text{stage}}}{N_{\text{L}}} = \frac{-G}{1+G}, \quad (3.28)$$

$$\frac{X_{\text{stage}}}{X_{\text{GND}}} = \frac{G+P_s}{1+G}, \quad (3.29)$$

where G denote the open loop gain which is given by $P_a F_{fb} S_L$. The sensor response is described by S_L in this system. In this case, response from the actuator noise and from the sensor noise are same as those in the feedback system with an inertial sensor. However, the seismic noise coupling has a contribution from the controller as shown in eq (3.29).

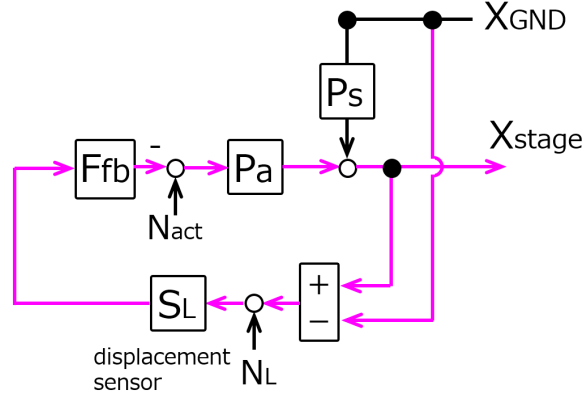


Figure 3.14: Block diagram of the system shown in Figure 3.12 (*right*).

Actually used feedback system

Since displacement sensors are more robust in lower frequency region, for the purpose of robust mechanical damping, we typically use the displacement sensors. However, after the system becomes calmed down enough, we then start using the inertial sensors in order to get more suppression of the seismic noise coupling. On the other hand, practically at lower frequency the inertial sensor becomes less useful since it start to sense tilt motion and its self noise. Also at higher frequency, the displacement sensor noise becomes dominant.

We then combine these signals of the inertial sensor and displacement sensor virtually using high-pass and low-pass filters. This is called sensor blending technique. The block diagram of the Feedback control with blended sensors are shown in Figure 3.15. The more details are discussed in [37, 33]. This sensor blending is done by applying a low-pass filter with frequency response $B_{LP}(s)$ to the LVDT signal and a complimentary high-pass filter $B_{HP}(s) = 1 - B_{LP}(s)$ to the inertial sensor. By doing this we avoid phase distortion around the blending frequency. The blending filters can be derived from seventh order polynomial function of the Laplace variable (s) as

$$B_{LP}(s) = \frac{35\omega_b^4 s^3 + 21\omega_b^5 s^2 + 7\omega_b^6 s + \omega_b^7}{(s + \omega_b)^7}, \quad (3.30)$$

$$B_{HP}(s) = \frac{s^7 + 75\omega_b s^6 + 215\omega_b^2 s^5 + 355\omega_b^3 s^4}{(s + \omega_b)^7}, \quad (3.31)$$

where ω_b denotes the crossover frequency of the two blending filters. Since the displacement sensor measures the relative position between the stage and the ground, the active control using the displacement sensor will re-introduce seismic vibration to the stage. In the GW detectors, since we want to isolate the mirror from the ground motion, especially from the microseismic peak, the blending crossover frequency is set below 0.1 Hz, in order to avoid degradation of attenuation performance at about the frequency region between 0.2 and 0.5 Hz. On the other hand, practically the sensor noise of the inertial sensor becomes dominant at such lower frequency, the the blending crossover frequency and the order of the polynomial function in the blending filters also depends on the sensitivity at the lower frequency region of the inertial sensor.

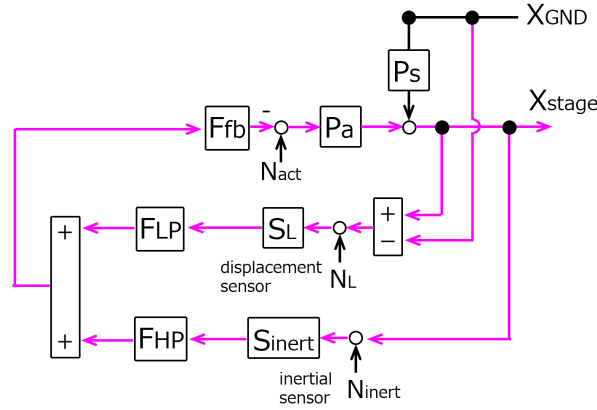


Figure 3.15: Block diagram of the feedback system with virtually signal blended sensor.

Using the above blending filters B_{LP} and B_{HP} , the actuator noise coupling X_{stage}/N_{act} , the sensor noise coupling X_{stage}/N_{inert} and the seismic noise coupling X_{stage}/X_{GND} of this system are obtained respectively as the followings, assuming an ideal case where the sensor responses $S_{inert} = S_L = 1$ and using $B_{HP} + B_{LP} = 1$:

$$\frac{X_{stage}}{N_{act}} = \frac{P_a}{1 + G}, \quad (3.32)$$

$$\frac{X_{stage}}{N_{inert}} = \frac{-GB_{HP}}{1 + G}, \quad (3.33)$$

$$\frac{X_{stage}}{N_L} = \frac{-GB_{LP}}{1 + G}, \quad (3.34)$$

$$\frac{X_{stage}}{X_{GND}} = \frac{GB_{LP} + P_s}{1 + G}, \quad (3.35)$$

where G is given by $P_a F_{fb}$. By using a low-pass filter whose crossover frequency is below about 0.1 Hz, the contribution of the controller is mode suppressed, compared to eq (3.29). The sensor blending technique is commonly used system in the GW detectors, however, in order to make use of this effectively, it is

important to have inertial sensors which has good enough sensitivities at the frequency lower than about 0.1 Hz.

3.3.2 Feedback control with feed-forwarding

As another option to suppress the seismic noise coupling level, we can use a sensor on the ground with feed-forward technique. This subtract the seismic noise coupling using the ground-motion sensor. Figure 3.15 shows the block diagram of the Feedback control system using a displacement sensor with a feed-forwarding.

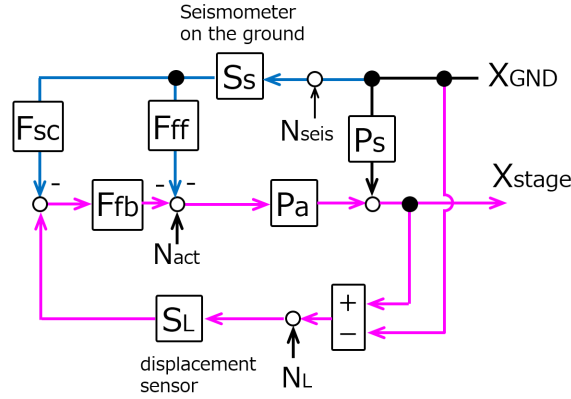


Figure 3.16: Block diagram of the feedback system using a displacement sensor with a feed forward system.

In this system, the ground vibration sensed by a seismometer on the ground is sent to the displacement sensor signal before applying the control filter with a filter F_{sc} , and also sent to the actuation port with a filter F_{ff} , in order to subtract the seismic noise coupling. The actuator noise coupling X_{stage}/N_{act} , the sensor noise coupling X_{stage}/N_{inert} and the seismic noise coupling X_{stage}/X_{GND} of this system are obtained respectively as

$$\frac{X_{stage}}{N_{act}} = \frac{P_a}{1 + G}, \quad (3.36)$$

$$\frac{X_{stage}}{N_L} = \frac{-G}{1 + G}, \quad (3.37)$$

$$\frac{X_{stage}}{N_{seis}} = \frac{S_s P_a}{1 + G} (F_{sc} F_{fb} - P_a F_{ff}), \quad (3.38)$$

$$\frac{X_{stage}}{X_{GND}} = \frac{1}{1 + G} \left[G \left(1 + \frac{S_s}{S_L} F_{sc} \right) + (P_s - P_a S_s F_{ff}) \right], \quad (3.39)$$

where G is given by $P_a F_{fb} S_L$. By selecting the condition for the F_{sc} and F_{ff} described by eq (3.40) and eq (3.41), the seismic noise coupling becomes zero in an ideal case. This is a case where the F_{sc} subtracts the ground motion from the displacement sensor, and F_{ff} compensates the mechanical seismic noise coupling

P_s , F_{sc} and F_{ff} are called the sensor-correction filter and feed-forwarding filter respectively.

$$F_{\text{sc}} = -\frac{S_L}{S_s}, \quad (3.40)$$

$$F_{\text{ff}} = \frac{P_s}{PaS_s}, \quad (3.41)$$

In this condition, the sensor noise coupling from the ground motion sensor becomes

$$\frac{X_{\text{stage}}}{N_{\text{seis}}} = \frac{-P_a}{1+G} (S_L F_{\text{fb}} + P_s). \quad (3.42)$$

As another option, a feedback control system using a blended sensor with a feed-forwarding is also used for further seismic noise suppression in the GW detectors as discussed in [38].

KAGRA Type-A Seismic Attenuation System

As in the previous section, in order to have enough seismic attenuation in the detection band (> 10 Hz), a vibration isolation system composed of multi-stage pendulum system is used for the mirrors of the GW detectors. We then have to damp the mechanical resonances of the pendulum based suspension system and also have to freeze the mirror for the interferometer lock. For this purpose, passive/active damping system is adopted.

This chapter describes the mechanical aspect of the actual seismic attenuation system used in KAGRA detector, which realize the required performance, focusing on Type-A suspension. The implemented sensors and actuators for the active control system is also introduced.

4.1 Optical layout of KAGRA detector

The designed optical configuration of KAGRA detector is shown in Figure 4.1. A seed laser beam from a Nd:YAG non-planar ring oscillator (NPRO) is passed through amplifiers, and is increased in power up to about 200 W. The laser beam is sent to a pre-stabilization system, and phase/amplitude modulation is applied for interferometer sensing and controls. After this process, the laser enters the input mode cleaner (IMC), which filters the spatial modes and polarization of the laser beam with a triangular optical cavity composed of suspended mirrors with a double-stage suspension. The output beam is input to the main part of the interferometer part as described in section 1.3. In order to improve the spatial mode stability of the recycling cavities, the beam between recycling mirrors and the beam splitter is folded into a Z-shape. The transmitted beam from the signal recycling mirror is filtered by an output mode cleaner (OMC), which aims to remove unwanted higher-order spatial modes from the beam. The detailed optical design of the KAGRA interferometer are described in reference [4].

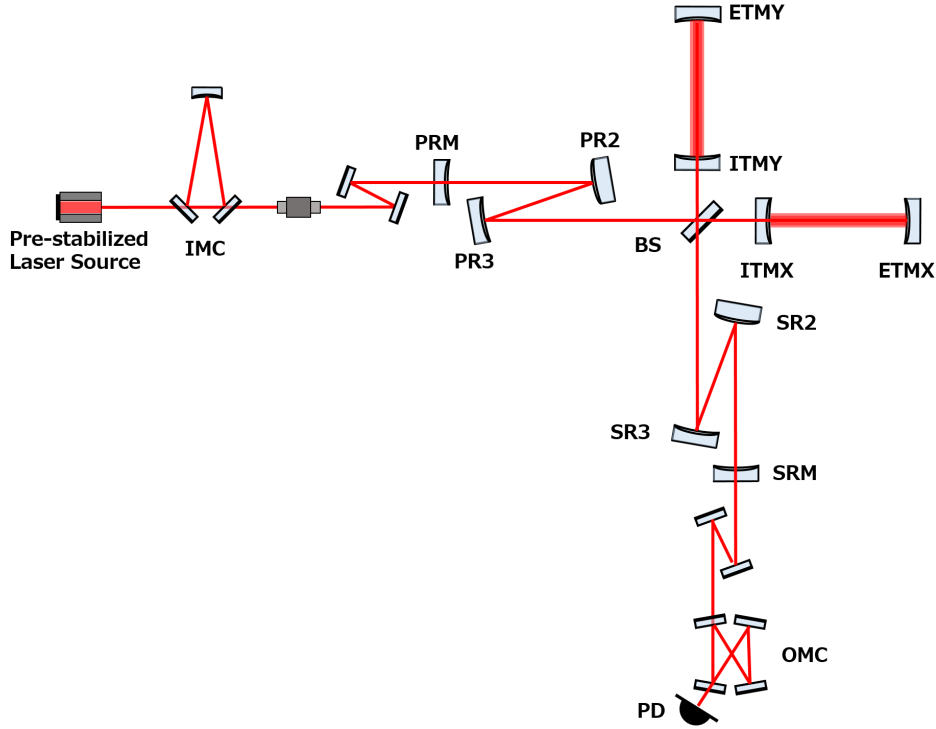


Figure 4.1: The Optical layout of KAGRA detector. The laser beam from the pre-stabilized laser source goes into the input mode cleaner (IMC), and then go through the power recycling mirrors located in Z-shape (PRM, PR2 and PR3). The beam which incidents to the AS port passes through the signal recycling mirrors put with Z-shape (SRM, SR2 and SR3). Test masses are located at ITMX, ITMY, ETMX and ETMY (Input/End Test Mass X/Y). OMC and PD represent the output mode cleaner and photo diode respectively.

4.2 Displacement noise requirement

In the gravitational wave detectors, differential length variation of the arm cavities, which is called DARM signal¹, is the most important dof, since it contains information of gravitational waves. Since the displacement noise of the optics forming the Fabry-Perot cavities (which is conventionally called test masses, TMs) directly affects to the DARM signal, and thus these optics have the strictest requirement on their displacement noise. Displacement noise of auxiliary optics also couples to the detector sensitivity via the length sensing and control schemes of the interferometer [39]. Hence the displacement noise of those auxiliary optics also should be suppressed, although the requirements for these optics are less strict than for the test masses.

One of the requirements of these suspension system is to reduce the seismic noise level well below compared to other noise levels, such as the thermal noise or

¹This stands for differential arm signal

quantum noise, in the detection band of gravitational waves. The requirement for the seismic noise level is to be lower by a factor of 10 in spectrum densities than other noise levels above 10 Hz. The required displacement noise level of the core optics of the KAGRA detector is shown in Figure 4.2, which shows two optional detection modes called BRSE (Broadband Resonant Sideband Extraction) and DRSE (Detuned Resonant Sideband Extraction) [40]. These two modes can be switched by changing the resonant condition of the signal recycling cavity. Table 4.1 summarizes the maximum permitted displacement noise level at 10 Hz. The folding mirrors, PR2 and PR3 (SR2 and SR3) have more strict displacement noise requirements than PRM (SRM) by a factor of 2, since the folding mirrors can change the optical path of the power recycling cavity by twice, compared to the optical-path change due to PRM (SRM).

In addition, when we consider the optic displacement, we consider the vertical motion coupling since 1 % since 0.1-1 % of the mechanically vertical-longitudinal couplings can happens, as described in subsection 3.2.1. In the KAGRA detector, except for the mechanical couplings, the vertical motion is coupled to the longitudinal direction at least by 0.3% since the KAGRA detector is not constructed in the horizontal plane for a practical reason. Since the Kamioka mine, where the site of the KAGRA detector, has a lot of groundwater sources in it, the interferometer arm tunnels have a tilt of 1/300 for drainage. Based on this, 1 % of vertical motion transferred to the longitudinal direction is assumed in the following discussion.

Table 4.1: Requirements on longitudinal displacement noise of the core optics for the KAGRA detector.

Optic	Spectrum density at 10 Hz
PRM	$1.5 \times 10^{-15} \text{ m}\sqrt{\text{Hz}}$
PR2,3	$7.5 \times 10^{-16} \text{ m}\sqrt{\text{Hz}}$
SRM	$2.5 \times 10^{-18} \text{ m}\sqrt{\text{Hz}}$
SR2,3	$1.3 \times 10^{-18} \text{ m}\sqrt{\text{Hz}}$
BS	$3.4 \times 10^{-18} \text{ m}\sqrt{\text{Hz}}$
TM	$8.0 \times 10^{-20} \text{ m}\sqrt{\text{Hz}}$

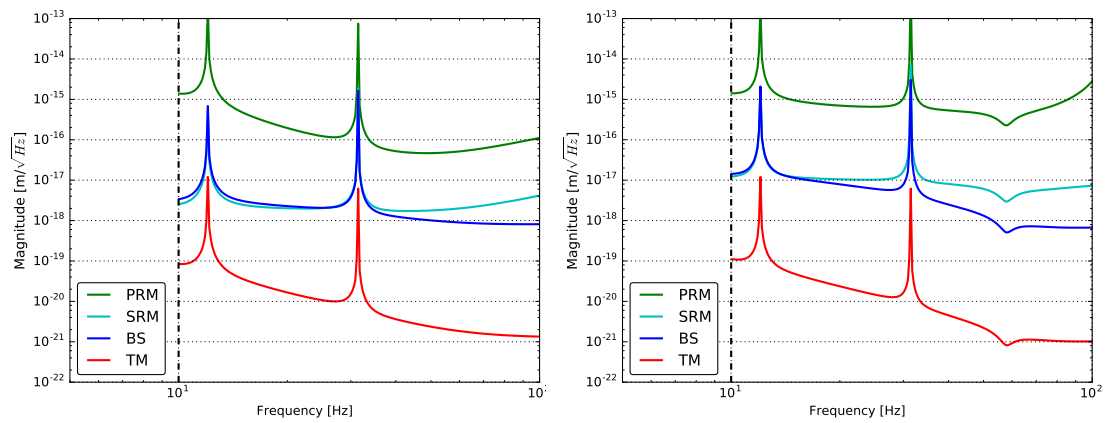


Figure 4.2: Requirement for displacement noise in BRSE detection mode (*left*) and DRSE detection mode (*right*). PRM, SRM, BS, and TM denote power recycling mirror, signal recycling mirror, beam splitter, and test mass respectively.

4.3 Overview of KAGRA suspensions

KAGRA detector has three types of the suspension system for the core optics depending on the required seismic attenuation levels in the detection band. The four TMs are suspended by the longest vibration isolation system called Type-A suspension. BS and the signal recycling mirrors, four optics in total, are suspended by the middle size system called Type-B suspension. For the three power recycling mirrors, a compact system called Type-Bp suspension is used. Only the payloads of the four TMs suspended by Type-A suspension system is to be cooled down to the cryogenic temperature.

Type-A suspension is composed of 9 stages for horizontal isolation and 6 stages for vertical isolation, and its height is 13.5 m. The upper five stages are operated in the room-temperature, while the lower four stages are cooled down to cryogenic temperature. In Type-A suspension, a stage called pre-isolation stage, is supported by three IPs from the ground and the other whole pendulum system is suspended from the stage. Other details are described in section 4.4 and 4.5 .

Type-B system is composed of 5 stages for horizontal isolation and 3 stages for vertical isolation. Three IPs are used for the pre-isolation of the ground motion and the other components are suspended by the Type-B system stage, which is similar to Type-A suspension system.

Type-Bp suspension is composed of 3 stages for horizontal isolation and 2 stages for vertical isolation. This system does not include the IP stage. A damping system is implemented at the BF-stage instead, in order to suppress the large RMS displacement and velocity caused by absence of the IP stage. For the horizontal static position alignment of the suspended optic, a motorized stage is implemented on the top of the suspension chain, which is called the traverser.

The three types of KAGRA suspensions and their location are shown in Figure 4.4 and 4.3 respectively.

The basic role of the suspension component is summarised as follows:

- The top part, such as IP-stage, is used for the pre-isolation of the seismic motion and static-control stage at the top of the chain.
- middle part, the chain of GAS filters, is used to achieve the required seismic attenuation.
- The payload part, the mirror suspension is for providing control system for lock acquisition and its alignment.

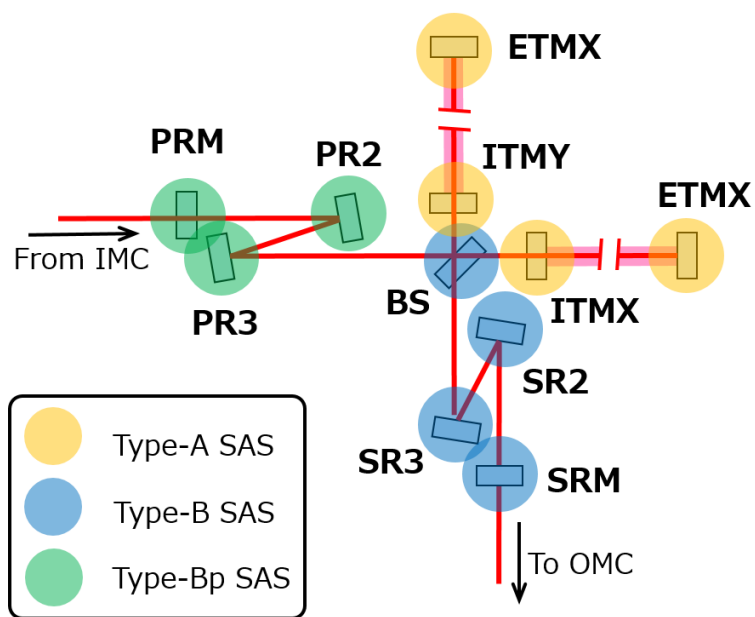


Figure 4.3: The Location and the type of the suspensions in the KAGRA main interferometer. PRM, PR2 and PR3 (the power recycling mirrors) are suspended by TypeBp system, while SRM, SR2 and SR3 (the signal recycling mirrors) are suspended by TypeB system. The four TMs are suspended by TypeA system.

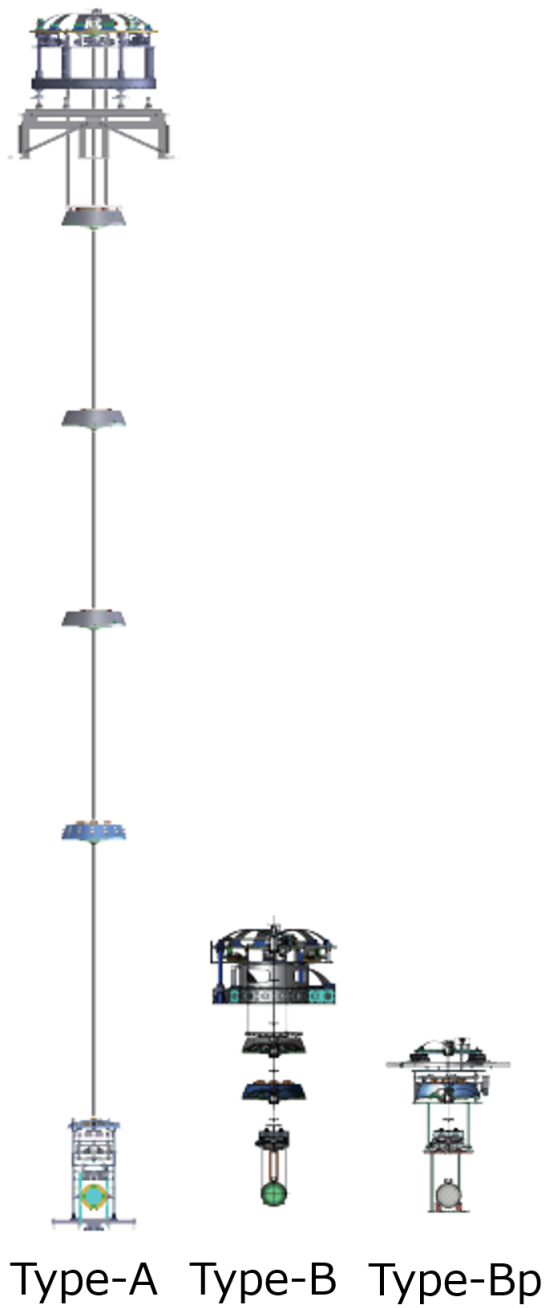


Figure 4.4: Overview of the suspension system for KAGRA detector. Type-A system is used for TMs, Type-B is for BS and SR mirrors, and Type-Bp system is used for PR mirrors

4.4 Mechanical Systems of Type-A suspension

The Type-A suspension is a nine-stage pendulum composed of the pre-isolation stage supported by IPs, the chain of GAS filters and the payload to be operated in an cryogenic temperature. The 3D overview is shown in *left* of Figure 4.5.

The Type-A system extends over two stories and the legs of the inverted pendulum table are fixed onto the second floor. The top stage called pre-isolation stage, is supported by three IPs from the ground, and the whole system is suspended by this stage. From the top, we have five GAS filter chain which called filter 0, 1, 2, 3 and bottom filter(F0, F1, F2, F3 and BF in short). As an auxiliary mechanics, magnetic damper (MD) ring is suspended from the underneath of the pre-isolation stage with three maraging rods. It is planned to use this for viscous-damping system with a conductive body attached on the top of the F1-body. The other four stages suspended from the BF is called cryogenic payload (or cryo-payload). The most upper stage of the cryo-payload is called platform (PF). From the PF, two chains of three-stage pendulum system are suspended separately, and they are called test mass (TM) chain and recoil-mass (RM) chain respectively. The three stages in the TM chain is called the marionette (MN), intermediate mass (IM) and the test mass (TM) from the top. The RM chain has stages which surround the corresponding TM chain components to apply actuation force which is isolated from the ground disturbance. They are called recoil-marionette (RMN), intermediate-recoil-mass (IRM) and recoil-mass (RM).

The suspension wires above the PF is made of maraging steel with heat treatment to increase their tensile strength. In the payload, the sapphire fibers are designed as the four suspension wires between the IM and TM in order to extract the heat of TM. Other wires in the payload is made of maraging steel or copper beryllium.

As another structure, heat links (HLs) are connected to RMN from the cooling bar via a vibration isolation system for the HLs, for the purpose of quick cooling via conductive heat transfer.

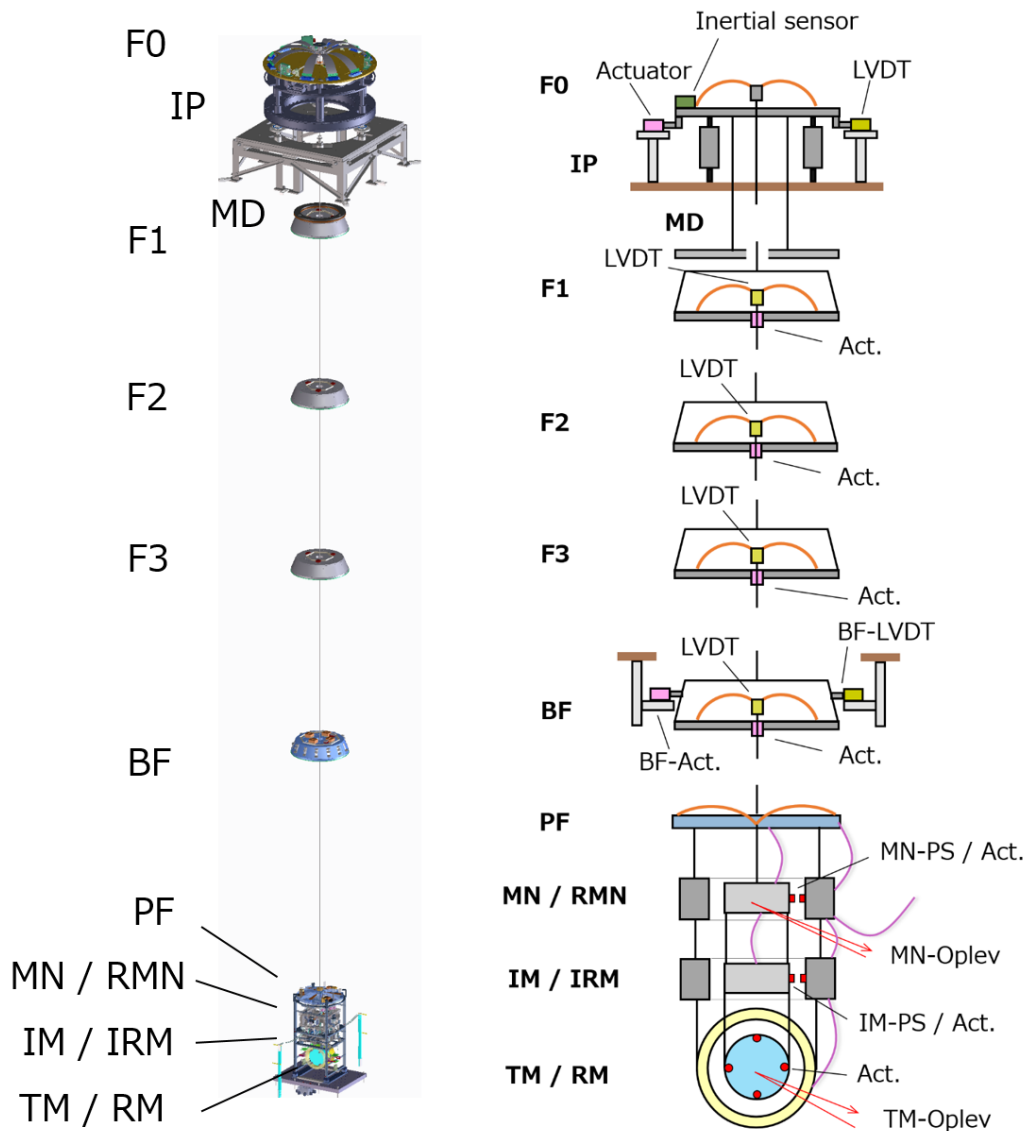


Figure 4.5: The overview of the Type-A suspension system. In the schematic view (*left*), the implemented sensors and the actuators information is included, which is described in section 4.7. The boldfaced letters represent the names of the suspension stages, while the small characters show the implemented sensors and actuators.

4.4.1 Pre-isolation stage

The IP pre-isolation stage (oftenly called IP stage) has a set of IP legs and a base ring, and the top GAS filter. The main role of this stage is to provide the first mechanical resonance below 0.1 Hz for horizontal motion in order to suppress the micro seismic coupling. This stage also aims to deal with the static control of horizontal position and yaw orientation of the mirror. An overview of the pre-isolator is drawn in Figure 4.6.

The top stage is supported by three IP legs in each 120° rotation. On the top stage, the thinner tip of the cantilever blades is connected to the keystone F0 GAS filter. The IP stage has three sets of coil-magnet actuators and two kinds of sensors arranged in a pinwheel configuration. Originally linear variable differential transformers (LVDTs) are used at lower frequency, and inertial sensors are used for higher frequency with a crossover around 50 mHz². One of the suspension wires for the main chain is hooked at the keystone of the top GAS filter, while the other three wires are for the magnetic damper and they are hooked on underneath of the top plate.

The details of the IP leg is shown in Figure 4.7. This IP has the flexure joints, which are made of maraging steel, at both ends of the hollow cylinder of the leg. A structure around the bottom flexure where the counter weights are mounted enables to coincide the center of percussion to the fixing point of the flexure. by introducing the counter weights, the saturated attenuation factor is expected to be improved. Each IP stands on the cone bellows supported by in-air screw jacks which enables us to adjust the height of the IP 's feet so as the ground plane to be horizontal.

²In the current plan, we use the geophone L-4C for the two ETMs and accelerometers which were used in TAMA detector, for ITMs for O3 phase. Then in O4, we would replace the accelerometers with geophones due to some constraints.

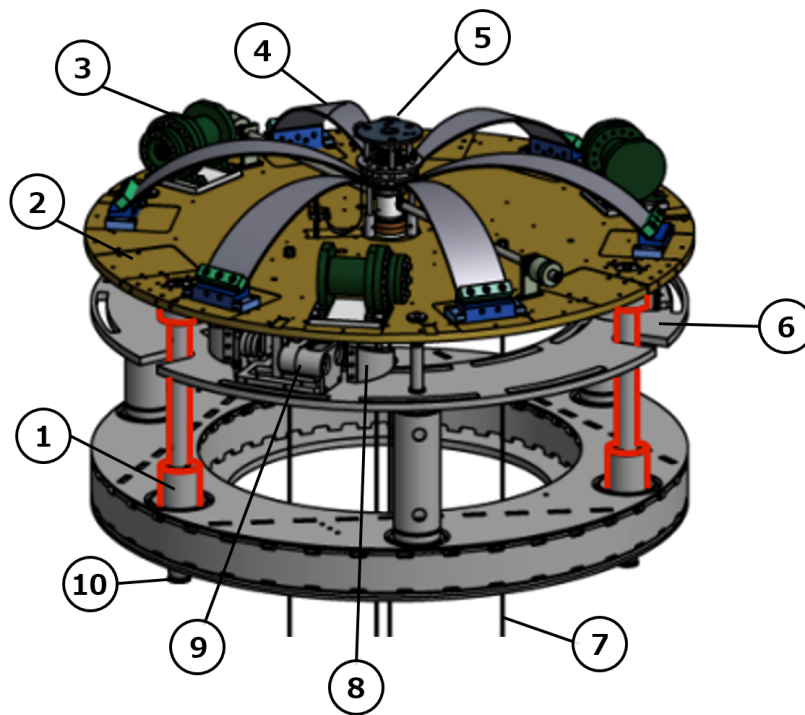


Figure 4.6: The overview of pre-isolation stage. 1) IP leg, 2) top plate, 3) inertial sensor for sensing the IP top stage motion, 4) the cantilever of F0 GAS filter, 5) keystone and its surrounding structure of F0 GAS filter, 6) base-ring where one end of the LVDTs and the motorized blade spring are attached, 7) suspension wires, 8) motorized blade spring, 9) LVDT and the coil-magnet unit, 10) cup of cone bellows.

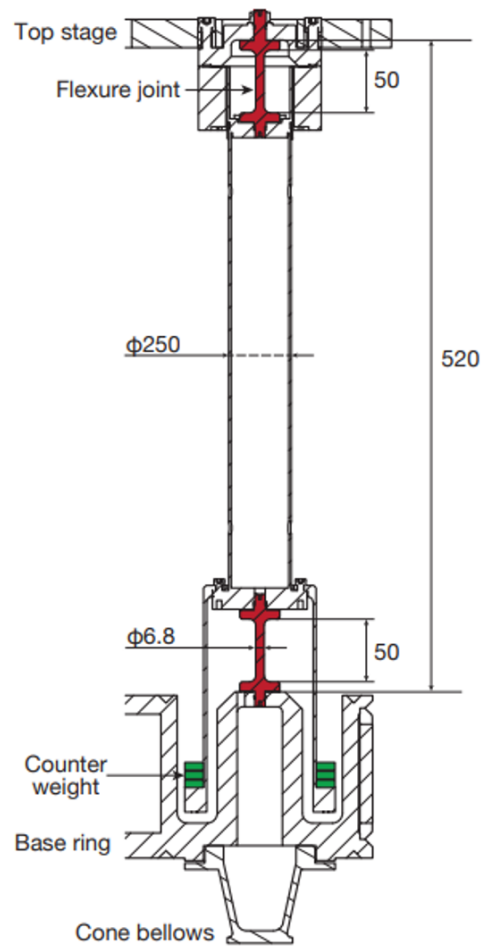


Figure 4.7: The details of the IP leg. The counter weight is implemented in order to the saturation level in the displacement transfer function.

4.4.2 GAS filter chain

The mechanical overview of the typical GAS filter, called standard filter is shown in Figure 4.8 and 4.9. The cantilever blades are clamped to the base plate at an inclination of 45° and their other ends are attached to the central moving ring called the keystone at an incidence angle of -33° . The cantilever blades are made of maraging steel [41]. The maraging steel is selected in order to avoid creep under highly stressed conditions. The width and number of the cantilever blades are selected so that the optimal load of the GAS filter coincides with the weight of the suspended masses. The optimal load of a GAS blade can be estimated from

$$F_{\text{optimal}} = G \frac{Et^3w}{12L^2}, \quad (4.1)$$

where t , L , w and E denote the thickness, length and base width of the cantilever blade, and the Young's modulus of the blade material, respectively. G represents a geometrical factor depending on the blade shape. The vertically relative motion of the keystone and the outer frame is controlled by using an Linear Variable Differential Transformer (LVDT) and a coil-magnet actuator, as described in section 4.7. The static vertical position is to be tuned by a motorized spring with a thin cantilever blade. At the most top and BF stage, a The static yaw position control system is implemented with a motorized spring as shown in Figure 4.9.

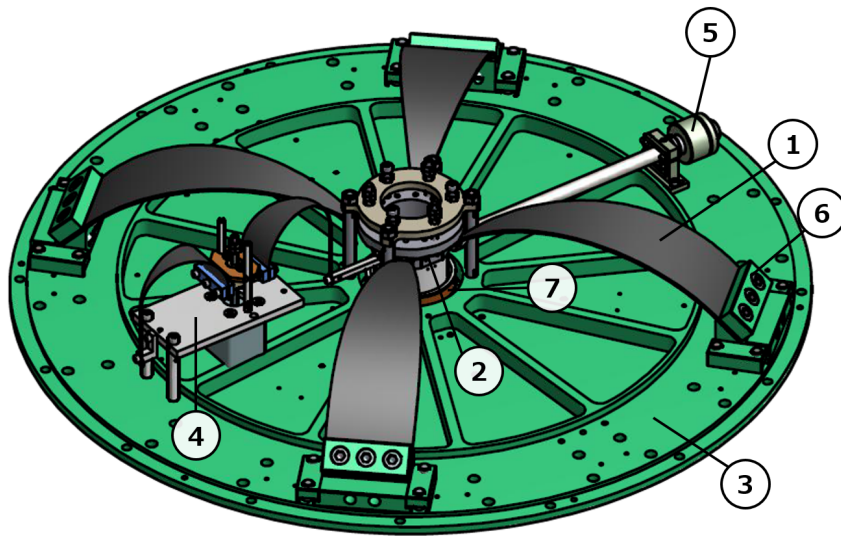


Figure 4.8: The mechanical overview of the typical GAS filter, called standard filter. 1) The cantilever blade, 2) the keystone, 3) the baseplate, 4) the motorized spring for initial positioning of the keystone, 5) the magic-wand for compensating CoP effect, 6) the base clamp, 7) the LVDT to monitor the displacement of the keystone.

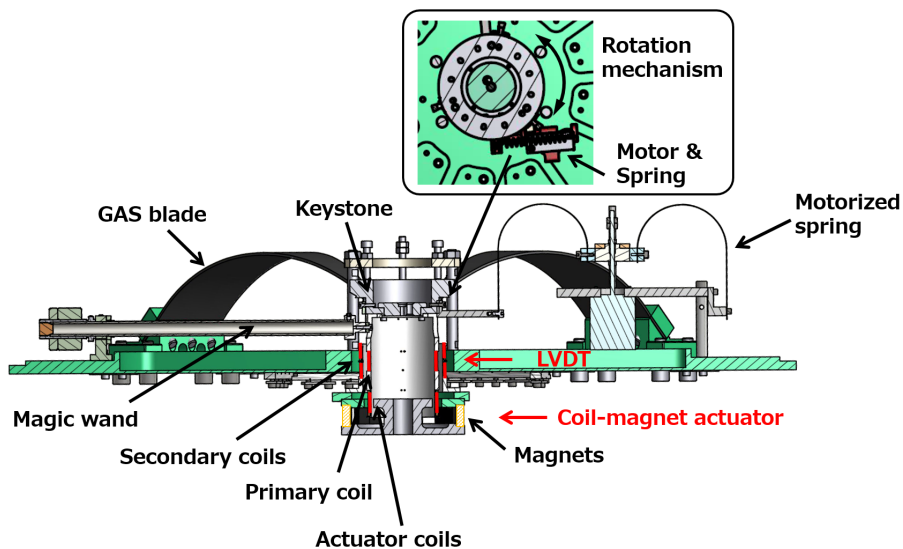


Figure 4.9: The cross-section of GAS filter.

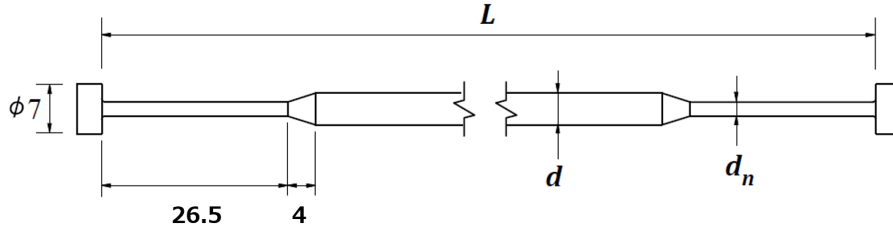


Figure 4.10: Overview of the typical suspension rod made of maraging steel.

4.4.3 Suspension rod

The suspension rods are also made of maraging steel.

The designed rods have larger thickness in the middle and have smaller thickness at the ends, as shown in Figure 4.10. This aims to effectively increase the torsion stiffness of the suspension rods without degrading the horizontal attenuation performance of the suspension system caused by the bending elasticity. The suspension wire is hooked to the suspension components by the nail-head shapes machined into both ends of the wire.

4.4.4 Magnetic damper

A single-wire suspension chain behaves as a torsion pendulum with a very low resonant frequency (lower than 0.1 Hz). Due to its high quality factor, this torsional oscillation lasts for a long time and disturbs the quick recovery of the interferometer lock. The magnetic damper (MD) is a passive damping mechanism using eddy currents and originally aims to damp such torsion mode. An eddy current damper consists of permanent magnets fixed on the reference side and conductive plates attached on the oscillator side to be damped, as described in section 3.2.1.

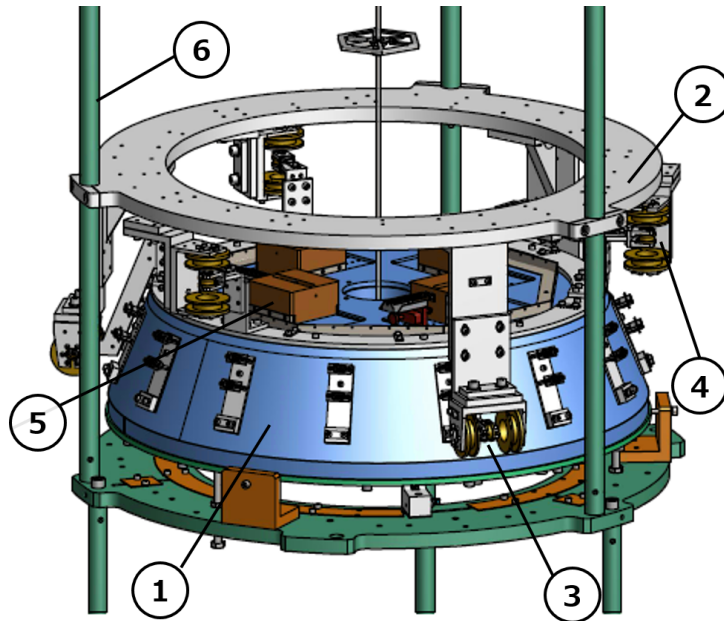
The design of the magnetic damper is a ring-shaped plate with arrayed permanent magnets, which is suspended from the pre-isolation stage by three wires and is placed just above the copper plates attached on the F1 GAS filter with a gap of about 5 mm. The magnets are arranged so that the overall magnetic dipole moment cancels out.

However, empirically it is known that a single magnetic damper is not adequate to damp the target torsion mode of the whole chain of the Type-A system, since the magnetic damper can apply a braking torque only onto the F1 stage. In addition, from the installation aspect, it is found that making a tiny gap such as 5 mm between the MD and F1-body is difficult. Consequently another torsion-mode-damping system is mainly used at the bottom filter in the Type-A suspension, called BF damping system.

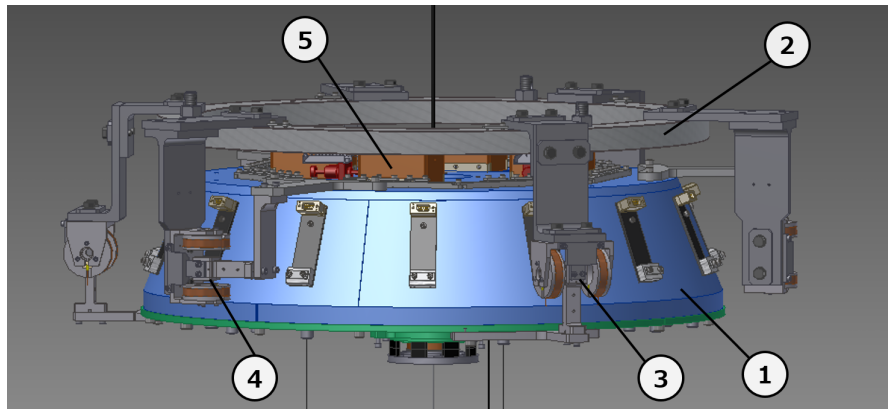
4.4.5 Bottom-Filter damping system

In order to actively damp some resonant modes involving swinging motion and torsion mode of the whole chain pendulum, a unit which utilises the displacement sensors and coil-magnet actuators, so-called BF-LVDT unit (in section 4.7.1), is implemented at BF-stage.

In type-A system, the damping system is realized by sensing the relative motion between the suspension and its security frame. While in the type-Bp, this is done by sensing the relative motion between the main suspension and a recoil mass for the BF, which is suspended from beneath the standard GAS filter by three maraging rods. BF-LVDT units are arrayed so that they can sense and control the relative motion in every translational and rotational DoF. The overview of the mechanical system of the Bottom-Filter damping system is drawn in Figure 4.11.



(a) 1) The body of the bottom GAS filter, 2) the BF-damper structure attached to the security frame, 3) the horizontal BF-LVDT and coil-magnet actuator unit, 4) the vertical BF-LVDT and coil-magnet actuator unit, 5) the motorized BF-tilt adjustment system, 6) the security frame.



(b) 1) The body of the bottom GAS filter, 2) the suspended recoil mass for the bottom GAS filter, 3) the horizontal BF-LVDT and coil-magnet actuator unit, 4) the vertical BF-LVDT and coil-magnet actuator unit, 5) the motorized BF-tilt adjustment system.

Figure 4.11: Overview of the bottom filter damping system in TypeA suspension (a) and in TypeBp suspension (b).

4.4.6 Cryogenic payload

The payload in the Type-A suspension, which is called cryogenic payload, will be cooled down and be operated at cryogenic temperature. The cryogenic payload consists of four stages with a parallelized pair of chains as shown in Figure 4.5. A detailed 3D-CAD drawing of the cryogenic payload is shown in Figure 4.12.

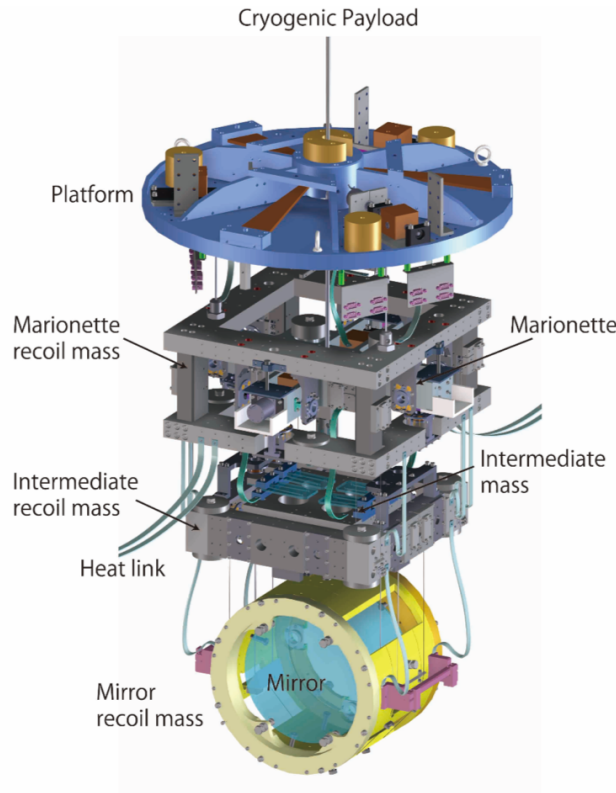


Figure 4.12: Overview of the cryogenic payload.

A disc-shaped stage is called platform (PF) and is suspended from the bottom filter with a single maraging wire, which is 3.3-meter-long. Then two chains are suspended from the PF-stage in parallel, which are TM-chain and RM-chain. The most upper stage of the TM-chain is marionette (MN), a cross-shaped mass suspended at a point close to its center of mass with a single maraging wire. The middle stage, which is called intermediate mass (IM) is suspended from the MN with four wires made of beryllium copper. The most lower stage is the sapphire test mass (TM), which is suspended with four sapphire fibers. Each of the sapphire fiber has 350 mm-long and 1.6 mm-diameter, and is hooked on a sapphire blade springs attached on the IM. In order to make use of better thermal conductivity of the assembled system, the same same material is used for the TM substrate and the fibers.

These bottom three stages have their recoil masses, which provide controllability of their relative position and alignment of the TM, independent of the

seismic disturbances. The recoil masses are called recoil-marionette (RMN), intermediate recoil mass (IRM) and recoil mass (RM) from the top respectively. There are permanent magnets on the TM-chain masses and coils on the RM-chain masses functioning as coil-magnet actuators to control each six differential motion of the MN-MNR and IM-IMR and three differential motion of the TM-RM position in longitudinal, pitch and yaw dof. For the sensors, cryogenic reflective photo-sensors in section 4.7.4 are arranged in the configuration coincident with the coil-magnet actuators to produce local relative displacement of the TM-chain masses and the RM-chain masses. In addition, for the purpose of static alignment control with respect to the ground and of the damping control of the TM-chain modes, local angular/displacement sensors called optical levers are implemented. The angular optical lever is installed at the MN- and TM-stages, which senses pitch and yaw motion of the TM-chain. Only the TM has the displacement optical lever which is called length optical lever as illustrated in Figure 4.5.

4.5 Cooling system

The cryogenic payload is cooled down based on the two paths of heat transfer, which are radiation cooling and conduction cooling. The payload is housed in a double-layered cryostat which is formed by a 8 K inner shield and 80 K outer shield. For the purpose of efficient radiation cooling, the surfaces of the cryostat, the payload, and the security frame are treated with black coating. In addition, for the purpose of conduction cooling, the stages of the payload are connected each other with high purity aluminum cables, called heat links [42, 43]. The absorbed heat on the mirror flows to upper stages and is then extracted to the cryostat structure through the heat links including its vibration isolation system and cooling bars. Since this mechanical conduction path could introduce additional vibration from the cooling bars to the isolated stages, a three-stage vibration isolation system is implemented on the cryostat to relay the heat links connected on the MNR.

These cryogenic instruments are put under cryogenic condition with four units of pulse-tube cryocoolers. The cryocoolers have a doubled vibration attenuation stages whose first stage is connected to the 80 K outer shield and whose second stage is connected to the payload cooling system and the 8 K inner shield. The shields of the cryostat have bore holes in front of the TM so that the laser beam goes through, however, the holes can threaten the cooling time and attainable lowest temperature of the TM by allowing intrusion of 300 K radiation from the room-temperature vacuum ducts. Based on this, 80 K duct shields are used inside the neighboring vacuum ducts to reduce the solid angle of the incoming 300 K radiation. The cooling down system around the cryostat is schematically summarized in Figure 4.13 and 4.14.

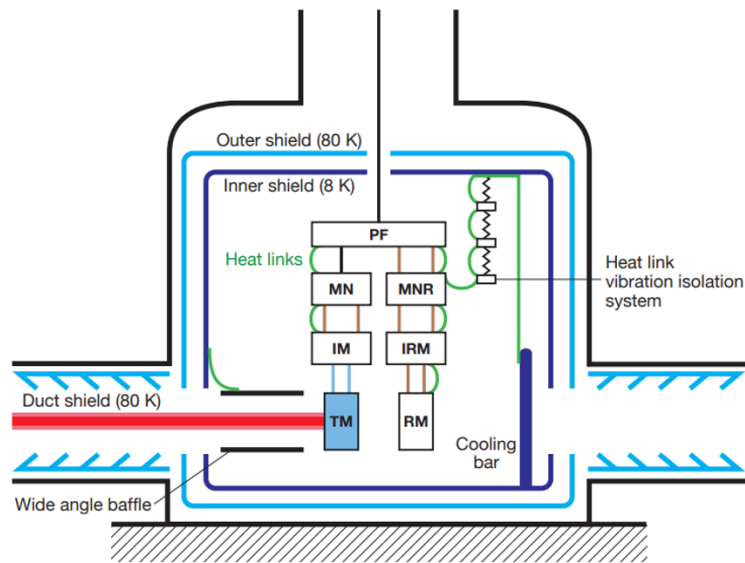


Figure 4.13: A schematic view inside the cryostat from [32]. The colors of cryogenic payload denote the difference of the materials; blue, brown and black wires represent sapphire, copper beryllium and maraging steel respectively.

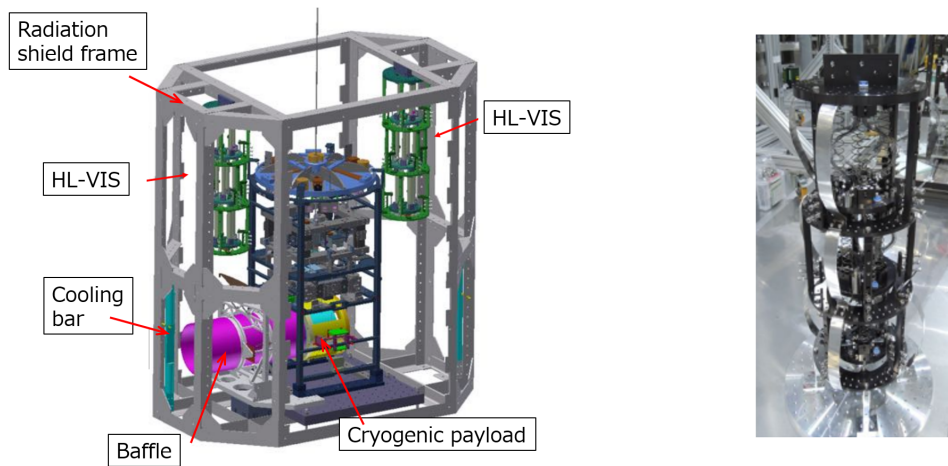


Figure 4.14: 3D-CAD drawing of the system inside the cryostat (*left*) and the actual structure of the vibration isolation system for the heat links (*right*). The heat link vibration isolation system is abbreviated as HLVIS.

4.6 Expected isolation performance

The estimated mechanical vibration isolation performance of the Type-A system is shown in Figure 4.15. In this calculation, 1% coupling from vertical motion is assumed. Since the heat links are mechanically connected to the cryostat via the heat link vibration isolation system, an extra vibration from the cryostat is introduced to the suspension system. The heat links are loosely connected so that they do not provide much stiffness in lower frequency region, on the other hand, the vibration would be transmitted and enhanced at high frequencies by the internal resonances of the wires. The contribution from the heat link system is included assuming that the RMN is connected to the inner shield of the cryostat with the heat links via heat link vibration isolation system. This simulation also assumes that the vibration of the cryostat is the same level of the ground vibration. Even though the mirror vibration will become enhanced by the heat link system at about above 2 Hz, the mirror will be mechanically suppressed by the heat link vibration isolation system as same level as the requirement at 10 Hz. I note that vibration of the cryostat will be enhanced due to its internal resonances and cryocooler operations [44]. This implies that the mirror vibration will be enhanced at the detection band and thus the contribution of the heat link system have to be further investigated.

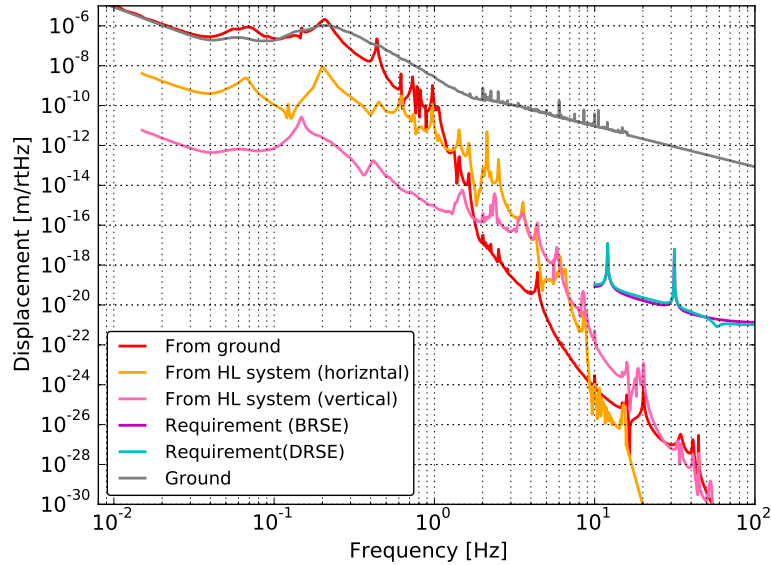


Figure 4.15: Expected vibration isolation performance assuming 1% coupling from vertical motion.

4.7 Sensors and Actuators

4.7.1 Linear Variable Differential Transducer

Linear Variable Differential Transducer, called LVDT, is a relative position sensor making use of coil inductance and modulating magnetic fields [45]. The LVDT consists of two kinds of coils. They are called the primary coil and the secondary coils, are set coaxially aligned. The detailed LVDT structure is shown in Figure 4.16. The working principle can be summarized as follows. We send sinusoidal modulation signals at 10 kHz to the primary coil which produces oscillating magnetic field around it. Then the secondary coils sense the variation of the magnetic field and generate induced voltages. The induced voltage will be canceled when the primary coil is placed at the center of the secondary coils since the two secondary coils are identical but counter-wound to each other. Consequently if the primary coil shifts from the center, the mutual inductance is changed and the differentially induced voltages appear as net voltages at the readout. The net differential voltage is then amplified and sent to the mixer which demodulates the oscillating voltage to obtain low-frequency signals (below 100 Hz) of the displacement of the primary coil.

The suspension systems in KAGRA have two types of LVDTs. One is used for the IP-stage and GAS filters, and the other one is a dedicated one for the BF damping system which is called BF-LVDT. The BF-LVDT is designed so that the secondary coils of the LVDT are shared by the actuator coil [46].

The typical linear range and the noise floor of the LVDTs is shown in Figure 4.17.

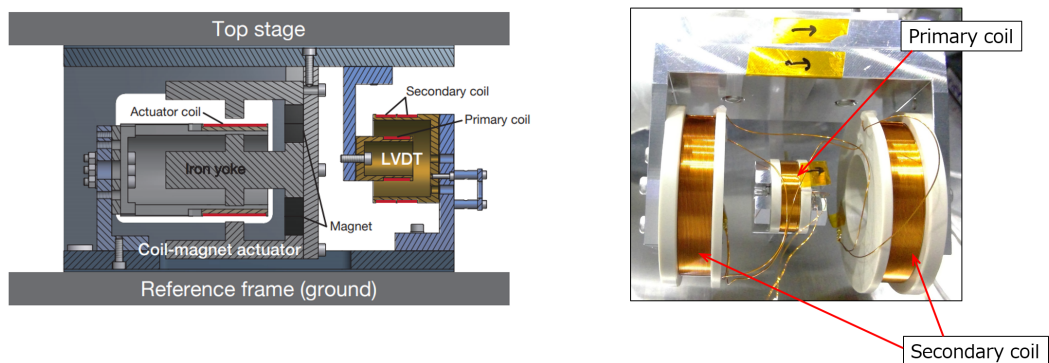


Figure 4.16: The detailed LVDT structure which is used for the IP-stage from [32] (*left*) and is used for BF-damping system (*right*). The structure of the LVDTs used for GAS filter is included in Figure 4.9.

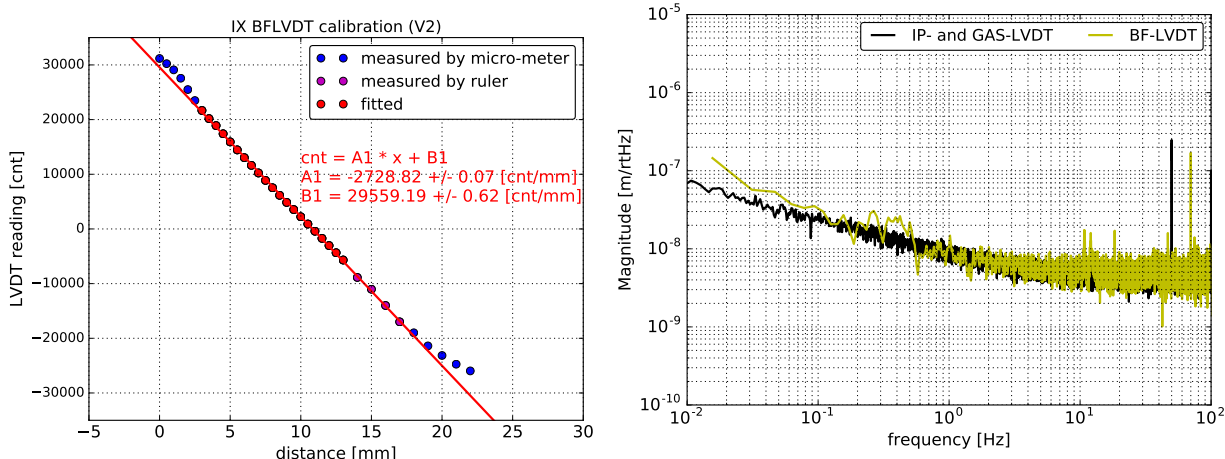


Figure 4.17: The typical linear range (*left*) and the noise floor (*right*) of the LVDTs. The *left* panel draws a measured calibration curve and the vertical axis denotes values which is proportional to voltage. In the *right*, measured noise floors for the LVDTs used in IP-stage and GAS filters and that in BF-damping system are shown.

4.7.2 Inertial sensor

Due to some constraints, we have two kinds of inertial sensors in the period of this work, which are an accelerometer and a commercial speedmeter, geophone L-4C. The accelerometers are used in the two ITM suspensions, while the geophones are implemented to the two ETM suspensions.

Accelerometer

The accelerometers are originally developed for TAMA-SAS [47]. They are based on the folded pendulum (FP) geometry to eliminate all elastic restoring forces and thus minimize material losses and (presciently) hysteresis effects. An FP proof mass is supported by two legs. The leg at one end of the proof mass is a normal pendulum with a positive restoring force. The other half of the proof mass is supported by an equal-length inverted leg which contributes to a negative restoring force. The mechanical resonant frequency can be tuned to about 0.5 Hz.

The acceleration signal of the proof mass is obtained from a force by a feedback control system which tries to keep the proof mass position. The feedback control is done with electrical circuits. The measured noise floor of the implemented ITMX-accelerometer³ estimated by the three-channel correlation analysis [48] is shown in Figure 4.18.

³Due to some technical problems, the accelerometers were not achieved their expected sensitivities. Especially the noise floor of the ones for ITMY suspension were much worse than those of ITMX suspension.

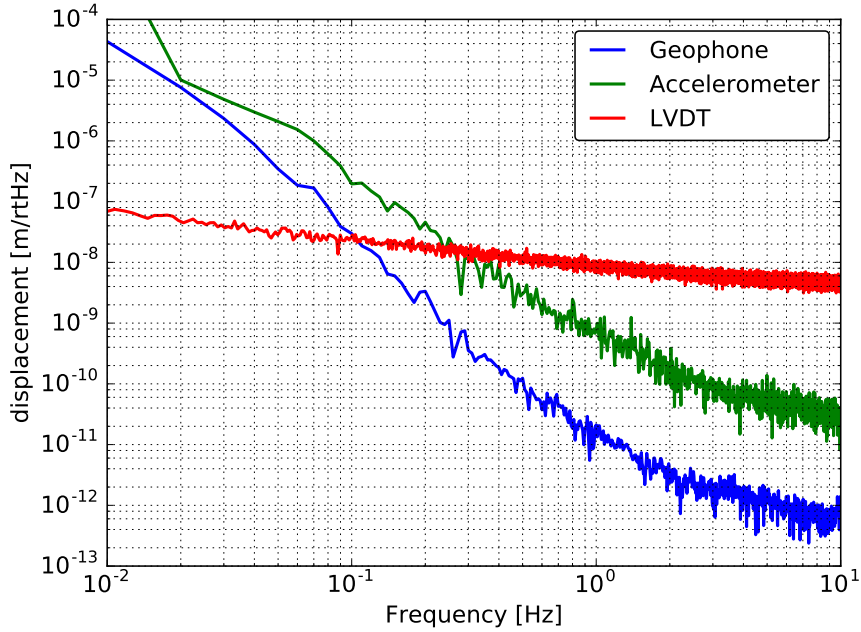


Figure 4.18: The measured noise floor of the implemented inertial sensors compared to that of LVDTs.

Geophone L-4C

A geophone L-4C is a commercial instrument of seismometer manufactured by Sercel. The output of geophone is the voltages proportional to velocity of its proof mass with respect to its frame. The geophone passively outputs the velocity signal and it does not need controls. The proof mass with the weight of 1 kg is softly suspended with a spring and a damper with its resonant frequency of about 1 Hz. A coil wound on the proof mass which generates voltages induced by a permanent magnet attached on the frame. The frequency response of the geophone is given by

$$H_{\text{geo}}(\omega) = \frac{G_e \omega^2}{\omega_0^2 + 2i\eta\omega_0\omega + \omega^2}, \quad (4.2)$$

where G_e is the generator constant, η is the damping coefficient, ω and ω_0 are the angular frequency and angular resonant frequency, respectively. The geophone frequency response with the typical parameters are shown in *left* of Figure 4.18. The actual geophones are calibrated with already calibrated seismometers in section 4.7.6. The typical noise floor of the geophone estimated with [48] is shown in Figure 4.18.

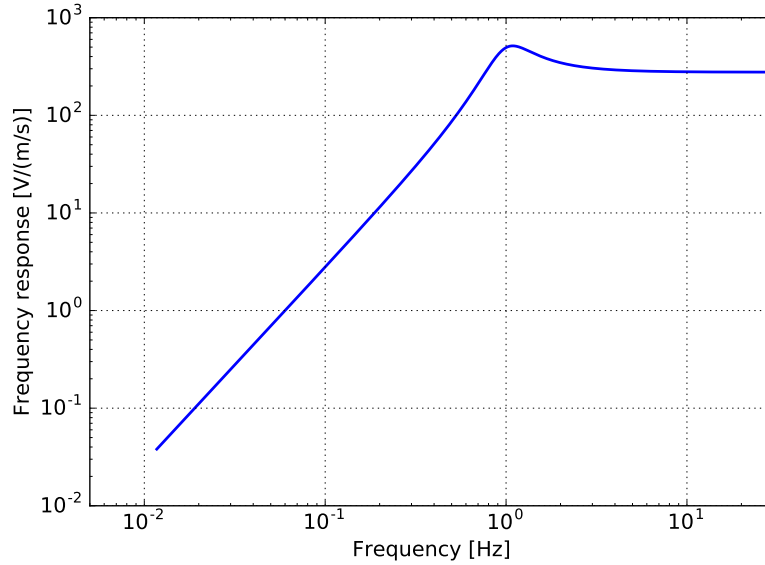


Figure 4.19: The geophone frequency response with the typical parameters. In this plot G_e , f_0 , η are set to 276.8 V/(m/s), 1.0 Hz and 0.28 respectively.

4.7.3 Optical levers

Optical lever consists of a light source and a Quadrant Photo-Diode (QPD) outside vacuum chambers. The fiber-collimated light from a Super Luminescent Diode (SLD) is injected to the mass which we want to measure the motion, and the reflected light is guided to a QPD fixed on an X-Z stage. The launcher after collimation and the QPD are placed as close as to the viewports possible, in order to reduce the air-current noise. The optics outside the chamber are covered by a windshield made of aluminum foils for the reason. The linear range is typically a few hundred μrad .

The details of the optical lever which senses the displacement signal, called length-sensing optical lever, is summarized in [49]. The length-sensing optical lever is calibrated with X/Y-arm cavity by injecting a sinusoidal signal to each TM actuator. A schematic view of the optical lever set ups for the TM- and MN-stage are shown in Figure 6.2. The noise floor of the optical lever and the length-sensing optical lever estimated from a measurement⁴ is shown in Figure 4.20.

4.7.4 Reflective photo sensor

The reflective photo sensor (PS) is a non-contacting sensor which works even in the cryogenic temperature 20 K was developed mainly for the purpose of mechanical resonance damping of the RM-chain modes [50]. One photo-sensor unit consists of a LED and 2 photo-detectors, and six of this photo-sensor units are

⁴An (rough) estimation with free swinging spectra with the air-shield.

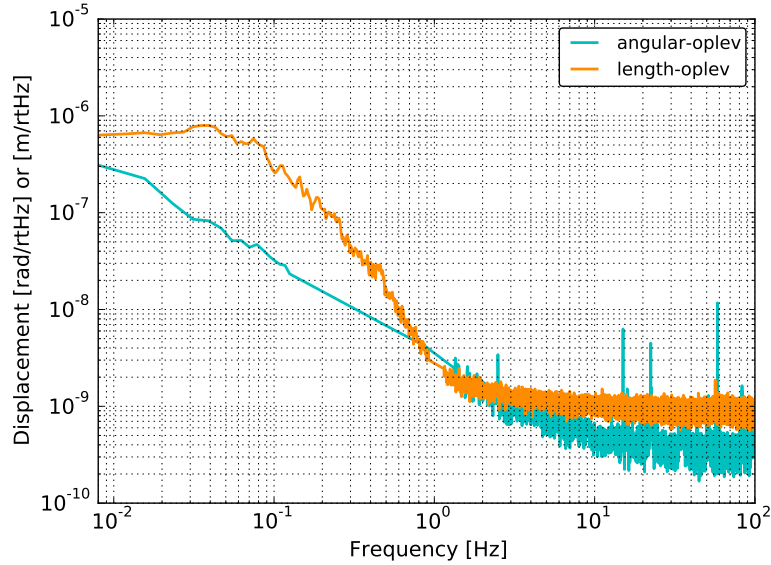


Figure 4.20: An estimated noise floor of the (angular) optical lever and the length-sensing optical lever. This plot includes the environmental noise. Oplev denotes the optical lever.

arranged at each MN- and IM-stage so that they can sense the 6 dofs. Even though the calibration factor depends on the operation temperature, it was experimentally confirmed that the calibration factor at the cryogenic temperature is obtained by multiplying a factor to the calibration factor at measured room-temperature. It is also known that this photo-sensors have individual differences in terms of the calibration factors. Judging by a measurement, the difference can come from the difference of the beam profile of the LED. An estimation of the noise floor of the implemented photo-sensor⁵ is shown in Figure 4.21.

⁵Since we could not get a chance to do the detailed calibration for the actually implemented photo-sensors due to a time constraints, this calibration factor is estimated from a force transfer function measurement; according to the simulation, the DC-gains of the following two transfer functions will be equal. from MN-Yaw excitation to MN-Yaw in PS, and to MN-Yaw in optical lever. Then assuming this is available, calibration factor is obtained. the noise floor of one PS is then roughly calculated from the result.

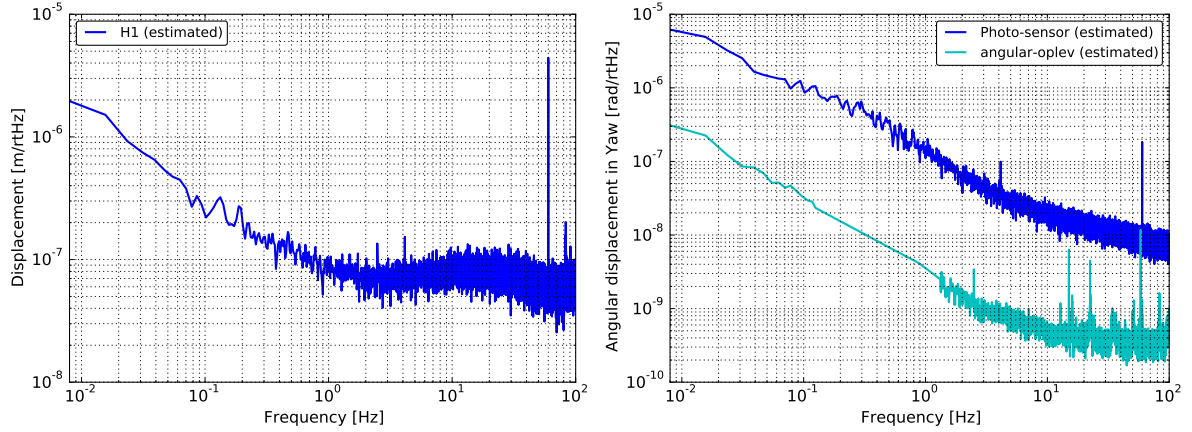


Figure 4.21: An estimation of the noise floor of the implemented photo-sensor (*left*) and a comparison of the noise floor to that of angular optical lever in Yaw dof (*right*). Oplev denotes the optical lever.

4.7.5 Coil-magnet actuator

A coil-magnet actuator is a non-contacting actuator, which consists of permanent dipole magnets and solenoid coils, and is used for the suspension control. It utilizes force of electromagnetism generated by the interaction between the static field of the permanent magnets and current sent to the coils. For the suspension control, two kinds of coil-magnet actuators are used. One is voice-coil type and the other one is coaxial moving-magnet type. The details of them are described in [32]. In the Type-A suspension, IP-stage and GAS filters have the voice-coil type actuators. While for the BF-damping system and payload the coaxial type actuators are used.

4.7.6 Seismometer

The ground vibration at each front- and end- station is measured by a seismometer Trillium120QA [51]. For the Type-A system, the seismometer is set at the second floor of each station in KAGRA underground. Its self-noise level compared to the typical noise level of LVDT is shown in Figure 4.22. The noise floor itself is relatively low for the suspension related control even at frequency between 10 mHz to 100mHz, however, the seismometer observes local tilt change at the frequency below 0.1 Hz. Due to these fact, the use of the seismometer at below 0.1 Hz is preferred to be avoided.

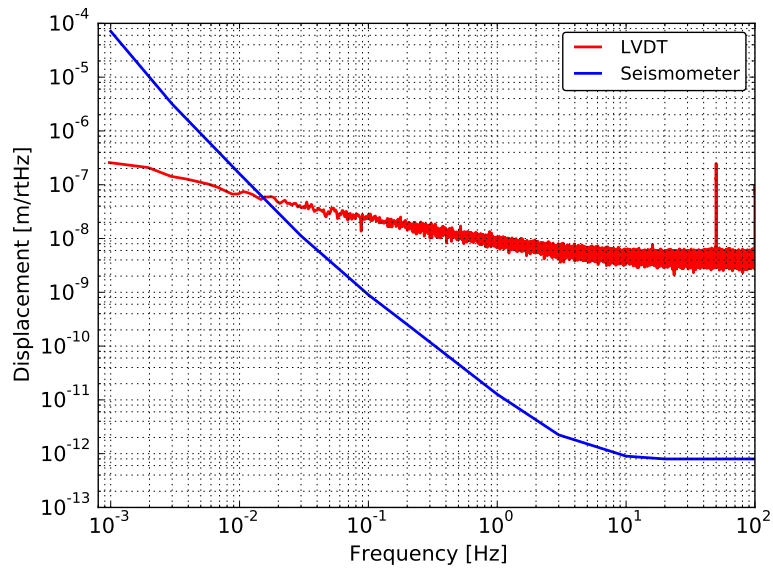


Figure 4.22: Self-noise level of Trillium120QA compared to the typical noise level of LVDT.

4.7.7 Digital signal processing

We use a digital control system for the active controls of the suspensions. Real-time signal processing for the digital control is performed by a real-time OS machine customized for high-speed signal processing and data communication. The signal processor is connected to a PCIe extension board which contains a timing clock, Analog-to-Digital Convertors (ADCs) and Digital-to-Analog Convertors (DACs). Details of signal processing are implemented and controlled from a Linux machine connected to the real-time machine through a Local Area Network (LAN). Digital system uses signal conditioning filters called anti-aliasing (AA) and anti-imaging (AI) filters as analog circuits. They cut off the signals at frequencies higher than the Nyquist frequency in order to mitigate noise caused by quantization errors. As described in the following section, the actuation current sent to the coil is controlled with a digital system. The output ranges of ADC and DAC are $\pm 20\text{V}$ and $\pm 10\text{V}$ respectively, and they limit the maximum actuation current to the coils.

The more details of the KAGRA digital system can be found in [33].

Suspension control design

This chapter focuses on the active control system for one Type-A suspension. We apply the active control system based on linear feedback control sensors, contactless actuators which are introduced in the previous chapter, and digital servo systems. The main targets which are introduced in the previous chapters are to damp the mechanical resonances of the seismic attenuation system, and also to keep the mirror position and the orientation.

5.1 Requirements

The requirements for the local Type-A suspension control system depends on the interferometer control state in section 5.1.1. From the description in section 5.1.2 to section 5.1.5, the requirements for the each states are summarized in Table 5.2 consequently.

5.1.1 Control phases

In the point of view of the suspensions, the states of the interferometer control can be categorized into the following three phases:

- the calm-down phase,
- the lock-acquisition phase,
- the observation phase.

The purpose of the calm-down phase is to reduce large-amplitude motion of the mechanical resonances excited by external disturbances. In this phase, the active controls are required to minimize the decay time of the resonances to allow fast recovery to the lock-acquisition and observation phase.

The target of the lock-acquisition phase is to freeze the mirror motion and to bring the operation points so that the mirror is trapped into the linear regime of the interferometer. More concretely, the speed of the mirrors has to be suppressed since the linear region of the interferometer (PDH) signals is considerably small. In this phase, the local control is also required to suppress the angular fluctuation

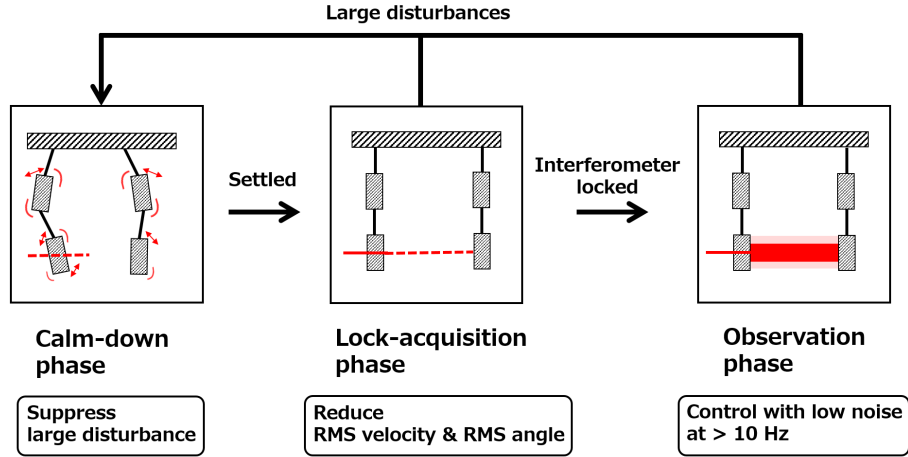


Figure 5.1: Suspension control operation phases categorized into the three phases. The main purposes of the active suspension controls are included.

so that other control loop with more sensitive sensors of the interferometer such as the wave front sensors can be available.

The aim of the observation phase is to suppress the mirror fluctuation due to technical noise such as sensor noise couplings at the frequency higher than 10 Hz, which is the detection band of GWs. This phase also requires to keep the mirror displacement and its orientation at the same time.

The operation phases of the interferometer summarized in Figure 5.1.

5.1.2 Requirement on damping time

For a quick recovery of the interferometer lock, the excited mechanical resonances of the suspension have to be damped. This is hence the requirement for the calm-down phase. The requirement is set that the $1/e$ decay time of the mechanical resonances which disturbs the interferometer lock acquisition is less than 1 minute. This value is empirically determined so as not to prevent the interferometer from trying lock acquisition for a long time.

5.1.3 Requirement on RMS velocity

Interferometer lock acquisition

The length sensing and controls of the interferometer is operated by using modulated laser beams which is called Pound-Drever-Hall (PDH) technique or frontal modulation technique [52]. In this method, the laser frequency or the amplitude is modulated at radio frequencies before being injected into the main interferometer. By demodulating the detected laser power with the proper phase, an error signal proportional to the length displacement around the operation point

is obtained. The width of the linear range ΔL_{lin} is obtained from the finesse of the cavity \mathcal{F} , and the wavelength of the laser λ as

$$\Delta L_{lin} = \frac{\lambda}{2\mathcal{F}}. \quad (5.1)$$

The finessees are set at 38 for the signal recycling cavity, 57 for the power recycling cavity and 1550 for the arm cavities, and the wavelength of the laser is 1064 nm for the KAGRA detector.

For acquiring the interferometer lock, the velocity of the cavity length change have to be close to zero while the mirrors pass through the linear regime. I.e., the time scale where the mirror goes across the linear regime of the PDH signal is sufficiently longer than the duration of the control bandwidth. The momentum which can be applied to the suspended optic by feedback force is limited by the time that the optics spend in the linear range Δt , control bandwidth and the maximum actuation force.

For the lock-acquisition of the arm cavities, however, the KAGRA detector uses the green-lock scheme [53] for the guide as follows. This method introduces an auxiliary green laser with half the wavelength of the main laser. The auxiliary laser has a resonance in the arm cavities with a lower finesse of about 50. Since the cavity length signals are fed back to voltage controlled oscillators (VCOs) which modulate the frequencies of the green (auxiliary) laser, the phase of the green laser is locked to the arm cavity length variation. The VCOs are free from mechanical resonances of the suspension system and then the control bandwidth can be set up to 10 kHz. The frequency of the green laser is then compared to that of the infrared (main) laser by using the frequency of their heterodyne beat. The beat frequency indicates how far the main laser is from resonating in the arm cavity. Then the feedback control derived from these signals is sent to the coil-magnet actuators on the optics. This method expands the linear regime of the cavity length measurement and gives a looser requirement on the velocity of the optic.

Control bandwidth limit

Based on the consideration of control bandwidth, The incident velocity of the mirror to acquire the lock should satisfy:

$$v_{in} \lesssim \omega_b \Delta L_{lin} = \omega_b \frac{\lambda}{2\mathcal{F}}, \quad (5.2)$$

where ω_b represents control bandwidth. The maximum incident velocities based on the control bandwidth limit for the power recycling, signal recycling, arm cavities are summarized Table 5.1.

Actuation force limit

Following the consideration in [54], the force in order to stop the mirror F can be estimated from the relationship between the mirror momentum and the impulse,

$$F = \frac{mv}{\Delta t}, \quad (5.3)$$

where m , v and Δt are the mass, the velocity of the mirror and the time it takes to pass the linewidth ΔL_{lin} of the cavity, respectively. Assuming $\Delta t = \Delta L_{\text{lin}}/v$, the velocity required incident velocity for the mirror can be given by

$$v_{\text{in}} \lesssim \sqrt{\frac{F_{\text{max}}\Delta L_{\text{lin}}}{m}}, \quad (5.4)$$

For the lock-acquisition of the arm cavities, the discussion above is not applied since we use the laser frequency actuator of the arm-length stabilization system. The maximum incident velocities based on the actuation force limit for the power recycling, signal recycling, arm cavities are also summarized Table 5.1.

Table 5.1: Requirements on the velocity of the cavity length variation. The control band width is set to 50 Hz, and the values of actuation limit is obtained from [54]. For the lock-acquisition of the arm cavities, The control band width and the finesse are set to 10 kHz and 50 respectively assuming to use the laser frequency actuator of the arm-length stabilization system.

Cavity	BW limit [$\mu\text{m/s}$]	Actuation limit
Arm cavity	330	—
Power recycling cavity	2.9	7.3
Signal recycling cavity	4.4	0.44

RMS velocity requirement

In order to get the more realistic requirement, we have to consider that the mirror is driven by random disturbances. Since the optics of the optical cavities vibrate randomly, the incident velocity changes each time the optics pass by the linear range. Assuming that the velocity of the optics has a Gaussian distribution, the probability distribution of the incident velocity of the optical cavity length variation $f(v)$ is [55]

$$f(v) = \frac{v}{v_{\text{rms}}^2} \exp\left(-\frac{v^2}{2v_{\text{rms}}^2}\right), \quad (5.5)$$

where v_{rms} means the RMS velocity of the cavity length variation. To obtain the lock-acquisition with higher than 50% probability in this model, the RMS

velocity v_{rms} has to be reduced lower than $0.72 v_{\text{req}}$, where v_{req} denotes the maximum permitted velocity to lock the cavity. Based on these considerations, the requirements on the RMS velocity of the suspended optics with the KAGRA suspensions is set to $2.0 \mu\text{m/s}$ for the type-A SAS, $0.31 \mu\text{m/s}$ for the type-B SAS and $2.0 \mu\text{m/s}$ for the type-Bp system. The velocity requirement for the type-A suspensions comes from a fact that PR and SR cavities include the input test masses (ITMs). Even though the requirement on the velocity for the arm cavity mirrors is set to $240 \mu\text{m/s}$, the two ITMs are also part of the power and signal recycling cavities. The vibration of these ITMs affect the length variation of these cavities. The requirement of the type-A SAS is calculated from the bandwidth limit of PR and SR cavities.

5.1.4 Requirement on RMS angular fluctuation

Since the angular fluctuation of the optic, especially in pitch and yaw dof induces fluctuations of the beam spot and spatial mode mismatch of the interferometer, the optic RMS angles need to be suppressed for stable operation of the interferometer and for preventing degradation of the sensitivity of the detector due to the mode mismatch. For the lock-acquisition phase, the requirement is set to 880 nrad so that the intracavity power does not degrade with the loss more than 5% [56]. While for the observation phase, the requirement is set to 200 nrad so that the induced beam spot fluctuation on the optics smaller than 1 mm in RMS [57]. In addition, in order to keep the interferometer lock for 1 day, angular beam position drift is required to be smaller than 400 nrad/h [57].

5.1.5 Requirement on longitudinal displacement

In the lock acquisition phase and the observation phase, the mirror longitudinal displacement have to be suppressed so that the interferometer lock is kept with the interferometer control signals by coil-magnet actuators. In order to keep the lock, the amplitude of the actuation force should be smaller than the maximum force of the actuators. It was reported in [54] that the actuation efficiency at DC by using the maximum force which can be applied at MN-, IM- and TM-stage were $3.9 \times 10^{-7} \text{ m/V}$, $1.7 \times 10^{-8} \text{ m/V}$ and $1.8 \times 10^{-9} \text{ m/V}$ respectively. Since the maximum digital-to-analogue converter (DAC) output of 10 V , the maximum permitted longitudinal displacements for each stage become $3.9 \mu\text{m}$, $1.7 \times 10^{-1} \mu\text{m}$ and $1.8 \times 10^{-2} \mu\text{m}$ at MN-, IM- and TM-stage respectively. By assuming that the longitudinal displacement compensation is done at MN-stage, and a factor of 10, the requirement on longitudinal displacement can be set to $0.39 \mu\text{m}$.

5.1.6 Requirement on Type-A suspension control

The requirements for the active controls of the Type-A SAS is summarized in table 5.2. The requirement for the mirror transverse and vertical displacement set to 0.1 mm in order to avoid a mis-centering of the beam spot on the mirror.

The RMS value is defined as integration of the spectrum density down to 0.01 Hz, assuming the corresponding time scale (~ 100 sec.) is sufficiently long to cover the lock-acquisition process. The integration with this bandwidth also covers the frequency band of the micro-seismic peak around $0.2 \sim 0.5$ Hz, which makes a large contribution to the RMS velocity or angle of the optic.

In the observation phase, the control noise, which couples to the optic longitudinal displacement in the detection band (> 10 Hz), is to be suppressed lower than the required vibration level.

Table 5.2: Requirements on the Type-A suspension control. The column labeled as ref. describes the section which explains the reason of the requirements.

Items	Requirements	ref.
The calm-down phase		
1/e decay time	< 1 min.	§ 5.1.2
RMS displacement (transverse, vertical)	< 0.1 mm	§ 5.1.6
The lock acquisition phase		
RMS velocity (longitudinal)	$< 2.0 \mu\text{m}/\text{sec.}$	§ 5.1.3
RMS angle (pitch, yaw)	< 880 nrad	§ 5.1.4
RMS displacement (longitudinal)	$< 0.39 \mu\text{m}$	§ 5.1.5
RMS displacement (transverse, vertical)	< 0.1 mm	§ 5.1.6
The observation phase		
Control noise at 10 Hz (longitudinal)	$< 8.0 \times 10^{-20} \text{ m}/\sqrt{\text{Hz}}$	§ 4.2
RMS displacement (longitudinal)	$< 0.39 \mu\text{m}$	§ 5.1.5
RMS displacement (transverse, vertical)	< 0.1 mm	§ 5.1.6
RMS angle (pitch, yaw)	< 200 nrad	§ 5.1.4
DC angle drift (pitch, yaw)	< 400 nrad	§ 5.1.4

5.2 System modeling

Modeling of the suspension system is done with three-dimensional rigid body model, assuming that we ignore the internal dynamics of the suspension components. We use that model since empirically this assumption is accurate for the lower frequency region ($\lesssim 10$ Hz) and since that the frequency region of the interested for the suspension control.

Control issues for the suspension system is addressed by the framework of linear control theory, assuming that the suspension system is operated in a small region around the equilibrium point which the linear approximation is kept valid.

5.2.1 3D rigid-body dynamics

This work uses a tool of 3D rigid-body modeling cite. The dynamics of of the multi-dofs mechanical oscillator is characterized based on the linearized equation of motion. In a nutshell, the linearized equation of motion is obtained as following, using a set of positions and velocities of the system \mathbf{x} and $\dot{\mathbf{x}}$:

1. Calculate the potential energy $U(\mathbf{x})$, dissipation function $R(\mathbf{x}, \dot{\mathbf{x}})$ and kinetic energy $T(\mathbf{x}, \dot{\mathbf{x}})$ of the system and then find the equilibrium point \mathbf{x}_{eq} by minimizing the potential energy.
2. Get the *stiffness matrix* \mathbf{K} by differentiating $U(\mathbf{x})$ with respect to the coordinate position, also calculate the *damping matrix* \mathbf{G} and the *mass matrix* \mathbf{M} by by differentiating $R(\mathbf{x}, \dot{\mathbf{x}})$ and $T(\mathbf{x}, \dot{\mathbf{x}})$ with respect to the coordinate velocity at equilibrium point

$$K_{ij} = \left. \frac{\partial^2 U(\mathbf{x})}{\partial x_i \partial x_j} \right|_{\mathbf{x}=\mathbf{x}_{eq}}, \quad (5.6)$$

$$G_{ij} = \left. \frac{\partial^2 R(\mathbf{x}, \dot{\mathbf{x}})}{\partial \dot{x}_i \partial \dot{x}_j} \right|_{\mathbf{x}=\mathbf{x}_{eq}}, \quad (5.7)$$

$$M_{ij} = \left. \frac{\partial^2 T(\mathbf{x}, \dot{\mathbf{x}})}{\partial \dot{x}_i \partial \dot{x}_j} \right|_{\mathbf{x}=\mathbf{x}_{eq}}. \quad (5.8)$$

3. Write down the linearized equation of motion as

$$\mathbf{M}\ddot{\mathbf{x}} + \mathbf{G}\dot{\mathbf{x}} + \mathbf{K}(\mathbf{x} - \mathbf{x}_{eq}) = \mathbf{0}. \quad (5.9)$$

Based on this calculation, each suspension component has 6 dofs. For the IP-stage, however, we assumed only three horizontal motion, longitudinal, transverse and yaw. The GAS is regarded as one-dimension vertical spring with the saturation of the attenuation performance caused by the center of percussion effect. We also assume that the suspension wire can be treated as massless springs with torsional elasticity and load elongation ignoring their violin modes. For the treatment of the dissipation due to the internal friction of the elastic material,

the spring constants of the vertical springs and wires have imaginary parts representing finite loss angle assuming that the loss is constant over all frequency region (equivalent to structural damping process).

5.2.2 State-space representation

In the simulation of this work, the dynamics of the suspension system with multi-inputs and multi-outputs is represented as a state-space model. A brief summary of the state-space representation and the interpretation of the suspension's equation of motion to the representation is described in this subsection.

When the state of the system can be determined by a set of variables \mathbf{x} , which is called state variables, its time evolution with a given input \mathbf{u} will follow the equation,

$$\dot{\mathbf{x}}(t) = \mathbf{A}\mathbf{x}(t) + \mathbf{B}\mathbf{u}(t), \quad (5.10)$$

with the matrices \mathbf{A} called system matrix which and \mathbf{B} called input matrix. More concretely \mathbf{A} characterizes the dynamics of the state with dimension of $n \times n$ where n is the number of states corresponding to the length of \mathbf{x} . In this case, the order of the system is n , and when the input \mathbf{u} has a dimension of m , the input matrix \mathbf{B} should have a dimension of $n \times m$.

On the other hand, the output from the system \mathbf{y} will be a superposition of the system's state projected via matrix \mathbf{C} called output matrix, and direct couplings from the input via matrix \mathbf{D} which is called feedthrough matrix. The output \mathbf{y} is then given by:

$$\mathbf{y}(t) = \mathbf{C}\mathbf{x}(t) + \mathbf{D}\mathbf{u}(t), \quad (5.11)$$

The combination of eq (5.10) and eq (5.11) which can determine the dynamics of the system uniquely is known as state-space representation, summarized as

$$\begin{aligned} \dot{\mathbf{x}}(t) &= \mathbf{A}\mathbf{x}(t) + \mathbf{B}\mathbf{u}(t) \\ \mathbf{y}(t) &= \mathbf{C}\mathbf{x}(t) + \mathbf{D}\mathbf{u}(t). \end{aligned} \quad (5.12)$$

Since the equation of motion for the suspension system has a form of second-order differential equation, in order to enable to write the equation of motion as a form of state-space model, we would have to introduce additional differential equation $\mathbf{v} = \dot{\mathbf{x}}$. Consequently, by using the state variables as (\mathbf{x}, \mathbf{v}) , the state-space model of the suspension system is obtained from eq (5.9) as follows:

$$\frac{d}{dt} \begin{pmatrix} \mathbf{x}(t) \\ \mathbf{v}(t) \end{pmatrix} = \begin{pmatrix} \mathbf{O} & \mathbf{I} \\ -\mathbf{M}^{-1}\mathbf{K} & -\mathbf{M}^{-1}\mathbf{G} \end{pmatrix} \begin{pmatrix} \mathbf{x}(t) \\ \mathbf{v}(t) \end{pmatrix} + \mathbf{B}\mathbf{u}(t) \quad (5.13)$$

The equation of motion determines only the components of the system matrix \mathbf{A} , the other matrices will be designed depending on the configuration of the sensors and actuators.

Generally, the merit of using state-space representation is that it can simply describe the dynamics of the system as a time evolution of the state variables even if the system has multi-inputs and multi-outputs (MIMO). In the conventional way of frequency domain analysis, on the other hand, the system is described by means of transfer function which projects the input onto the output, which is a useful to express a single-input-single-output (SISO) system.

5.3 Basic control topology

In this work, the local control system is composed of a set of parallelized single-input-single-output (SISO) feedback loops. The basic idea of the suspension control in KAGRA is to process the displacement signals on the Cartesian basis defined shown in Figure 3.5. The Cartesian signals are obtained from the sensor readouts in their own basis through the matrix operation, and then the generated feedback signals in Cartesian coordinate are distributed to the real actuators through the matrix operation to produce feedback forces in a proper direction.

The control topology in this work is summarized in Figure 5.2. The IP control loops are used to provides resonance damping of the horizontal motions and DC positioning of the whole suspension chain. This loop also takes care the control to suppress the mirror RMS motion due to the micro-seismic peak. The GAS control loops are closed for resonance damping and for the compensation of the DC drift of the keystone 's height. The BF control loops are used to for torsion mode damping of the whole chain which is unfeasible in the IP control. Finally the payload control are used for damping of the internal mode inside the payload and alignment control of the mirror.

In the control simulation in the following subsections, the dynamics of the suspension system is represented as a state-space model. The inputs and outputs of the model are reshaped so as to correspond to the practical setup such as differential inputs and outputs.

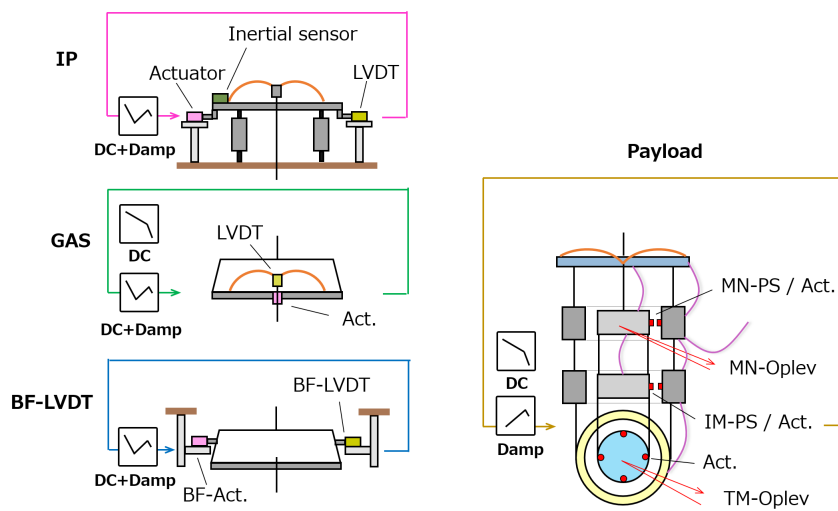


Figure 5.2: Basic control topology of the Type-A suspension system in this work.

5.4 Controls for calm-down phase

As described in section 5.1.1, the primary target of the calm-down phase is to reduce large-amplitude motion of the mechanical resonances excited by external disturbances. In this phase, the active controls are required to damp resonances so that the $1/e$ decay time of the mechanical resonances which disturbs the interferometer lock acquisition, is less than 1 minute.

Assuming that the suspension system is characterized by the 3D rigid-body, and also assuming that the heat-link system does not affect to the main suspension is also considered, the Type-A suspension originally has 75 resonant modes as summarized in section B.1. In this work, however, we concentrate on the resonances whose frequency is lower than 30Hz, since the resonant modes which have a huge impact to the lock acquisition are the lower frequency modes rather than the higher frequency one. The value of 30Hz is set due to a practical aspect that the sensors actuators locally implemented to a suspension can sense the motion and can actuate the system at up to around that frequency. For the detector sensitivity, such higher frequency modes also have to be damped though, dealing with those modes are beyond the scope of this work and will be investigate as further development. In addition to this, some modes which would not affect to the lock-acquisition are excluded from this discussion. Consequently the total number of the resonances to be damped becomes 54.

5.4.1 Servo system

Table 5.3 shows the feedback filters designed for the calm down phase. For the estimation of the damping performance, $1/e$ decay time constant with and without the controls is summarised in Figure 5.3. There are four remaining resonances below 30 Hz which exceed the requirement of 1 minute. However, since they are the tilt modes of the F1 and F2 GAS stages (mode #25, #26, #29 and #30 in section B.1) and the coupling to the mirror will be small, we do not consider them here¹. Based on this, this control system will satisfy the requirement for the calm-down phase.

¹On the other hand, according to the model prediction, for the mode #29 and #30 seems to connect to the mirror tilt motion. We might have to take care of them in the actual system if this mode affect to the lock acquisition.

Table 5.3: The servo loops for the calm down phase with the used sensors. In the below oplev and PS represent the optical lever and the photo sensor. We have the optical levers at MN- and TM-stages and they are labeled as MN-oplev and TM-oplev respectively.

Loop	Loop dof	Sensor	Actuation dof	Purpose
IP	L, T, Y	LVDT	IP	DC and damp
BF	Y	BF-LVDT	BF	DC and damp
F0	GAS	LVDT	F0	DC and damp
F1	GAS	LVDT	F1	DC
F3	GAS	LVDT	F3	DC and damp
BF	GAS	LVDT	BF	DC
MN	L, T, V, R, P, Y	PS	MN	damp
from TM to MN	P	TM-oplev	MN-P	DC and damp
from TM to IM	P	TM-oplev	IM-P	damp
from TM to MN	Y	TM-oplev	MN-Y	DC
from TM to IM	Y	TM-oplev	MN-Y	damp

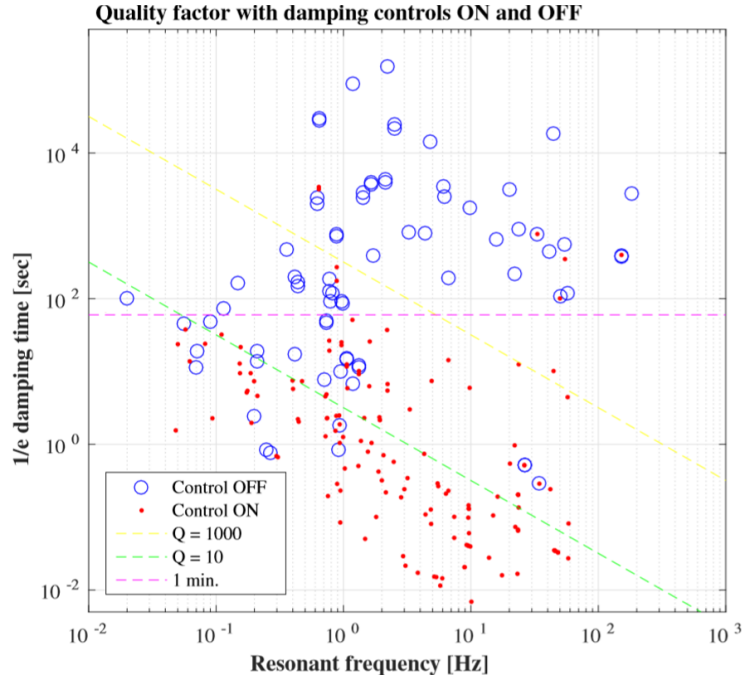


Figure 5.3: $1/e$ decay time constant with and without the designed controls. The blue-edged points and the red dots show the decay time constant without and with the control system. This control loop takes care below 30 Hz.

5.5 Controls for lock-acquisition phase

In order to lock the optical cavities, the RMS velocities and the angular fluctuations of the mirrors are required to be less than the requirement in the table 5.2. Typically the biggest contribution to the RMS velocity/displacement of the mirror comes from the ground motion at around 0.2 Hz, which is called micro-seismic peak.

Conventionally this issue is treated with a DC coupled damping control with blended sensors at IP-stage, or that system with sensor-correction and/or feed-forwarding system. However, in the actually given situation, it was found that some of the implemented inertial sensors were not sensitive enough to sense the suspension motion at KAGRA site, especially at the frequency below 0.1 Hz. Due to this fact, a active control system using IP-LVDTs which are sensor-corrected by the seismometer on the ground, is developed in this work.

We assume that the sensor correction system is implemented to the upper stages such as IP-stage. For the other control loop, especially for the payload and the GAS stages, we assume to use same ones as the ones used in the calm-down phase.

5.5.1 Suppression with sensor correction technique

Sensor correction at IP-stage

The block diagram where the sensor correction system is implemented to the IP-stage is shown in Figure 6.20. In this system, the sensor correction part is additionally implemented to the feedback control of the IP-stage. In this configuration, the seismic noise coupling will be most effectively suppressed when the sensor correction filter F_{sc} satisfies $F_{sc} = -S_L/S_s$ where S_L and S_s are the sensor response of the LVDT and the seismometer.

Assuming the inter-calibration between the IP-LVDT and the seismometer sensors are perfectly done, i.e, $S_L/S_s = 1$, the sensor correction filter F_{sc} should have gain of 1 at the frequency where we want to subtract the seismic motion. On the other hand, since the seismometer becomes more sensitive to the local tilt motion at the frequency below 0.1 Hz, the F_{sc} should also have a high-pass filter which keeps the phase shift as 0 deg as much as possible in the demanded frequency band. Based on this using a elliptic high-pass filter, the F_{sc} can be shaped as shown in Figure 5.5.

Expected mirror suppression

Using the above filter, the expected impact to the mirror motion in L dof is calculated as shown in Figure 5.6. In this calculation 90 percentile seismic motion level is assumed, and this is obtained by calculating the sensor noise coupling of this system. The RMS velocity and displacement down to 10 mHz, obtained from this calculation are summarized in Table 5.4. Figure 5.6 and Table 5.4 indicate

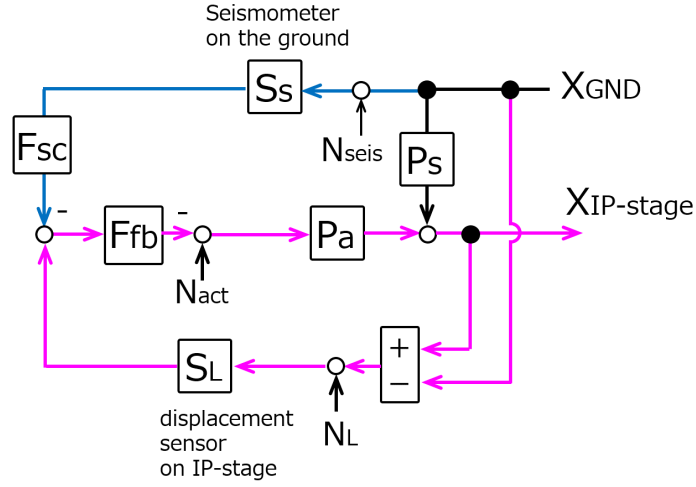


Figure 5.4: Block diagram of the feedback control with the sensor correction system at the IP-stage. Each parameters are defined with the same manner as in section 3.3. This is the case where F_{ff} is set to zero.

that the RMS velocity requirement will be satisfied by using the IP control system with the sensor-corrected LVDTs. On the other hand, the RMS displacement requirement will not be satisfied if the integration is done down to 10 mHz due to the seismometer self-noise contribution. If the RMS integration is stopped at 13.5 mHz (time scale is about 75 sec), the RMS displacement requirement will be satisfied. Since this displacement amplitude enhancement comes from the seismometers, this issue can be solved by implementing a sensor correction system for the seismometer using a sensor which senses the local tilt motion. This is a further improvement plan and is not feasible practically for the time period of this work. Since the primary target of implementing of the sensor correction system is to suppress the motion at the frequency region where the micro seismic peak is dominant, especially in the lock acquisition phase, this sensor correction system will work for that purpose.

Thus taking care of the displacement compensation system whose time scale is longer than 1 minute is set as a work beyond of this research, and this work focuses on the suppression at the frequency mainly above 0.1 Hz where the seismometer contribution is not dominant.

Consequently, this sensor correction system at IP-stage will suppress the residual motion of the mirror and will satisfy the RMS velocity requirement and also the displacement requirement at 10 Hz. Concerning the RMS displacement, this system will satisfy the requirement within the time scale of 1 minute.

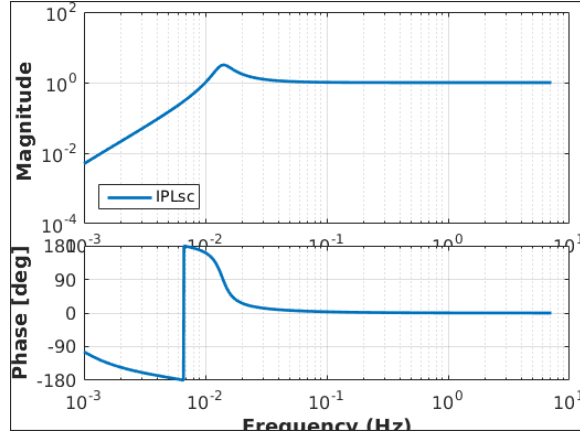


Figure 5.5: Designed sensor-correction filter for IP-stage. The horizontal axis shows frequency in Hz.

Table 5.4: The estimated RMS displacements and velocities of the mirror with the integration down to 10 mHz. IP_{sc} in the labels denote the sensor-correction system in this work.

Configuration	velocity [$\mu\text{m/s}$]	Displacement [μm]
Without any controls	0.48	0.56
with IP control, without IPsc	1.1	0.99
with IP control, with IPsc	0.15	0.75

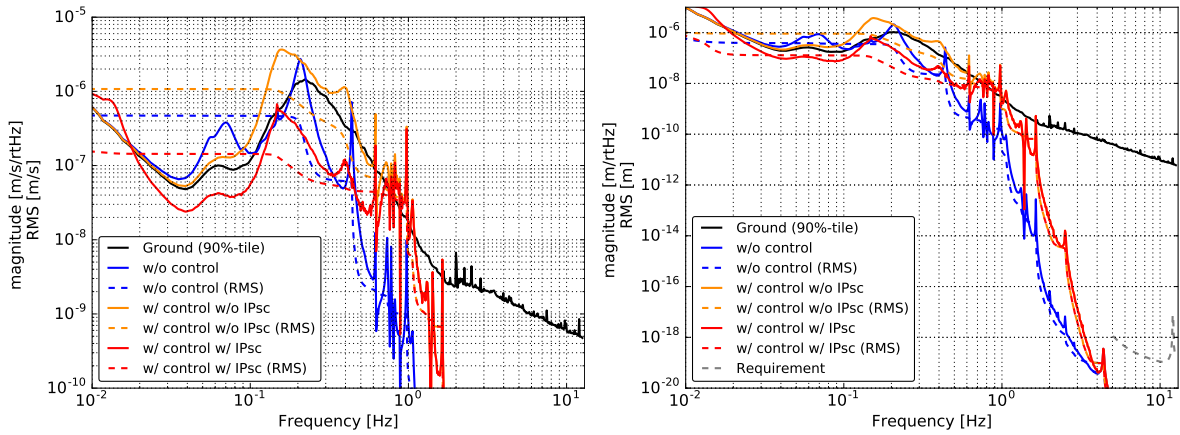


Figure 5.6: Spectra of expected mirror residual motion in L dof in displacement (*left*) and in velocity (*right*). The colors show the difference of the configuration. IP_{sc} in the labels denote the sensor-correction system in this work. The dashed curves draw the RMS integrated down to 10 mHz. In this calculation 90 percentile ground motion is assumed.

5.6 Controls for observation phase

In this phase, the mirror fluctuation due to technical noise such as sensor noise couplings have to be well suppressed at above 10Hz in order to meet the requirement in table 5.2. Figure 5.7 shows an estimated sensor noise coupling to the mirror in L dof assuming to use the control loops for the calm down phase and the lock acquisition phase, and same sensors. This tuning of the control system for the observation phase is beyond the scope of this work, however, the figure indicates that the sensor noise coupling via the following loops have to be more suppressed at above 10Hz in that system:

1. MN to MN loop with the photo-sensors,
2. TM to MN loop with TM optical lever
3. F3GAAS to F3GAS and F0GAS to F0 loops with the LVDTs.

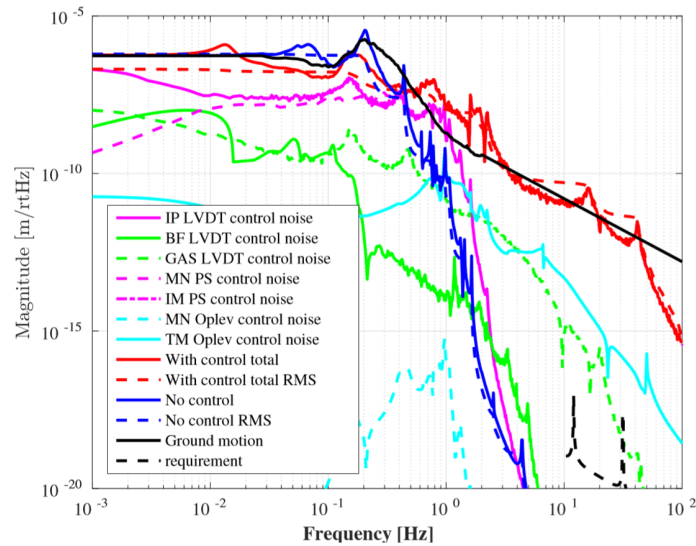


Figure 5.7: stimated sensor noise coupling to the mirror with this control system.

Performance test of local control for KAGRA Type-A suspension

This chapter describes the results of the performance tests of suspension local controls done while the interferometer lock is acquired. The goal is to confirm that the suspensions have the designed mechanical response, and also to verify if the control system meets the requirements for the damping phase and lock-acquisition phase summarised in section 5.1.

This test is conducted with ETMX suspension which is one of the Type-A SAS. Section 6.1 gives the information about the suspension configuration during the measurement. Section 6.2 describes the characterization of the mechanical responses of the Type-A SAS. Section 6.3 reports the result of the mechanical vibration isolation performance measured with the interferometer. Section 6.4 describes the actually installed controls filters and the performance test for the damping control. Section 6.5 summarizes the performance test for the control system for the reduction of the mirror residual motion focusing on the frequency region around the micro-seismic peak.

6.1 Suspension configuration

6.1.1 Mechanical and environmental configuration

During the measurement, it was known that one of GAS filter, which is the third GAS filter from the top and is called F2-filter, was mechanically stacked for a technical reason¹. It was also known that this could not be solved unless disassembling the upper structure, and there was not enough time to solve this issue. We then decided to keep using the ETMX suspension with the F2 GAS filter stacked, since the requirement for the displacement noise at 10 Hz should be satisfied even with the configuration as shown in Figure B.7.

¹Nevertheless all the coils of the sensors and actuators were electrically connected and the expected resistances were measured, no free-swinging was observed when a actuation was sent. In addition to this, it seemed that one peak disappeared from the force transfer function in vertical dof. We then started to believe that the keystone of the GAS filter somehow hit the lock screws which had been installed for a safety.

Concerning the other setting, the temperature of the payload during the test was about 250 K.

6.1.2 Sensor and actuator arrangement

The implemented sensor positions are summarized as shown in Figure 6.1 and Figure 6.2.

IP and BF stage

The IP-stage has three sets of coil-magnet actuators and two kinds of sensors (LVDTs and inertial sensors) arranged in a pinwheel configuration as shown in *left* of Figure 6.1. In ETMX suspension case, the geophone L-4C is used as the inertial sensors. The BF-stage has three sets of horizontal and horizontal LVDTs and coil-magnet actuator units also in a pinwheel configuration as shown in *right* of Figure 6.1.

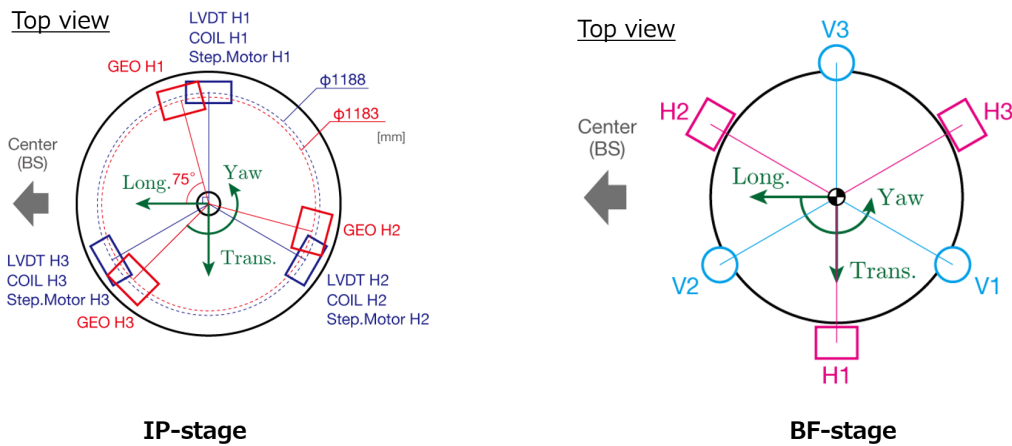


Figure 6.1: Geometrical position of the installed sensors and actuators at IP-stage(*left*) and BF-stage (*right*) for ETMX suspension case. GEO and COIL denote the geophone and actuator respectively. Three LVDT units are installed at IP- and BF-stage in order to sense the horizontal 3 dofs. BF-damping system has 3 other LVDT units for the vertical and rotational dofs.

Optical levers

An (angular) optical lever and length-sensing optical lever are installed at the TM-stage, and they sense the TM motion in the three dofs, i.e, longitudinal, pitch and yaw. On the other hand, only the (angular) optical lever is implemented at the MN-stage. In the MN-stage optical lever, the incident light beam is sent to the mirror attached on the MN-body and it is reflected to the same place where it is injected. In addition, the mirror is mounted onto the MN-body with an angle, the sensor output of this MN-stage optical lever in pitch dof becomes a superposition of the MN-body motion in pitch and roll. Those signals are degenerated and cannot be distinguished.

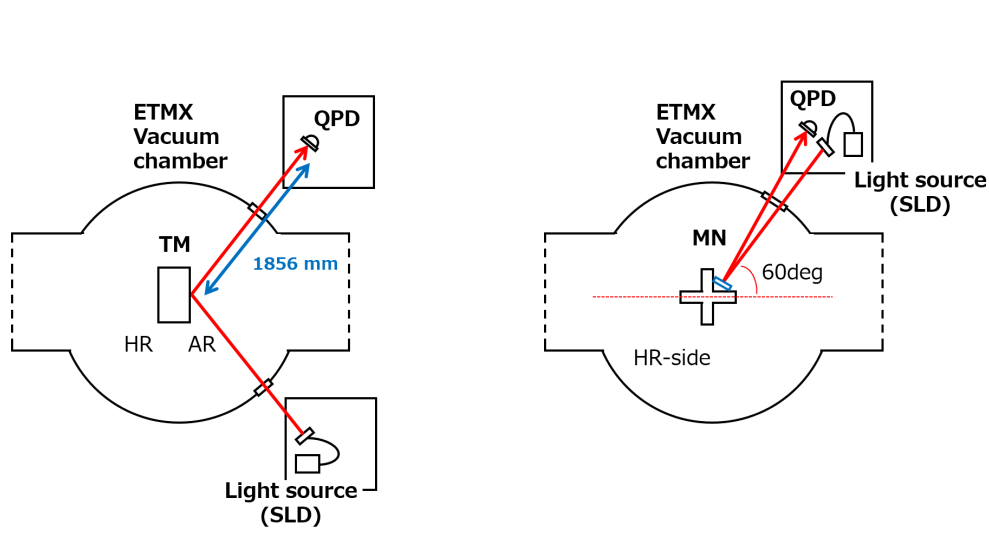


Figure 6.2: Geometrical configuration of the installed optical lever systems at the TM-stage (*left*) and MN-stage (*right*). HR and AR denote high-reflectivity coating and anti-reflectivity coating respectively.

6.2 Mechanical response

In order to confirm if the assembled suspension works as designed, its mechanical response is investigated by comparing to the simulation.

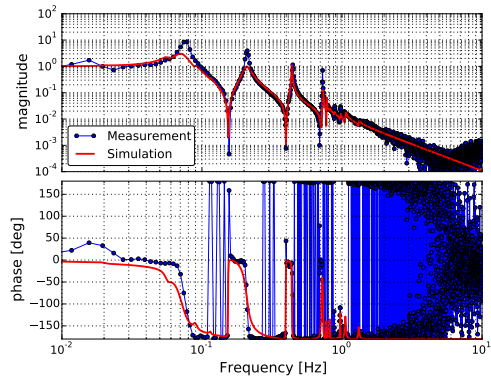
6.2.1 Diagonal transfer functions

We measure the force transfer function of each component by injecting white noise at each component actuator, and compared to the simulation. The simulation model used for this comparison does not include the heat-link system assuming that the effective stiffness of the heat link system is soft enough and the system does not affect the mechanical system of the main suspension.

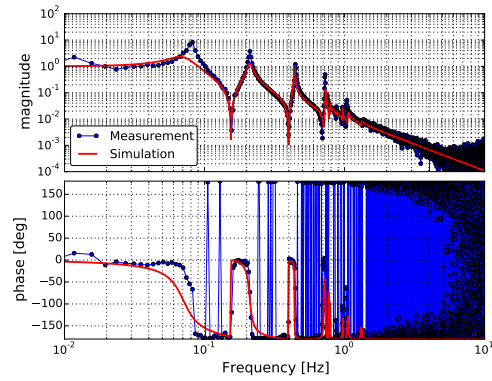
IP stage

Before the measurement, at the IP-stage, the LVDT sensors are diagonalized to the Cartesian basis by measuring the geometrical position. The coil-magnet actuators are diagonalized along with the LVDTs by checking the transfer function from each actuator to the L, T and Y dof defined by LVDTs with an injection of a sinusoidal signal at 2 Hz. This frequency is selected since the highest mechanical resonance is about at 1 Hz. The inertial sensors, i.e, geophones for ETMX suspension, are then inter-calibrated to LVDTs by comparing the transfer function from LVDT signal in yaw dof to each geophone signal. After the operation, the sensor matrix for the geophone is diagonalized by referring the transfer function from LVDT signal in L, T, Y to each geophone signal with an injection of a sinusoidal signal at 2 Hz.

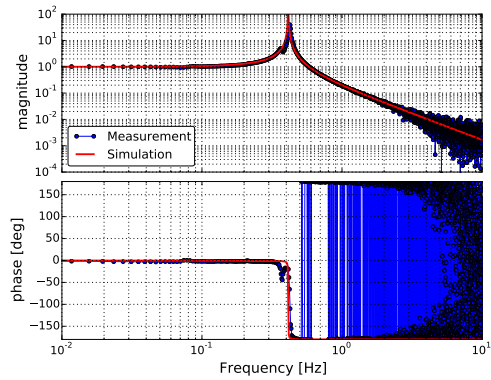
After the above procedure, we measure the mechanical transfer functions and the results are shown in Figure 6.3. Even though the Q factors of some of the peaks in the model have to be tuned more precisely, basically the measured resonant frequency and the slope at higher frequencies agree with the rigid-body simulation.



(a) Longitudinal



(b) Transverse



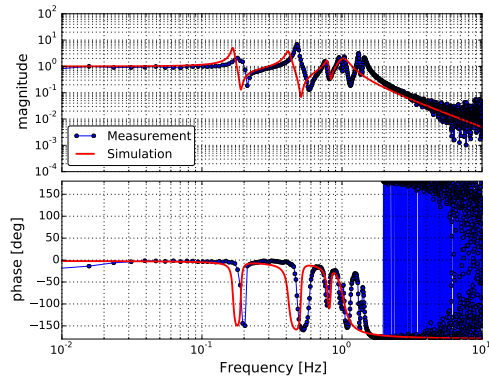
(c) Yaw

Figure 6.3: Diagonal mechanical transfer functions of the IP-stage in longitudinal (a), transverse (b) and Yaw (c) dof with the simulated curve. The dots and the curves show the measured result and the simulated one.

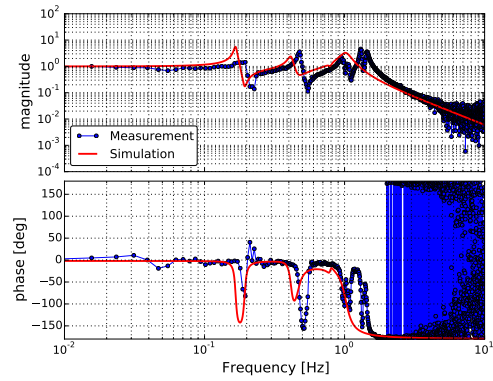
GAS stages

The measured transfer functions of each GAS stage are shown in Figure 6.4. Since the F2 GAS stage is mechanically stacked, one GAS spring is removed in the simulation. The noise becomes dominant at frequency higher than about 7 Hz. As Figure 6.4 indicates clearly, the model fails to explain the actual system. This is since the resonant frequencies of each GAS filter are not estimated well enough. For the lowest three modes (about the 180 mHz, 410 mHz and 480 mHz modes) in the model could be tuned based on the current model with system identification. However, the model fails to predict the the resonances at 1.29 Hz and 1.44 Hz, and also a peak at 4.4 Hz mode, which is the payload vertical resonance, is not found. In addition, a resonance at 9.7 Hz is found.

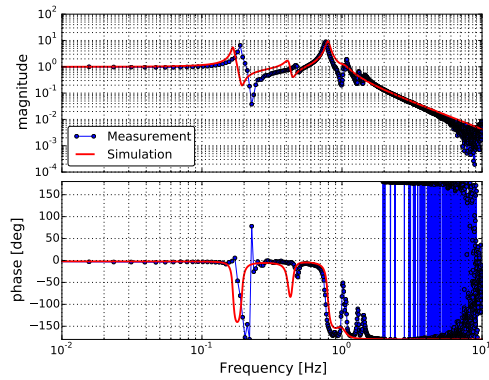
Consequently, the current model cannot explain the actual GAS filter responses and it has to be modified. We have to further investigate the system and to confirm if the discrepancies are well affected with the heat link system, and if the F2-GAS treatment is reasonable enough for this purpose. Even though this model fails to explain the actual resonant frequencies, the measured slopes at higher frequency agreed with the model. This implies that the vibration isolation performance at above 10 Hz will satisfies the requirement, as shown in Figure B.7. The details of the higher frequency performance will be confirmed with high sensitive sensor such as the main interferometer.



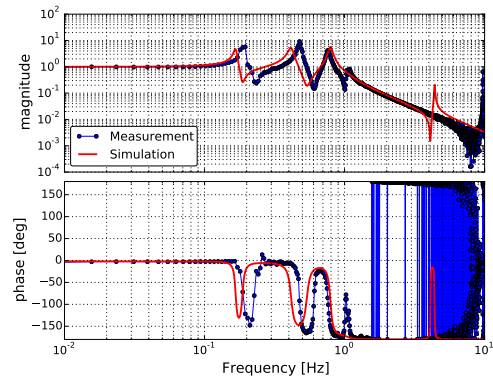
(a) F0 GAS



(b) F1 GAS



(c) F3 GAS



(d) BF GAS

Figure 6.4: Mechanical transfer functions of F0 GAS (a), F1 GAS (b) F3 GAS (c) and BF GAS stage with the simulated curve. The dots and the curves show the measured result and the simulated one.

BF stage

In the BF-stage, both the sensors and actuator are diagonalized by measuring the geometrical LVDT-unit position. Figure 6.5 shows the measured transfer function in the 3 horizontal dofs. At high frequencies above about 1.5 Hz in L/T, 2 Hz in Y dof, all the transfer functions have f^2 dependency. This is known as a spurious coupling in the BF-LVDT. The excitation signals sent to the actuator directly transmit to the sensor coil due to the implementation of the shared coil.

For L and T dof, the measurement agrees with the simulation, except for the Q factors and the resonant frequencies of the first and the second modes, similar to the IP-stage case. Concerning the yaw dof, the used model totally fails to predict the frequency response. In addition, for all the L, T, Y dofs, this measurement do not agree with the previous measurement which was conducted when payload and the heat link system were not installed. This issue is discussed in section 6.2.2.

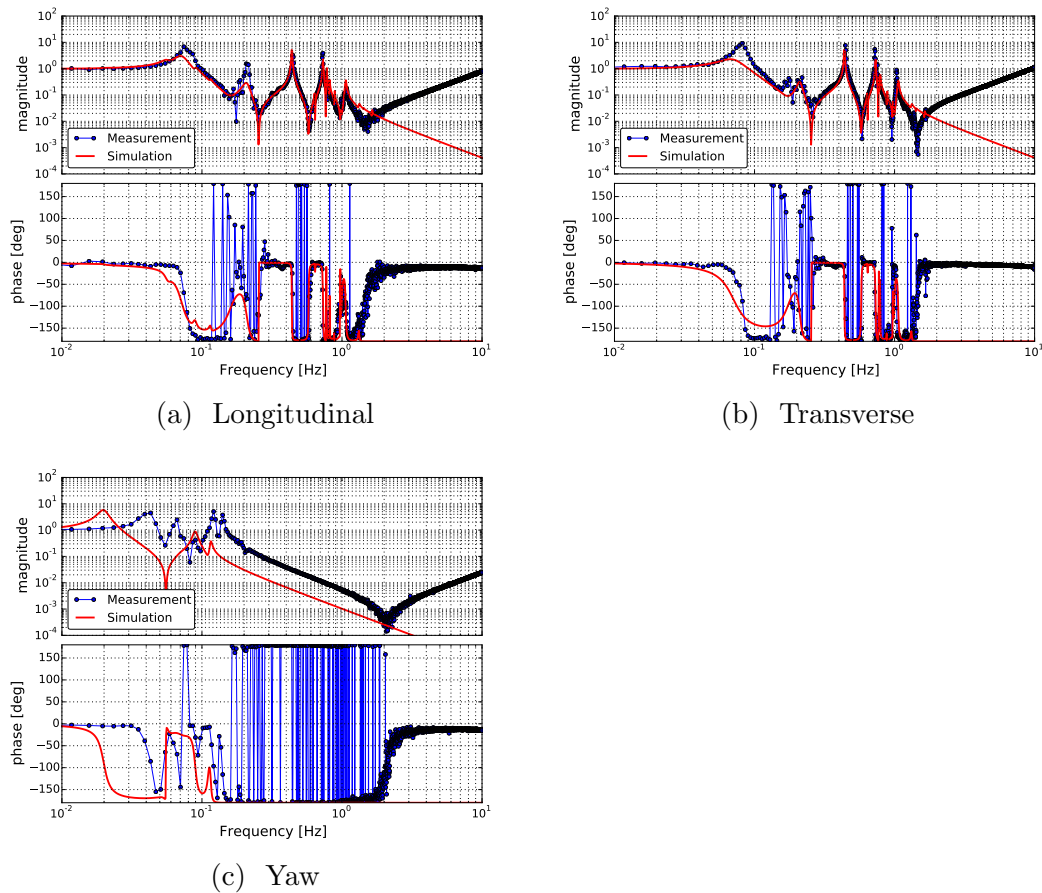


Figure 6.5: Diagonal mechanical transfer functions of the BF-stage in longitudinal (a), transverse (b) and Yaw (c) dof with the simulated curve. The dots and the curves show the measured result and the simulated one.

MN stage

For the payload part, the actuators are balanced by using the already calibrated optical lever so that the each coil pushes/pulls the mass by the same amount. The photo-sensor diagonalization is done geometrically. Figure 6.6 and 6.7 show the measured response of the MN-stage sensed by the optical lever and by the photo-sensors respectively. The noise becomes dominant at frequency higher than about 20 Hz for the transfer functions by optical lever and above a few Hz for the ones by the photo-sensors.

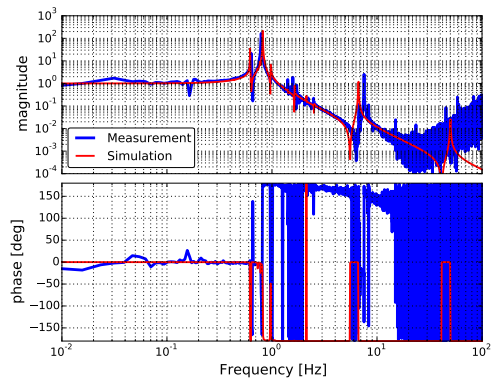
Figure 6.6 indicates that the model can explain the actual system, except for the two modes observed at 0.32 Hz in yaw dof and 7.5 Hz in pitch dof. The 0.32 Hz in yaw dof can come from the discrepancy of the material parameters since this model uses the parameters at 20 K. Another possible reason would be the heat link system, however, we do not have good explanation for this in this work. The discrepancy of the 7.5 Hz in pitch dof, which is the TM-chain mode, can be connected to the hanging situation. Since the TM is suspended with four rods of the sapphire fiber and it is glued on the mirror with ears [43], and we do not have much experience the suspension system with that rods.

might be uneven so that one of the four wires suspension of the payload. The material parameter can be also one of this reason.

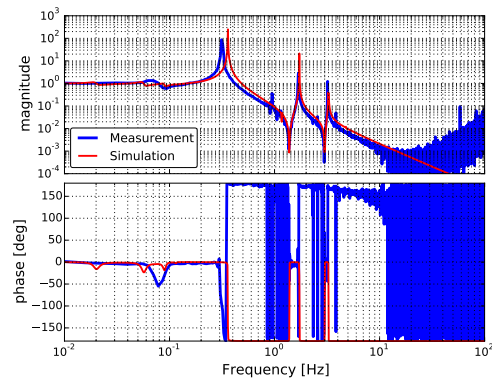
Figure 6.7 shows that the model agrees with the measurement except for:

1. the two modes observed in Figure 6.6, i.e, the 0.32 Hz mode in yaw dof and 7.5 Hz in pitch dof,
2. the highest resonance in L and T dof at 5.2 Hz and 5.0 Hz respectively as shown in Figure 6.7a and 6.7b,
3. vertical dof as shown in Figure 6.7c.

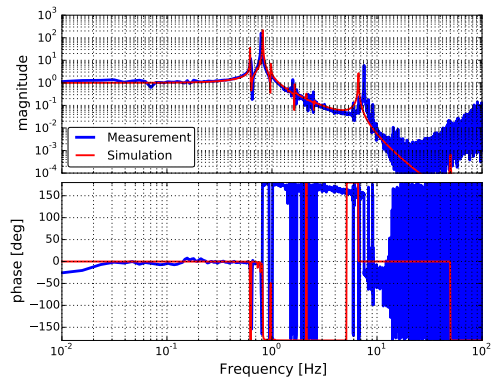
The discrepancy of the L and T dof, which are the RMN resonances, can come from the hanging condition similar to the 7.5 Hz case found in Figure 6.6. The failure of the vertical dof come from the failure of the photo-sensor diagonalization. The vertical photo-sensor signal obtained by the matrix operation based on the geometrical factors, actually it senses the yaw motion as shown in Figure 6.7c and as shown in Figure 6.7f. Thus the vertical dof cannot be tested with the photo-sensor. In order to sense the vertical motion with the photo-sensors further sensor matrix diagonalization is necessary.



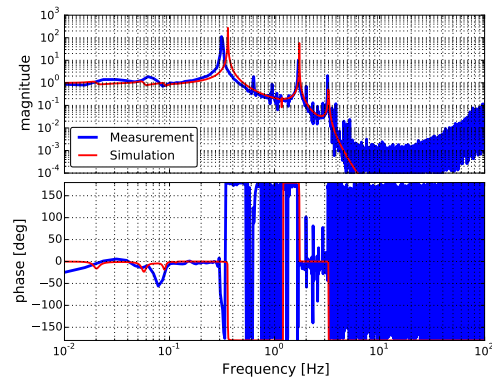
(a) MN to MN in pitch



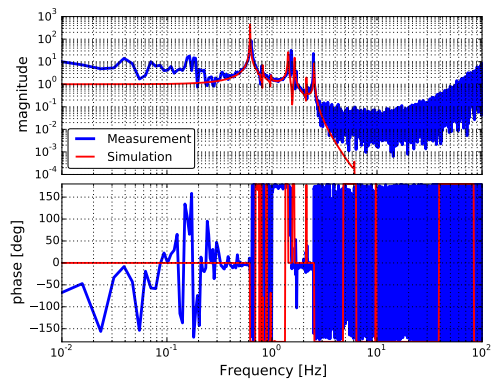
(b) MN to MN in yaw



(c) MN to TM in pitch



(d) MN to TM in yaw



(e) MN to TM in longitudinal

Figure 6.6: Diagonal mechanical transfer functions of the MN-stage in pitch (*left*) and yaw (*right*) sensed by the optical lever. The upper panels show the response from MN to MN, while the lower panels represent the ones from MN to TM.

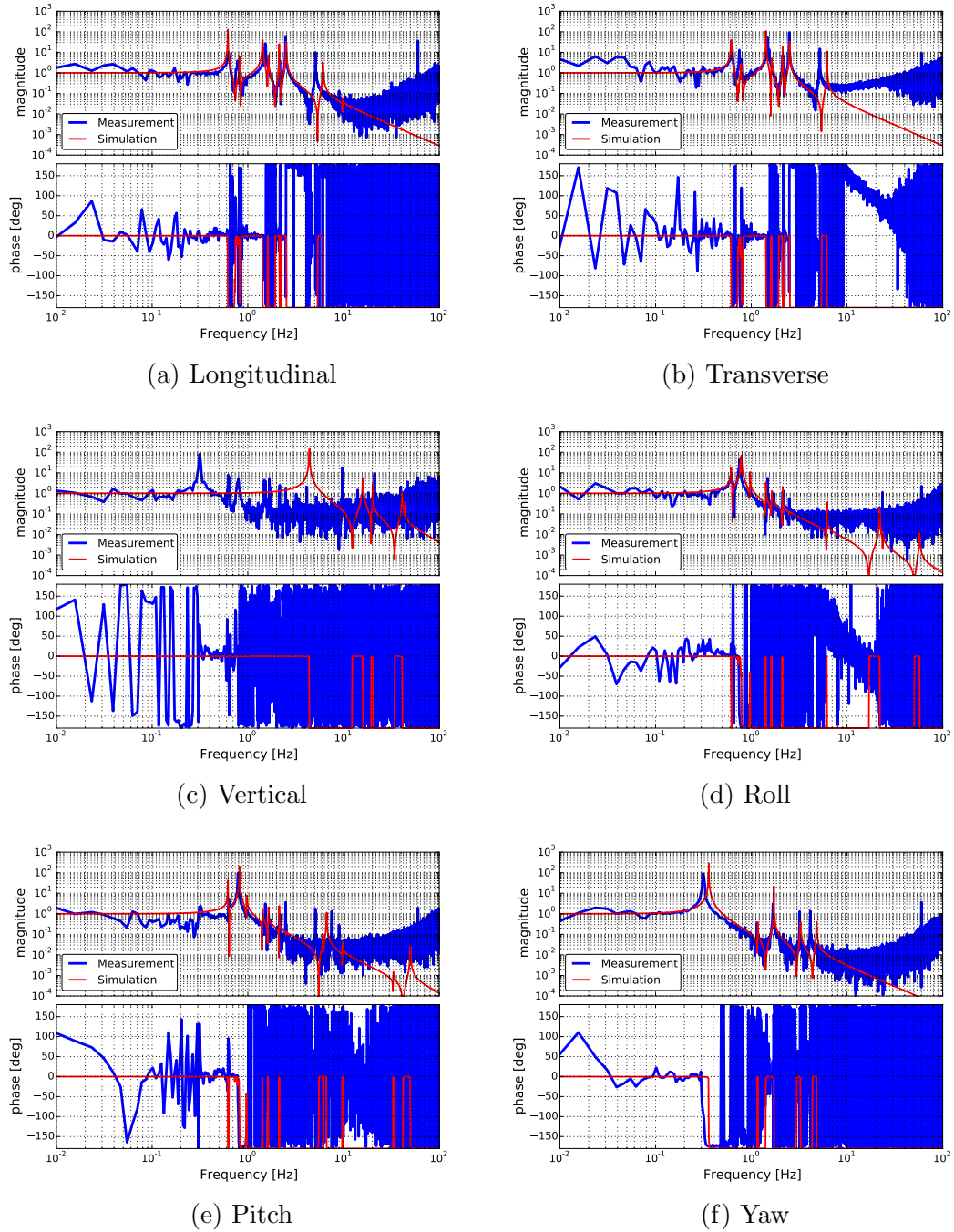


Figure 6.7: Diagonal mechanical transfer functions of the MN-excitation to MN-stage sensed by the photo-sensors.

IM stage and TM stage

Basically the model agrees with the actual system except for the two modes at 0.32 Hz in yaw dof and 7.5 Hz in pitch dof. These transfer functions are measured with the optical levers at the TM stage.

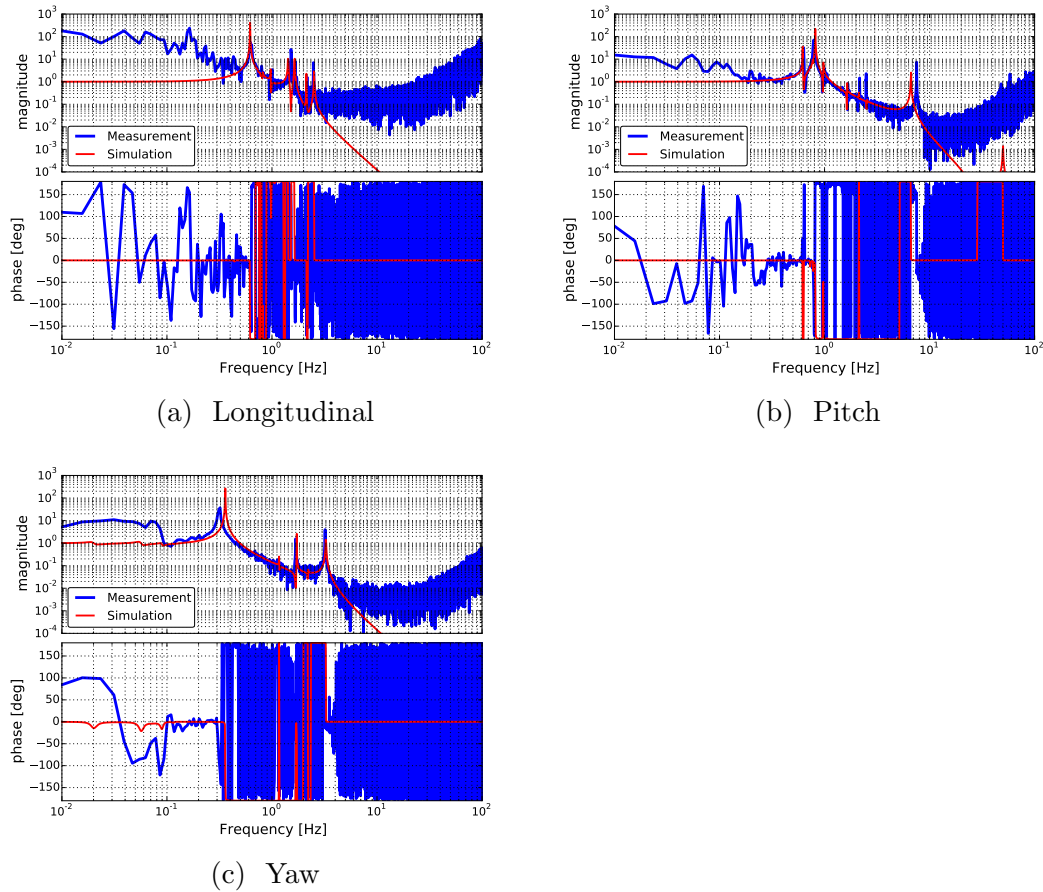
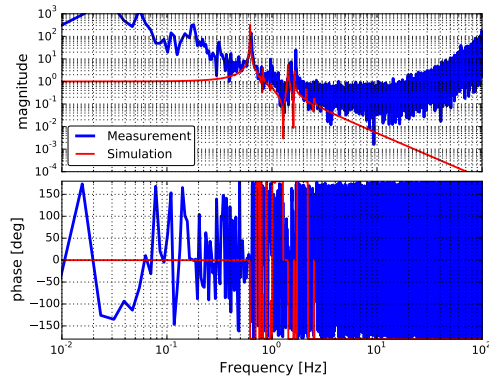
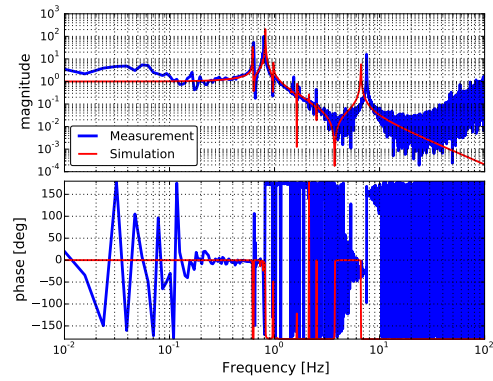


Figure 6.8: Diagonal mechanical transfer functions from IM-stage excitation to TM in longitudinal (a), transverse (b) and Yaw (c) dof with the simulated curve. They are measured with the optical levers at the TM stage.

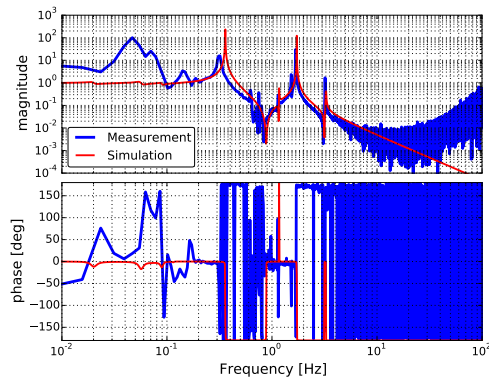
TM stage



(a) Longitudinal



(b) Pitch



(c) Yaw

Figure 6.9: Diagonal mechanical transfer functions from TM-stage excitation to TM in longitudinal (a), transverse (b) and Yaw (c) dof with the simulated curve. They are measured with the optical levers at the TM stage.

6.2.2 Effect of heat-links and its vibration isolation system

According to the force transfer function measurement in the above, some significant discrepancies from the model without heat link system are reported at the BF-stage measurement as follows:

- The first resonant frequency of the BF-stage excited transfer functions in Yaw degree of freedom become higher than the those predicted by the model. The measured first resonant frequencies for Yaw dof is 40 mHz while that by model is 20 mHz.
- One peak at 0.14 Hz is newly found in the BF-stage excited transfer functions in Yaw degree of freedom. This peak is found in all the equipped sensors when the BF-stage is excited in Yaw. On the other hand, this peak is not observed with Optical levers when the lower stage such as MN-stage is excited.

Similar measurement was already done in [32] and it reports that if there is not payload, heat link nor the heat link vibration isolation system, the first resonant frequency in L, T and Yaw was dof measured at 55 mHz, 65 mHz and 20 mHz, respectively. On the other hand, the newly measured frequencies in this work are 74 mHz, 82 mHz and 40 mHz for L, T and Yaw dof respectively. It also reported the measured results were in agreement with simulation. Compared to the suspension configuration in [32], the total length of the suspension becomes longer in this work, it is more natural to predict that the fist resonance would be found at lower frequencies. The resonant frequency depends on the temperature, and the temperature during the measurement is actually lower than the room-temperature, 250 K. However, this is not enough to explain the difference of the elastics constant by factor of about 4 (in yaw case). Thus this implies that the current system should have additional springs to the current model. The most possible origin of this additional spring is the heat link system.

6.2.3 Summary of mechanical system characterization

The measured characteristics in terms of the frequency response agrees with the rigid-body simulation (which does not include the heat link system) except for the BF-stage and GAS filters, with some exception of resonant frequency and the Q factors. The model fails in predicting the frequency response of the BF-stage, especially in the yaw dof. It is confirmed that the each suspension component has the characteristics of a pendulum, however, the details of the system have to be more precisely identified and modeled. Especially the rigid-body modeling without including heat link system fails to explain some of the actual Type-A suspension response and resonant frequencies.

6.3 Performance of mechanical vibration isolation

In order to test the vibration isolation performance of the suspension in the longitudinal dof, transfer functions from the upper stages to the mirror motion has been investigated.

6.3.1 Measurement set up

For this purpose, force transfer functions are measured by actuating on the IP- and BF-stages and sensing the mirror motion with either the length-optical lever or the FPMI² with green and IR laser.

For evaluating the vibration isolation performance, we can measure either the displacement transfer function from a sensor to a sensor, or force transfer function from an excitation to a sensor. Since we use the LVDT for this measurement and also since it was observed that in the LVDT signal, the direct coupling between the sensor and the actuator becomes dominant at frequencies above a few Hz when that stage is excited, as shown in Figure 6.5a for example, we select the force transfer function for this measurement.

For the lower frequency part (< 1 Hz), white noise is injected to the upper stages and then the length-optical lever is used as the sensor. On the other hand, for the higher frequency part (> 1 Hz), a sinusoidal noise is injected and the FPMI is used as the sensor. In the sinusoidal noise injection measurement, the length-optical lever signal is also measured as a reference.

Control configuration

During the measurement with the local optical lever, all the local controls are off in order to get the open loop mechanical response. On the other hand, during the measurement with the FPMI, some of the loops which does not disturb the measurement are kept closed. This is necessary in order to avoid the mirror angular drift especially in yaw dof, since otherwise we cannot keep the locked condition of the interferometer. For this purpose, during the FPMI measurement, all the payload controls are opened, however, the controls for each GAS stage, BF-stage in Yaw dof and IP-stage in T and Yaw dof are kept closed (The details about these filters are summarized in section 6.4.1). These loops are kept closed since the controlled dof is different from the target L dof, and the coupling levels are not large. In addition to this, a DC-control filter for the longitudinal dof at IP-stage whose unity gain frequency (UGF) is lower than about 0.3 Hz is closed. The LVDT is used for this loops. This is done since the measurement with FPMI focuses on the frequency only higher than 1Hz, and also otherwise the lock of the FPMI was easily lost in the timescale of a few minutes due to the drift. The open loop transfer function used for the IP-stage in L dof is shown in *left* of

²FPMI stand for Fabry-Perot Michelson Interferometer. The difference of the wave length of teh laser corresponds to the difference of the sensitivity of the sensors (interferometers). During this measurement, the ETMY is globally controlled for keeping its lock.

Figure 6.10. Since the seismic motion enhanced the residual motion in the period when the measurement by FPMI with IR laser was conducted, the filter shape is changed so that the filter can damp the 0.2 Hz mode accordingly.

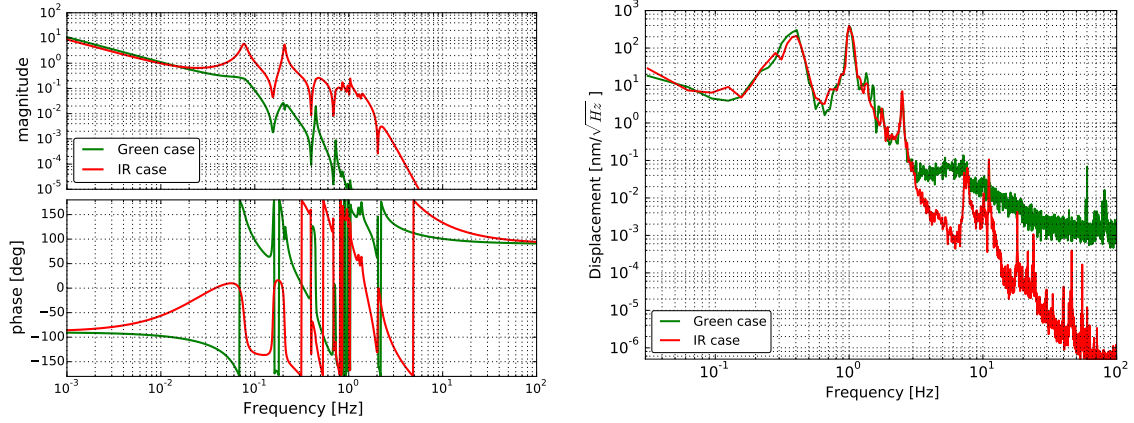


Figure 6.10: The used open loop transfer function used for the IP-stage in L dof (*left*) and the typical noise floor of the FPMI with green and IR laser during the measurement (*right*).

6.3.2 Measurement

The measured force transfer functions when the IP- and BF-stage is excited in L dof are shown in *top* and *bottom* of Figure 6.11 respectively.

As described above, the response at frequency below 1.1 Hz and 1.8 Hz is measured by the length-optical lever with white noise injection for IP- and BF-stage excitation respectively. The response above those frequencies is measured by both the length-optical lever and FPMI with one sinusoidal noise injection. For the measurement with single sinusoidal injection, we selected the measurements whose coherence is higher than 0.7. The FPMI measurement fails above 1.4 Hz for IP-stage excitation and 4.2 Hz for the BF-stage excitation since the induced mirror displacement becomes comparable to the FPMI noise level. At frequencies higher than 3 Hz, the coupling from the other dofs becomes dominant in the length-optical lever signal as shown in Figure 6.11b

Figure 6.11a indicates that except the IP-excited measurement in the frequency band between 1.1 Hz to 1.4 Hz, the model used in section 6.2, can explain the actual suspension response in both excitation cases, except for the Q factors of the lowest and the second lowest resonances. As shown in Figure 6.11a, in the frequency band between 1.1 Hz to 1.4 Hz, there is no agreement among the model, the measurement by length-optical lever and that by FPMI, even though the slopes are mostly consistent. This could come from the coupling with the other dofs and that makes the coupling ratio difference to the length-optical lever and to the FPMI. For the more details, further investigation will be necessary.

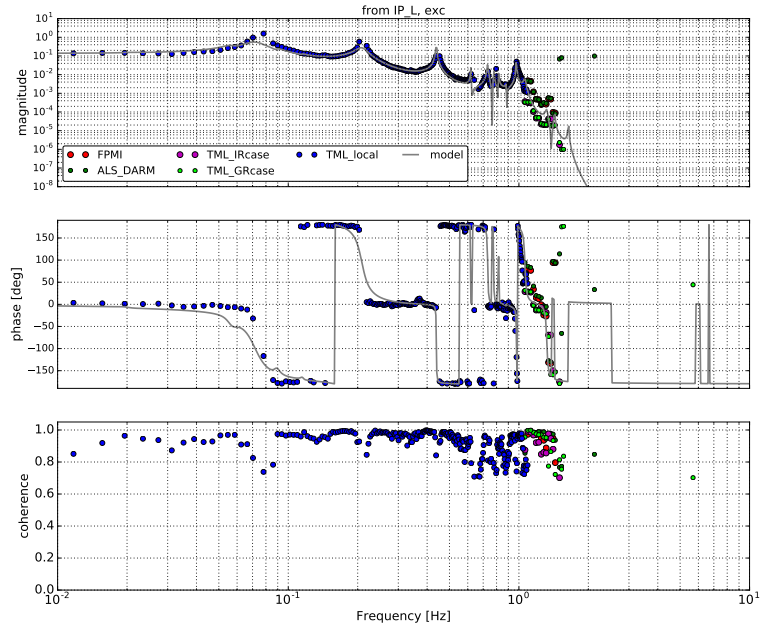
On the other hand, Figure 6.11b reports that the actual system agrees with the model up to 4.2 Hz.

This would imply that even though the designed mechanical transfer function might not be realized in the actual system in the the frequency band between 1.1 Hz to 1.4 Hz³, the vibration isolation performance is realized at 4.2 Hz.

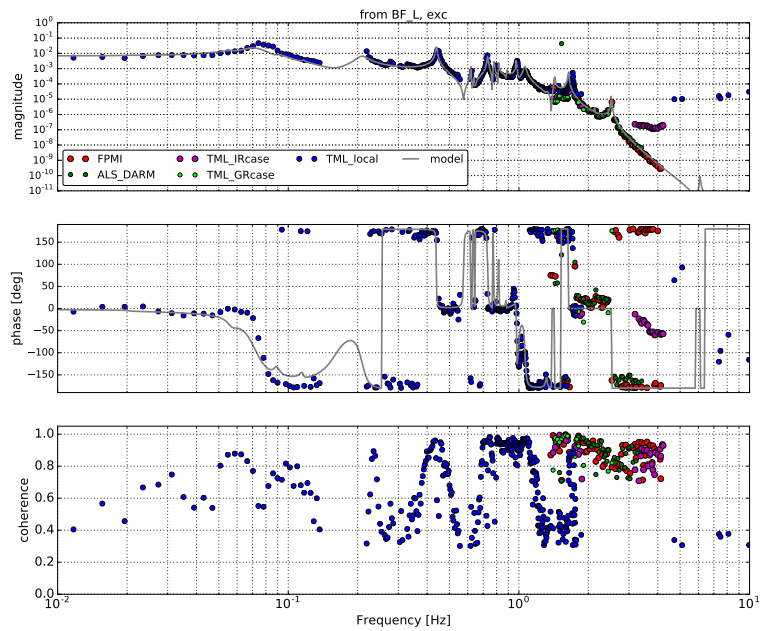
6.3.3 Summary

A direct vibration isolation performance is tested in terms of the force transfer function measurement. The measurement indicates that the response of the actual system is consistent with the prediction by the model used in section 6.2 except for that at the frequency higher than 1.1 Hz in the IP-excited measurement. The result would imply that the designed vibration isolation performance at 4.2 Hz agrees with the model. For more the details, we have to conduct further investigation.

³Assuming that the discrepancy does not comes from the coupling from the other degree of freedoms



(a) From the IP-stage excitation



(b) From the BF-stage excitation

Figure 6.11: Measured force transfer functions from the IP-stage excitation (a) and from the BF-stage excitation (b) in L dof. The grey colored curves show the prediction of the model used in section 6.2. The blue dots represents the measurement with the length-optical lever and with white noise injection. The other colored dots show the results by sinusoidal noise injection. The green and red dots are obtained from FPMI while the magenta and lime dots are the measurements by the length-optical lever when the FPMI measurements are conducted.

6.4 Performance of damping control

The installed feed-back servo system for the calm-down phase is summarized in section 6.4.1 and its performance test is described in the section 6.4.2.

6.4.1 Servo system

As shown in Figure 5.2, the upper part (IP and BF) has DC-coupled damping filters for the horizontal and the vertical dof, and lower part (payload) is more focused on the payload mode damping and mirror angular DC control. The implemented servo loops with the used sensors is summarized in Table 6.1 and the open loop transfer functions are show in Figure 6.12. In this system we use optical lever at MN-stage to sense the MN motion in the roll dof. We also use the optical levers at two stages; MN- and TM-stage. Oplev at the MN-stage (MN-oplev) senses the two angular motion in P and Y, while the optical lever at TM-stage (TM-oplev and TM-length oplev) senses the L, P and Y dof.

Table 6.1: The implemented servo loops with the used sensors. The loops for the IP- and BF-stage and the GAS filters are closed in each stage. In the below oplev represents the optical lever. We have the optical levers at MN- and TM-stages and they are labeled as MN-oplev and TM-oplev respectively.

Loop	Loop dof	Sensor	Actuation dof	Purpose
IP	L, T, Y	LVDT	IP	DC and damp
BF	Y	BF-LVDT	BF	DC and damp
F0	GAS	LVDT	F0	DC and damp
F1	GAS	LVDT	F1	DC
F3	GAS	LVDT	F3	DC and damp
BF	GAS	LVDT	BF	DC
from MN to MN	Y	MN-oplev	MN-Y	damp
from TM to MN	Y	TM-oplev	MN-Y	DC
from TM to MN	P	TM-oplev	MN-P	DC and damp
from TM to IM	P	TM-oplev	IM-P	damp
from MN to MN	R	MN-oplev	MN-R	damp

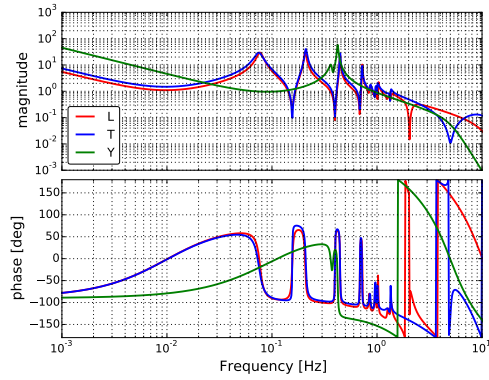
In this control system for the payload, due to a technical issue found in the PS signal of ETMX suspension shown in section 6.4.3, the control system for the payload is basically built with the optical levers, even though it has smaller linear range compared to the photo-sensors. The resonant modes of #51, #52, #55, #56 and #57 are the exception and they are taken care by the photo-sensors at the MN-stage. The implemented filters are shown in *left* of Figure 6.13.

Based on this, we additionally use fourth order Butterworth band-pass filters for the payload damping [58]. We refer to this as band-pass comb filters. This

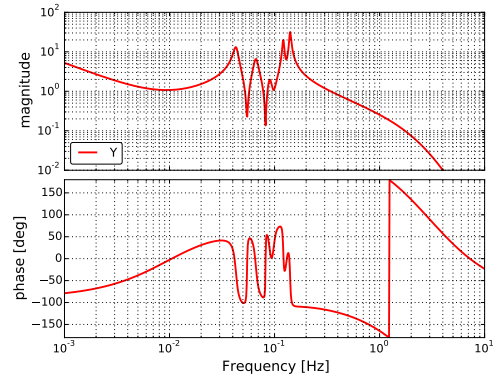
control system is implemented in order to damp the RM chain modes which are to be sensed by the photo-sensors in the design. This band-pass filter can also minimize the control noise re-injection at higher frequency region. The filter is designed with band-pass frequency around the target mode frequency ($f_0 - \Delta f_1, f_0 + \Delta f_2$) where f_0 is the frequency of the target mode and Δf_1 and Δf_2 decide the band-width. We select an optical lever signal which observes the target resonance and tuned the phase by tweaking Δf_1 , Δf_2 and the gain. The optimization is done manually so that the decay time of the mode becomes smaller than the requirement. The implemented band-pass comb filters are summarized in Table 6.2 and shown in *right* of Figure 6.13.

Table 6.2: The implemented band-pass comb filters for the payload modal damping with the used sensors and actuators. The frequencies of the target resonance are included. The combination of the stage and the dof is written by stage-dof.

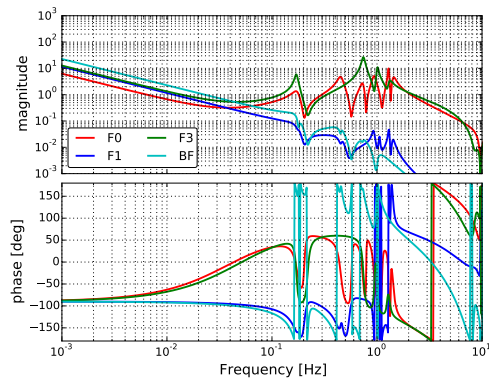
ID	Sensing	Actuation	Target frequency [Hz]
BP-comb 1	TM-P	MN-L	1.53 Hz (#44)
BP-comb 2	MN-P	MN-R	23.5 Hz (#63)
BP-comb 3	TM-L	IM-L	2.17 Hz (#49)
BP-comb 4	TM-P	MN-V	9.69 Hz (#59)
BP-comb 5	TM-L	MN-L	2.5 Hz (#52)
BP-comb 6	TM-P	MN-P	7.5 Hz (#58)
BP-comb 7	TM-Y	MN-Y	3.21 Hz (#53)
BP-comb 8	TM-Y	MN-Y	1.15 Hz (#39)



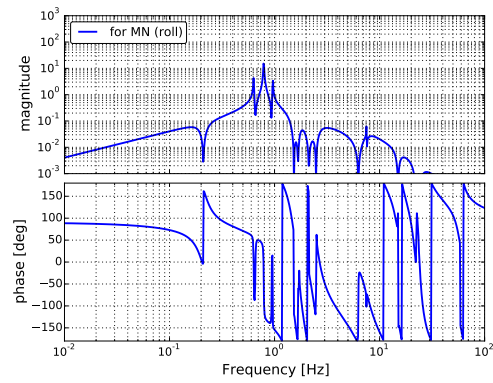
(a) IP loops in L, T and Y dof.



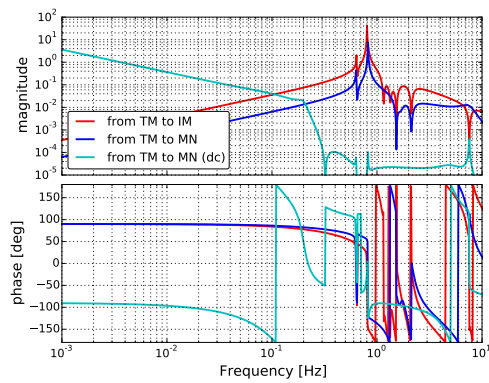
(b) BF loops in Y dof.



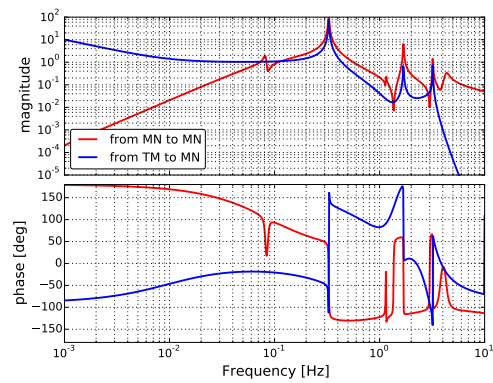
(c) F0, F1, F3 and BF GAS loops.



(d) Payload loops in R dof.

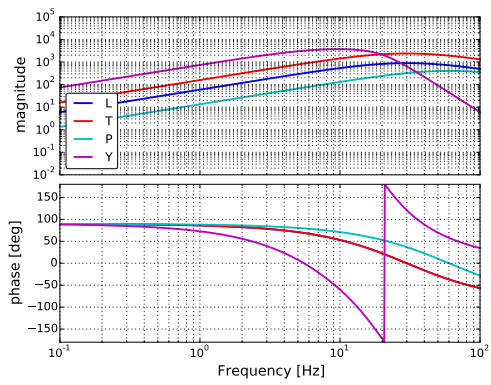


(e) Payload loops in P dof.

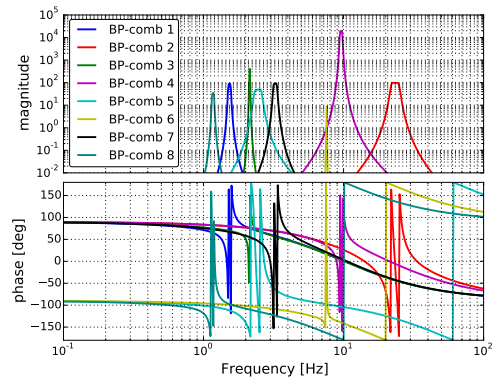


(f) Payload loops in Y dof.

Figure 6.12: Open loop transfer functions of the implemented servo filters for the calm-down phase.



(a) PS loop filters at MN-stage in L, T, P and Y dof.



(b) Implemented band-pass comb filters.

Figure 6.13: Implemented servo filters in addition to the ones in Table 6.1.

6.4.2 Decay time measurement

In order to check that the installed control system satisfy the requirement ($1/e$ decay-time constants < 1 min.), the decay-time constant of each mechanical resonance is measured. Since the target for the system is to damp all the mechanical resonances which disturbs the lock acquisition, some of the mode which are expected to less couple to the mirror such as shown in Figure 6.14 (a), are not considered. In addition, only the modes whose resonant frequency are lower than 30 Hz are examined, since the resonances which disturbs interferometer locking are basically the lower frequency modes. As another reason that frequency is selected since it is difficult to sense the resonances higher than 30Hz with the local sensors and also to actuate them. Then the total number of the measured resonances are 53.

The decay time measurement was conducted as follows: first, a target resonant mode is excited by using an appropriate virtual actuator with a sinusoidal signal at the resonant frequency. After the resonance is excited enough, the actuation is then turned off and the decay signal is measured by the built-in sensors. The measured decay time series is approximately fitted by an exponential-decay sine wave function eq (6.1): When it is difficult to excite only one resonance and a beating signal is measured, a double or a triple decay sine wave function is used for the fitting. This situation occurs when some modes have close resonant frequencies.

$$f(t) = \sum_i^n \left[A_i \exp\left(-\frac{t}{\tau_{e,i}}\right) \sin(2\pi f_{0,i}t) \right] + x_0, \quad (n = 1, 2 \text{ or } 3) \quad (6.1)$$

where τ_e is the $1/e$ decay time.

An example of this measurement is shown in figure 6.15. These are obtained by exciting MN-stage in Yaw dof and by measuring with the optical lever.

The measured decay time constants for each resonance without and with the control are summarized in section B.5. They include the resonance modes whose resonant frequencies are below 30 Hz. The measured $1/e$ decay time constants for each resonant frequency are plotted in figure 6.16. According to the plot, the requirement is satisfied except for the two cases. I note that one resonance predicted at 4.4 Hz reported in in Figure 6.14 (b), is not found in this work. The investigation for that mode is ignored since no vertical resonances which would disturb the lock acquisition, are observed at around 4 to 5 Hz region.

For the one case found at 1.5 Hz, this would not be a problem for the lock acquisition since the resonance is the mode in roll and transverse dof labeled mode #43 in section B.1. Even if this mode becomes problematic, we can damp it using the optical lever at the MN-stage and the virtual actuator in roll dof at MN-stage for example. Thus the case at 1.5 Hz does not break the requirement.

Concerning the case at 0.14 Hz, this mode is found at Yaw motion of the BF-stage, and is not identified by the model which does not have the information of the heat-link system The counterpart of this mode is not found in the table

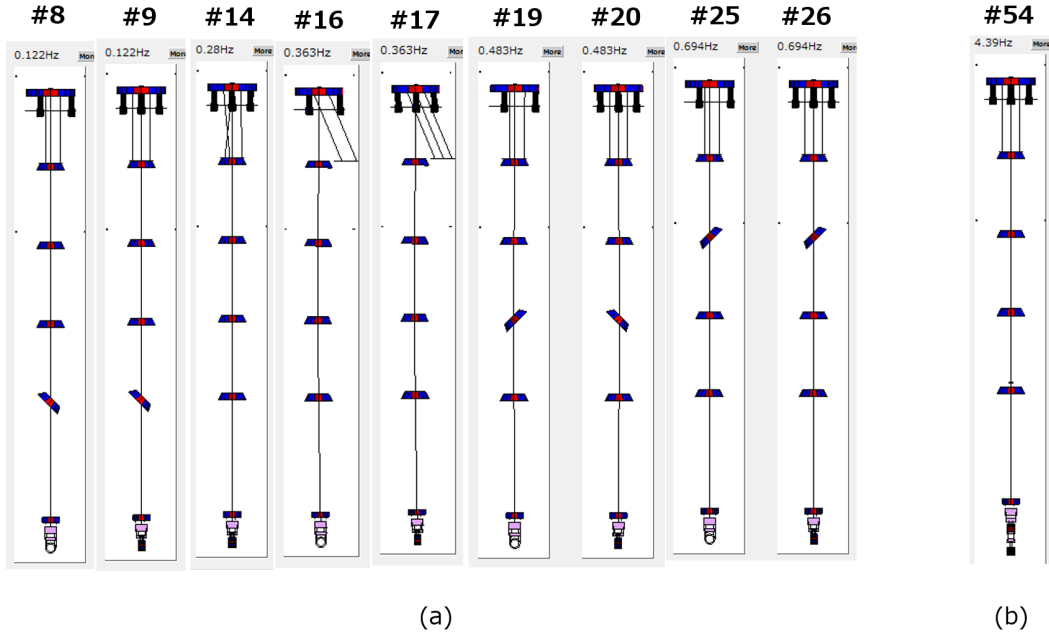


Figure 6.14: Eigen modes which are not considered in this test (a), and the eigen mode which is not found (b), at the frequency region lower than 30 Hz.

in section B.1. This is the highest mode observed in the force transfer function from BF-stage excitation in Yaw dof to BF-stage in Yaw dof in Figure 6.5c. Based on the fact that the BF-stage Yaw control loop failed to damp this mode effectively nevertheless the open loop gain is larger than 1 as in Figure 6.12b, it implies that this issue is connected to payload part especially the heat-link system. Generally speaking, further investigation would be necessary for more details about this resonance. However, this peak is visible at the BF-Yaw and TM-chain-Yaw sensors, when the BF-stage is excited in Yaw as in Figure 6.17a. On the other hand, when the MN-stage is excited in Yaw, the peak is observed in only BF-stage and both the optical lever at MN-stage and the photo-sensor do not sense the peak as shown in Figure 6.17b. This implies that unless the BF-stage is not kicked, this resonance would not be excited. Since the feedback signals for the global control is fed back to the TM- and MN-stage in the current interferometer control, we do not kick BF-stage at the lock loss.

These observed facts lead a conclusion that this mode would not be problematic for the lock acquisition in the lock-recovery mode. Although this 0.14 Hz Yaw motion would be problematic when the upper stages such as BF- and IP-stages are used for the interferometer control, that consideration is to be done as further improvement. Consequently, the installed control system satisfies the requirement in the lock-recovery mode.

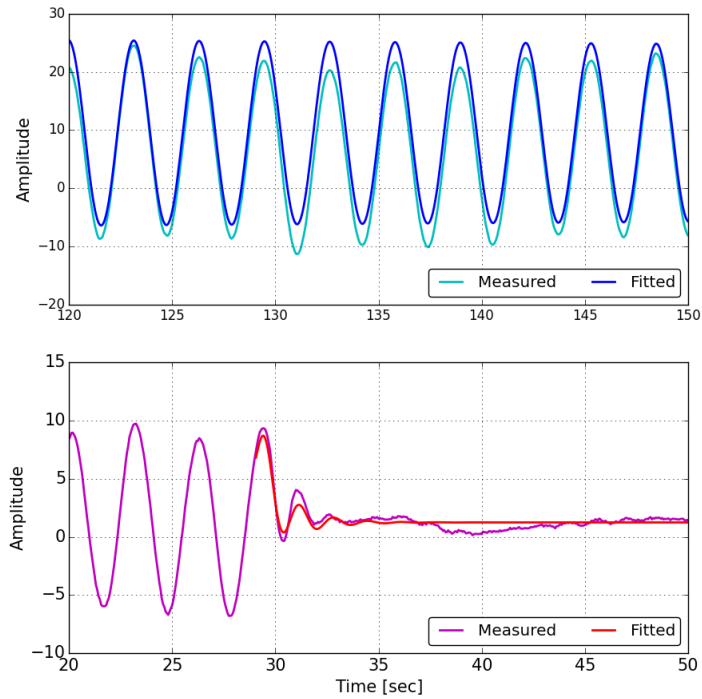


Figure 6.15: An example of the $1/e$ decay-time measurement. The time series, when one resonant mode is excited by a sinusoidal injection and when it is cut off, is drawn in. The upper and the lower panel show the case where the control is off and on respectively. Yaw motion excited at MN-stage and sensed by the optical lever. The (cyan, magenta) colored curves show the measured time series, while the (blue, red) colored time series represent the fitted time series.

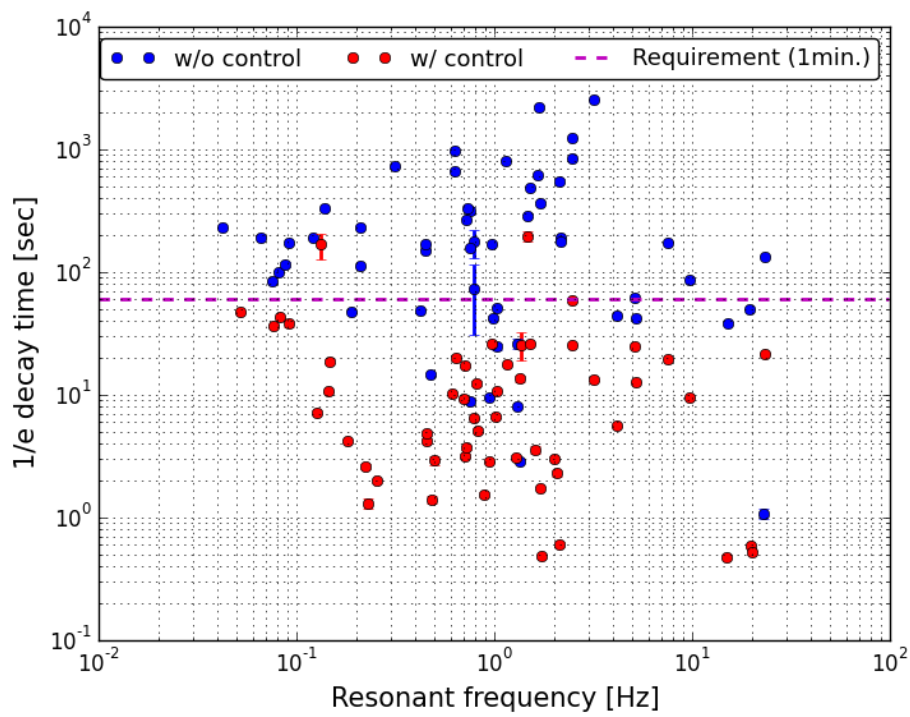
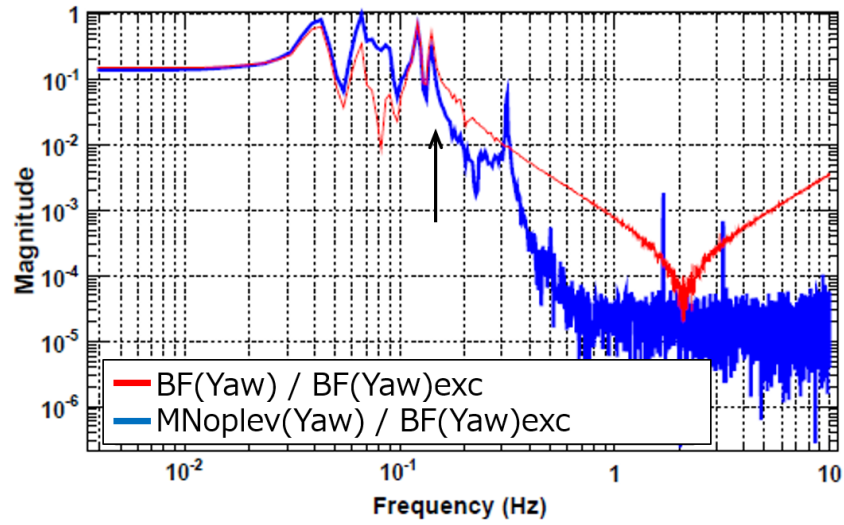
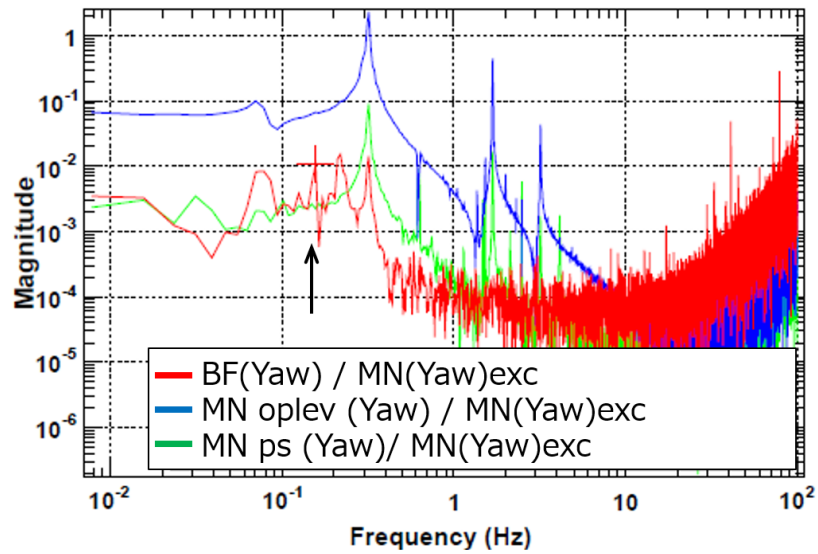


Figure 6.16: The result of the $1/e$ decay time constant as the function of the measurable mechanical resonances. The dashed line shows the requirement of 1 minute.



(a) Force transfer function from BF-Yaw excitation to BF-Yaw (blue) and to MN-Yaw measured by the optical lever (red). The unit is a.u.



(b) Force transfer function from MN-Yaw excitation to BF-Yaw (blue), and to MN-Yaw with the optical lever, and to MN-Y with the reflective photo-sensors at MN-stage (blue and green respectively.).

Figure 6.17: The measured force transfer functions in Yaw. The unit is a.u. The arrows point the peak at 0.14 Hz.

6.4.3 Further steps for the damping system

In this work, it is failed to find one resonance which is the vertical motion predicted at 4.4 Hz with the model which does not have heat-link system. Investigation for this mode would be also important to understand the whole suspension system, however, the corresponding resonance should have smaller decay time since such vertical mode is never appeared during this work.

In addition, this control system uses mainly optical levers in order to avoid to use the reflective photo-sensors due to the technical issue that the photo-sensors sometimes becomes unstable depends on time⁴ and has a spectra such as shown in Figure 6.18.

The implemented control system based on the optical levers satisfied the requirement, however, since the linear range of the optical lever is relatively small (typically about a few hundred μrad) and the signal easily goes outside the available range when a big disturbance happens such as large earthquakes, a large kick is happened at a lock loss. In order to construct a more robust damping system, it is demanded to use the photo-sensors effectively especially when the relatively large disturbance happens, since the linear range is larger than the that of the optical lever.

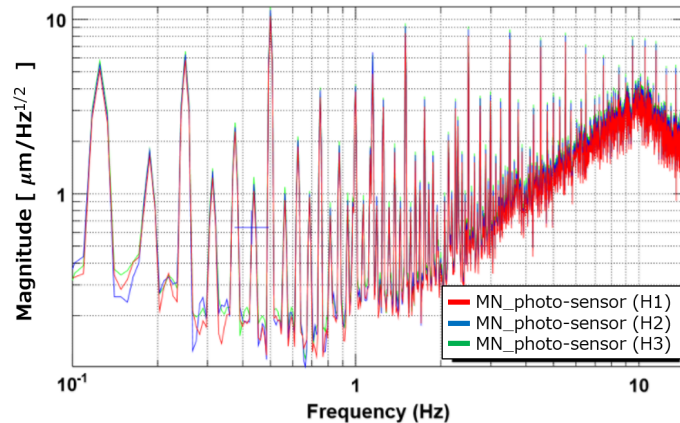


Figure 6.18: Spectra of the photo-sensor when it becomes noisy. The unit is calibrated based on an estimation.

In addition, we want to improve the sensitivity of the photo-sensors, or we want to have sensors which observes the RM-chain motion and whose sensitivity is comparable to the optical lever. Since the current photo-sensors are not enough to measure the mass motion when the mirror motion becomes smaller than typically

⁴It was known that this issue came from somewhere in the electrical circuits, however, it was impossible to solve the issue during my available time at the site.

1 μ m and 1 μ rad. If we can solve the issue shown in Figure 6.18 and also improve the sensitivity, we can utilize the photo-sensors effectively. Implementing better-sensitivity photo-sensors (or optical lever for the RM-chain) would also help to reduce the current work load on the designing the band-pass comb filters⁵.

⁵Since the band-pass comb filter is so sensitive to the resonant frequency, and thus the temperature of the payload is changed (this can cause the resonant frequency shift), we have to tune the filter accordingly. In a situation where the commissioning is ongoing, this makes the situation quite inconvenient.

6.5 Performance of seismic noise suppression control

In order to reduce the RMS velocity and displacement of the mirror at the frequency around 0.2 Hz, the feedback control with sensor-correction system, which is described in section 5.5.1 is implemented to the actual Type-A system. As in the designing part, the sensor correction system is additionally implemented to the feedback controls at the most upper stage, i.e the IP-stage. For the other control loop such as the payload and the GAS stages, we use same ones as the ones used in the calm-down phase.

6.5.1 Control system

The ground vibration signal measured by a seismometer Trillium120QA [51] at the second floor of the X-end station is sent and added to the LVDT signal with a sensor correction filter F_{sc} . Then the corrected LVDT signals are used for the feedback control system. Figure 6.19 show the main signal flow of the system, while Figure 6.20 draws the corresponding block diagram with a schematic view of the actual control system. The signals sensed at each IP-LVDTs are converted to the Cartesian signals with the sensor matrix. The filtered seismometer signal on the ground is added to the Cartesian signals and then the combined signals are used as the error signal of the feedback system. The correction signals are sent to each coils after applying the force distribution matrix.

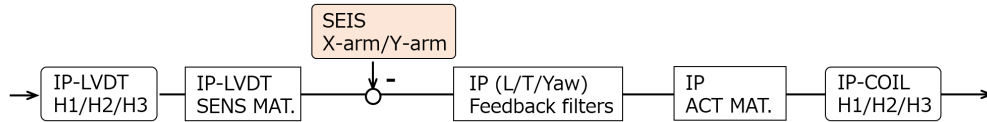


Figure 6.19: Main signal flow of the feedback control with the sensor correction system at the IP-stage. The signals sensed at each IP-LVDTs are converted to the Cartesian signals with the sensor matrix (SENS MAT.). The filtered seismometer signal on the ground is added to the Cartesian signals and then the combined signals are used as the error signal of the feedback system. The correction signals are sent to each coils after applying the force distribution matrix (IP ACT MAT.).

Filter shaping

Since the optimal sensor-correction filter is obtained by $F_{sc} = -S_L/S_s$ where S_L and S_s are the sensor response of the LVDT and the seismometer, we intercalibrate the signals between the IP-LVDT and of the seismometer on the ground so that the seismometer signal has same unit as the LVDT one. This is done by measuring the mechanical displacement transfer function from ground to IP-stage by LVDT and then tuned the gain by finding a frequency region which should be

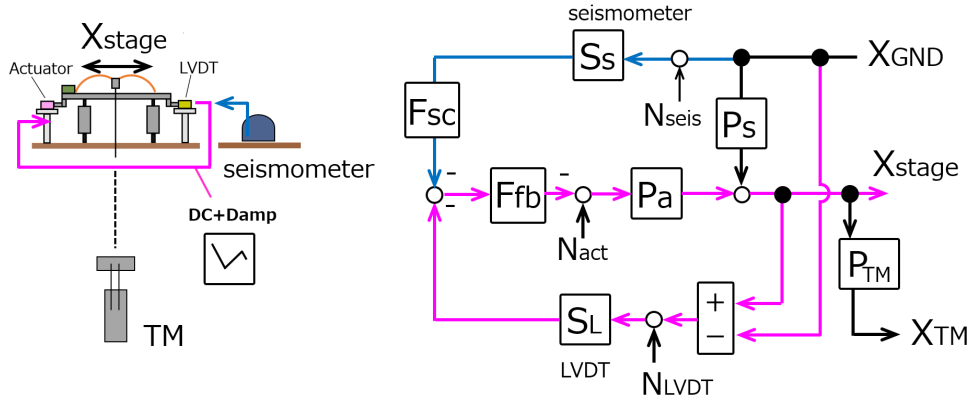


Figure 6.20: Block diagram of the feedback control with the sensor correction system at the IP-stage with its schematic view. Each parameters are defined with the same manner as in section 3.3. This is the case where F_{ff} is set to zero. P_{TM} denotes the displacement transfer function from IP-stage to TM-stage.

equal to 1, which is around at 0.6 Hz, as shown in Figure 6.21. As the result, we obtain the factors 0.99 and 0.93 for the L and T dof respectively.

After tuning the gain, we apply the high-pass filter with cut-off frequency of 10 mHz in order not to send too much noise of the seismometer. In order to avoid large amount of phase shift at above 0.1 Hz, we select a second order elliptic high-pass filter whose passband ripple and attenuation are set to 10 dB and 100 dB respectively. In addition we add one more high-pass filter at 0.5 mHz. A forth order Butterworth filter has been chosen to this purpose in order to cut-off the seismometer noise. This filter is necessary since the used seismometer measure the velocity and for this we have to additionally implement f^{-1} component for the conversion to the displacement signal. Since we wanted to avoid to enhance the noise at low frequency, we selected Butterworth filter for the lower high-pass filter.

The sensor-correction filter shape which is applied to the displacement seismometer signal is shown in Figure 6.22. The phase shift due to this filter shown in Figure 6.22 is 3.3 deg which gives 0.2 % difference compared to the ideal signal which we want to subtract. The sensor-correction filter shape which is applied to the velocity seismometer signal is obtained by applying a pure integration filter $1/s$ where s is the Laplace variable.

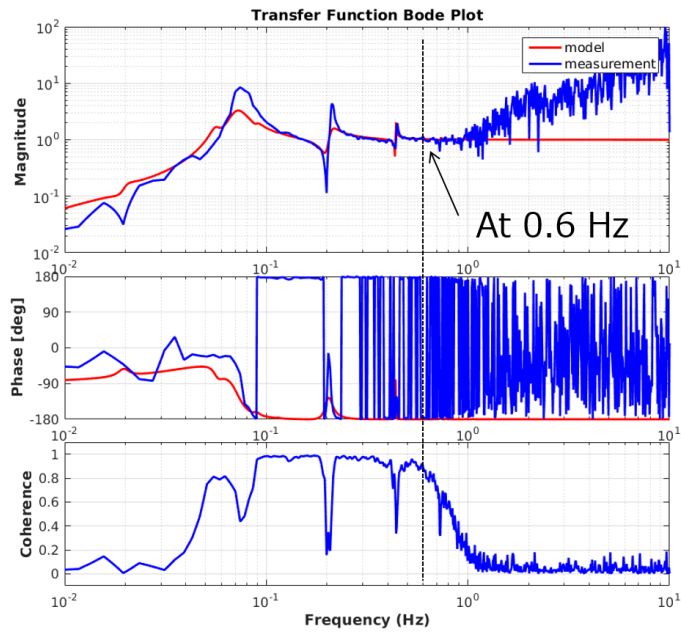


Figure 6.21: Displacement transfer function from ground to IP-stage by LVDT.

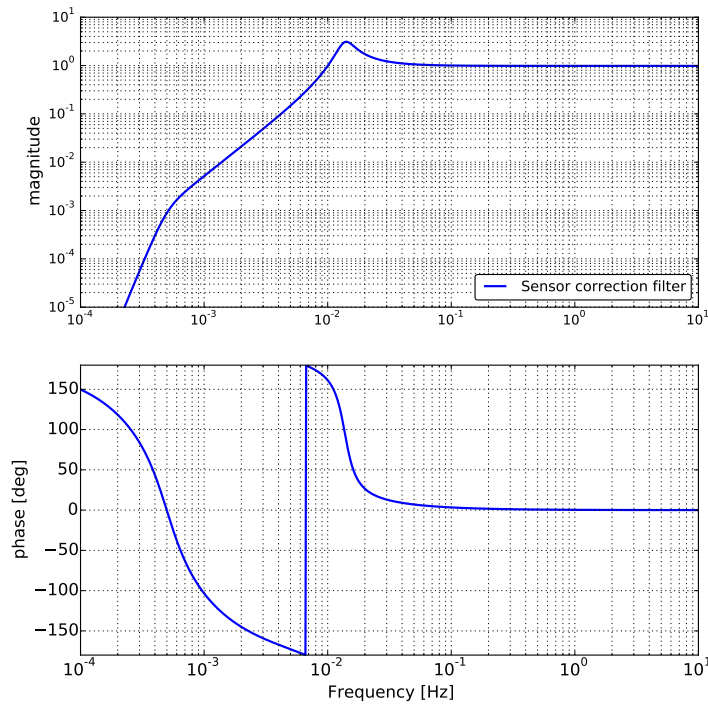


Figure 6.22: The sensor-correction filter shape which is applied to the displacement seismometer signal. This is the filter used in ETMX suspension. since the output of the used seismometer is velocity, $1/s$ is applied to this filter practically and then the seismometer signal is filtered.

6.5.2 Impact on a local suspension

After implementing the sensor-correction filter at the IP-stage, we investigate the suppression performance with the local sensors which are implemented around the ETMX suspension, and test if the residual mirror RMS velocity and displacement satisfy the requirements on them. In the following subsections the sensor-correction system at the IP-stage by the seismometer on the ground is abbreviated to IPsc. First we test the performance with the situation where the IPsc is implemented to only the L dof.

IP-stage performance

Figure 6.23 shows the comparison of the IP-stage displacement spectrum measured by the inertial sensor, geophone (*left*) and by the LVDT (*right*), when the IPsc is on and off. The seismometer signals are included in order to confirm the ground motion can be regarded as identical between the two measurements, since the ground motion always affect the shape of the spectra. Figure 6.23 (*right*) shows that the IP-stage motion as measured by the LVDT is suppressed by the IPsc at the frequencies below 1 Hz. where the LVDT signal had larger than its noise level when the IPsc was off. Indeed in this frequency range, the LVDT signal is above noise in both conditions (IPsc ON/OFF). On the other hand, however, the sensor-corrected IP-LVDT signal indicates that the LVDT is less corrected at the frequency below 70 mHz. Especially at the frequency below 40 mHz, the amplitude becomes larger compared to the case where the IPsc is off, due to the seismometer noise and the sensor-correction filter shape. This performance at such low frequency region is unavoidable in the sensor-corrected system with a seismometer which loses the sensitivity to the horizontal motion at such frequency region. Since the main target of this work is to reduce the RMS connected to the micro-seismic peak, which is around 0.1 to 0.5 Hz, we do not discuss the lower frequency displacement fluctuation here.

Figure 6.24 reports the comparison between the sensor-corrected IP-LVDT signal and the geophone signal when the IPsc is on. This figure reports that there is a discrepancy between the geophone signal and the sensor-corrected IP-LVDT signal. The amplitude is different by factor of 2 at around 0.2 Hz. In addition, the frequencies of the dips are also different each other. This seems to connect to the fact that the geophone can sense the tilt motion, while the LVDT does not see the tilt. This happens since the two sensors are sensing other motion. The more detailed investigation for this issue will be necessary, however, in this work we assume the geophone observes the IP-stage motion at that frequency and test the RMS requirements.

BF-stage and TM-stage performance

Figure 6.25 (*left*) shows the comparison of the BF-stage displacement spectrum measured by the LVDT, when the IPsc is on and off. The BF-LVDTs in this

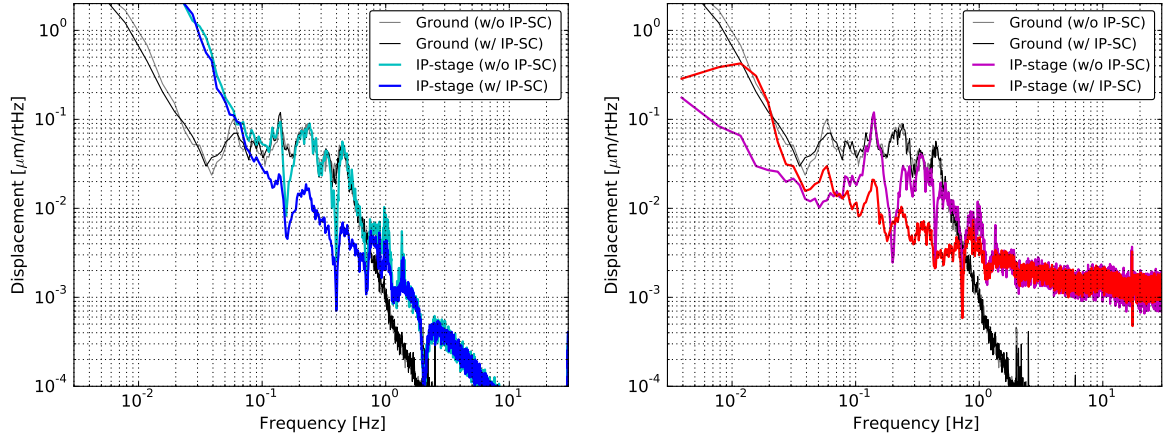


Figure 6.23: Comparison of the IP-stage displacement spectrum measured by the inertial sensor geophone (*left*) and by the LVDT (*right*) when the IPsc is on and off. I note that in the *right* panel, the LVDT signal with and without IPsc is not compatible since one measures the displacement, while the other one observes the inertial motion basically.

measurement are not sensor-corrected and thus they observe the relative motion between the security frame (mechanical ground) and the BF-body. This figure implies that the IPsc works for the whole upper part, since it is observed that the amplitude of the spectra in the frequency region between 0.1 Hz to 1 Hz is suppressed with the IPsc, and the amplitude at the frequency below about 40 mHz is enhanced due to the seismometer self-noise and the correction filter. Since the motion of the BF-body becomes smaller than seismic motion, all the feature of the BF-body displacement is buried into the seismic spectrum.

On the other hand, Figure 6.25 (*right*) shows the comparison of the TM-stage displacement spectrum measured by the length-optical lever when the IPsc is on and off. A consistent improvement is observed, however, the sensitivity of the TM length optical lever is not good enough to measure the TM motion.

Displacement transfer function measurement in L dof

After testing the single-dof correction system, we installed the IPsc to both L and T dof, and investigate the mirror motion suppression performance. In order to evaluate the suppression performance, the displacement transfer function from the ground to the mirror in L dof is measured by combining two displacement transfer functions; the displacement transfer function from the ground to the IP-stage, and that from the IP-stage to the TM-stage. The first transfer function is passively measured with the seismometer on the ground and the geophone on the IP-stage. The second one is measured by exciting IP-stage and the geophone signal is used at frequency higher than 0.1 Hz, while LVDT signal is used at frequency lower than 0.1 Hz. Those signals are selected based on the measured

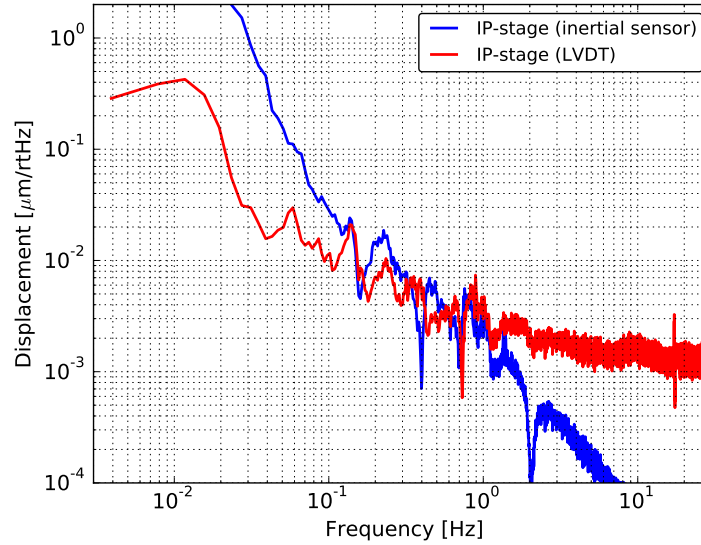


Figure 6.24: Comparison between the sensor-corrected IP-LVDT signal and the geophone signal when the IPsc is on.

coherence. The obtained transfer function from the ground to the mirror in L dof is shown in Figure 6.26. Using these transfer functions and the measured ground motion at KAGRA site, Figure 6.27 estimates the mirror displacement and velocity with the 90 percentile ground motion in Figure 3.1. The estimated RMS displacements and velocities of the mirror with the integration down to 20 mHz are summarized in Table 6.3. RMS velocity can satisfy its requirement even without the IPsc though, the RMS velocity is suppressed by factor of 5 using the IPsc technique. On the other hand, RMS displacement satisfy the requirement at 20 mHz though, this is not the case at 10 mHz and the RMS value can become larger than 1 μm .

Table 6.3: The estimated RMS displacements and velocities of the mirror with the integration down to 20 mHz.

Configuration	velocity [$\mu\text{m/s}$]	Displacement [μm]
Without IPsc	0.79	0.64
With IPsc	0.14	0.23

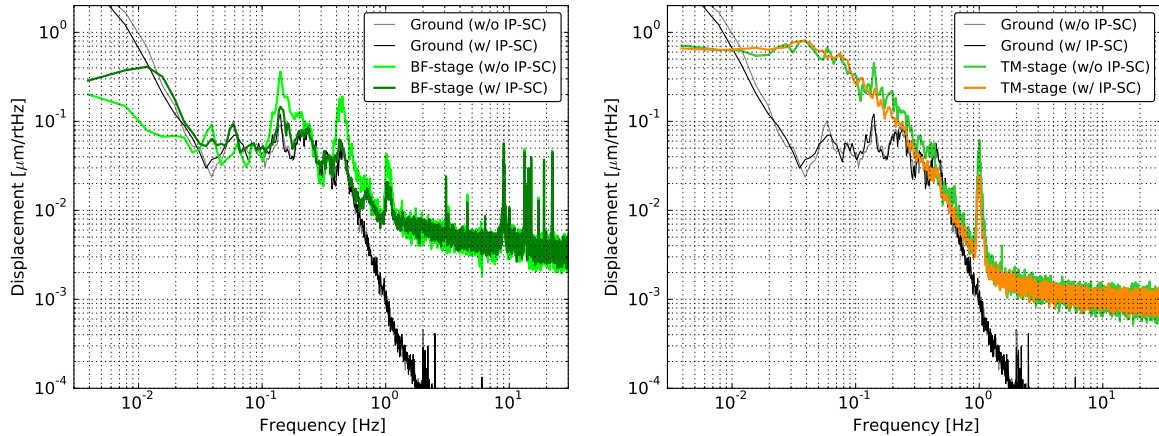


Figure 6.25: Comparison of the BF-stage displacement spectrum measured by the LVDT (*left*), and comparison of the TM-stage displacement spectrum measured by the length-optical lever when the IPsc is on and off. (*right*) when the IPsc is on and off.

Performance summary

Consequently, the implemented IPsc suppresses the residual motion of the mirror and it will give RMS displacement which satisfies the requirement for the lock acquisition phase, in the time-scale of 1 minute, which corresponding to the integration down to 20 mHz. The RMS velocity satisfies the requirement for the lock acquisition phase, independent on the IPsc system.

Since the RMS is estimated with the inertial sensor geophone which loses the high signal-to-noise ratio at such low frequency, those values can be upper limits. It is expected that the geophone spectra contain the tilt coupling which cannot be distinguished with the current setting. Finely tweaking the high-pass cut-off frequencies of the sensor-correction filter F_{sc} can realize a system which satisfies the requirements on RMS velocity and displacement at 10 mHz. However, this makes the time-scale longer by a factor of 2, from 50 sec to 100 sec which is not different, and also it is difficult to test the performance with the currently implemented local sensors. It is more natural to have another system which compensates such longer-term drift on the suspensions, which uses the baseline signal⁶ in DC and feeds back to the upper part of the suspension, such as IP-stage, at the end-station so that the ETMX/Y move along with the ITMX/Y respectively, for example.

In addition, originally this sensor-correction system is developed since the inertial sensor is not effectively useful in some of the suspensions. This low-frequency drift issue will be solved if we can build a inertial control system, by using the inertial sensors which has enough sensitivity at frequency below 0.1 Hz,

⁶such as interferometer signal or stain meter signal along with the arms.

at least same level as that of the current seismometers.

In conclusion, the implemented IPsc suppresses the residual motion of the mirror and satisfies the requirement for the lock acquisition phase in the time-scale of 1 minute. If the lock-acquisition takes much longer than 1 minute, another displacement drift compensation system is necessary. Building such drift compensation system is beyond the scope of this work and will be done as a further improvement.

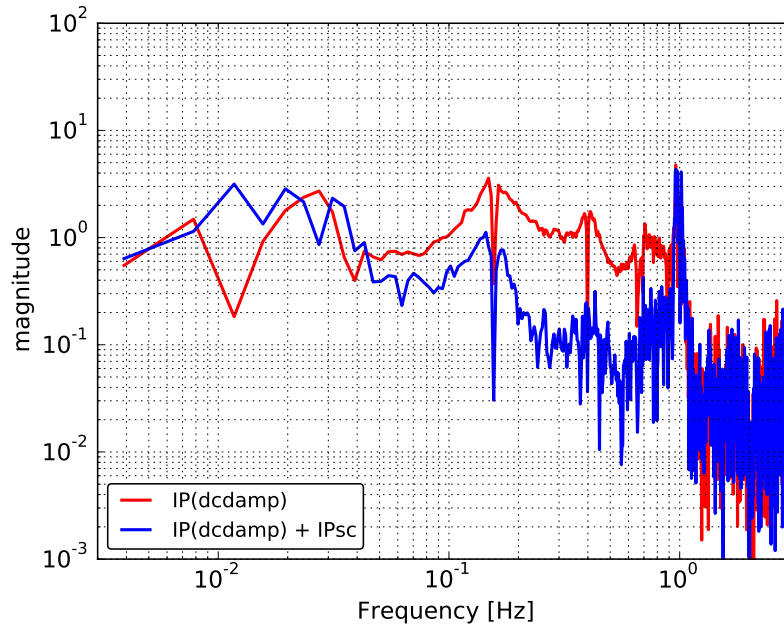


Figure 6.26: The measured displacement transfer function from the ground to the mirror in L dof. The colors show the difference of the configuration. At the frequency region higher than 1 Hz the sensor noise becomes dominant.

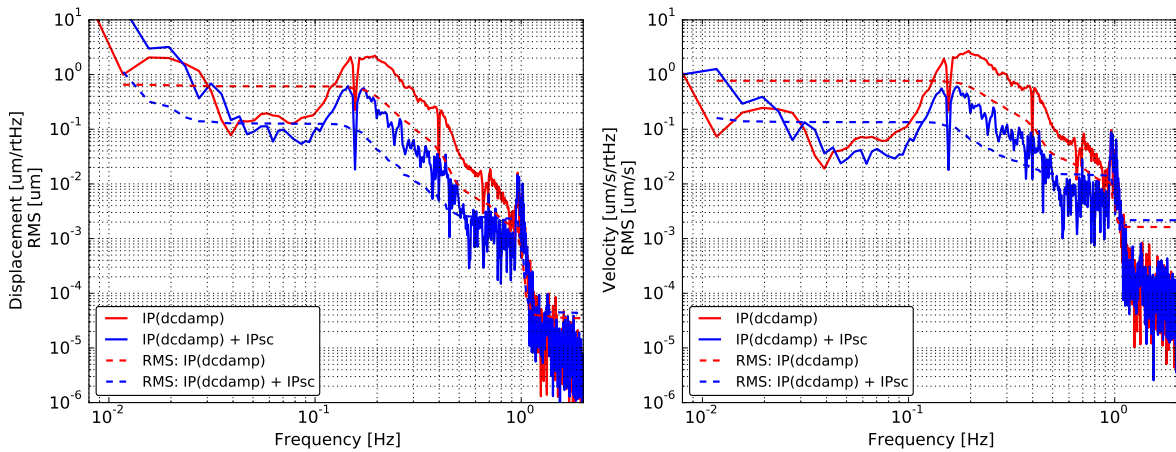


Figure 6.27: Comparison of the expected TM residual displacement (*left*) and TM velocity (*right*) in L dof when the IPsc is on and off. In this calculation 90 percentile ground motion is used.

6.5.3 Residual motion

Figure 6.28 shows the spectra of mirror residual motion in L, Pitch and Yaw dof, observed by the optical lever at the TM-stage. The TM motion in L dof is covered by the seismic motion and the spectrum does not show the TM motion. Instead the P and Y motion of the TM is measurable. The RMS angular motion in Pitch and Yaw dof is measured $0.20 \mu\text{rad}$ and $0.17 \mu\text{rad}$ respectively. The RMS of Pitch motion is on the requirement for the observation phase though, in the usual case, the requirement should be satisfied since this is measurement is done when the seismic motion level is high at around 50 mHz.

On the other hand, Figure 6.29 reports the spectra of the residual motion the IP-stage in T dof measured by the inertial sensor geophone and that of the BF-body in V dof measured by the displacement sensor LVDT. The residual RMS displacement of transverse IP-stage and vertical BF-body is measured at $0.3 \mu\text{m}$ and $0.13 \mu\text{m}$. Even though the suspension system does not have any sensors which can sense the T and V dof at the TM stage, however, the RMS will be limited by the upper part of the suspension. Assuming that the RMS displacements down to 10 mHz in these plots are the ones of TM, the requirement is satisfied. Even though the vertical spectra is measured when the seismic motion level is low, the RMS requirement will be also satisfied even if the amplitude increases by one order of magnitude (assuming that the ground moves as same level as the 90 percentile ground motion).

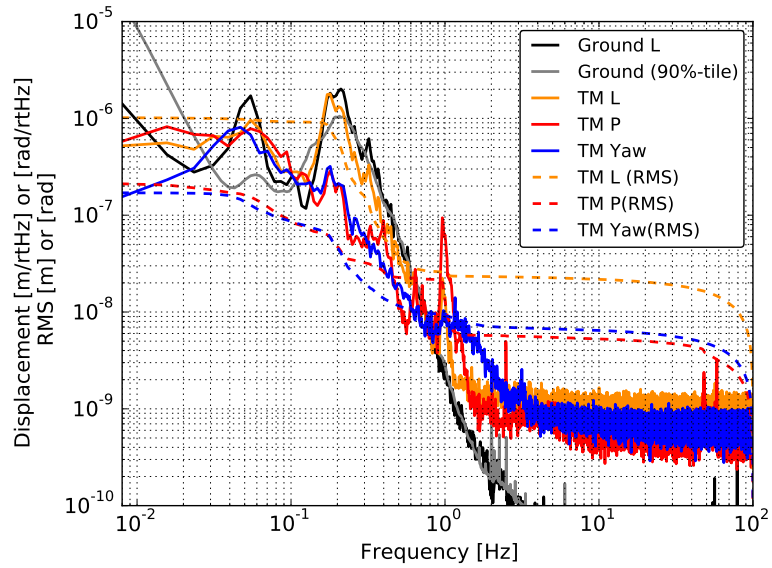


Figure 6.28: Spectra of mirror residual motion in L, Pitch and Yaw dof, observed by the optical lever at the TM-stage. The solid curves show the amplitude spectral density and the dashed ones indicate the amplitude in RMS.

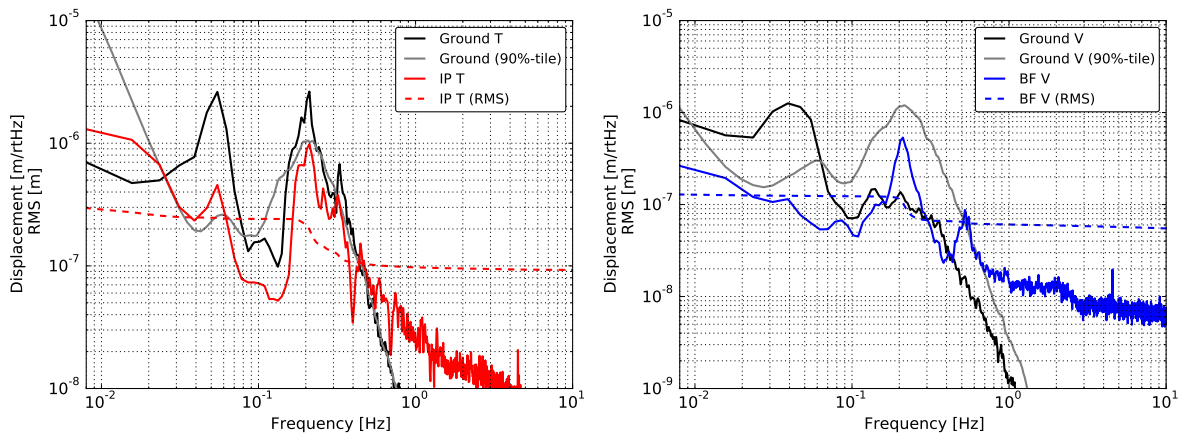


Figure 6.29: Spectra of residual motion the IP-stage in T dof measured by the inertial sensor geophone (*left*) and that of the BF-body in V dof measured by the displacement sensor LVDT (*right*)

6.6 Summary of the performance test

In this work we conduct the following tests for the evaluation of the suspension and its control system:

1. suspension mechanical response,
2. damping control performance for the calm-down phase,
3. RMS suppression control performance for the lock-acquisition phase.

Based on the first test, we conclude that the assembled Type-A suspension has the characteristics of the pendulum, although some of the unexpected resonances which would related to the heat link system are observed. From this issue, we find that we have to include the heat link system in the model of the suspension mechanics for the further precise estimation.

From the second test, we confirm that the installed damping control system satisfies its requirement for the lock-recovery mode.

The third test demonstrates the feedback control system using displacement sensors by a feed-forward system with seismometer on the ground effectively suppressed the mirror residual motion and it satisfies the requirement in the time scale of 1 min.

Conclusion and future works

7.1 Conclusion

7.1.1 Fast localization with heterogeneous detector network

We investigate the expected performance regarding fast sky localization of coalescing binaries with a network of three or four GW detectors having heterogeneous sensitivities, such as the LIGO-Virgo, LIGO-KAGRA and LIGO-Virgo-KAGRA network. A hierarchical approach can be used in order to make an effective use of information from the least sensitive detector. In this approach, the presence of an event seen in coincidence in the two more sensitive detectors triggers a focused search in the data of the third (and fourth), less sensitive, detector(s) with a lower SNR threshold.

Using MBTA and Bayestar, we show the expected fast localization performance for GWs from compact binary coalescence when a hierarchical search is implemented into a GW-EM follow-up pipeline. We confirm that the hierarchical search will improve both the localization accuracy and precision compared to those achieved by a double coincidence search with the two LIGO detectors alone. The hierarchical network effectively improves the localization accuracy and precision when threshold SNR for the lower sensitivity detector is set to around 3.5 provided that the BNS range of that the detector is greater than 20% of the more sensitive detectors in the case where the detector network is composed of the two LIGO detectors and the Virgo detector. In the case where the detector network is composed of the two LIGO detectors and KAGRA detector, we found a clear sky localization improvement when the relative sensitivity of KAGRA becomes greater than 20% of the more sensitive detectors. In addition, the hierarchical network by four detectors will improve the localization accuracy and precision when threshold SNR for the lowest sensitivity detector is set to around 3.5 provided that the BNS range of that the detector is greater than 30% of most sensitive detectors. This result assumes that the sensitivity of the middle sensitive Virgo detector is half of the LIGO one.

Consequently, we conclude that once the sensitivity of the third or fourth

detector reaches the required one, the search with this hierarchical approach will be most useful when adding new, less sensitive detectors to the network, as they are undergoing commissioning.

7.1.2 Type-A local suspension control

In this work we conduct the following tests for the evaluation of the suspension and its control system:

1. suspension mechanical response,
2. damping control performance for the calm-down phase,
3. RMS suppression control performance for the lock-acquisition phase.

The measured performance is summarized in Table 7.1.

Based on the first test, we conclude that the assembled Type-A suspension has the characteristics of the pendulum, although some of the unexpected resonances which would related to the heat link system are observed. From this issue, we find that we have to include the heat link system in the model of the suspension mechanics for the further precise estimation.

From the second test, we confirm that the installed damping control system satisfies its requirement for the lock-recovery mode.

The third test demonstrates the feedback control system using displacement sensors by a feed-forward system with seismometer on the ground effectively suppressed the mirror residual motion and it satisfies the requirement in the time scale of 1 min.

Consequently, we conclude that this work contributes to accomplishment of KAGRA suspension local control system toward the more robust operation.

Table 7.1: Requirements on the Type-A suspension control. The column labeled as ref. describes the section which explains the reason of the requirements. In this table, L, T, V, P and Y denote longitudinal, transverse, vertical, pitch and yaw.

Items	Requirements	Experimental results	ref.
The calm-down phase			
1/e decay time	< 1 min.	< 59 sec.	§ 6.4.2
RMS displacement (T, V)	< 0.1 mm	(0.3 μm , 0.13 μm)	§ 6.5.3
The lock acquisition phase			
RMS velocity (L)	< 2.0 $\mu\text{m}/\text{sec}$.	0.14 $\mu\text{m}/\text{s}$	§ 6.5.2
RMS angle (P, Y)	< 880 nrad	(200 nrad, 170 nrad)	§ 6.5.3
RMS displacement (L)	< 0.39 μm	0.23 μm	§ 6.5.2
RMS displacement (T, V)	< 0.1 mm		§ 6.5.3
The observation phase			
Control noise at 10 Hz (L)	< $8.0 \times 10^{-20} \text{ m}/\sqrt{\text{Hz}}$	not measured	
RMS displacement (L)	< 0.39 μm	0.23 μm	§ 6.5.2
RMS displacement (T, V)	< 0.1 mm	(0.3 μm , 0.13 μm)	§ 6.5.3
RMS angle (P, Y)	< 200 nrad	(200 nrad, 170 nrad)	§ 6.5.3

7.2 Future works

7.2.1 Type-A local suspension control

Mechanical suspension characterization

During this test we face on a fact that the model without the heat link system cannot fully explain the actual mechanical system, especially the BF motion in Y dof. The most possible origin is the heat link system. We have to include the heat link system in the model of the suspension mechanics for the further precise estimation.

In addition this work could not investigate the feature of the suspension system at frequencies above 4.2 Hz, where the heat link system can introduce external vibration from the inner shield of the cryostat. We have to confirm that the vibration induced by the actual heat link system satisfies the displacement requirement at 10 Hz.

Payload control

For the more robust operation, utilizing higher sensitive photo-sensors are demanded. The control system only with the optical levers is possible with the band-pass comb (BP-comb) filters. However, since it takes time for the tuning and maintain the BP-comb filters. Since the filters are much sensitive to the target resonant frequency and the mechanical resonant frequency can be shifted by the temperature change. The higher sensitive photo-sensors can reduce such work load.

Residual motion suppression control

In this work, a seismometer on the ground is used for the suppression control and we observe that the displacement residual at below 10 mHz enhanced due to the noise relate to the used seismometer. In order to avoid this, we should have inertial sensors which is sensitive enough at below 100 mHz.

Long-term tidal compensation

Even though the mirror displacement is suppressed locally with the sensor correction technique, the arm cavity drift related to the tidal deformation have to be compensated with the sensors which can sense the strain of the arm in order to keep the locked condition longer. This would be realised by sending the interferometer signal to the IP-stage actuators.

Chapter A

Supplemental note for study of fast localization

A.1 Typical parameters for data analysis

Effective distance

The effective distance D_{eff} is the distance of an optimally located and oriented source that would produce the same signal strength. The distance D_{eff} is defined as

$$D_{\text{eff}} = \frac{R}{\sqrt{\frac{1}{4}F_+^2(1 + \cos^2 \iota)^2 + F_\times^2 \cos^2 \iota}}, \quad (\text{A.1})$$

where R is the actual physical distance to the source, ι is the inclination angle of the source.

Horizontal distance

The horizontal distance R_{H} is the distance at which an optimally located and oriented source would produce a certain SNR ρ_0 in a detector. Usually, the ρ_0 is set at 8. The horizontal distance is defined by using sensitivity of a detector. Using an inner product is defined as:

$$(a|b) = 4\text{Re} \left[\int_0^\infty df \frac{\tilde{a}(f)\tilde{b}^*(f)}{S(|f|)} \right], \quad (\text{A.2})$$

the SNR of the detector ρ for a given signal h is calculated by

$$\rho^2(t) = (h|h). \quad (\text{A.3})$$

The corresponding detector sensitivity σ in dimension of length is expressed by

$$\sigma^2 = \rho^2 \times D_{\text{eff}}^2. \quad (\text{A.4})$$

The signal amplitude ρ is proportional to the D_{eff}^{-1} . Then, the horizontal distance, which is described as the effective distance at the SNR $\rho_0 = 8$, is described by

$$R_{\text{H}} = D_{\text{eff}}(\rho = \rho_0) = \frac{\sigma}{\rho_0} = \frac{\sigma}{8}. \quad (\text{A.5})$$

Detection range

The detection range R_{det} is the spherical radius, whose volume is equal to the volume surrounded by detection radius r_{det} . The detection radius r_{det} is the distance that the detector can sense the signals in each direction for an orientation of the source. The detection radius r_{det} is defined as

$$r_{\text{det}} = R_{\text{H}} \sqrt{\frac{1}{4} F_+^2 (1 + \cos^2 \iota)^2 + F_-^2 \cos^2 \iota}, \quad (\text{A.6})$$

where R_{H} is the horizontal distance. By using the detection radius r_{det} , the detection range R_{det} is obtained as follows.

$$\begin{aligned} R_{\text{det}}(\iota, \psi) &= \left(\frac{3}{4\pi} V(\iota, \psi) \right)^{1/3} \\ &= \left(\frac{3}{4\pi} \int_0^{r_{\text{det}}(\theta, \phi, \iota, \psi)} dr \int_0^\pi d\theta \int_0^{2\pi} d\phi r^2 \sin \theta \right)^{1/3} \\ &= \left(\frac{1}{4\pi} \int_0^\pi d\theta \int_0^{2\pi} d\phi (r_{\text{det}}(\theta, \phi, \iota, \psi))^3 \sin \theta \right)^{1/3}. \end{aligned} \quad (\text{A.7})$$

Relation between Horizontal distance and detection range

Due to the directional sensitivity or antenna pattern of the detectors, the detection range R_{det} is smaller than the horizontal distance R_{H} by a factor of 2.26, for the same SNR threshold[18, 59]. Then the relation is given by

$$\frac{R_{\text{H}}}{R_{\text{det}}} = 2.26. \quad (\text{A.8})$$

Expected SNR

The SNR of a detector is deduced from the detection range and the effective distance. By combining (A.4), (A.5), (A.8), the SNR ρ is given by

$$\rho = \frac{\sigma}{D_{\text{eff}}} = \frac{\rho_0 R_{\text{H}}}{D_{\text{eff}}} = \frac{\rho_0 \times 2.26 \times R_{\text{det}}}{D_{\text{eff}}} = \frac{8 \times 2.26 \times R_{\text{det}}}{D_{\text{eff}}}. \quad (\text{A.9})$$

A.2 Triggered event population

A.2.1 LIGO-Virgo network case

The population of the HL, HLV_i and HLV_n events are summarized in Figure A.1. In these plots, V_r denotes V_n triggers.

A.2.2 LIGO-KAGRA network case

The population of the HL, HLK_i and HLK_n events are summarized in Figure A.2. In these plots, K_r denotes K_n triggers.

A.2.3 LIGO-Virgo-KAGRA network case

The population of the HL, HLV_i , HLV_n , HLK_i , HLK_n , HLV_iK_i , HLV_nK_i , HLV_nK_i and HLV_nK_n events are summarized in Figure A.3 to A.8. In these plots, V_r and K_r denote V_n and K_n triggers respectively.

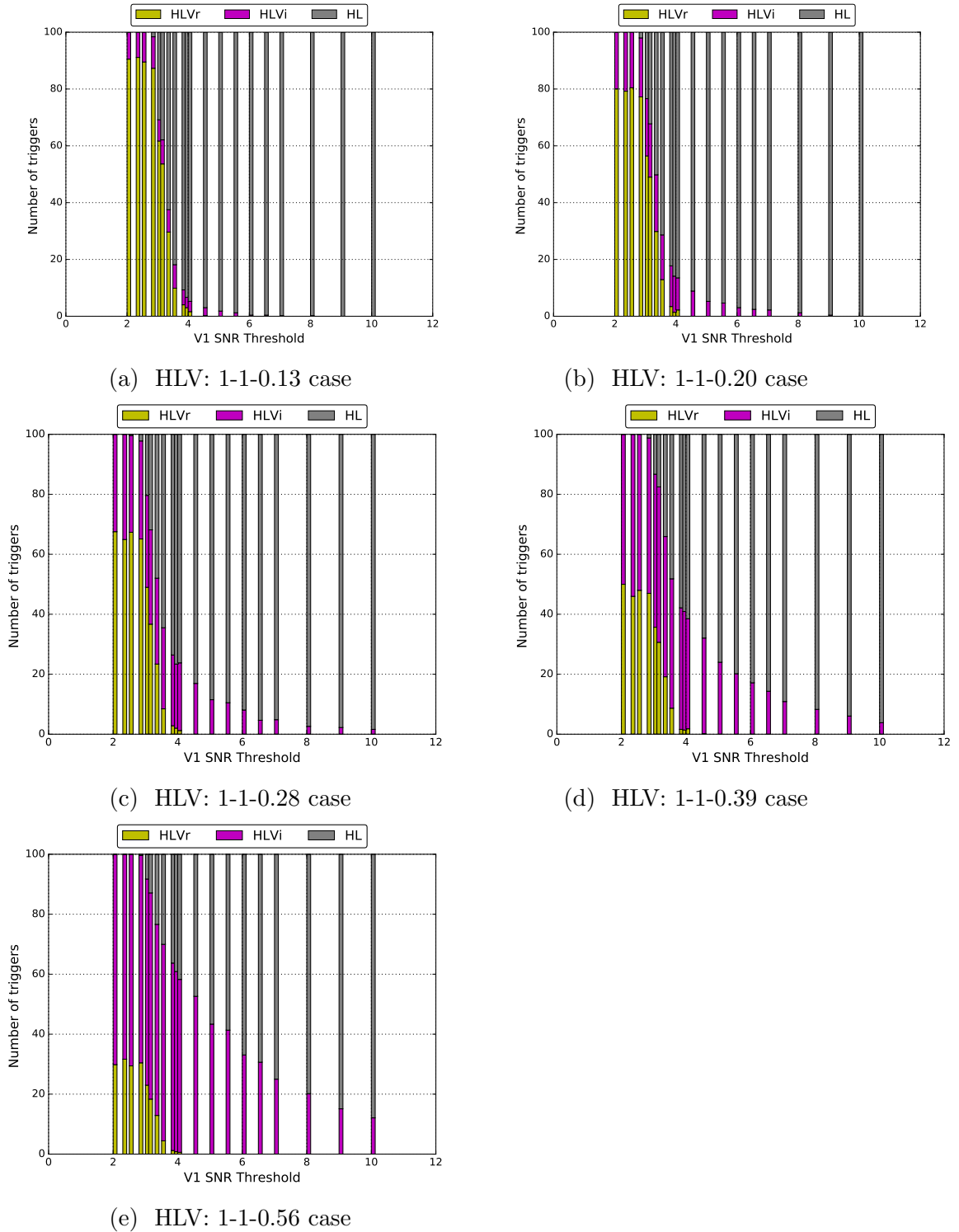


Figure A.1: The trigger population, HL, HLVi and HLVR events, in percentage with LIGO-Virgo network. The relative detector sensitivities are written down as 1-1- x , with x the ratio of the Virgo sensitivity compared to the two LIGO detectors.

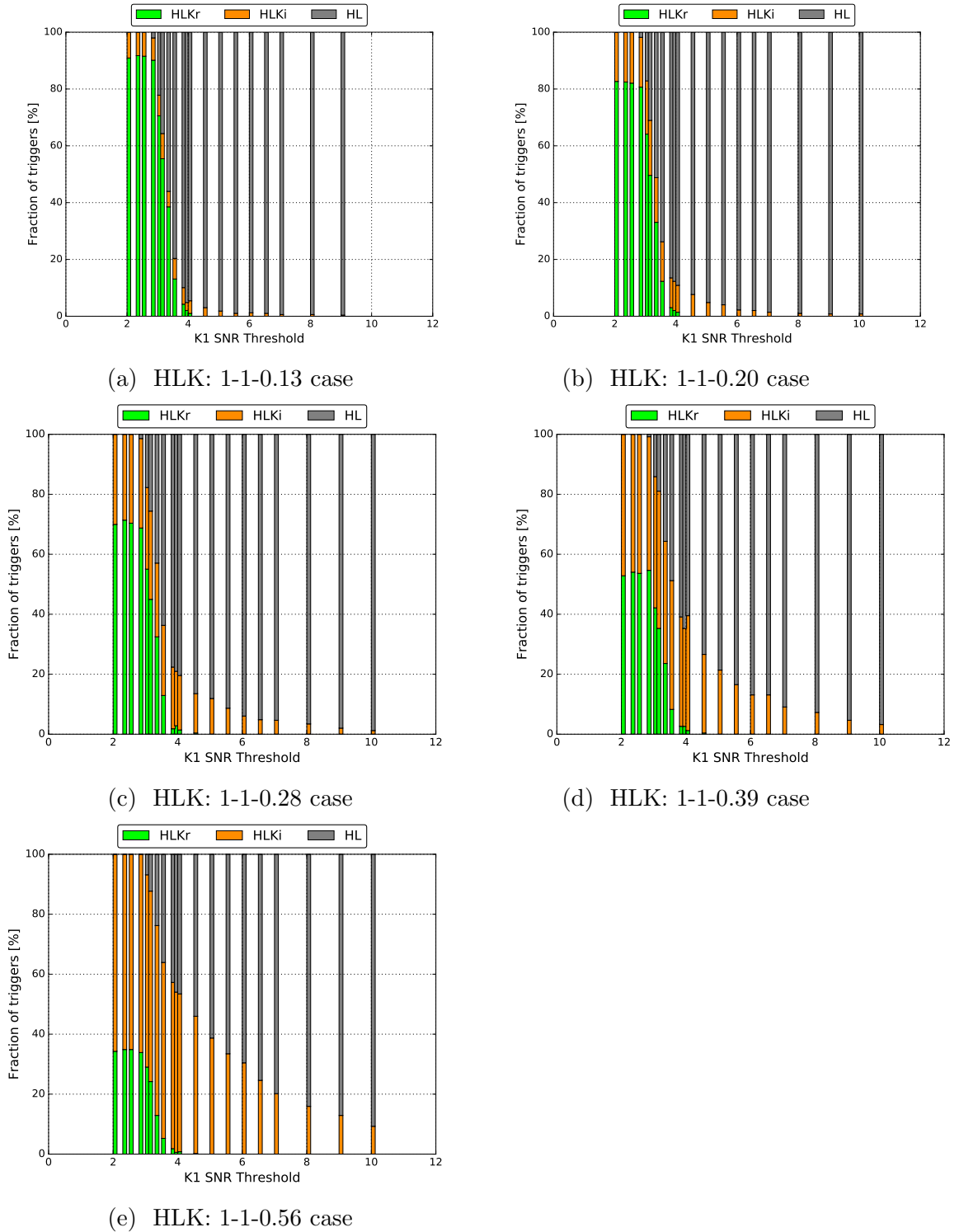
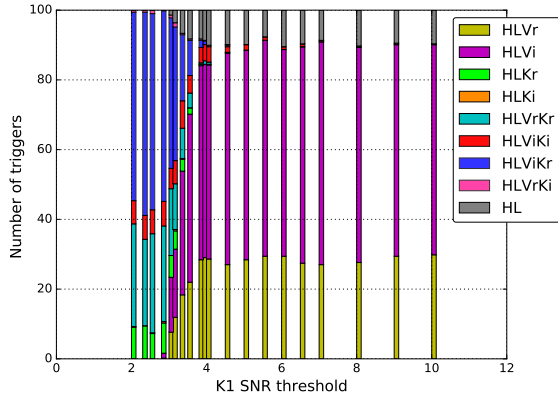
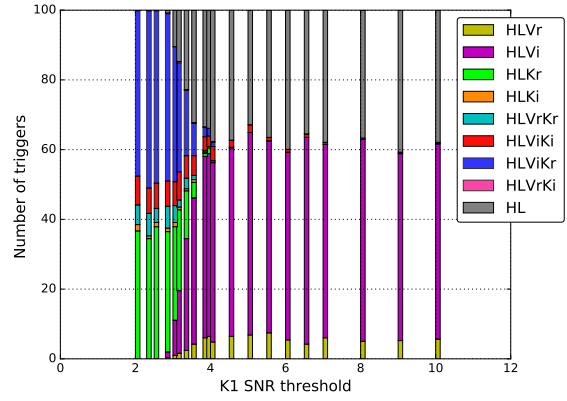


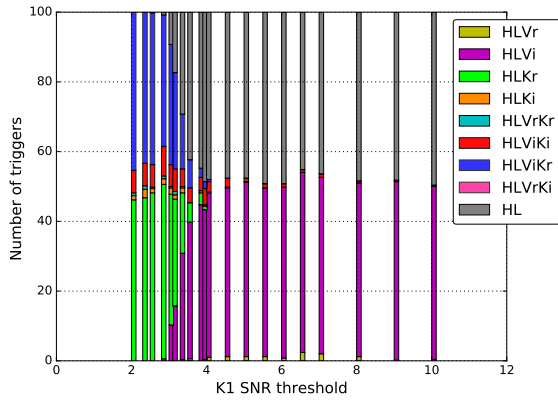
Figure A.2: The trigger population, HL, HLK_i and HLK_r events, in percentage with LIGO-KAGRA network. The relative detector sensitivities are written down as 1-1- x , with x the ratio of the KAGRA sensitivity compared to the two LIGO detectors.



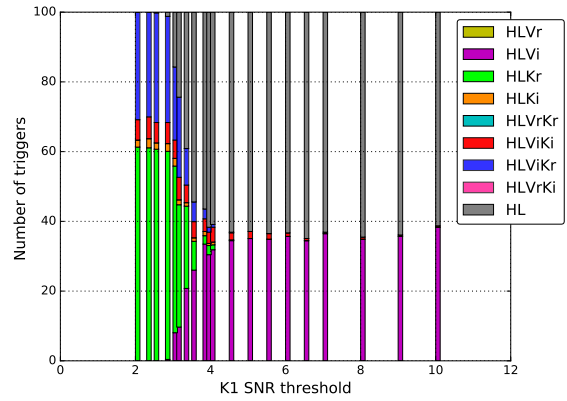
(a) SNR threshold for HL: 5-5-3.0 case



(b) SNR threshold for HL: 5-5-3.5 case

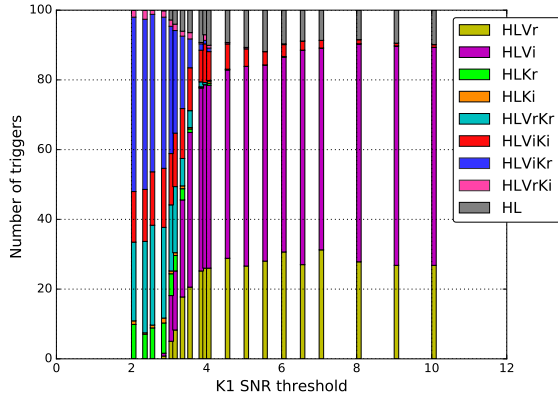


(c) SNR threshold for HL: 5-5-4.0 case

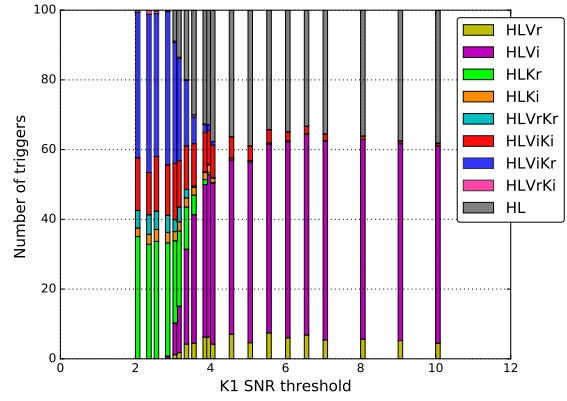


(d) SNR threshold for HL: 5-5-5.0 case

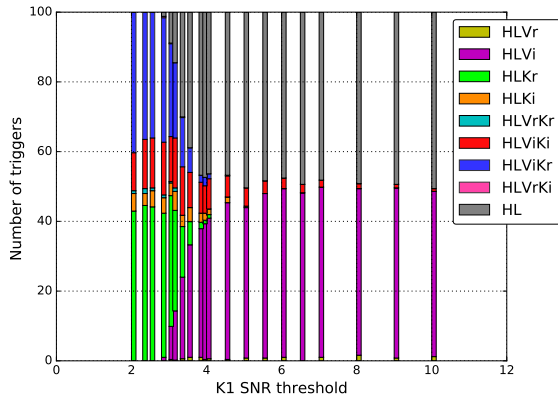
Figure A.3: The trigger population in percentage with LIGO-Virgo-KAGRA network, where the relative detector sensitivities are set to HLVK: 1-1-0.5-0.13, with the ratio of the Virgo and KAGRA sensitivities compared to the two LIGO detectors.



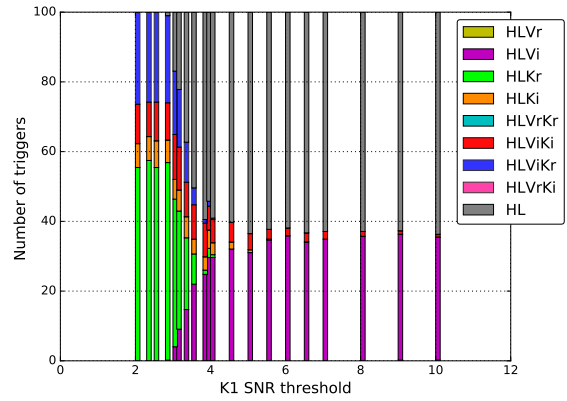
(a) SNR threshold for HLV: 5-5-3.0 case



(b) SNR threshold for HLV: 5-5-3.5 case

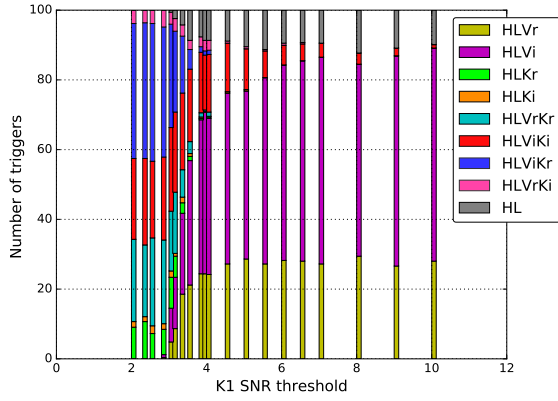


(c) SNR threshold for HLV: 5-5-4.0 case

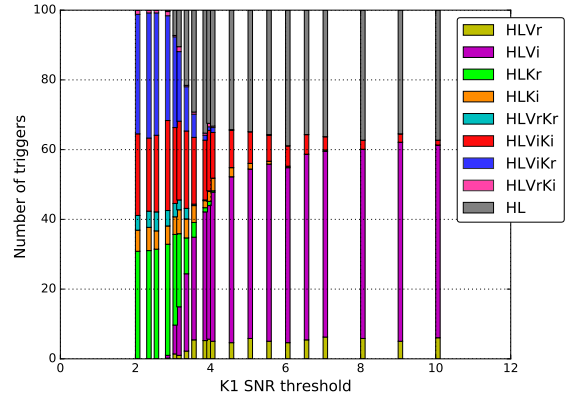


(d) SNR threshold for HLV: 5-5-5.0 case

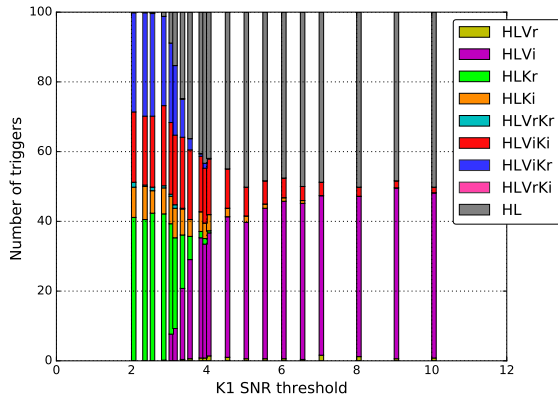
Figure A.4: The trigger population in percentage with LIGO-Virgo-KAGRA network, where the relative detector sensitivities are set to HLVK: 1-1-0.5-0.20, with the ratio of the Virgo and KAGRA sensitivities compared to the two LIGO detectors.



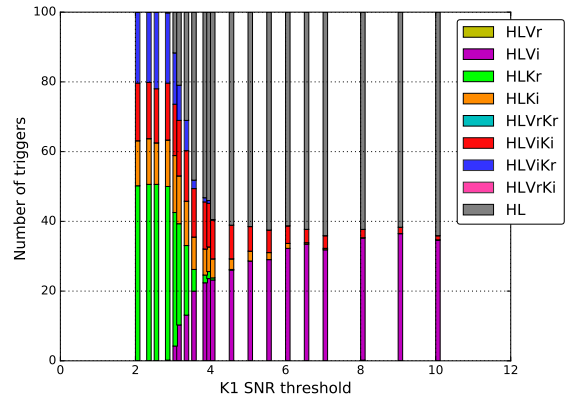
(a) SNR threshold for HLV: 5-5-3.0 case



(b) SNR threshold for HLV: 5-5-3.5 case

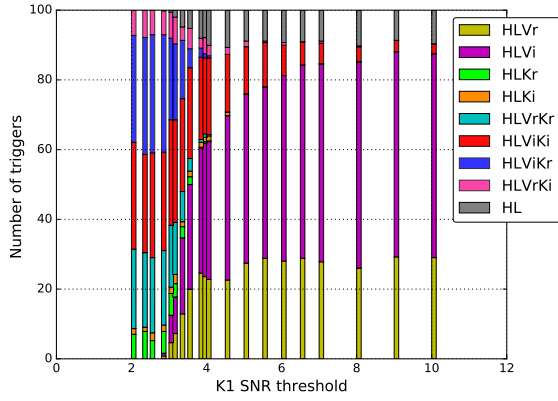


(c) SNR threshold for HLV: 5-5-4.0 case

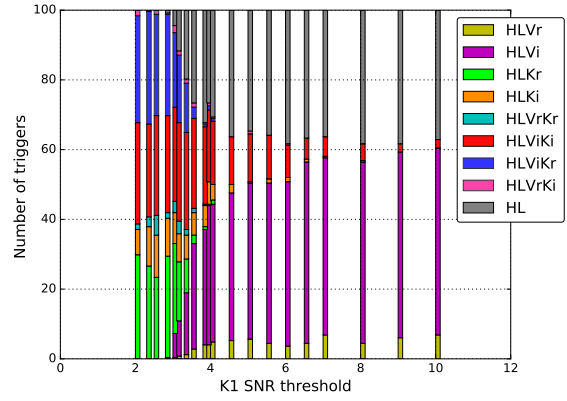


(d) SNR threshold for HLV: 5-5-5.0 case

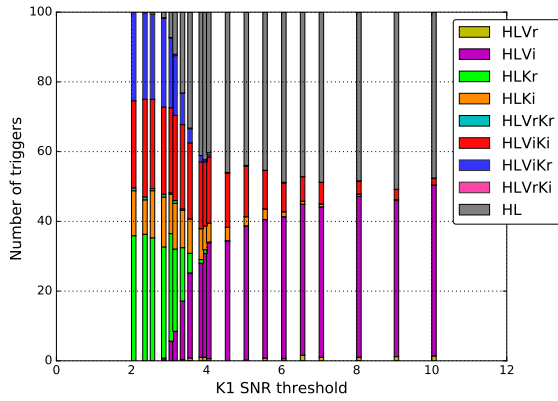
Figure A.5: The trigger population in percentage with LIGO-Virgo-KAGRA network, where the relative detector sensitivities are set to HLVK: 1-1-0.5-0.28, with the ratio of the Virgo and KAGRA sensitivities compared to the two LIGO detectors.



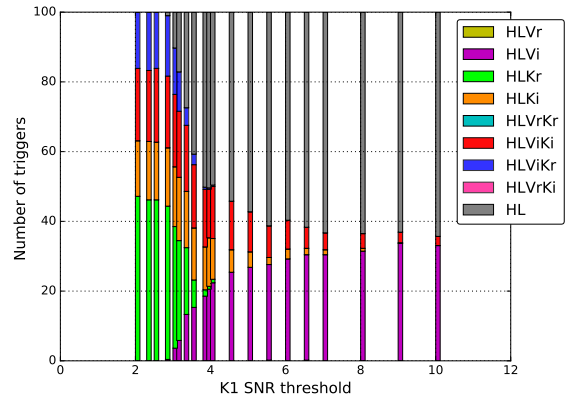
(a) SNR threshold for HLV: 5-5-3.0 case



(b) SNR threshold for HLV: 5-5-3.5 case

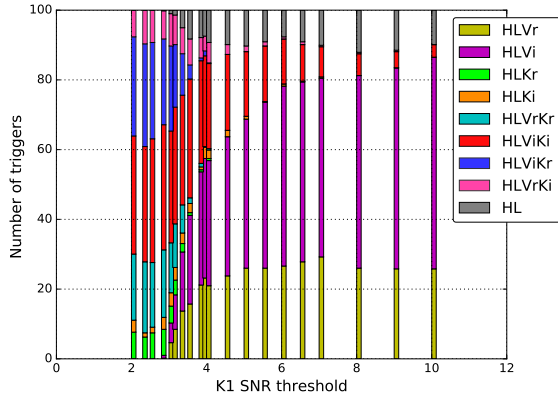


(c) SNR threshold for HLV: 5-5-4.0 case

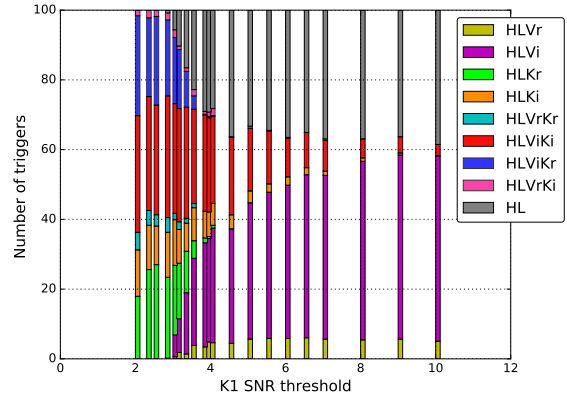


(d) SNR threshold for HLV: 5-5-5.0 case

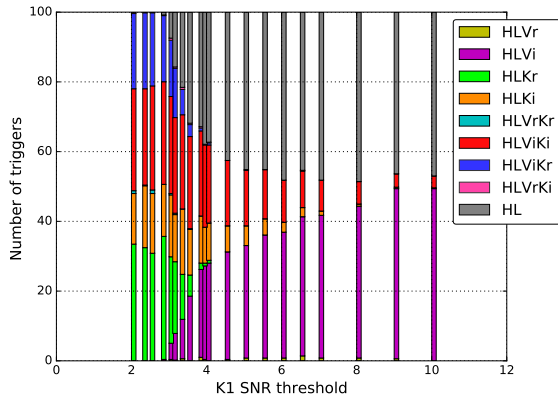
Figure A.6: The trigger population in percentage with LIGO-Virgo-KAGRA network, where the relative detector sensitivities are set to HLVK: 1-1-0.5-0.33, with the ratio of the Virgo and KAGRA sensitivities compared to the two LIGO detectors.



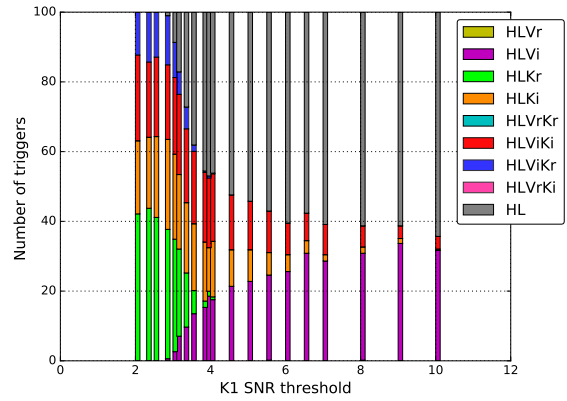
(a) SNR threshold for HLv: 5-5-3.0 case



(b) SNR threshold for HLv: 5-5-3.5 case

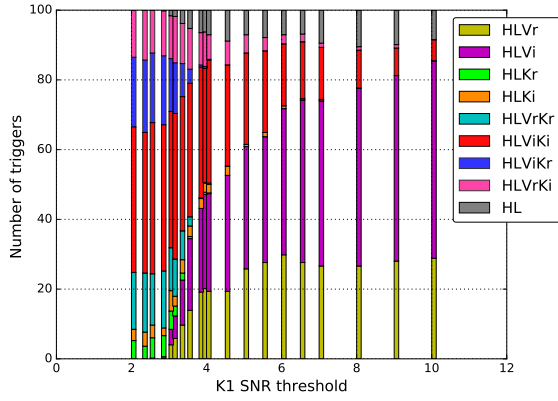


(c) SNR threshold for HLv: 5-5-4.0 case

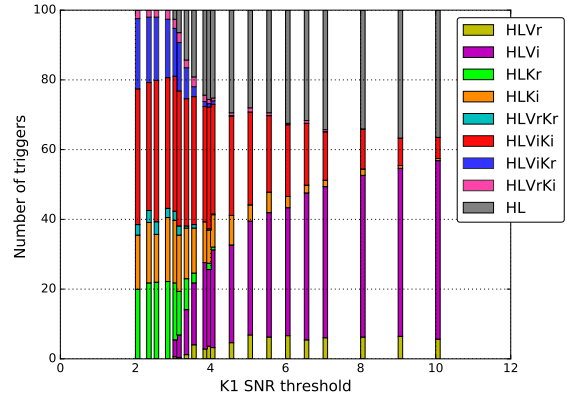


(d) SNR threshold for HLv: 5-5-5.0 case

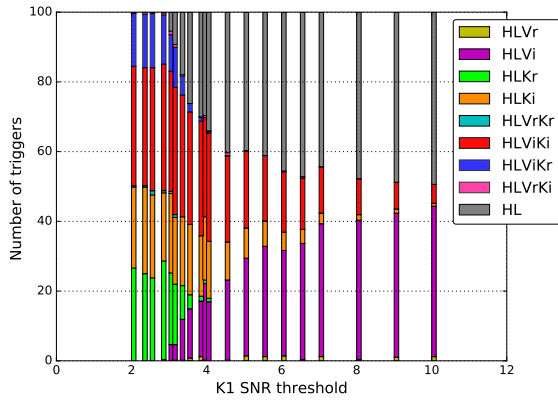
Figure A.7: The trigger population in percentage with LIGO-Virgo-KAGRA network, where the relative detector sensitivities are set to HLvK: 1-1-0.5-0.39, with the ratio of the Virgo and KAGRA sensitivities compared to the two LIGO detectors.



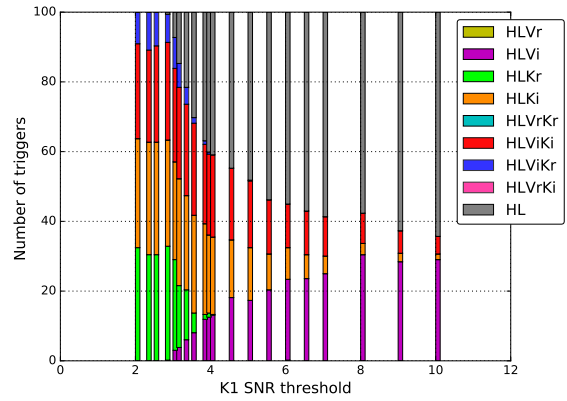
(a) SNR threshold for HLv: 5-5-3.0 case



(b) SNR threshold for HLv: 5-5-3.5 case



(c) SNR threshold for HLv: 5-5-4.0 case



(d) SNR threshold for HLv: 5-5-5.0 case

Figure A.8: The trigger population in percentage with LIGO-Virgo-KAGRA network, where the relative detector sensitivities are set to HLvK: 1-1-0.5-0.5, with the ratio of the Virgo and KAGRA sensitivities compared to the two LIGO detectors.

A.2.4 Dependence on the sensitivity of the fourth detector KAGRA with different SNR thresholds in Virgo

The expected performances of the searched area and the 90% confidence area with different SNR thresholds in Virgo are summarized in this subsection. Figure A.9 and A.10 are the case where the SNR threshold for Virgo is set to 4.0, while Figure A.11 and A.12 are the case where it is set to 3.0.

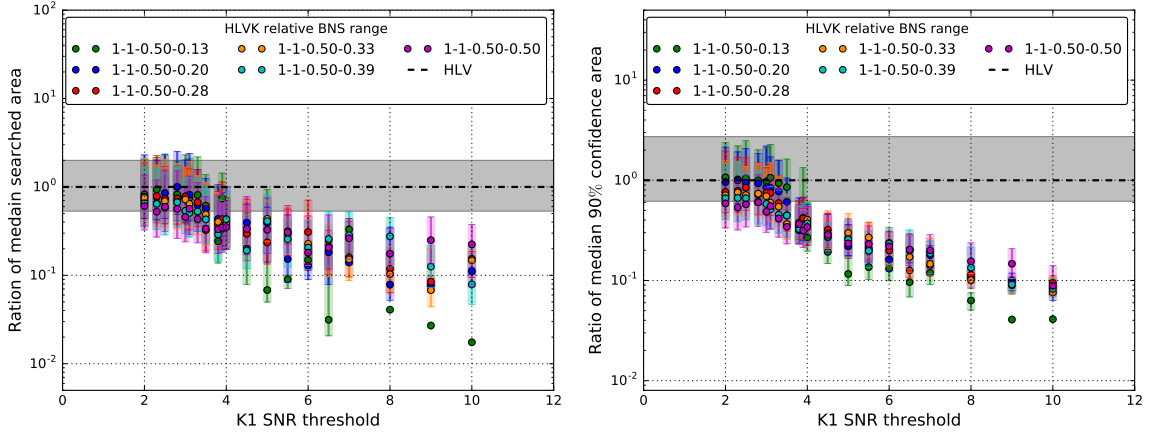


Figure A.9: Ratio of the median searched area (*left*) and 90% confidence area (*right*) of HLVK triggers to that of the same triggers treated as HLV coincidences, when the sensitivity of the KAGRA detector is varied. The colors show the network configuration. This is the case where the sub-threshold for Virgo is to 4.0.

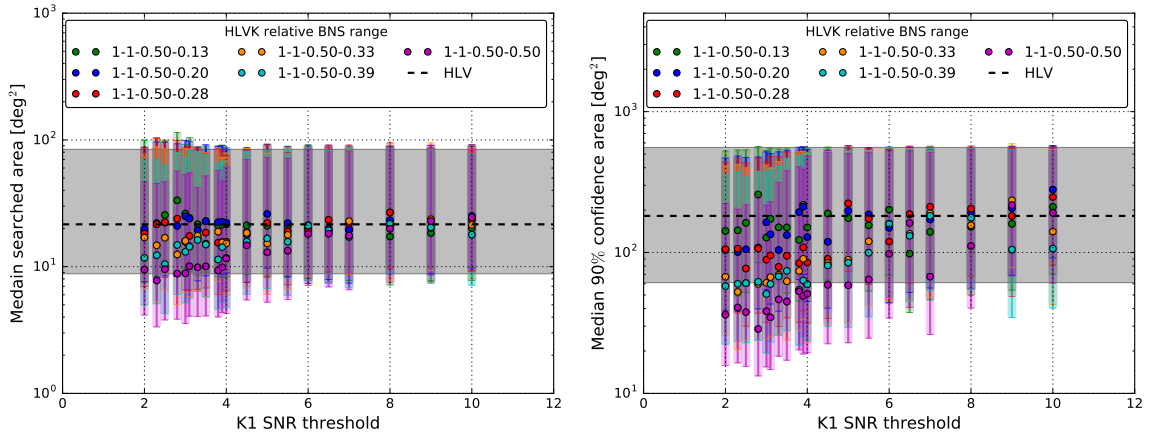


Figure A.10: The median searched area (*left*) and 90% confidence area (*right*) are shown as a function of the SNR threshold used in KAGRA. Expected sky localization performance with the hierarchical search when the sensitivity of the KAGRA detector is varied. The colors show the network configuration. This is the case where the sub-threshold for Virgo is to 4.0.

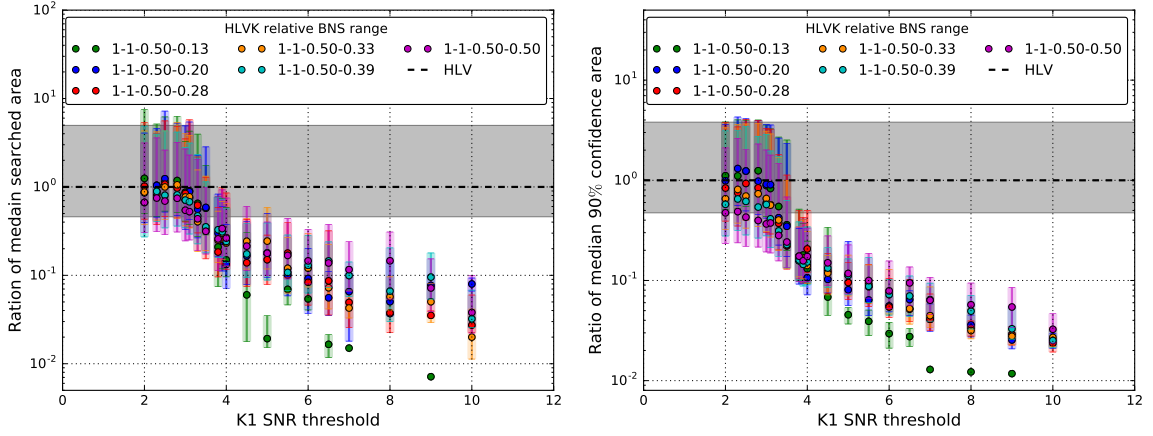


Figure A.11: Ratio of the median searched area (*left*) and 90% confidence area (*right*) of HLVK triggers to that of the same triggers treated as HLV coincidences, when the sensitivity of the KAGRA detector is varied. The colors show the network configuration. This is the case where the sub-threshold for Virgo is to 3.0.

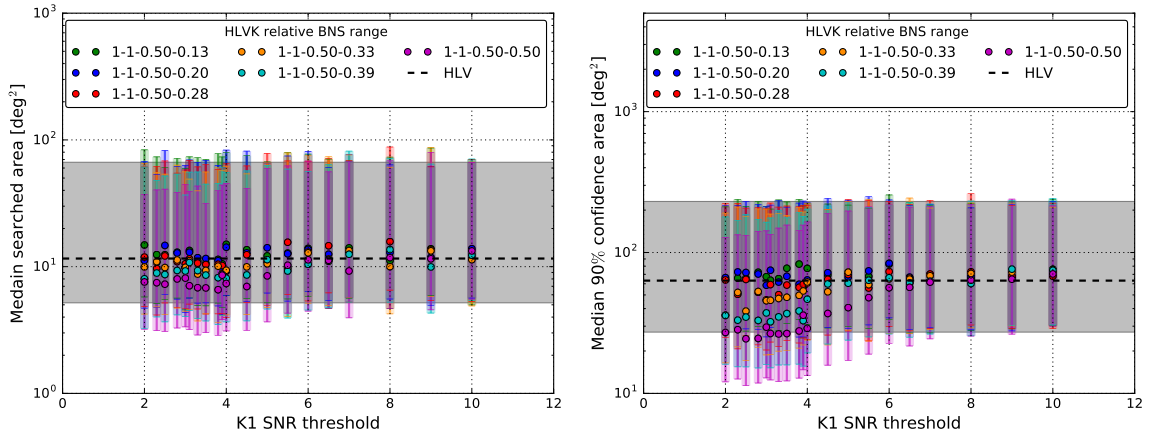


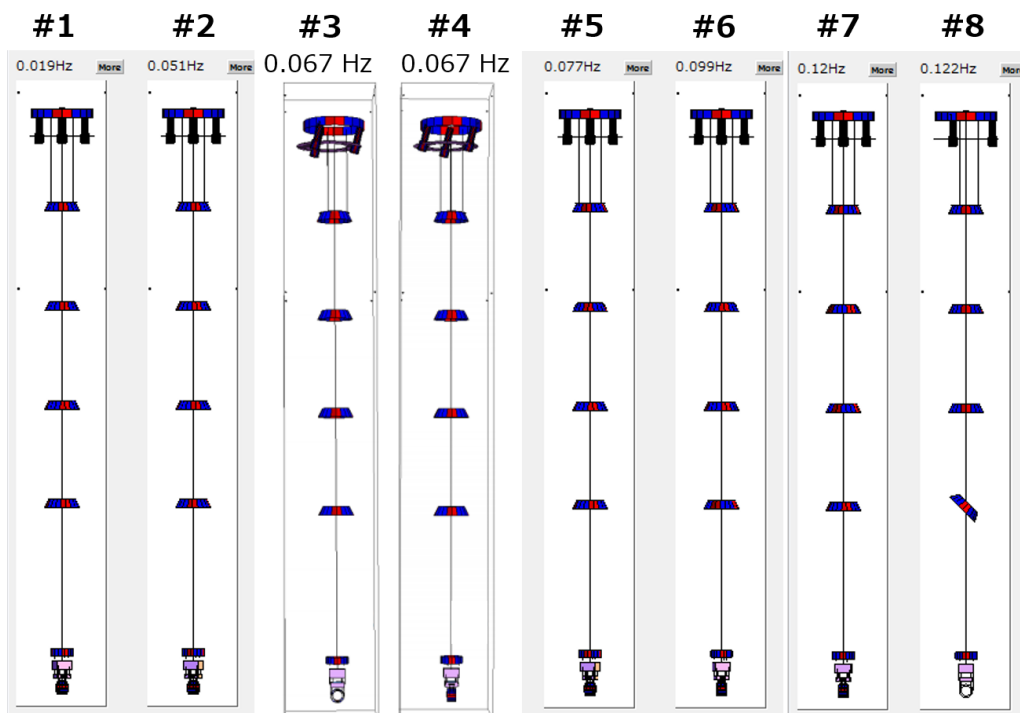
Figure A.12: The median searched area (*left*) and 90% confidence area (*right*) are shown as a function of the SNR threshold used in KAGRA. Expected sky localization performance with the hierarchical search when the sensitivity of the KAGRA detector is varied. The colors show the network configuration. This is the case where the sub-threshold for Virgo is to 3.0.

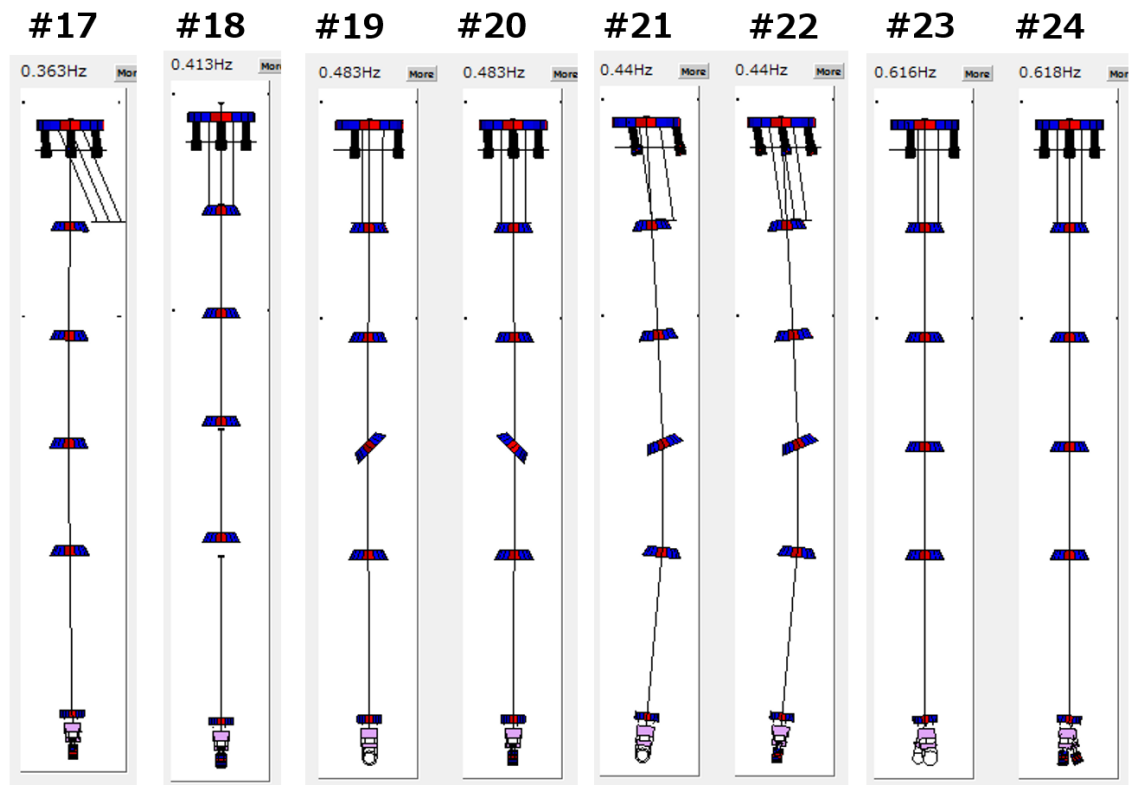
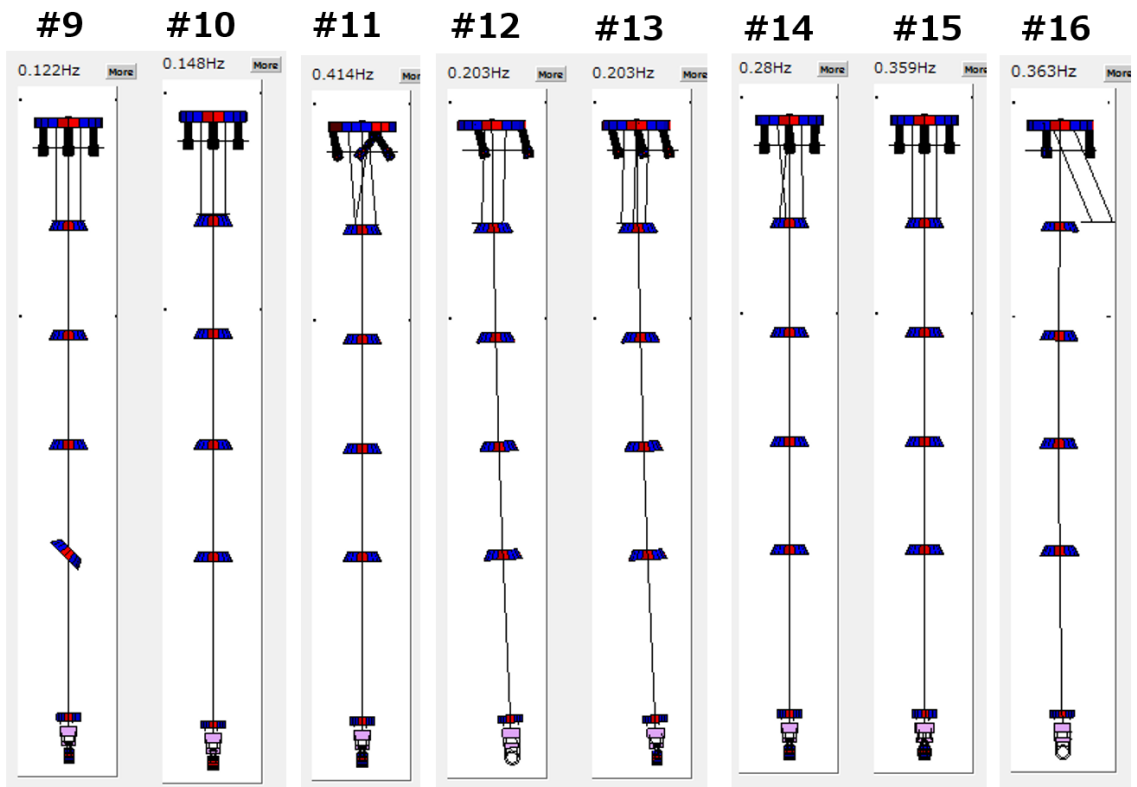
Chapter B

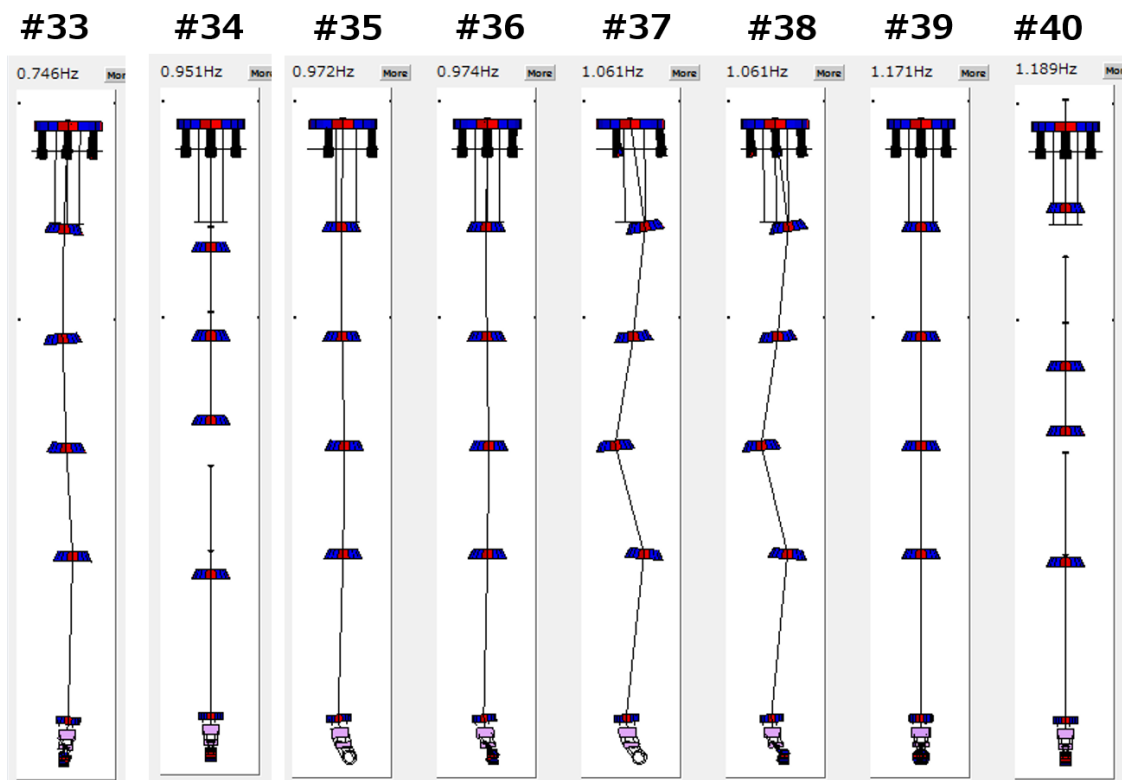
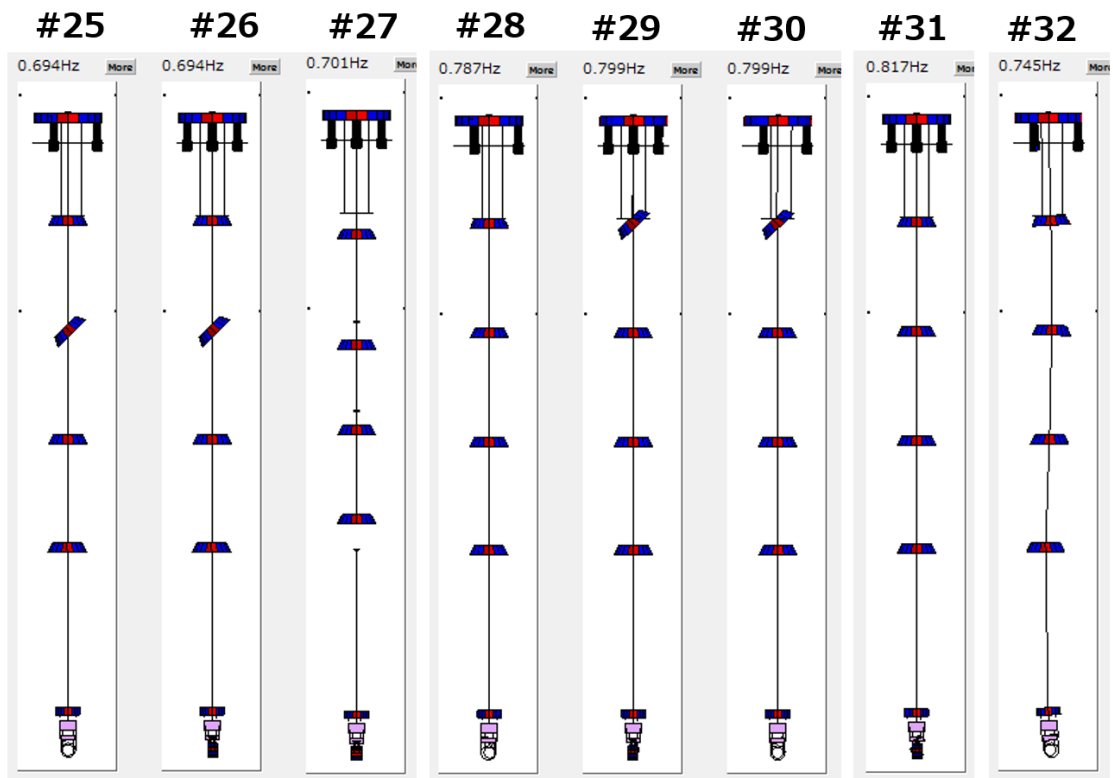
Detailed characteristics of Type-A suspension

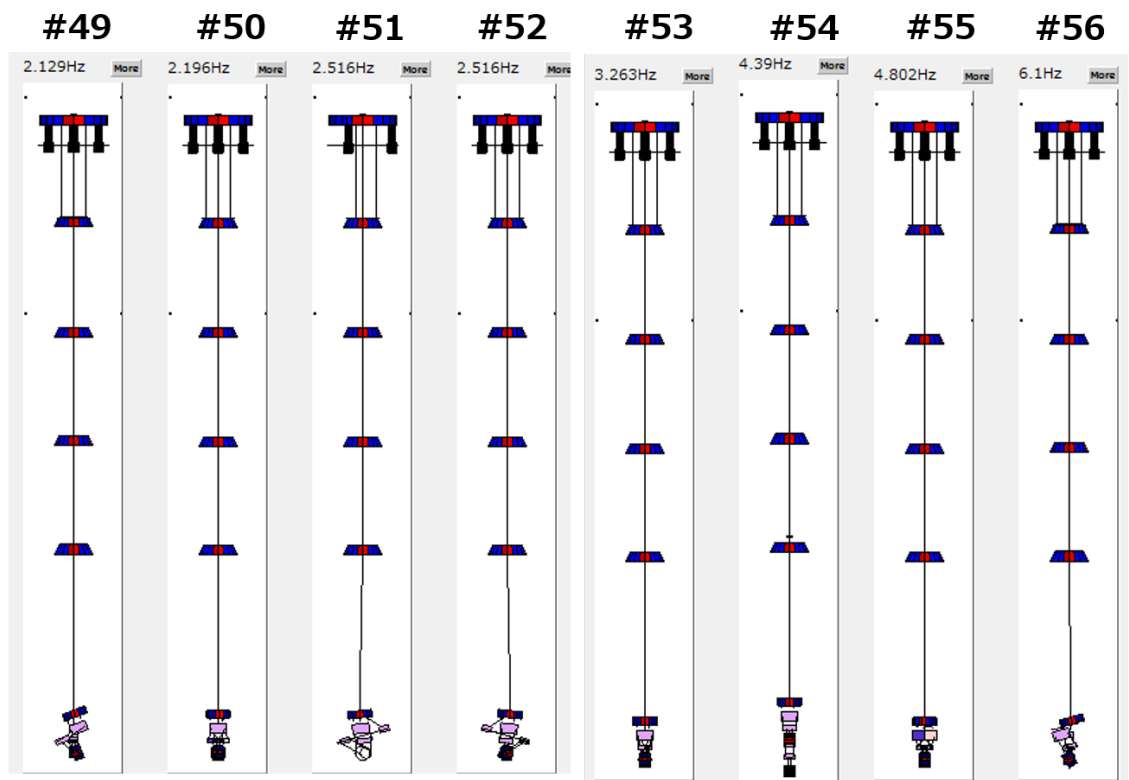
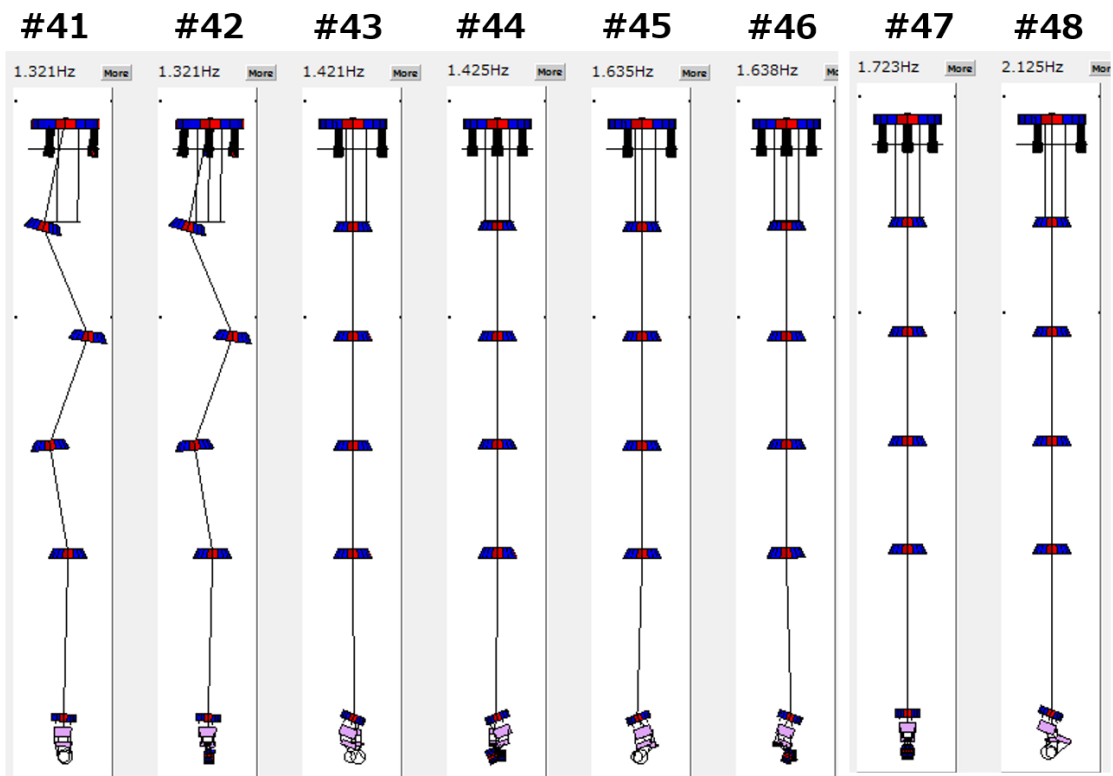
B.1 Simulated eigen mode list of Type-A suspension

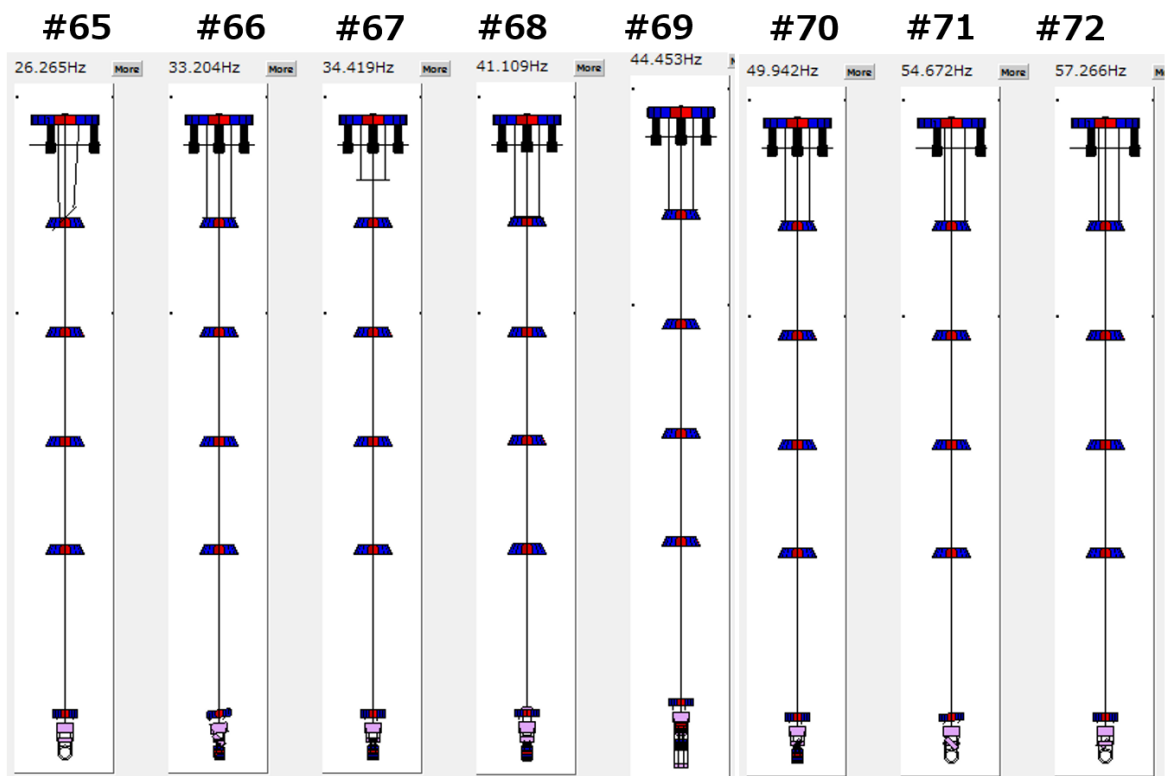
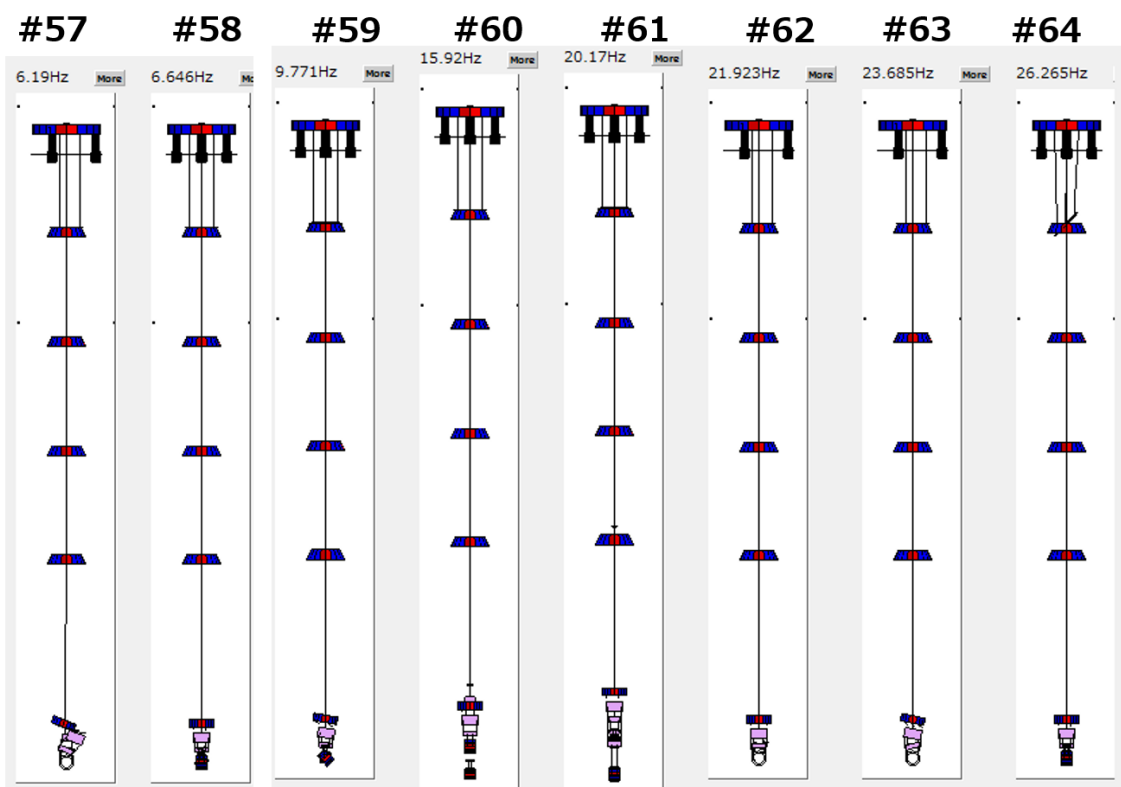
The eigen mode shapes of the designed Type-A suspension is listed here.

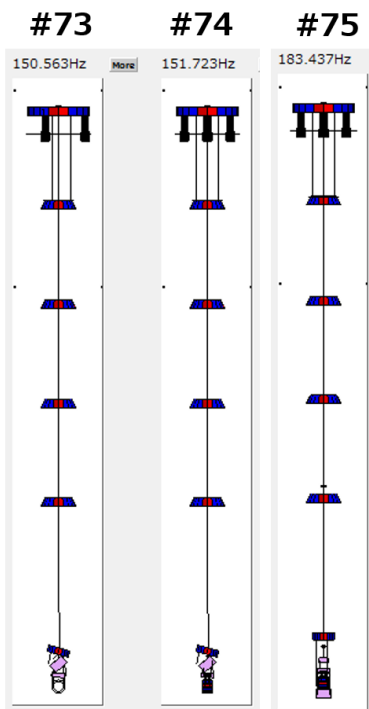












B.2 Type-A suspension configuration during the measurement

During the measurement period, we had to face on a situation where at least on GAS filter is mechanically stacked or locked in all the Type-A suspensions. Concerning ETMY suspension, we found that second and third GAS stages seemed to be mechanically stacked with same reason as the issue of ETMX F2-GAS filter. For the two input suspensions, we had to intentionally lock the first GAS filter (called F0-GAS) keystone in order to hold the other suspension components, especially the mirror, at the target height¹. For all these suspensions we decided to keep using them with such configuration for the O3 period. Figure B.7 shows the expected mechanical seismic attenuation performance where one or two GAS stage are not working as spring, assuming the vertical mirror vibration couples to the longitudinal dof by 1%.

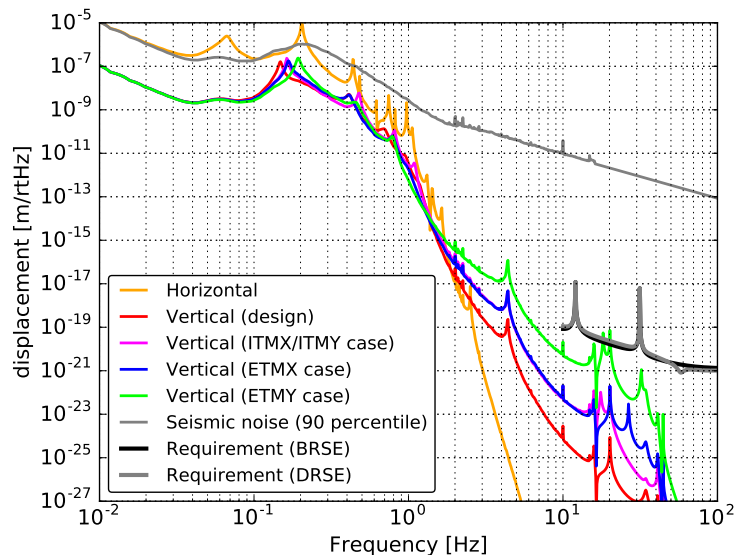


Figure B.7: Expected mechanical seismic attenuation performance where one or two GAS stage are not working as spring, assuming the vertical mirror vibration couples to the longitudinal dof by 1%.

¹This issue has the following history: we originally had GAS blades made in abroad which would suspend the mirror properly. We then found that the original blade was actually broken, cracked because of hydrogen embrittlement in Maraging steels [60]. We remade and replaced the blades with the new ones made in Japan, we finally found that the newly made GAS blades were too weak to hold the whole suspension at the desired height.

B.3 Axis difference among the X-arm cavity and X-arm suspensions

As a preparation of the transfer function measurement with the FPMI signals, which is called DARM, the difference of the X-arm cavity axis and the local sensor axes of the X-arm suspension is investigated. The angle offset is estimated by comparing two displacement transfer functions at 10 mHz; one is from longitudinal vibration of the mass to the X-arm displacement signal, and the other one is from transverse vibration of the mass to the X-arm displacement signal. For example, for the IP-stage case, the angle offset θ is obtained by

$$\theta = \arctan\left(\frac{X_{\text{arm}}}{IP_{\text{T}}}\bigg/\frac{X_{\text{arm}}}{IP_{\text{L}}}\right). \quad (\text{B.1})$$

During this measurement, the X-arm cavity was locked with IR laser and the displacement signal is reconstructed from its control signal. The estimated angle offset is summarized in Figure B.8. The angle offset from the X-arm cavity axis to the longitudinal axis of the ITMX-IP and ETMX-IP is obtained as 8.2 deg and 5.0 deg. This implies that the ITMX-IP motion and ETMX-IP motion in L dof couples to the motion in the orthogonal axis of X-arm cavity axis by 1% and 0.4% respectively.

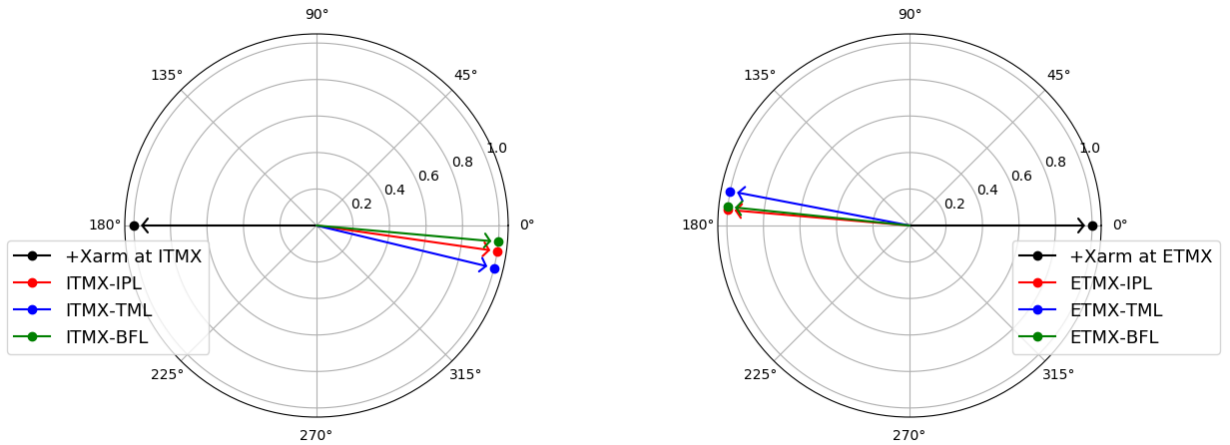


Figure B.8: Estimated angle offset of X-arm suspensions compared to the X-arm cavity axis.

B.4 Position dependence of LVDT noise floor

The sensor noise floor of the LVDT at several point inside its linear range is measured as illustrated in Figure B.9 and B.10. This reports that of the primary coil is much close to the secondary one (at the edge of the linear range), the noise floor can be enhanced by factor of 10 in the current system.

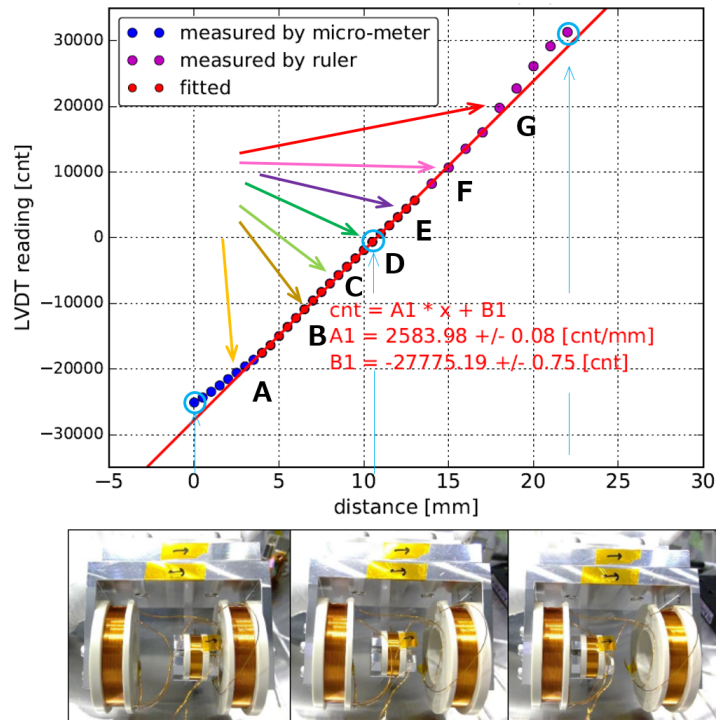


Figure B.9: A LVDT calibration curve. The noise floor is measured at the points which are denoted by the alphabets from A to B.

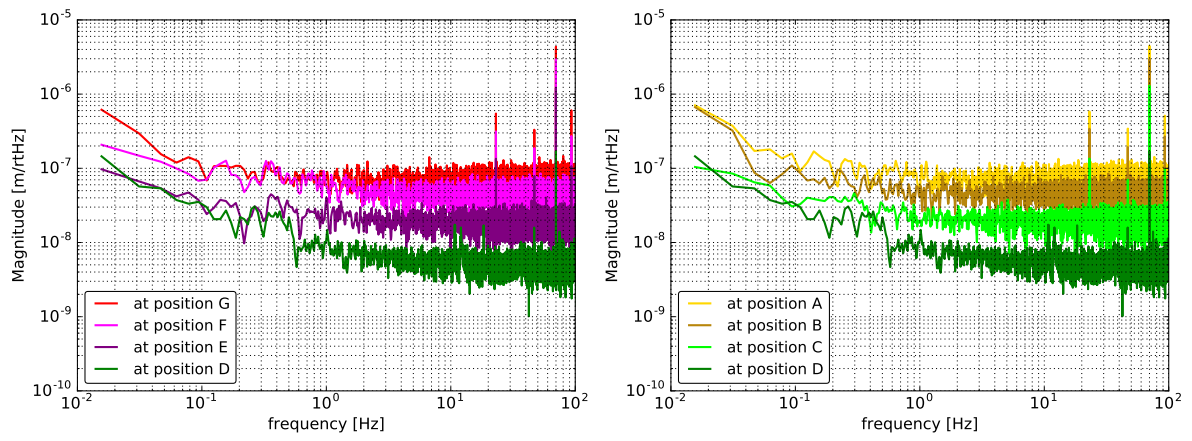


Figure B.10: LVDT sensor noise floors measured at the points shown in Figure B.9.

B.5 Measured decay time constant table

The measured resonant frequencies and the decay time constants are listed in Figure B.11 and B.12. The yellow colored modes are the ones which we pay less attention, while the red colored one is the mode which is not found in this work. The mode numbers correspond to ones in section B.1. Standard deviations are removed from the below figures however, they are included in Figure 6.4.2.

mode number	fitted frequency[Hz]	decay time [s]	excitation point
#1	0.04	233.6	BFY
#2	0.07	193.2	BFY
#3	0.08	83.9	IPT
#4	0.08	100.9	IPL
#5	0.09	116.0	BFY
#6	0.09	174.1	BFY
#7	0.12	191.8	MNoplevY
#8			
#9			
#10	0.19	48.1	F0GAS
#11	0.42	49.1	IPY
#12	0.21	233.1	IPT
#13	0.21	111.5	IPL
#14			
#15	0.32	726.6	IMY
#16			
#17			
#18	0.47	14.7	F0GAS
#19			
#20			
#21	0.45	152.0	IPT
#22	0.45	169.3	IPL
#23	0.63	671.4	MNR
#24	0.63	982.3	MNR
#25			
#26			
#27	0.76	8.9	F3GAS
#28	0.75	316.9	IPT
#29	0.79	73.3	MNP
#30	0.79	177.2	MNR
#31	0.75	157.7	MNR
#32	0.72	268.8	IPT
#33	0.73	328.7	IPL
#34	0.94	9.5	F1GAS
#35	0.97	167.6	IPT
#36	0.98	42.6	IPL
#37	1.03	51.4	IPT
#38	1.04	24.7	IPL
#39	1.15	811.7	MNY
#40	1.31	8.0	F1GAS
#41	1.34	2.9	IPT
#42	1.31	26.3	IPL
#43	1.48	288.2	MNR
#44	1.52	488.6	MNP
#45	1.71	365.9	MNP
#46	1.67	615.8	MNP
#47	1.68	2201.1	MNY
#48	2.16	192.2	MNT
#49	2.16	176.6	MNL
#50	2.12	555.2	MNY
#51	2.49	845.5	MNT
#52	2.49	1241.0	MNL
#53	3.20	2552.2	MNY
#54			
#55	4.14	44.6	MNY
#56	5.20	42.2	MNT
#57	5.09	61.3	MNL
#58	7.52	172.9	MNP
#59	9.70	86.9	BFGAS
#60	15.05	38.6	MNR
#61	19.39	49.6	BFGAS
#62	22.89	1.1	MNR
#63	23.49	134.9	MNR
#64			
#65			
#66			
#67			
#68			
#69			
#70			
#71			
#72			
#73			
#74			
#75			
NOT_IDed	0.14	329.6	MNoplevY

Figure B.11: Measured decay time constants without controls.

mode number	fitted frequency[Hz]	decay time [s]	excititon point
#1	0.05	47.1	BFY
#2	0.08	36.6	BFY
#3	0.15	18.8	IPT
#4	0.15	10.6	IPL
#5	0.08	42.9	BFY
#6	0.09	37.9	BFY
#7	0.13	7.2	BFY
#8			
#9			
#10	0.18	4.2	F0GAS
#11	0.48	1.4	IPY
#12	0.25	2.0	IPT
#13	0.22	2.6	IPL
#14			
#15	0.23	1.3	MNY
#16			
#17			
#18	0.50	2.9	F0GAS
#19			
#20			
#21	0.46	4.2	IPT
#22	0.45	4.9	IPL
#23	0.61	10.2	MNR
#24	0.64	20.1	MNP
#25			
#26			
#27	0.82	5.1	F3GAS
#28	0.71	17.2	MNR
#29	0.71	3.2	MNP
#30	0.81	12.4	MNR
#31	0.79	6.5	MNP
#32	0.70	9.2	IPT
#33	0.72	3.7	IPL
#34	0.89	1.5	F1GAS
#35	0.95	2.9	IPT
#36	0.97	26.2	IPL

mode number	fitted frequency[Hz]	decay time [s]	excititon point
#37	1.03	10.8	IPT
#38	1.01	6.7	IPL
#39	1.16	17.7	MNY
#40	1.29	3.1	F1GAS
#41	1.36	25.7	IPT
#42	1.36	13.5	MNP
#43	1.48	197.4	MNT
#44	1.52	26.3	MNL
#45	1.73	0.5	MNR
#46	1.60	3.6	MNP
#47	1.70	1.7	MNY
#48	2.08	2.3	MNR
#49	2.00	3.0	MNP
#50	2.13	0.6	MNY
#51	2.49	58.6	MNT
#52	2.49	25.6	MNL
#53	3.19	13.3	MNY
#54			
#55	4.19	5.6	MNY
#56	5.20	12.6	MNT
#57	5.09	25.1	MNL
#58	7.53	19.7	MNP
#59	9.68	9.5	BFGAS
#60	14.97	0.5	MNR
#61	19.85	0.6	MNR
#62	20.17	0.5	MNR
#63	23.48	21.8	MNR
#64			
#65			
#66			
#67			
#68			
#69			
#70			
#71			
#72			
#73			
#74			
#75			
#NOT_IDed	0.13	168	BFY

Figure B.12: Measured decay time constants with controls.

Chapter C

Supplementary note for sensor correction system

C.1 Impact on X-arm cavity displacement signal

After implementing the same sensor-correction system at the IP-stage by a seismometer which senses the local ground motion (named IPsc), to the ITMX suspension, the impact of the IPsc to the X-arm cavity displacement is investigated. During this measurement, the X-arm cavity was locked with IR laser and the displacement signal is reconstructed from its control signal.

C.1.1 Setting for ITMX suspension

The high-pass filter cut-off of the sensor-correction filter for ITMX suspension is tweaked since the seismometer noise coupling at the frequency about below 0.1 Hz is more dominant compared to the ETMX case. The filter used is the obtained by multiplying high-pass filter at 0.5 mHz with forth order of Butterworth and an elliptic high-pass filter with 20 mHz cut-off whose order, passband ripple and the attenuation are set to second, 10 dB and 80 dB respectively. The phase shift due to this filter is given by 6.3 deg, which give 0.6 % difference. This filter is applied to the seismic displacement signal. The inertial sensors on the ITMX IP-stage are the accelerometers which are introduced in section 4.7.2.

The impact on the local ITMX suspension is shown in Figure C.1 to C.2. The TM-stage signal is not included since the measured spectra show only the self noise.

C.1.2 Impact on X-arm cavity displacement

The impact of the IPsc to the X-arm cavity displacement signal is summarized in Figure C.3. This figure shows the spectra and the coherence between some signals when the IPsc is off (*left*) and on (*right*). In this plot, differential and common motion of the IP-stages and the seismometers of ETMX (X-end station) and ITMX (X-front station) are denoted as *diff.IP_inertial*, *diff_seis* and *common_IP_inertial*. The signals labeled *sc_out* show the sensor-correction filtered signals which sent to the LVDT signals, and one labeled *gif* shows the

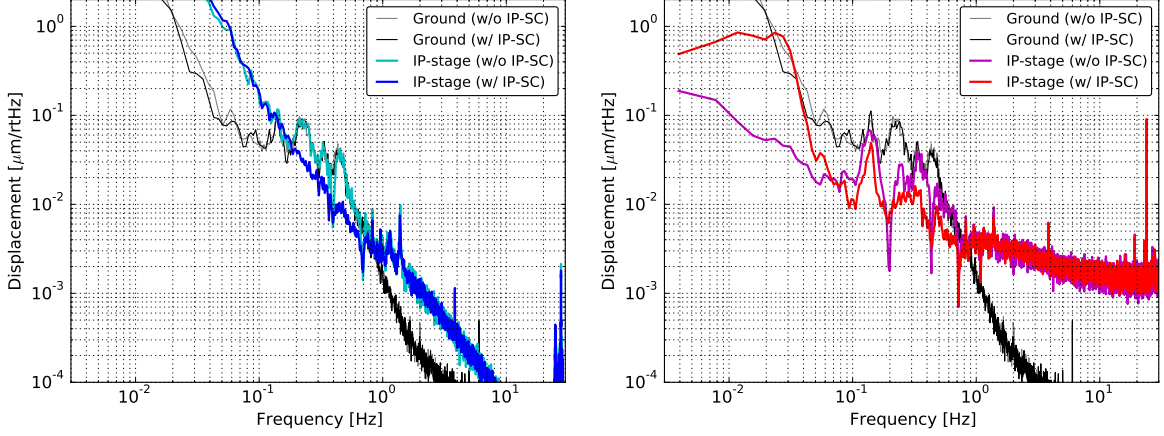


Figure C.1: Comparison of the IP-stage displacement spectrum measured by the inertial sensor, the accelerometer (*left*) and by the LVDT (*right*) when the IPsc is on and off at ITMX suspension. I note that in the *left* panel, the LVDT signal with and without IPsc is not compatible since one measures the displacement, while the other one observes the inertial motion basically.

strian meter signal which observes the differential motion of the ground along with the X-arm axis.

By comparing the spectra of common and differential IP-stage motion measured by the inertial sensors, it is observed both the amplitudes are suppressed with the IPsc as expected, even though this signals are reliable only in the frequency band between about 0.2 Hz to 1 Hz. In addition, the amplitude of X-arm cavity displacement signal becomes larger by roughly factor about 10 at 30 mHz due to the seismometer related noise.

Thus the sensor correction system with the local seismometers suppresses the local suspension motion at the frequency around 0.2 Hz, however, it is unavoidable to enhance the lower frequency amplitude. In addition, according to the coherence between the X-arm cavity displacement signal and the differential IP-stage motion measured by the inertial sensors, the coherence becomes smaller with the IPsc though still relatively high coherence is observed. This implies that the current IPsc system dose not compensate all of the suspension differential motion at the 0.2 Hz to 0.6 Hz. As another issue, the IPsc does not affect to the peak observed at about 150 mHz, which is the main residual motion of each suspension which IP sensor does not sense. In order to suppress this peak effectively, we need to sense the TM motion and to feedback to IP-stage (or BF-stage), except for the IPsc system. Since the current TM length optical lever is not sensitive enough to sense the TM motion except for the stormy condition, sensitivity improvement or other sensor for this purpose will be necessary in order to realize such system.

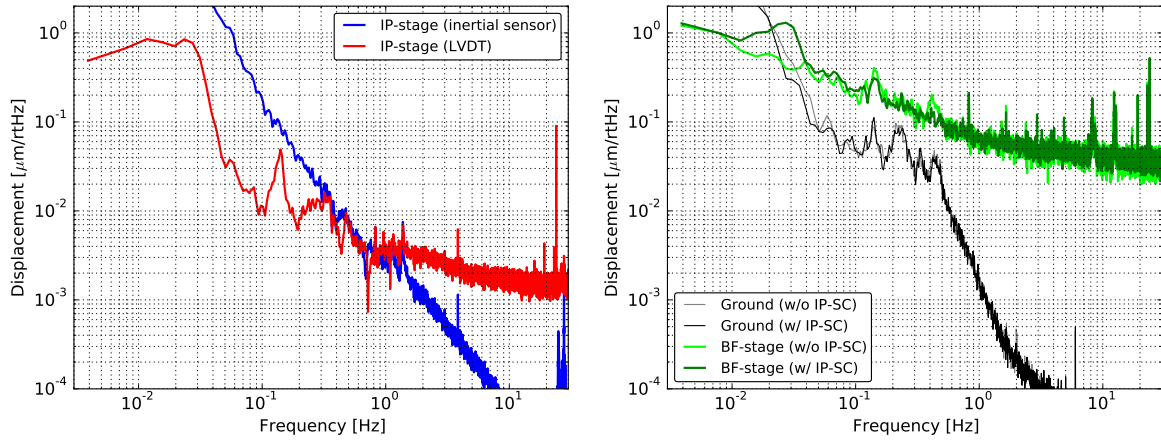


Figure C.2: Comparison between the sensor-corrected IP-LVDT signal and the accelerometer signal when the IPsc is on (*left*) and Comparison of the BF-stage displacement spectrum measured by the LVDT when the IPsc is on and off at ITMX suspension (*right*).

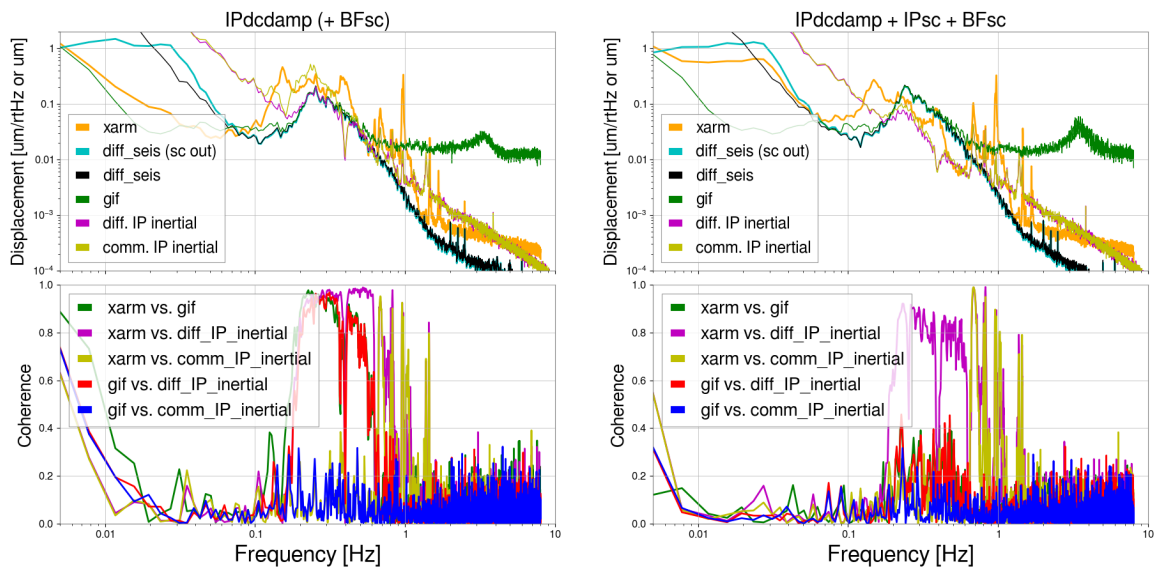


Figure C.3: spectra and the coherence between some signals when the IPsc is off (*left*) and on (*right*).

Bibliography

- [1] B. P. Abbott, R. Abbott, T. D. Abbott, F. Acernese, K. Ackley, C. Adams, T. Adams, P. Addesso, R. X. Adhikari, V. B. Adya, and et al. Multimessenger observations of a binary neutron star merger. *The Astrophysical Journal Letters*, 848:L12, October 2017.
- [2] B. P. Abbott et al. Prospects for observing and localizing gravitational-wave transients with advanced ligo and advanced virgo. *Living Reviews in Relativity*, 19(1):1, Feb 2016.
- [3] B. F. Schutz. Networks of gravitational wave detectors and three figures of merit. *Classical and Quantum Gravity*, 28(12):125023, 2011.
- [4] Y. Aso et al. Interferometer design of the kagra gravitational wave detector. *Phys. Rev. D*, 88:043007, Aug 2013.
- [5] T Akutsu et al. Construction of kagra: an underground gravitational-wave observatory. *Progress of Theoretical and Experimental Physics*, 2018(1):013F01, 2018.
- [6] C. S. Unnikrishnan. Indigo and ligo-india: Scope and plans for gravitational wave research and precision metrology in india. *International Journal of Modern Physics D*, 22(01):1341010, 2013.
- [7] A. Einstein. Die grundlage der allgemeinen relativitätstheorie. *Annalen der Physik*, 354(7):769–822, 1916.
- [8] B. P. Abbott et al. Observation of gravitational waves from a binary black hole merger. *Phys. Rev. Lett.*, 116:061102, Feb 2016.
- [9] Michele Maggiore. *Gravitational Waves: Volume 1: Theory and Experiments*. Oxford University Press, 2007.
- [10] Christian D Ott. The gravitational-wave signature of core-collapse supernovae. *Classical and Quantum Gravity*, 26(6):063001, feb 2009.
- [11] Thibault Damour and Alexander Vilenkin. Gravitational radiation from cosmic (super)strings: Bursts, stochastic background, and observational windows. *Phys. Rev. D*, 71:063510, Mar 2005.
- [12] K. Kawabe. PhD Thesis, University of Tokyo. 1998.

- [13] Akito Araya, Akiteru Takamori, Wataru Morii, Kouseki Miyo, Masatake Ohashi, Kazuhiro Hayama, Takashi Uchiyama, Shinji Miyoki, and Yoshio Saito. Design and operation of a 1500-m laser strainmeter installed at an underground site in kamioka, japan. *Earth, Planets and Space*, 69(1):77, 2017.
- [14] William J. Startin, Mark A. Beilby, and Peter R. Saulson. Mechanical quality factors of fused silica resonators. *Review of Scientific Instruments*, 69(10):3681–3689, 1998.
- [15] S. Rowan, G. Cagnoli, P. Sneddon, J. Hough, R. Route, E.K. Gustafson, M.M. Fejer, and V. Mitrofanov. Investigation of mechanical loss factors of some candidate materials for the test masses of gravitational wave detectors. *Physics Letters A*, 265(1):5 – 11, 2000.
- [16] T Tomaru, T Suzuki, T Uchiyama, A Yamamoto, T Shintomi, C.T Taylor, K Yamamoto, S Miyoki, M Ohashi, and K Kuroda. Maximum heat transfer along a sapphire suspension fiber for acryogenic interferometric gravitational wave detector. *Physics Letters A*, 301(3):215 – 219, 2002.
- [17] M. G. Beker. PhD Thesis, Vrije Universiteit. 2013.
- [18] Bruce Allen, Warren G. Anderson, Patrick R. Brady, Duncan A. Brown, and Jolien D. E. Creighton. Findchirp: An algorithm for detection of gravitational waves from inspiraling compact binaries. *Phys. Rev. D*, 85:122006, Jun 2012.
- [19] Stephen Fairhurst. Triangulation of gravitational wave sources with a network of detectors. *New Journal of Physics*, 11(12):123006, dec 2009.
- [20] Yoshinori Fujii, Thomas Adams, Frédérique Marion, and Raffaele Flaminio. Fast localization of coalescing binaries with a heterogeneous network of advanced gravitational wave detectors. *Astroparticle Physics*, 113:1 – 5, 2019.
- [21] T. Adams et al. Low-latency analysis pipeline for compact binary coalescences in the advanced gravitational wave detector era. *Class. Quant. Grav.*, 33(17):175012, 2016.
- [22] Cody Messick, Kent Blackburn, Patrick Brady, Patrick Brockill, Kipp Cannon, Romain Cariou, Sarah Caudill, Sydney J. Chamberlin, Jolien D. E. Creighton, Ryan Everett, Chad Hanna, Drew Keppel, Ryan N. Lang, Tjonnie G. F. Li, Duncan Meacher, Alex Nielsen, Chris Pankow, Stephen Privitera, Hong Qi, Surabhi Sachdev, Laleh Sadeghian, Leo Singer, E. Gareth Thomas, Leslie Wade, Madeline Wade, Alan Weinstein, and Karsten Wiesner. Analysis framework for the prompt discovery of compact binary mergers in gravitational-wave data. *Phys. Rev. D*, 95:042001, Feb 2017.

- [23] Alexander H. Nitz, Tito Dal Canton, Derek Davis, and Steven Reyes. Py-CBC Live: Rapid Detection of Gravitational Waves from Compact Binary Mergers. 2018.
- [24] GraceDB. Cited April 2019.
- [25] L. P. Singer and L. R. Price. Rapid bayesian position reconstruction for gravitational-wave transients. *Phys. Rev. D*, 93:024013, Jan 2016.
- [26] L. P. Singer et al. The first two years of electromagnetic follow-up with advanced ligo and virgo. *The Astrophysical Journal*, 795(2):105, 2014.
- [27] Jon R. Peterson. Observations and modeling of seismic background noise. Technical report, 1993. Report.
- [28] Peter M. Shearer. *Introduction to Seismology*. Cambridge University Press, 2 edition, 2009.
- [29] M. G. Beker, G. Cella, R. DeSalvo, M. Doets, H. Grote, J. Harms, E. Hennes, V. Mandic, D. S. Rabeling, J. F. J. van den Brand, and C. M. van Leeuwen. Improving the sensitivity of future gw observatories in the 1–10hz band: Newtonian and seismic noise. *General Relativity and Gravitation*, 43(2):623–656, Feb 2011.
- [30] Henry A. Sodano, Jae-Sung Bae, Daniel J. Inman, and W. Keith Belvin. Improved Concept and Model of Eddy Current Damper. *Journal of Vibration and Acoustics*, 128(3):294–302, 11 2005.
- [31] A. Takamori. PhD Thesis, University of Tokyo. 2002.
- [32] K. Okutomi. PhD Thesis, SOKENDAI. 2019.
- [33] T. Sekiguchi. PhD Thesis, University of Tokyo. 2016.
- [34] G. Cella, V. Sannibale, R. DeSalvo, S. Márka, and A. Takamori. Monolithic geometric anti-spring blades. *Nuclear Instruments and Methods in Physics Research Section A: Accelerators, Spectrometers, Detectors and Associated Equipment*, 540(2):502 – 519, 2005.
- [35] Alberto Stochino, Riccardo DeSalvo, Yumei Huang, and Virginio Sannibale. Improvement of the seismic noise attenuation performance of the monolithic geometric anti-spring filters for gravitational wave interferometric detectors. *Nuclear Instruments and Methods in Physics Research Section A: Accelerators, Spectrometers, Detectors and Associated Equipment*, 580(3):1559 – 1564, 2007.
- [36] H.M. Ledbetter and M.W. Austin. Elastic constant versus temperature behavior of three hardened maraging steels. *Materials Science and Engineering*, 72(1):65 – 69, 1985.

- [37] L. Trozzo. PhD Thesis, Università di Siena. 2018.
- [38] F Matchard, B Lantz, R Mittleman, K Mason, J Kissel, B Abbott, S Biscans, J McIver, R Abbott, S Abbott, E Allwine, S Barnum, J Birch, C Celerier, D Clark, D Coyne, D DeBra, R DeRosa, M Evans, S Foley, P Fritschel, J A Giaime, C Gray, G Grabeel, J Hanson, C Hardham, M Hillard, W Hua, C Kucharczyk, M Landry, A Le Roux, V Lhuillier, D Macleod, M Macinnis, R Mitchell, B O’Reilly, D Ottaway, H Paris, A Pele, M Puma, H Radkins, C Ramet, M Robinson, L Ruet, P Sarin, D Shoemaker, A Stein, J Thomas, M Vargas, K Venkateswara, J Warner, and S Wen. Seismic isolation of advanced LIGO: Review of strategy, instrumentation and performance. *Classical and Quantum Gravity*, 32(18):185003, aug 2015.
- [39] Y Aso, K Somiya, and O Miyakawa. Length sensing and control strategies for the LCGT interferometer. *Classical and Quantum Gravity*, 29(12):124008, jun 2012.
- [40] K. Somiya. Detector configuration of kagra—the japanese cryogenic gravitational-wave detector. *Classical and Quantum Gravity*, 29(12):124007, 2012.
- [41] F. Cordero, F. Corvasce, R. Franco, G. Paparo, E. Maiorana, P. Rapagnani, F. Ricci, S. Braccini, C. Casciano, R. De Salvo, F. Frascioni, R. Passaquieti, M. De Sanctis, A. Solina, and R. Valentini. Elastic and anelastic properties of marval 18 steel. *Journal of Alloys and Compounds*, 310(1):400 – 404, 2000. Intern. Conf. Internal Friction and Ultrasonic Attenuation in Solids (ICIFUAS-12).
- [42] Y. Sakakibara. PhD Thesis, University of Tokyo. 2015.
- [43] T. Yamada. Master’s Thesis, University of Tokyo. 2018.
- [44] T. Ochi. Master’s Thesis, University of Tokyo. 2018.
- [45] Hareem Tariq, Akiteru Takamori, Flavio Vetrano, Chenyang Wang, Alessandro Bertolini, Giovanni Calamai, Riccardo DeSalvo, Alberto Gennai, Lee Holloway, Giovanni Losurdo, Szabolcs Márka, Massimo Mazzoni, Federico Paoletti, Diego Passuello, Virginio Sannibale, and Ruggero Stanga. The linear variable differential transformer (lvdt) position sensor for gravitational wave interferometer low-frequency controls. *Nuclear Instruments and Methods in Physics Research Section A: Accelerators, Spectrometers, Detectors and Associated Equipment*, 489(1):570 – 576, 2002.
- [46] Virgo Internal Document. Advanced Virgo Technical Design Report, VIR-0128A-12. 2012.

- [47] Riccardo Desalvo. Review: Accelerometer development for use in gravitational wave-detection interferometers. *Bulletin of the Seismological Society of America*, 99, 05 2009.
- [48] R. Sleeman. Three-Channel Correlation Analysis: A New Technique to Measure Instrumental Noise of Digitizers and Seismic Sensors. *The Bulletin of the Seismological Society of America*, 96(1):258–271, Feb 2006.
- [49] S. Zeidler. KAGRA Internal Document, JGW-T1605788. 2016.
- [50] M. Fukunaga. Master’s Thesis, University of Tokyo. 2019.
- [51] Trillium120QA user’s guide. Cited December 2019.
- [52] Eric D. Black. An introduction to pound–drever–hall laser frequency stabilization. *American Journal of Physics*, 69(1):79–87, 2001.
- [53] Adam J. Mullavey, Bram J. J. Slagmolen, John Miller, Matthew Evans, Peter Fritschel, Daniel Sigg, Sam J. Waldman, Daniel A. Shaddock, and David E. McClelland. Arm-length stabilisation for interferometric gravitational-wave detectors using frequency-doubled auxiliary lasers. *Opt. Express*, 20(1):81–89, Jan 2012.
- [54] Yuta Michimura, Tomofumi Shimoda, Takahiro Miyamoto, Ayaka Shoda, Koki Okutomi, Yoshinori Fujii, Hiroki Tanaka, Mark A Barton, Ryutaro Takahashi, Yoichi Aso, Tomotada Akutsu, Masaki Ando, Yutaro Enomoto, Raffaele Flaminio, Kazuhiro Hayama, Eiichi Hirose, Yuki Inoue, Takaaki Kajita, Masahiro Kamiizumi, Seiji Kawamura, Keiko Kokeyama, Kentaro Komori, Rahul Kumar, Osamu Miyakawa, Koji Nagano, Masayuki Nakano, Naoko Ohishi, Ching Pin Ooi, Fabián Erasmo Peña Arellano, Yoshio Saito, Katsuhiko Shimode, Kentaro Somiya, Hiroki Takeda, Takayuki Tomaru, Takashi Uchiyama, Takafumi Ushiba, Kazuhiro Yamamoto, Takaaki Yokozawa, and Hirotaka Yuzurihara. Mirror actuation design for the interferometer control of the KAGRA gravitational wave telescope. *Classical and Quantum Gravity*, 34(22):225001, oct 2017.
- [55] K. Izumi. Master’s Thesis, University of Tokyo. 2009.
- [56] Y. Michimura Y. Enomoto and K. Izumi. KAGRA Internal Document, JGW-T1808343. 2018.
- [57] Y. Michimura. KAGRA Internal Document, JGW-T1202403. 2014.
- [58] D. Martynov. PhD Thesis, California Institute of Technology. 2015.
- [59] J. Abadie et al. Sensitivity Achieved by the LIGO and Virgo Gravitational Wave Detectors during LIGO’s Sixth and Virgo’s Second and Third Science Runs. 2012.

- [60] M. Barsanti, M. Beghini, F. Frasconi, R. Ishak, B.D. Monelli, and R. Valentini. Experimental study of hydrogen embrittlement in maraging steels. *Procedia Structural Integrity*, 8:501 – 508, 2018. AIAS2017 - 46th Conference on Stress Analysis and Mechanical Engineering Design, 6-9 September 2017, Pisa, Italy.